Third International Workshop on Low-Temperature Physics in Microgravity Environment (CWS-2002)

Fiz. Nizk. Temp. Fiz. Nizk. Temp. **29**, 611–617 (June 2003)

The Third International Workshop on Low-Temperature Physics in Microgravity Environment (CWS-2002) was held at the Chernogolovka Research Center of the Russian Academy of Sciences from the twelfth through the eighteenth of August 2002. CWS-2002 was one of the satellite conferences and seminars devoted to some rapidly developing area of low-temperature physics which are traditionally held in conjunction with the International Conference on Low-Temperature Physics, which meets once every three years (LT-23 was held in Hiroshima, Japan on August 20–27, 2002). CWS-2002 was organized by the Institute of Solid State Physics of the Russian Academy of Sciences (ISSP RAS) and the Space Materials Science Section of the Space Council of the RAS, with the support of the RAS, the Ministry of Industry, Science and Technology of the Russian Federation, the Russian Foundation for Basic Research, and the Russian Aerospace Agency (Rosaviakosmos). We are also grateful to the Organizing Committee of LT-23 (especially to Prof. Shun-ichi Kobayashi and Dr. Kimitoshi Kono), the U.S. National Aeronautics and Space Administration (NASA) and Jet Propulsion Laboratory (JPL) (Dr. M. C. Lee and Dr. U. E. Israelsson), and to the INTAS foundation (Grant 02-MO-263, principal investigator Prof. L. Esquivias). At the Workshop, roundtable discussions were held with participants from the various projects supported by INTAS in 2001 and 2002. [DOI: 10.1063/1.1542526]

An active role in preparing the scientific program and running the Workshop was played by the International Organization and Program Committee and members of the Local Committee, the staff of the ISSP RAS, M. Yu. Brazhnikov, V. B. Efimov, A. M. Kokotin, G. V. Kolmakov, N. F. Lazareva, E. V. Lebedeva, A. A. Levchenko, O. I. Levchenko, M. K. Makova, Yu. M. Romanov, and V. B. Shikin.

At the sessions of the CWS-2002 there were around 120 participants from 10 countries: Russia, Ukraine, USA, Finland, Kazakhstan, Denmark, France, England, Japan, and Gruziya (Georgia), who represented the National Space Agencies of Russia, Ukraine, USA, and Japan and also the administrations of the Academies of Sciences and universities of a number of countries doing research in low-temperature physics and engineering and having a potential interest in setting up the corresponding experiments onboard spacecraft. Seventy-two reports were presented at the talks and poster sessions, and the abstracts were published in Ref. 1. Since the volume of papers recommended for publication and revised by the authors in accordance with the remarks of the referees is too large to be published in one issue of *Low Temperature Physics*, only a portion of the final versions sent to the Program Committee, those closest to the theme of the Workshop, are published in this issue. It is assumed that the remainder of the submitted reports will be published in the journal in 2003 without additional refereeing, with a note indicating that they had been presented at CWS-2002.

The theme of the reports presented at the Workshop can be briefly summarized as follows:

— the main trends in low-temperature research in space; plans for doing new basic research and creating the necessary engineering base for doing low-temperature experiments onboard the International Space Station (ISS);

— modeling of the heat transfer processes at a solid–liquid helium boundary in a microgravity environment;

— nonlinear waves in the bulk and on the surface of quantum liquids; features of the growth of helium crystals and phenomena occurring on the surface of solid helium;

— nanocluster condensates in superfluid helium;

— cryofilms and cryocrystals;

— ultracold atoms and particles, Bose–Einstein condensates.

Since only about half of the 72 reports presented at talks and poster sessions were prepared by the authors for publication, let us briefly discuss the contents of the most interesting of them for a wider audience.

1. In their addresses at the opening of the sessions, Workshop Chairman Yu. A. Osip'yan and Rosaviakosmos representative Yu. E. Levitskiĭ noted that in the 45 years since the launching of the first artificial Earth satellite from the Baikonur Test Range, space engineering and technology has firmly entered the life of modern society (satellite communications and television, meteorological service, navigation, etc.). The use of the achievements of modern science in space engineering leads to a broader range of practical applications of space vehicles, which, in turn, stimulates new basic research in orbit. Meanwhile, the high cost of a space experiment makes it necessary to have a multistage government system of competitive selection, providing support in the first stage to a broad range of ground-based research to establish the necessary base for the subsequent choice of the most worthwhile and best-prepared experiments onboard spacecraft. All of this must be taken into account in formulating long-term plans for space-based research.

Progress in space research owes much to the widespread adoption of cryogenic techniques. Not only do cryogenic liquids, primarily liquid oxygen and hydrogen, serve as fuel elements for space propulsion, but detectors and electronic devices cooled to helium temperatures make it possible to improve the sensitivity and resolution of the monitoring and

measuring apparatus by orders of magnitude and thereby to realize the advantages of doing long-term scientific research in orbit under conditions inaccessible to ground-based experiments.[2] For example, the Infrared Space Laboratory (ISO), placed in a highly elliptical orbit by the European Space Agency (ESA) in 1995, was based on a cryostat with a capacity of 2200 liters, filled before launch by superfluid He II at a temperature of 1.8 K. The detector on the ISO was a set of cooled semiconductor resistors with working temperatures ranging from 1.8 to 10 K. In today's x-ray spectrometers the use of detectors cooled to 65 mK is projected.[2]

In the next two years the multiprofile ISS should be completely constructed, including, in particular, the large-scale Russian research segment (RS ISS). In 2005–2007, an atomic clock utilizing metal atoms cooled by a laser method to temperatures of hundredths to thousandths of a microkelvin will be installed onboard. This will improve the relative resolution in measurements of short (of the order of seconds) time intervals by several orders of magnitude (from 10^{-14} to 10^{-17}).[3] Programs of basic scientific research onboard the ISS and also on returnable space packages are being planned and carried out under the aegis of Rosaviakosmos, the national space agencies of the USA, the European Union, Japan, China, Canada, Ukraine, and other countries. Undoubtedly the discussion of the results of onboard experiments and of the plans for new research in a large auditorium with the participation of young scientists and of researchers specializing in this specific field of study will make for a more efficient selection process for future experiments and will draw in new investigators. This was among the main goals of the Third International Workshop on Low-Temperature Physics in Microgravity Environment.

2. The results of space experiments carried out in the last decade under the aegis of NASA to investigate kinetic phenomena in superfluid helium near the point T_λ of the phase transition of the liquid from the superfluid to the normal state and plans for new basic research onboard the ISS in the coming five years were discussed in the reports by U. Israelsson,[3] J. Pensinger,[4] and D. Strayer.[5] Three series of experiments were done in 1985, 1992, and 1997. They were able, in particular, to study the behavior of the specific heat of superfluid He II in the immediate proximity of T_λ (less than 10^{-9} K from the transition point under equilibrium conditions) and, accordingly, to refine the values of the parameters (critical exponents) appearing the theory of second-order phase transitions and also to investigate the influence of the pore size on the shift of the transition T_λ in He II filling a finely porous sample. We note that in a ground-based laboratory the pressure gradient in a column of superfluid liquid 1 cm in height under the influence of the Earth's gravity leads to a shift in T_λ from its equilibrium value by 10^{-6} K, and if one turns to thin films it is necessary to take into account the influence of the interaction of the liquid with the walls, i.e., making the measurements in microgravity permitted advancing into a temperature region near T_λ which was inaccessible in ground-based laboratories. To ensure the high temperature resolution, at a level of $\sim 1\times 10^{-10}$ K, the thermometers used were samples of a paramagnetic salt, the susceptibility of which was measured by a specially made high-resolution SQUID. The use of such high-resolution apparatus, in combination with the accumulated experience in low-temperature studies in orbit, made it possible to expand the possibilities of subsequent space experiments.

NASA's plans for basic research onboard the ISS in the coming five years include experiments in low-temperature and atomic physics, which should be begun in 2005 and continue until 2007, and research in gravitational physics, with onboard experiments projected to start in 2007. To provide for doing the low-temperature and gravitational research on an outlying unit of the Japanese research module of the ISS, it will be necessary to install special low-temperature equipment (the Low Temperature Microgravity Physics Facility, LTMPF), the ground-based testing of which is being done at the present time at JPL. LTMPF contains a 180-liter Dewar containing superfluid He II and electronic equipment for measurement and control of the temperature, pressure, liquid helium level, etc. in the Dewar and also for linking with the external sensors of the radiation environment and accelerometers (the first unit) and two units for control and measurement apparatus, including a SQUID magnetometer for precision measurements of the readings of the magnetic thermometers. This equipment will be used to conduct two independent experiments on two low-temperature platforms simultaneously, which are mounted inside the Dewar on special supports fastened to the ends of the cylindrical Dewar. Each of the platforms can be used for the main experiment and, in its spare time, for one or two additional experiments.

According to the presentation, the scientific research at the LTMPF should begin in the second half of 2005. The Dewar will be filled with helium and cooled to 1.7 K on Earth shortly before launch. The Dewar should operate in orbit for around 4.5 months. Then the LTMPF package will be returned to Earth. A repeat launch of the apparatus into orbit is projected for 16–22 months later.

The first two low-temperature experiments on the ISS will be devoted to a study of nonequilibrium phenomena near a phase transition point: a) critical phenomena near T_λ in He II (Critical Dynamics in Microgravity, DYNAMX), to determine the behavior of the thermal conductivity near a superfluid–normal liquid interface, where a substantial role is played by nonlinear effects (minimal acceleration is necessary to reduce the variations of the pressure along the column of liquid), and b) thermodynamic measurements near the liquid–gas critical point in ^{3}He (Microgravity Scaling Theory Experiment, MISTE), to determine the critical exponents in the immediate vicinity of the critical point T_{cr}. Additional experiments in this series include measurements of the heat capacity of He II at constant heat flux near T_λ (Capacity at constant Q, CQ) and measurement of the liquid–vapor coexistence curve of ^{3}He near T_{cr} (Coexistence Curve Experiment, COEX).

A second series of experiments in low-temperature physics at LTMPF include: a) a study of boundary effects in He II near T_λ (Boundary Effects near the Superfluid Transition, BEST), to investigate the properties of a superfluid in quasi-one-dimensional and three-dimensional vapors, to check the suitability of the dynamic scaling theory, and to study critical transport phenomena in vapors; b) experiments with a highly stable superconducting microwave oscillator (Superconducting Microwave Oscillator, SUMO), to study the features of

the interaction of bodies of different mass at small distances. The results of these studies may be of interest for refining the present-day concepts of the special and general theories of relativity, and the apparatus itself may be used in future experiments with atomic clocks in orbit on the ISS. The competitive selection of the most promising projects for additional experiments will continue.

Together with the low-temperature LTMPF facility, in 2005 it is planned to install a package for experiments with ultracold atoms with laser cooling (Laser Cooled Atom Physics, LCAP). The accompanying instrumentation for this experiment will be designed for a wide range of experiments and, foremost, to support long-term (over 1 year) experiments in gravitational physics with the use of a highly stable atomic clock (Primary Atomic Clock in Space, PARKS). The launch of PARKS in the second half of 2005 will permit an improvement by one to two orders of magnitude in measurements of time intervals of the order of seconds in comparison with the existing capabilities (expected resolution to 10^{-16} s) and to start experiments for checking Einstein's hypothesis of the invariance of time, by a comparison of the working frequency of different clocks at different parts of the orbit. At the end of 2007 a rubidium atomic clock should be installed (Rubidium Atomic Clock Experiment, RACE). It is assumed that this will give still another order of magnitude improvement in the time resolution as compared to PARKS and will thus permit the range of application of the atomic clock in basic research to be broadened substantially.

NASA's plans also include the creation of a condensed-state laboratory onboard the ISS (Condensate Laboratory Aboard the Space Station, CLASS), designed for cooling atoms substantially below 10^{-9} K and observing Bose–Einstein condensation (BEC) in mixtures of atomic gases in reduced gravity. Then, by using cooled rubidium and cesium atoms as test masses, one can test the principle of equivalence of gravitational and inertial mass (Quantum Interferometer Test of Equivalence, QuITE). The competition of plans for additional experiments in atomic and graviational physics with the use of the equipment mentioned above will continue in 2003.

According to the report by Yu. Okuda,[6] the Japanese Space Agency NASDA is also making a competitive selection of proposals for doing low-temperature experiments onboard the ISS. The list of projects adopted includes the following: ''Studies of non-equilibrium effects near the critical point,'' A. Onuki, Kyoto University; ''Non-linear dynamics on the non-equilibrium open system under control of laser,'' K. Yoshikawa, Kyoto University; ''Basic research on crystal growth and surface physics of quantum crystals under microgravity,'' Y. Okuda, Tokyo Institute of Technology; ''Instability of shear flow in a liquid near the critical point,'' A. Onuki, Osaka Prefecture University; ''Variation principle for non-equilibrium reaction-diffusion systems under gravity,'' K. Kitahara, International Christian University; and, ''Structure of particulate layer under microgravity,'' K. Nakamura, Kyoto University.

3. Plans for research in low-temperature physics and cryogenic technique onboard the RS ISS were presented at the Workshop in the report by the M. M. Tsymbalyuk[7] of the Central Scientific Research Institute of Mechanical Engineering (CSRIME) (see Table I) and V. A. Shuvalov[8] of Rosaviakosmos and in the address S. I. Bondarenko,[9] a representative of the Ukrainian Space Agency.

We note that the durations of experiments onboard the RS ISS have not yet been established, and discussions of the plans continues, so the list in Table I may be altered considerably in the future. For example, the possibility of doing the series of experiments included in the Kriokompleks, Kipenie, and Edinstvo projects, which call for a rather large expenditure of liquid helium in orbit, depends primarily on the choice of the overall organizational concepts for the low-temperature research onboard the RS ISS. In the Kriokompleks project, the content of which was discussed in the report cited as Ref. 8, in order to permit making prolonged measurements at several temperature levels it is proposed to install, outside the living unit of the RS, three stationary helium Dewars connected with a system for flooding with liquid helium and for collection, storage, and liquefaction of the cold gas, i.e., effectively it is proposed to assemble onboard the RS ISS an autonomous cryogenic station capable of simultaneously supplying three different experiments in orbit, including experiments on heat and mass transfer and the dynamics of the formation and motion of gas bubbles in liquid helium. The project Kipenie,[7,9] developed by the Ukrainian Space Agency, calls for the study of boiling processes in a rotating Dewar for studying the features of the heat transfer at the liquid helium–solid wall boundary under conditions of reduced gravity, with acceleration a level of $(10^{-2}-10^{-6})g$.

The projects Geliĭ and Volna share a common task—computer modeling and experimental studies of heat and mass transfer processes in the bulk of a freely boiling liquid (liquid helium or nitrogen) and of phenomena at the interface between the cryogenic liquid and the solid wall under conditions of microgravity (the mechanisms of boiling, the growth of bubbles, and the features of the heat transfer in a two-phase system). Several of these problems were discussed in the reports by A. P. Kryukov[10] and V. I. Polezhaev.[11] The experimental study of these topics is also necessary for solving practical problems arising in the use of cryogenic liquids in space propulsion units and in the cooling systems for onboard equipment.

In the framework of the Soliton project it is proposed to do a series of static and dynamic studies of phenomena occurring on a charged liquid hydrogen surface in a cell of finite size. As was mentioned in the report by A. A. Levchenko,[12] in a series of ground-based experiments performed at ISSP RAS a reconstruction of the shape of the liquid surface was observed: when an external pulling electric field was increased above a certain critical value E_{cr}, a hill (solitary standing wave) formed on the initially flat, uniformly charged surface of liquid hydrogen, and the height of the hill increased with increasing field. It follows from theoretical calculations that the observed reconstruction of the flat charged surface can be described in terms of the theory of second-order phase transitions, where the role of the external force is played not by temperature, as in the usual treatment, but by the pulling electric field. The reconstruction is observed under conditions such that the applied electric field compensates the force of gravity. The transition to mea-

TABLE I. The main research topics in low-temperature physics on the Russian segment of the International Space Station.

Name of experiments	Research content	Main proposed participants
Geliĭ (Helium)	Basic research on the helium interphase surface	MEI, RSC "Energiya," RSSRI Gagarin CTC, etc.
Volna-3 MKS (Wave-3 ISS)	Research on heat and mass transfer and hydrodynamics in a tank containing cryogenic liquid	M. V. Keldysh Research Center, RSC "Energiya," RSSRI Gagarin CTC
Kipenie (Boiling) group of space experiments	Basic research in the low-temperature physics, the development of methods and equipment for efficient and safe performance of cryogenic experiments in the infrastructure of the RS ISS	CSRIME, MEI, RRC "KIAE," Institutes of the RAS (ISP, IHT, FIAN), and ILTPE NASU
Edinstvo (Unity)	Basic and applied research in low-temperature physics and engineering	CSRIME, SRINP MSU, RSC "Energiya," and other organizations
Kryokompleks (Cryocomplex)	Implementation of a unified complex of onboard cryogenic equipment for the simultaneous performance of several experiments onboard the RS ISS	CSRIME, MEI, RSC "Energiya," and other organizations
Soliton	Basic research on nonlinear phenomena on the condensed hydrogen surface	ISSP RAS, RSC "Energiya," RSSRI Gagarin CTC, and other organizations
Submillimetron	Basic astrophysical research using cryogenic telescope in the submillimeter band of electromagnetic waves, inaccessible from Earth	AKTs FIRAS, RSC "Energiya," RSSRI Gagarin CTC, international cooperation
AMS	Implementation of basic physical and astrophysical research with the use of an alpha magnetic spectrometer with a superconducting magnet system	SRINP MSU, RRC "Kurchatov Institute," international cooperation
BSMK (OSFC)	Development of processes for drying biological preparations using onboard sublimation-freezing complex (OSFC)	RAO "Biopreparat," AOOT "Biokhimmash," RSC "Energiya," RSSRI Gagarin CTC
Kriokonservatsiya (Cryopreservation)	Development of methods and equipment for cryogenic preservation of biological preparations on the RS ISS	"Energiya," "Biokhimmash," "Biopreprat," Gagarin CTC
"Kristallizator," (Crystallizer)	Research on physical processes of protein crystallization with the use of cryogenic equipment	CSRIME, IC RAS
Poligon-1 (Polygon-1)	Development of methods for qualitative and quantitative determination of pollutants of the atmosphere and surface of the Earth with the use of cryogenic IR gas analyzers	CSRIME and other organizations

surements in microgravity, where a substantial role in a cell of finite size should be played by the interaction of the liquid with the walls of the vessel, can qualitatively alter the character of the observed phenomena. This is also indicated by the results of control studies of the evolution of the shape of a surface of a charged film of liquid hydrogen suspended from the surface of the upper plate of the horizontally situated parallel-plate capacitor, where the electric and gravitational forces act in the same direction. If an alternating electric field is applied in addition to the static field, then waves will arise on the surface of the liquid. The laboratory experiments have demonstrated the possibility of establishing a regime of weak wave turbulence at a liquid helium surface at rather high levels of excitation. Moreover, the high-frequency edge of the Kolmogorov spectrum of oscillations could be observed, where the wave regime of energy transfer gives way to viscous damping. The reconstruction of the surface markedly alters the shape of the dispersion curve $\omega(\kappa)$, which describes how the frequency of waves propagating along the liquid hydrogen surface depends on the wave vector, and this, in turn, should strongly influence the spectrum of nonlinear waves arising on the surface of the liquid under the influence of the alternating force. All of this indicates that doing experiments to investigate nonlinear waves on charged surfaces of liquid hydrogen onboard the space station can substantially broaden the existing ideas about nonlinear phenomena in condensed systems and, in particular, lead to an understanding of the features of the propagation of capillary waves on the surface of a liquid in microgravity.

The projects Submillimetron and AMS are proposed by a broad international cooperative with the particpation of Russian and foreign scientists collaborating with ESA and NASA: in the first-mentioned of these experiments the superconducting radiation detectors and electronics are furnished by foreign scientists, while the preparation of all the remaining equipment and the launching of the telescope into orbit is done by the Russian side; in the second of these

experiments it is assumed that the Russian side will prepare only the superconducting magnet system of the alpha spectrometer. A version of the magnet system devised at the Kurchatov Institute of Atomic Energy (KIAE) was presented at at the Workshop in a report by N. A. Chernoplekov.

In the last four projects listed in Table I, cryogenic techniques are used to provide the required temperature regimes for experiments in biology and Earth physics.

4. As may be seen from the previous Section, the reports presented at CWS-2002 were considerably broader thematically than the research in low-temperature physics included in the plans of Rosaviakosmos, NASA, and the other space agencies for the coming five years. Among the promising areas of study that can be recommended for inclusion in the list of ground-based research projects supported by the national space agencies is research on the property of cryofilms formed by condensation of the substance to be investigated on a cold substrate; these are discussed, for example, in the reports by M. A. Strzhemechny[13] and A. S. Drobyshev,[14] and the recent new fields of research on the properties of impurity nanocluster condensates (gels) which are formed in the condensation of a gaseous flow of superfluid He II containing a vaporous impurity of the substance to be investigated (the reports by V. V. Khmelenko, E. A. Popov, and L. P. Mezhov-Deglin[15–17]). The mechanism of formation of the impurity clusters in a cold helium jet, the features of the interaction of these clusters with one another and with the surrounding medium at temperatures of the order of 1 K, and the structure and properties of porous nanocluster systems—gels, the disperse system (skeleton) of which is formed by impurity clusters surrounded by a layer of solidified helium and the dispersion medium of which is the liquid helium, the influence of the gravitational environment on the properties of the condensates formed (terrestrial measurements, experiments in microgravity) are all questions whose elucidation will be important not only for modern materials science, including condensed-state physics, but also for astrophysics and cosmology (dust clouds in space at temperatures of the order of 3 K, cosmic ice, etc.). There is reason to think that impurity gels in superfluid He II may be used for accumulation and storage of free radicals (low-temperature fuel cells)[15] and also for the accumulation and storage of ultracold neutrons. Achievements in the physics of ultracold neutrons were the subject of a report by V. V. Nesvizhevsky[18] in a closed seminar.

Additional information about the workshop CWS-2002 can be found at the site http://www.issp.ac.ru/cws2002/.

[1] *The Third Chernogolovka Workshop on Low Temperature Physics in Mocrogravity Environment CWS-2002, -Book of Abstracts*, Chernogolovka, Russia (2002).
[2] B. Collaudin and N. Rando, "Cryogenics in space: a review of the missions and technologies," Cryogenics **40**, 797 (2000).
[3] U. E. Israelsson and M. C. Lee, "Use of the International Space Station for fundamental physics research," *Book of Abstracts CWS-2002*, p. 12.
[4] J. F. Pensinger, A. P. Croonquist, F. C. Liu, M. E. Larson, and T. C. Chui, "The Low Temperature Microgravity Physics Facility," *Book of Abstracts CWS-2002*, p. 15.
[5] D. M. Strayer, H. J. Paik, and M. V. Moody, "Short-range inverse-square law experiment in space," *Book of Abstracts CWS-2002*, p. 16.
[6] Y. Okuda, R. Nomura, Y. Suzuki, S. Kimura, and S. Burmistrov, "Manipulation of solid–liquid Interface of ^{4}He by acoustic radiation pressure," *Book of Abstracts CWS-2002*, p. 23.
[7] N. A. Anfimov, V. I. Lukjashchenko, V. V. Suvorov, M. M. Tsymbalyuk, and B. V. Bodin, "Major directions of research on low temperature physics and engineering on board the Russian segment of the International Space Station," *Book of Abstracts CWS-2002*, p. 11.
[8] S. V. Buskin, V. I. Lukjashchenko, V. V. Suvorov, I. Yu. Repin, V. A. Shuvalov, and Yu. E. Levitskii, "Technological integration of low-temperature studies at the ISS RS and optimization of experimental equipment," *Book of Abstracts CWS-2002*, p. 14.
[9] S. I. Bondarenko, R. V. Gavrylov, V. V. Eremenko, K. V. Rusanov, N. S. Shcherbakova, I. M. Dergunov, A. P. Kryukov, P. V. Korolyov, Yu. Yu. Selyaninova, V. M. Zhukov, V. S. Kharitonov, K. V. Kutsenko, V. I. Deev, and V. A. Shuvalov, "Physical research of microgravity influence on physical phenomenon in cryogenic liquids and general-purpose onboard cryogenic facility for realization of this research aboard International Space Station," *Book of Abstracts CWS-2002*, p. 13
[10] I. M. Dergunov, P. V. Korolyov, A. P. Kryukov, and Yu. Yu. Selyaninova, "Superfluid helium noiling in the model of porous structure at microgravity," *Book of Abstracts CWS-2002*, p. 63.
[11] V. I. Polezhaev and E. B. Soboleva, "Thermal gravity-driven convection of near-critical fluids in enclosures with different heating," *Book of Abstracts CWS-2002*, p. 19; A. A. Gorbunov and V. I. Polezhaev, "Isoenthropic equilibrium stability of the near-critical fluid under zero gravitation," *Book of Abstracts CWS-2002*, p. 63.
[12] A. A. Levchenko, M. Yu. Brazhnikov, G. V. Kolmakov, and L. P. Mezhov-Deglin, "Capillary turbulence at the charged surface of liquid hydrogen," *Book of Abstracts CWS-2002*, p. 29.
[13] M. A. Strzhemechny, "Properties of quenched hydrogen-based alloys with lighter elements from diffraction measurements," *Book of Abstracts CWS-2002*, p. 48.
[14] A. Drobyshev, A. Aldijarov, K. Abdykalykov, Sh. Sarsembinov, and A. Shelyagin, "Enthalpy of the hydrogen bonds from measurements made on thin water films," *Book of Abstracts CWS-2002*, p. 50.
[15] S. I. Kiselev, V. V. Khmelenko, and D. M. Lee, "ESR investigation of hydrogen and deuterium atoms in impurity–helium solids," *Book of Abstracts CWS-2002*, p. 37.
[16] E. A. Popov, J. Eloranta, J. Ahokas, and H. Kunttu, "Emission spectroscopy of atomic and molecular nitrogen in helium gas jet, bulk liquid He-II, and in impurity-helium solids," *Book of Abstracts CWS-2002*, p. 38.
[17] L. P. Mezhov-Deglin and A. M. Kokotin, "Water–helium condensate (watergel) in liquid helium," *Book of Abstracts CWS-2002*, p. 39.
[18] V. V. Nesvizhevsky, H. G. Boerner, A. K. Petukhov, H. Abele, S. Baessler, F. J. Ruess, Th. Stoeferle, A. Westphal, A. M. Gagarsky, G. A. Petrov, and A. V. Strelkov, "Quantum states of neutrons in the Earth's gravitational field," *Book of Abstracts CWS-2002*, p. 55.

Yu. A. Osip'yan, Workshop Chairman

Chairman of the Space Materials Science Section of the Space Council of the Russian Academy of Sciences

L. P. Mezhov-Deglin

Chairman of the Program and Local Committees

Main fields of study in low-temperature physics and engineering on the Russian segment of the International Space Station

N. A. Anfimov, V. I. Luk'yashchenko, V. V. Suvorov,* and M. M. Tsimbalyuk

Central Scientific-Research Institute of Mechanical Engineering, ul. Pionerskaya 4, 1401070 Korolev, Moscow Region, Russia

B. V. Bodin

Russian Aerospace Agency, ul. Shchepkina 42, 107996 Moscow GSP-6, Russia
(Submitted December 19, 2002)
Fiz. Nizk. Temp. **29**, 618–623 (June 2003)

The main trends in the evolutionary development of a long-term research program for the Russian segment of the International Space Station (RS ISS) are elaborated with allowance for the proposed changes in the final configuration of the ISS, the existing ideas about the conducting of joint experiments, and the desire of the scientific community for more efficient programs with real returns on the practical level. The main fields of study in low-temperature physics and engineering are analyzed. © *2003 American Institute of Physics.*
[DOI: 10.1063/1.1542527]

The ''Long-term program of applied scientific research and experiments planned for the Russian segment of the International Space Station (RS ISS)'' and the ''Programs for implementation of applied scientific research on the RS ISS in the deployment period (1999–2003)'' which were stated by Yu. N. Koptev, General Director of the Russian Aerospace Agency (Rosaviakosmos), and Acad. Yu. S. Osipov, President of the Russian Academy of Sciences[1] were developed with an appreciation of the enormous experience of Russian cosmonauts in the development and practical implementation of research programs on manned space platforms from the 1960s to the present. Among these programs were the ''Program of applied scientific research planned for the Mir orbital complex in the period 1997–1999,'' which was formulated in 1997 on the basis of an open competition of proposals.

The Science and Engineering Coordinating Council (SECC) of the Russian Aerospace Agency (Rosaviakosmos), which was started in 1994 by a joint resolution of Rosaviakosmos and the Russian Academy of Sciences (RAS) for the purpose of developing research programs for the long term and for the deployment stage of the RS ISS on a competitive basis, is working successfully to foster the evolutionary development and refinement of these programs to reflect the results of previously performed research and the arrival of new opportunities. Part of its mission is to develop research programs and experiments for manned space platforms and to provide the scientific and engineering resources required for carrying them out. In essence the SECC of Rosaviakosmos is a collegial council of experts responsible for the strategic planning of research on manned space platforms. In individual cases the Council members join in solving the most complex and important problems in the tactical planning and monitoring of the progress in the implementation of research on the RS ISS, with the development of specific recommendations for the purposeful utilization of the RS ISS.

The necessary scientific/methodological approaches along with mechanisms for developing and implementing scientific and applied research programs have already been worked out in the planning and execution of the previously mentioned ''Program of applied scientific research planned for the Mir orbital complex in the period 1997–1999'' and in the development of the Nauka–NASA program, in which 165 projects (selected from 210 proposals) for joint experiments on orbital stations in different fields of research were proposed to the American side. The projects included in the Nauka–NASA program were discussed and approved in three joint symposia and attracted a great deal of interest in the international scientific community, but unfortunately they have yet to be implemented.

The SECC of Rosaviakosmos consists of 11 sections headed by the most authoritative Russian scientists and specialists in the corresponding scientific fields. Each section determines the priority of the research projects in its own field, with consideration for the proposals for joint studies and commercial contract work which provide the financial basis for funding the projects recommended for implementation. The coordination of the projects under development and the preparation of specific proposals for their practical implementation is done by the Section for Complex Analysis and the Formation of Programs with the Participation of Scientists and Specialists, of the Central Scientific Research Institute of Mechanical Engineering (CSRIME) and the RSC ''Energiya'' named for S. P. Korolev. In the periods between sessions of the SECC of Rosaviakosmos and its Presidium the day-to-day work is carried out by the Operative Working Group of the SECC of Rasaviakosmos. A comparison of the functions of the expert structures of the international parters in the creation and utilization of the ISS shows that the SECC of Rosaviakosmos combines a number of the functions of the Advisory Council of NASA and the Council on the Utilization of the ISS.

The currently existing long-term Russian program of ex-

periments onboard the RS ISS provides for the implementation of over 300 projects, selected in an open competition from among more than 400 proposals. It was foreseen that the chosen research fields would evolve, and it was therefore proposed to hold regular discussions of modifications to the long-term program to reflect the current situation in regard to financial, material, and onboard resources, the results of completed studies, and new opportunities for joint scientific and commercial research.

At the present time the possible participation of scientists from the Republic of Belarus in joint projects is under consideration, and a ''Joint Russian–Ukrainian program of scientific research and engineering experiments on the RS ISS,'' which calls for the completion of 48 topical and meaningful research studies of scientific and practical interest, has been worked out. Particular attention is being paid to finding mutually agreeable conditions for this cooperation. First, this refers to defining the mutual obligations and responsibilities of the participants, the financial arrangements, ensuring the confidentiality and protecting intellectual property, and also the rights to the use of the results of the research. It appears that the principal result of this activity will be the formation of joint research programs in various fields of science on a mutually beneficial basis.

Despite the obvious difficulties, the construction of the ISS continues. However, the final version of the configuration of the ISS has not yet been agreed upon, and that makes it difficult to devise a clear program for utilization of the ISS. On the other hand, the existing indeterminacy is a stimulus for the international partners to look for more effective forms of international cooperation in the utilization of the ISS. For example, there is now a discussion of the possibility of devising and implementing on the ISS a joint program of Rosaviakosmos, the European Space Agency (ESA), and the European Commission on Space-Related Life and Physical Sciences.

NASA has issued an initiative for the development of a coordinated international program for utilization of the ISS in the years 2004–2008.

These circumstances must be taken into account in the discussion of the plans for the main fields of research in low-temperature physics and engineering onboard the RS ISS (see Table I). The topical and promising nature of low-temperature research in space is confirmed by analysts at home and abroad, who say that low-temperature technologies are key to the development of space science and engineering in the new millenium and will largely determine their direction. This relates both to the creation of precision devices for measurement and control and of a new generation of fuel cells and to the possibility of making inroads into previously inaccessible areas of scientific research.

For example, included in the approved long-term program is the project Geliĭ (Helium), involving proposed studies of phenomena occurring at the superfluid helium–vapor and liquid helium–solid interfaces in microgravity. The project Soliton, which is devoted to the study of steady-state and dynamic nonlinear phenomena occurring on the charged surface of liquid hydrogen, may bring about substantial advances in the theory of nonlinear phenomena on the liquid surface and, in particular, will provide an experimental check of the possibility of creating a new type of ultrasensitive gravimeter.

Also included in the long-term program is the high-priority experiment Submillimetron, which is to make astronomical observations in 12 spectral intervals spanning the range from 3 μm to 1.5 mm with the use of a cryogenic space telescope with record sensitivity and angular resolution. The importance of basic research in this spectral range for developing the existing ideas in the fields of extra-atmospheric astronomy and astrophysics is due to the fact that the properties of the cold matter of the Universe are most clearly manifested there, and a study of those properties will yield additional information about the evolution of matter, stellar and planetary formation processes, and the origin of life. In the cryogenic telescope the detectors and optics of the telescope are inside a cryostat containing around 200 liters of liquid helium, which, together with a multistage system of radiation shields and an active cooling system for the inner shields and the blind of the objective can give an active lifetime of the telescope in orbit of at least 1 year, according to preliminary estimates.

In the space biotechnology field the approved program includes two experiments calling for the utilization of the onboard low-temperature equipment. These are the BSMK (OSFC) experiment, which includes the eventual completion of the onboard sublimation–freezing complex (OSFC), which is intended for the sublimation drying of biological preparations under conditions of space flight, and a cryopreservation experiment, which is devoted to the development of cryogenic methods of preserving biological preparations in order to improve the reliability of preserving biological materials investigated and produced onboard.

It is proposed to use cryogenic technologies to enhance the sensitivity of detectors and the resolution of the registration apparatus in the experiments carried out as part of the Poligon-1 project, which is devoted to the development of technology, methods, and algorithms for the qualitative and quantitative analysis of pollutants in the atmosphere and on the surface of the Earth.

Finally, the last of the approved low-temperature experiments is the project Volna-3 MKS (Wave-3 ISS), which is designed to study processes of heat and mass transfer and hydrodynamics in a two-phase cryogenic medium during a prolonged exposure to a microgravity environment, with the goal of solving problems in the creation and application of proposed space propulsion systems.

In the preparation of the Joint Russian–Ukrainian Program of Scientific Research and Engineering Experiments on the Russian Segment of the International Space Station (RS ISS), scientists at the B. Verkin Institute for Low Temperature Physics and Engineering, National Academy of Sciences of Ukraine (ILTPE NASU) proposed an experiment called Penta–Kipenie, which is included in the Kipenie (Boiling) series of space experiments which involves the participation of Russian specialists and is designed to study the influence of microgravity on the boiling of liquid helium and to solve the following problem: to study the growth and breakaway of vapor bubbles in liquid helium under various conditions of gravitation and for different properties of the boiling surfaces; to study heat exchange, the stability of boiling regimes

TABLE I. The main research topics in low-temperature physics and engineering on the Russian segment of the International Space Station.

Provisional name of experiments	Research content	Stages to be completed	Main proposed participants	Main results of preliminary experiments
Geliĭ (Helium)	Basic research on the helium interphase surface	Space experiments included in the approved research program. Versions of practical implementation are under development	MEI, RSC ''Energiya,'' RSSRI Gagarin CTC, etc.	Topical experiment. Questions of efficiency and safety of implementation remain
Soliton	Basic research on nonlinear phenomena on the condensed hydrogen surface	Space experiments included in the approved research program. Versions of practical implementation are under development	IFTT RAN, RSC ''Energiya,'' RSSRI Gagarin CTC	Topical experiment. Questions of efficiency and safety of implementation remain
Submillimetron	Basic astrophysical research using cryogenic telescope in the submillimeter band of electromagnetic waves, inaccessible from Earth.	Space experiments included in the approved research program. Versions of practical implementation are under development	ARC Physics Institute RAS, RSC ''Energiya,'' RSSRI Gagarin CTC with broad intra- and international cooperation	Topical experiment. Questions of efficiency and safety of implementation remain
Volna-3 MKS (Wave-3 ISS)	Research on heat and mass transfer and hydrodynamics in a cryogenically cooled tank	Space experiments included in the approved program. The necessary apparatus and equipment is under development	M. V. Keldysh Research center, RSC ''Energiya,'' RSSRI Gagarin CTC	Topical experiment with significant scientific and practical implications. Recommended for implementation
BSMK (OSFC)	Development of processes for drying biological preparations using onboard sublimation-freezing complex (OSFC)	Space experiments included in approved program. Agreements reached on engineering tasks. Equipment being designed.	RAO ''Biopreparat,'' AOOT ''Biokhimmash,'' RSC ''Energiya,'' RSSRI Gagarin CTC	Topical experiment with significant scientific and practical implications. Recommended for implementation
Kriokonservatsiya (Cryopreservation)	Development of methods and equipment for cryogenic preservation of biological preparations on the RS ISS	Space experiment included in approved program. Agreements reached on engineering tasks. Techniques and equipment under development	RAO ''Biopreparat,'' AOOT ''Biokhimmash,'' RSC ''Energiya,'' RSSRI Gagarin CTC	Topical experiment with significant scientific and practical implications. Recommended for implementation
Poligon-1 (Polygon-1)	Development of methods for qualitative and quantitative determination of pollutants of the compound and surface of the Earth with the use of cryogenic IR gas analyzers	Space experiment included in approved program. Agreements on engineering tasks are in the works	CSRIME	Variants for practical implementation need to be worked out
Kipenie (Boiling) group of space Experiments	Basic research in the low-temperature physics, the development of methods and equipment for efficient and safe performance of cryogenic experiments in the infrastructure of the RS ISS	Proposed as part of the ''Joint Russian–Ukrainian program of scientific and engineering experiments on the RS ISS,'' Engineering tasks worked out an agreed upon	CSRIME, ILTPE NASU, MEI, ISP RAS, RRC ''Kurchatov Institute,'' ISSP RAS, Physics Institute RAS, IHTAS with cooperation	Topical group of experiments with significant scientific and practical implications. Variants for the efficient and safe implementation need to be worked out
Edinstvo (Unity)	Basic and applied research in low-temperature physics and engineering	Group of space experiments approved for pin in the ''Long-term program of scientific and applied research on the RS ISS''	CSRIME, SRINP MSU, RSC ''Energiya'' with cooperation	Variants for practical implementation need to be worked out
Kryokompleks (Cryocomplex)	Scientific and applied research in implementing a unified complex of onboard cryogenic equipment in order to perform a group of simultaneous low-temperature experiments	Group of space experiments proposed for pin in the ''Long-term program of scientific and applied research on the RS ISS.'' The engineering tasks have been worked out	CSRIME, MEI, RSC ''Energiya'' with cooperation	Topical space experiment. Variants for practical implementation in the infrastructure of the RS ISS need to be worked out

TABLE 1. (*Continued.*)

Provisional name of experiments	Research content	Stages to be completed	Main proposed participants	Main results of preliminary experiments
"Kristallizator" (Crystallizer)	Fundamental and applied research on physical processes of protein crystallization with the use of cryogenic equipment	Group of space experiments proposed for pin in the "Long-term program of scientific and applied research on the RS ISS." Engineering tasks have been worked out	CSRIME, IC RAN	Topical space experiment recommended for implementation during the deployment stage of the RS ISS
AMS	Implementation of basic physical and astrophysical research with the use of an alpha magnetic spectrometer with a superconducting magnet system	The participation of Russian scientists and specialists in the implementation of the project has been proposed by Prof. Samuel Ting	SRINP MSU, RRC "Kurchatov Institute"	Feasibility and advisability of the participation of Russia in implementing the project are being assessed

to local temperature perturbations, and the dynamics of crisis transitions from the nucleate (bubble) boiling to the film boiling regime under various conditions of microgravity; to study the dynamics of the liquid helium–vapor interphase surface, the heat transfer, and the crisis transitions to the film boiling regime at a superfluid helium–solid wall boundary under various conditions of microgravity. In the course of reviewing these proposals it was recommended that a study of nonlinear phenomena in liquid helium be included, with consideration of the influence of the temperature fields, the pressure, and the properties of different surfaces on the convection and heat transfer under microgravity conditions.

The possibility of implementing a comprehensive space experiment called Edinstvo (Unity) is being discussed. It is oriented toward the joint utilization of a powerful cryomagnet system and an extensive complex of scientific instrumentation. The proposed program of research includes: a study of the properties of an artificial magnetosphere and its interaction with the ionospheric plasma, neutral gas, and charged particle beams; a study of the physical problems of creating a magnetic radiation shield for spacecraft; a study of the force of interaction between an artificial magnetosphere and the Earth's magnetic field and an assessment of the possibility of using it for control of the angular orientation of a spacecraft; a study of the behavior of cryogenic liquids in space and the working out of the basic design and construction solutions for the creation of onboard cryogenic equipment and the corresponding scientific apparatus.

The proposal for the Cryocomplex experiment is directed toward the creation of an efficient cryogenic complex for onboard scientific research, and the determination and the optimization of algorithms for controlling the working of the unified equipment and for solving fundamental problems of the influence of volume forces, heat exchange, and heat and mass transfer on the structure and physical properties of the liquid state of matter. It is assumed that this project can be implemented onboard the Progress cargo vessel, possibly when docked with the RS ISS. The scientific equipment will be designed to fit within the dimensions of the refilling tanks so that it can be mounted in the compartment in place of one of them. Both a version with an autonomous experiment onboard the Progress cargo vessel and a version drawing on the resources of the station are being considered.

The possibility of using cryogenic techniques in onboard experiments in the field of biotechnology is currently under active investigation. In particular, the proposal for the Crystallizer experiment calls for the use of cryogenic media for crystallization of biological macromolecules and for obtaining biocrystalline films in microgravity. The goal of the proposed experiments is to study protein crystallization processes in order to obtain structurally perfect protein single crystals suitable for x-ray structural analysis.

Scientific and industrial organizations in a number of countries are participating in the preparation of experiments onboard the ISS to search for antimatter in space with the use of a unique onboard device—an alpha magnetic spectrometer (the AMS project). For this it is proposed to use a magnet system based on helium-cooled superconducting solenoids (with a supply of $\sim$2500 liters of liquid helium) and precision instrumentation with cryogenic cooling. At the present time a decision is being reached as to the feasibility and advisability of official participation of Russian scientists in this project.

It may be seen from what we have said that experiments in the low-temperature physics and engineering have a major place in the research program for the RS ISS. For this reason the necessary design planning has been done to optimize the arrangements for low-temperature experimentation from the standpoint of efficiency and safety.

Estimates show that one way to increase the efficiency of cryogenic research is to equip a unified cryogenic workplace (UCWP) on the RS ISS. This would make it possible to combine the separate low-temperature experiments into a single complex with a reasonable expenditure of resources. In different versions the UCWP is placed on free-flying modules and on connected service modules incorporated in the infrastructure of the RS ISS. The use of an autonomous free-flying module ensures that the research program will be reliably and completely carried out but requires additional material expenditures. One of the possible variants of the

UCWP concept is to place its main elements and to carry out the planned low-temperature experiments on a manned version of the Progress cargo vessel, since at acceptable reliability and demands on the crew it requires the least expense, and it can be recommended for implementation.

*E-mail: vadim_suvorov@hotmail.com

[1] V. F. Utkin, V. I. Lukjashchenko, V. V. Borisov, V. V. Suvorov, and M. M. Tsymbaljuk, J. Low Temp. Phys. **119**, 183 (2000).

Translated by Steve Torstveit

An overview of the low temperature microgravity physics facility capabilities

J. F. Pensinger,* A. P. Croonquist, F. C. Liu, M. E. Larson, and T. C. Chui

Jet Propulsion Laboratory, California Institute of Technology, Pasadena, CA 91109, USA
(Submitted December 19, 2002)
Fiz. Nizk. Temp. **29**, 624–627 (June 2003)

The Low Temperature Microgravity Physics Facility currently in the design phase is a multiple user and multiple flight facility intended to provide a long duration low temperature environment onboard the International Space Station. The Facility will provide a unique platform for scientific investigations requiring both low temperature and microgravity conditions. It will be attached to the Japanese Experiment Module's Exposed Facility and can house two science instruments each flight. The Facility consists of a 180-liter superfluid helium dewar, a support enclosure, and control electronics. The facility will be launched full of cryogen, and retrieved after the cryogen is depleted. Industrial partners are responsible for building the reusable facility and standard parts of the instruments. Principal Investigators from universities and other institutions are contracted to develop major parts of the science instrument package. An overview of the detailed technical capabilities of the facility will be presented in this paper. [DOI: 10.1063/1.1542528]

INTRODUCTION

The Low Temperature Microgravity Physics Facility (LTMPF)[1] is the next step in a series of three very successful space flight low temperature experiments—The Superfluid Helium Experiment[2] (1985), the Lambda Point Experiment[3] (1992), and the Confined Helium Experiment[4] (1997). This series of experiments have proven that very high-resolution experimentation can be implemented in the hostile environment of space. For example, it was shown that temperature can be measured to better than 0.1 nK in space using Superconducting Quantum Interference Device (SQUID) magnetometers.[4] These high-resolution components, which require operating at low temperatures, when combined with the microgravity condition due to the International Space Station's (ISS) orbit, open the door to many exciting new investigations with the potential of making breakthrough findings. The LTMPF is designed to broaden investigation opportunities requiring these high-resolution capabilities in Space. Science selection is done through a NASA Research Announcement (NRA) periodically to select investigations to fly on each mission. Already, there are six investigations planned for the first two flights, but these investigations are not discussed in this paper. To meet the demands of the science community, the Jet Propulsion Laboratory has partnered with Ball Aerospace and Technologies Corporation (BATC) to build the dewar and the facility enclosure. Design-Net Engineering has been selected to develop the electronics and software, and Swales Aerospace has been selected to help build the instrument thermal mechanical structure. In the following, we will describe an overview of the design and technical capabilities of the facility.

SYSTEM DESIGN AND CAPABILITIES

Figure 1 below shows the LTMPF. It consists of the dewar, the electronics, the radiators, the science instruments which mount inside the dewar, and the facility enclosure that houses the dewar, the electronics and various interface components.

These interface components will be provided to LTMPF by ISS and NASA. They consist of the Grapple Fixture for the Japanese Experiment Module's (JEM) robotic arm to hold onto; the Flight Releasable Attachment Mechanism (FRAM) for attaching to the launch carrier and the ISS robotic arm, and the Payload Interface Unit (PIU) for attaching to the JEM-EF and accessing the 120 V dc electrical power and the communication interfaces. The first of three VME chassis is used to control the dewar and to communicate with the ISS; the other two electronics assemblies are used to control experiments in the two cryogenic inserts. Tools on the end of the space station robotic arm also interface with the *H*-Fixture for transferring the payload to and from the Shuttle. The maximum power available to the electronics during the mission is limited by the ability of the radiators to reject heat of about 235 W. Uplink low rate commands of no more than 864 bits/s are provided for the payload through a 1553B interface, and the high-speed downlink telemetry for the data is capable of handling 1.5 Mbps using Ethernet. Total mass of the LTMPF is limited to 600 kg and the envelope size is 1.85 m by 0.816 m by 1.037 m.

DEWAR DESIGN AND CAPABILITIESQ

The dewar contains approximately 180 liters of liquid helium and is expected to last about 4.5 months on orbit. The cross section is not cylindrical, but oblong in shape to maximize the use of the available volume within the Standard Japanese Experiment Module's Exposed Facility (JEM-EF) envelope. This large volume also helps the dewar to stay below the superfluid transition temperature, without active evacuation, for 112 hours prior to launch, so that full science time can be achieved if launched within the first two attempts. If launched at the third and later attempts the onorbit science time will be reduced. The dewar is designed to op-

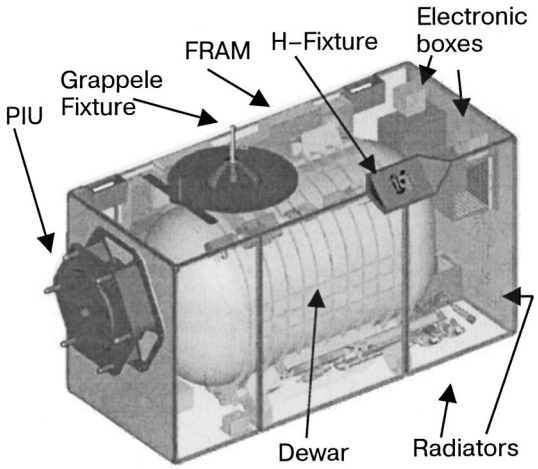

FIG. 1. The Low Temperature Microgravity Physics Facility overview.

erate at a base temperature of 1.6 K. It has two 20 cm diameter openings, one on each end, to allow two separate science instruments to be mounted. Shielded low conductivity wires are routed through the dewar vacuum space, while high current leads and coaxial cables are routed through the vent line tubing to allow for better heat exchange with the vent gas. The superfluid in the dewar permits the maintenance of a heat sink (<8 mW) at a stable temperature $\sim (1.7\pm0.05)$ K over many months.

ENCLOSURE DESIGN AND CAPABILITIES

The dewar's Vacuum Shell is the primary structural component of the LTMPF system. The electronics boxes and JEM-EF interface are mounted inside aluminum honeycomb panels that form a rectangular box around the system. The nadir-, wake, and part of the zenith-facing surfaces are thermal radiators while blankets cover the remaining panels. A separate honeycomb panel is used to support the releasable mechanism (FRAM) that attaches LTMPF to its launch carrier. These panels and the thermal design are being provided by BATC.

ELECTRONICS CAPABILITIES

There are three main electronic assemblies each housed in a separate VME box with its own single board computer. The Facility Electronic Assembly controls the function of the dewar and handles power and communication with the JEM-EF. It provides housekeeping data on various parts of the dewar and controls the vent valves of the two instruments. Small heat pulses can be used to estimate the amount of helium remaining. In addition, it provides environmental data on charged particle radiation and acceleration by interfacing with an onboard charged particle monitor and a Space Acceleration Measurement System (SAMS) accelerometer provided by Glen Research Center.

The two Experiment Electronic Assemblies each control one science instrument. The standard boards support resistance measurements of germanium elements to determine the temperature; low-, high-, and very high-precision heaters; high resolution measurements over extremely large dynamic ranges are made using dc superconducting quantum interference device magnetometers. Capability for relatively coarse temperature control is provided using germanium resistance thermometers and microwatt heater elements. For more precise control at and near the science cell a paramagnetic salt pill coupled to a SQUID with a high-precision heater can control the temperature to better than 1 nK. There are spare slots for Investigator's custom electronics boards unique to their experiment. All boards must conform to the VME 64 standard with a 6 U form factor and run with VxWork real time operating system.

The Facility electronics also include SQUID preamplifier/controller boxes that on one side interface with the high-resolution sensors inside the dewar and on the other a digital interface to a board in a VME chassis. On ascent a pressure-sensitive device or baroswitch and a battery pack are used to open a valve that allows the vacuum of space (above 100,000 feet) to pump on the liquid helium in the dewar and cool it down. In addition for the first mission a custom electronics box, the Capacitance Bridge Box, will be used to make high-precision measurements of the pressure and density in one of the experiment cells.

Because of the ultra-high sensitivity of LTMPF's science cells and sensors the small amounts of heat left behind when a charged particle passes through these components represents a noise source; measurements from a charged-particle monitor can be correlated with the sensor-data noise to reduce their impact. In a similar fashion the accelerometer provided by the SAMS Project allows comparison of small vibrations with increases in signal noise. In this way Investigators are able to understand and mitigate a couple unwanted features of space experiments.

INSERT DESIGN AND CAPABILITIES

LTMPF provides to each Investigator a standard frame on which to build their cryogenic Insert. The assembled Insert for each science instrument is 20 cm diameter and 45 cm long. An Insert consists of a base plate (or Cold Plate) to which is mounted a thermo-mechanical truss (the Probe) which in turn supports the science cell and its actuators and sensors (the Instrument Sensor Package, or ISP). The science team integrates the unique components that they have developed in their laboratories on the standard Probe; they then attach the many wires and capillaries between the ISP and the Cold Plate required to control the experiment. The Cold Plate feeds those connections through a vacuum-tight interface into the Dewar vacuum space and ultimately to the outside of the dewar. The Probe interfaces the science instrument package to the dewar providing mechanical support and thermal isolation.

The thermal mechanical structure, or Probe, provides mechanical support and thermal isolation to the science instrument package. It consists of high strength and low thermal conductivity struts intercepted by thermal isolation stages made of high thermal conductivity material. It is designed to support 8 kg of mass during launch and provide enough thermal isolation for the inner most stage to be operating at sub-nano-Kelvin stability. Figure 2 shows a picture of one such structure made of stainless steel struts and aluminum thermal isolation stages. In tests, this structure survived 7.7 g rms random vibration while supporting a 6.2 kg

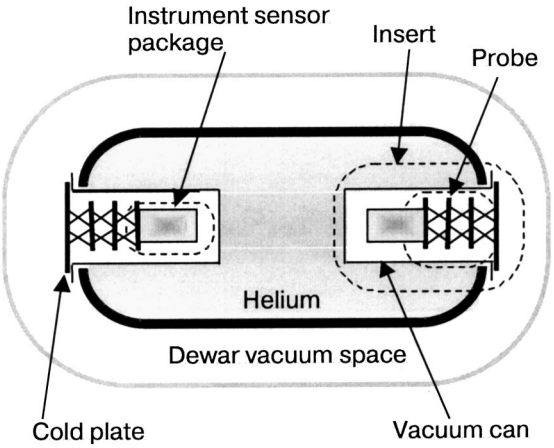

FIG. 2. Dewar interior.

mass. Each thermal stage has also demonstrated an ability to intercept most of the heat variations from the previous stage, allowing only one part in 7000 to leak through to the next stage. With 3 stages, this is more than enough to allow thermal control to sub-nano-Kelvin stability.

The resonance frequency of the structure together with the supported mass is an important parameter in mitigating the launch-heating problem. It was successfully demonstrated by Cui *et al.*[5] that if this resonance frequency is sufficiently higher than the resonance frequency of the dewar, there is very little launch-heating. This implies that most of the heating arises from the flexing of the mechanical members of the instrument package. During testing, the structure shown in Fig. 3 and discussed above had a resonance of 72 Hz compared with the 48 Hz resonance expected of the dewar. Thus we expect some mitigation of launch heating from this structure.

VACUUM CAN AND THE ADSORPTION PUMP

A vacuum can maintains a high vacuum around each Insert for thermal isolation purposes. As long as the vacuum can is leak tight against the surrounding helium in the dewar, maintaining a high vacuum should not be a problem, since all gases except helium freeze. It has been learned in previous flights that the science instrument package can heat up to close to 10 K under the strong vibration of the launch if the Insert is launched in a vacuum. During these previous launches, it was necessary to fill the vacuum can with ^{3}He-exchange gas to conduct the heat away from the science instrument to prevent it from heating up. Once on orbit, the exchange gas was vented to space and an adsorption pump, with activated charcoal, was used to absorb the rest of the gas. We inherited the adsorption pump design and modified it to make it lighter. The operation sequence is also inherited. The adsorption pump's design and operation are described in detail by Lysek *et al.*[6]

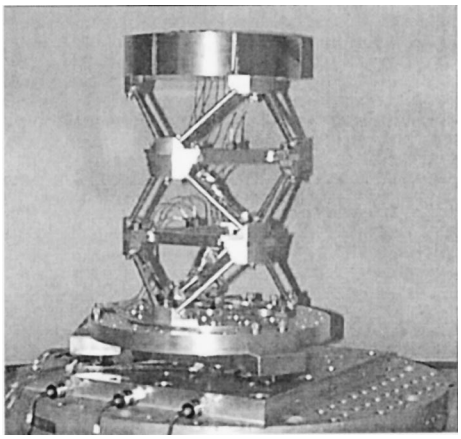

FIG. 3. A picture of the thermal mechanical structure.

Due to their high sensitivity to magnetic fields, SQUIDs are usually operated inside a dewar with an external magnetic shield. This type of magnetic shield is heavy, weighing perhaps as much as 30 kg. A way to reduce weight is to locate the shield outside the vacuum can instead. The shield is being developed and will be made of a special magnetic material—Cryoperm 10,[7] which is known to have permeability of 50,000 at low temperatures. It is expected to weigh less than 6 kg and provides a magnetic environment with less than 10 mG of field variation inside.

FACILITY, TEST, LAUNCH AND OPERATION

The integration of the LTMPF payload, its instruments and the verification of the mechanical, thermal, power, telemetry, and command interfaces with the ISS is an integral part of the qualification process. This integration process starts at the Jet Propulsion Laboratory (JPL) and is completed at the launch site where the payload will be launched on a crossbay carrier in the shuttle following a successful Certification of Flight Readiness Review. The ISS Program will transport the LTMPF Facility Class Payload on an STS flight, perform all the payload accommodation and accommodation engineering, and all necessary transportation integration services.

Then the ISS Program and NASDA IP will install the LTMPF on ISS as an externally attached payload furnishing onorbit services to the payload for commanding, telemetry and for ancillary data. The LTMPF payload after completing its 5 month onorbit mission life will be transferred from the ISS to an STS return flight for return of the payload to KSC. The payload will be returned to JPL for refurbishment and installation of two new instruments for the next mission.

CONCLUSION

The LTMPF currently under development will provide a unique environment of low temperature and microgravity for long duration. When the facility is ready for launch of the first mission in late 2005, it will open up exciting new science investigation opportunities onboard the International Space Station. JPL will provide the necessary infrastructure and services to enable a user-friendly interface to the scientific community, making easy and low cost access to space a reality for scientists.

This work is being carried out at the Jet Propulsion Laboratory, California Institute of Technology under contract to the National Aeronautics and Space Administration. The work was funded by NASA's Office of Biological and Physical Research, Physical Sciences Division. We thank BATC for providing the picture in Fig. 1.

*E-mail: john.f.pensinger@jpl.nasa.gov

[1] T. Chui, A. Croonquist, M. Larson, F. Liu, W. Holmes, D. Langford, and J. Pensinger, AIAA J. **6**, No 4, 4932 (2001).
[2] P. V. Mason, D. Petrac, D. D. Elleman, T. Wang, H. W. Jackson, D. J. Collins, P. Cowgill, and J. R. Gatewood, Adv. Cryog. Eng. **21**, 869 (1985).
[3] J. A. Lipa, D. R. Swanson, J. A. Nissen, T. C. P. Chui, and U. E. Israelsson, Phys. Rev. Lett. **76**, 944 (1996).
[4] J. A. Lipa, D. R. Swanson, J. A. Nissen, P. R. Williamson, Z. K. Geng, T. C. P. Chiu, U. E. Israelsson, and M. Larson, Phys. Rev. Lett. **84**, 4894 (2000).
[5] W. Cui, R. Almy, S. Deiker, D. McCammon, J. Morgenthaler, W. T. Sanders, R. L. Kelley, F. J. Marshall, S. H. Moseley, C. K. Stahle, and A. E. Szymkowiak, SPIE **2280**, 362 (1994); D. McCammon, R. Almy, S. Deiker, J. Morgenthaler, R. L. Kelley, and F. J. Marshall, Nucl. Instrum. Methods Phys. Res. A **370**, 266 (1996).
[6] M. J. Lysek, U. E. Israelsson, T. C. P. Chui, M. E. Larson, D. Petrac, S. E. Elliott, D. R. Swanson, X. Qin, and J. A. Lipa, in *Adv. Cryogenic Eng. Proc. of the 16th International Cryogenic Engineering Conference*, P. Kittel (ed.), Vol. 42, Portland, Oregon (1997).
[7] Cryoperm 10, Amuneal Corp., 4737 Darrah St., Philadelphia, PA 19124-2705.

This article was published in English in the original Russian journal. Reproduced here with stylistic changes by AIP.

Physical research on the effect of microgravity on physical phenomena in cryogenic liquids; a general purpose onboard cryogenic facility for implementing this research on the International Space Station

S. I. Bondarenko,R. V. Gavrylov, V. V. Eremenko, K. V. Rusanov, and N. S. Shcherbakova

Special Research and Development Bureau for Cryogenic Technologies of the B. Verkin Institute for Low Temperature Physics and Engineering of the National Academy of Sciences of Ukraine, 47 Lenin Ave., Kharkov 61103, Ukraine

I. M. Dergunov, A. P. Kryukov, P. V. Korolyov, and Yu. Yu. Selyaninova

Moscow Power Engineering Institute, Russia, 14 Krasnokazarmennaya Str., Moscow 111250, Russia

V. M. Zhukov

Institute for High Temperature of the Russian Academy of Sciences, Russia, 13/19 Izhorskaya Str., Moscow 127412, Russia

V. S. Kharitonov, K. V. Kutsenko, and V. I. Deev

Moscow Institute of Physics and Engineering, Russia, 31 Kashirskoe Shosse, Moscow 115409, Russia

V. A. Shuvalov

Central Research Institute of Machine Building, Russia, 4 Pionerskaya Str., Moscow Region 141070, Russia
(Submitted December 19, 2002)
Fiz. Nizk. Temp. **29**, 628–632 (June 2003)

A combined research plan, called ''Boiling,'' is created on the basis of several cryogenic research projects developed by experts in Russia and Ukraine for the International Space Station. The ''Boiling'' plan includes eight initial experiments aimed at investigating the influence of microgravity on boiling, heat transfer, and hydrodynamics in liquid helium under normal or superfluid conditions. The experiments are supposed to be performed with individual cells all placed inside a single onboard cryogenic experimental facility. The experiments to be performed as part of the international research program have the following special features: several artificially simulated microgravity levels produced by rotating the experimental helium cryostat; visualization of the processes occurring in liquid helium; research on boiling and hydrodynamics in a large volume of stationary liquid and in a liquid flow through a channel. When the ''Boiling'' research plan is completed the onboard cryogenic facility created for the International Space Station should find applications in further scientific and experimental research with helium. [DOI: 10.1063/1.1542529]

1. INTRODUCTION

The history of research on the effect of microgravity on the boiling of liquid helium is further proof of the benefits of the Chernogolovka conferences, where the international scientific community reports and debates new concepts and further development work is given an impetus. After making substantial progress and reaching milestones, such as the publications by Ukrainian[1–5] and Russian[6–8] scientists, this initial idea has been transformed into a joint international Russian and Ukrainian project to investigate liquid helium onboard the Russian segment of the International Space Station (ISS).

The joint program incorporates the experience gained at five research institutions in both countries, reflecting their scientific interests and goals. Now, after the problem has been studied thoroughly and novel approaches have been developed, this joint program promises to shed light on the effect of microgravity (MG) on heat transfer and hydrodynamics at boiling of normal and superfluid liquids.

2. ONBOARD CRYOGENIC FACILITY

The joint international project is based on the integration of two initial technical concepts. On the one hand the idea is to employ in the investigations performed onboard the ISS a universal helium cryostat, which will contain several experimental cells, making it possible to perform scientific research using several controlled MG levels (which are produced by rotating the cryostat) and visualizing the liquid He-related processes (Fig. 1).

On the other hand there is the idea of organizing a universal cryogenic workstation onboard the ISS (see Ref. 7 for details), where, among other things, in order to increase the number of experiments that can be performed in space an additional cryostat with liquid helium would be provided to refill the research cryostats. This project would be implemented by the Central Research Institute of Machine Building (CRIMB).

The rotating research cryostat would contain three to five experimental cells (Fig. 2) (to arrange a step-by-step se-

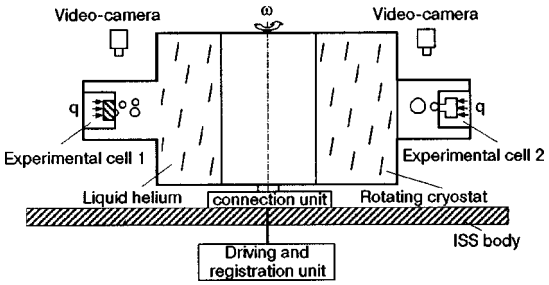

FIG. 1. Schematic diagram of the helium cryostat with the experimental cells.

quence of experiments in space) and a video recording system.

Both cryostats would be connected to one another by a pipeline which feeds normal or superfluid helium from a standby cryostat to the research cryostat. This will solve two problems in performing heat-transfer experiments in space: hydrodynamics under a forced supply of liquid helium and planned refilling of the research cryostat.

The concept of all space-based experiments includes the following functions: supplying thermal power to the experimental cell heaters according to a preset program, recording the component temperature readings, recording the pressure drop, identifying boiling phenomena such as nucleation, and propagation of vapor bubbles or vapor-film rearrangement of two-phase flow structure.

3. SPACE-BASED EXPERIMENTAL PLANS

A. The special research and development bureau for cryogenic technologies (SRDB) would implement the "Bubble" space-based experiment

The objective of this space-based experiment is to obtain a video record of vapor-bubble growth and departure from a single center of bubble boiling in normal liquid helium at four MG levels. The expected result is a determination of the dependence of the departure diameter of bubbles and the bubble departure rate in liquid helium on the microacceleration in the range from $\eta=1$ (based on data from ground-based esperiments) to $\eta\approx10^{-5}$.

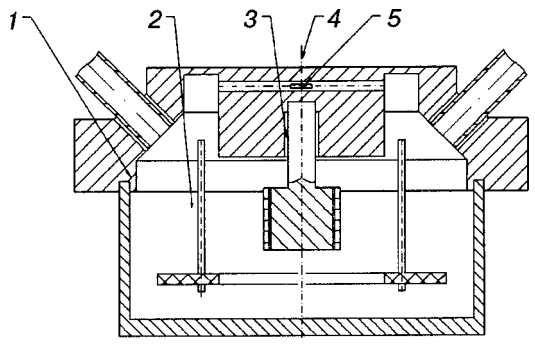

FIG. 2. Experimental cell for the "Bubble" experiment: heater body (*1*); vacuum insulation (*2*); heating unit (*3*); center of boiling (*4*); temperature sensor (*5*).

B. The SRDB would implement the "Borbatage" space-based experiment

The objective of this space-based experiment is to obtain a video record of vapor-bubble growth on and departure from a single center under excessive pressure in the normal state or superfluid helium at four MG levels. The expected result is a determination of the dependence of the bubble departure diameter and bubble departure rate from liquid helium on the microacceleration and excess vapor pressure.

C. The SRDB would implement the "Autowave" space-based experiment

The objective of this space-based experiment is to obtain (by video recording and temperature measurements) experimental data on the direction and speed of propagation (on the boiling surface) of the boundary between bubble and film boiling regimes for normal state liquid helium at four MG levels. Initially, the boiling surface would be heated uniformly and bubble-boiling phenomena would occur on it. A local thermal disturbance (i.e. additional heating) would create a source for the film regime, which differs in physical appearance and temperature from the bubble boiling process. The newly born source of phenomena can either collapse or cover the entire boiling surface, depending on whether the disturbance rate is below or above a critical level, respectively. As a result, the microacceleration dependence of the critical local thermal disturbance and the dynamic characteristics of the autowave process at a change of boiling regimes for normal state liquid helium on surfaces of different dimensional categories can be determined.

D. The moscow power engineering institute (MPEI) would implement the "Film" space-based experiment

The objective of this space-based experiment is to obtain (by video recording and temperature measurements) experimental data on the conditions of vapor-film birth, the dynamics and decay of superfluid liquid helium, and heat transfer at four MG levels. If the thermal flow density is below the critical value, heat transfer will take place in a regime with single-phase convection of superfluid liquid helium. Above the critical level a vapor film separating the superfluid liquid helium from the heated surface appears. As a result of the consequent power decrease, a reverse transition occurs and leads to the decay of the vapor film. The parameters to be measured in this space-based experiment are the thermal power, the temperature of the boiling surface, and the microacceleration. The values to be determined from the video recording are the outer diameter of the vapor film, the velocity of the vapor film extension or collapse variations, and the rate of extension/collapse variations. To obtain superfluid helium boiling under microgravity the He II must be confined in the experimental volume containing the heater. We believe that capillary porous media can be used for this purpose. The situation depicted in Fig. 3 can occur when He II boils in a porous medium.

This problem has been solved in Ref. 8. In the present work the approach of Ref. 8 is extended to the general case of a helium II filled system consisting of two vessels connected by a capillary of length l. The heater is placed at the

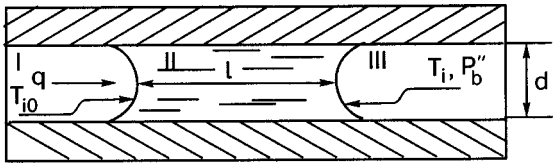

FIG. 3. He II column in the capillary of a porous structure: zone I and III are occupied by vapor; zone II is occupied by He II.

top of the left-hand vessel of diameter D_0. This vessel is hermetically sealed. A vapor film exists between the heater and the liquid helium. The left-hand vessel and the side surface of the capillary are adiabatically insulated. A heat flux is delivered from the heater to the interface through the vapor film. The vapor pressure P_b'' is maintained constant at the right-hand vessel of diameter D. The problem is to describe the behavior of the superfluid helium in this system.

The following solution of the problem is obtained on the basis of the conservation laws given in Ref. 8 and the equation of heat and mass transfer at interfaces.

The He II flow velocity is given by

$$\overline{V'}=\frac{d^2}{32\eta l}\frac{(q_w/r)\sqrt{2\pi RT_i}}{\left(1-\dfrac{\rho''}{\rho'-\rho''}\dfrac{r}{ST}\right)}\left[0.6\left(\frac{D_0}{D}\right)^2+\frac{r}{8RT}+\frac{\rho' g(h_1-h_2)}{(q_w/r)\sqrt{2\pi RT_i}}\right]-\frac{q_w}{\rho' ST}\left(\frac{D_0}{d}\right)^2,$$

where h_1 and h_2 are the heights of the superfluid helium columns in the left- and right-hand vessels, respectively; d is the diameter of the capillary tube; R is the ideal gas constant for helium; r is the latent heat of evaporation; and, q_w is the heat flux density.

For some height difference $\Delta h=h_1-h_2$ the superfluid helium velocity $\overline{V'}$ vanishes. This height difference is given by the formulas

$$\Delta h=\frac{q_w}{\rho' g}\left[\left(1-\frac{\rho''}{\rho'-\rho''}\frac{r}{ST}\right)\frac{32\eta l}{\rho' STd^2}\left(\frac{D_0}{d}\right)^2-0.6\frac{\sqrt{2\pi RT_i}}{r}\left(\frac{D_0}{D}\right)^2-\frac{\sqrt{\pi}}{4\sqrt{2RT_{i0}}}\right],$$

$$\Delta h=\frac{S\Delta T}{g}\left[1-\frac{\rho''}{\rho'-\rho''}\frac{r}{ST}-\frac{d^2\rho'\sqrt{2\pi RT}}{32\eta l}\frac{ST}{r}\left(0.6\left(\frac{d}{D}\right)^2+\frac{r}{8RT}\left(\frac{d}{D_0}\right)^2\right)\right],$$

where ΔT is he temperature difference along the capillary. (When the temperature difference in the vessels is much less than the temperature drop along the capillary, the temperatures in the vessels are independent of depth.) This formula has the form of the relation for the well-known fountain effect: $\rho' g\Delta h=\rho' S\Delta T$.

However, our formula contains the term

$$\frac{d^2\rho'\sqrt{2\pi RT}}{32\eta l}\frac{ST}{r}\left(0.6\left(\frac{d}{D}\right)^2+\frac{r}{8RT}\left(\frac{d}{D_0}\right)^2\right).$$

This term is due to the viscosity of normal flow in the capillary and the kinetic effects at the interfaces in the system. As the capillary diameter $d\to 0$ and since

$$\frac{\rho''}{\rho'-\rho''}\frac{r}{ST}\ll 1$$

the formula transforms into the latter relation. Thus it is apparent that this phenomenon is similar in nature to the fountain effect.

Analysis of the formulas for Δh shows that Δh is zero at some distance which can be denoted as L_{01}:

$$L_{01}=\frac{d^2\rho'\sqrt{2\pi RT_i}}{32\eta\left(1-\dfrac{\rho''}{\rho'-\rho''}\dfrac{r}{ST}\right)}\frac{ST}{r}\left(0.6\left(\frac{d}{D}\right)^2+\frac{r}{8RT}\left(\frac{d}{D_0}\right)^2\right).$$

Thus the difference $\Delta h=h_1-h_2$ of the heights of the superfluid helium columns in the vessels can be both less and greater than zero in general. However, if the vessel diameters are much greater than the capillary diameter, then the following peculiarity arises. For zero difference between the heights of the superfluid columns in the vessels the ''critical length'' is very small compared with the analogous length for a single capillary. Therefore even for a very small capillary length the superfluid helium moves in the vessel with the heater, while in the single capillary the He II flows toward the heater only if the length of the columns is large (greater than the critical length). If the column length is smaller than the critical length, the column moves away from the heater just as for an ordinary liquid.

The result expected is a determination of the microacceleration dependence of the heat transfer coefficient, the critical heat flux densities, and the vapor film dynamics index in superfluid liquid helium.

E. The moscow institute of physics and engineering (MIPE) would implement the "Impulse" space-based experiment

The objective of this space-based experiment is to obtain (by video recording and temperature measurements) experimental data on the conditions and delay time of bubble and film boiling for normal liquid helium with different modes of heat supply to the boiling surface at four MG levels.

The expected results are a determination of the dependences of the typical delay times in boiling and onset of stationary regimes of liquid helium boiling at ''attacking'' heat supply on the microacceleration and the heat pulse peaks and a determination of the relation between rapid temperature variations on a solid surface and vapor formation in liquid helium.

F. The institute for high temperatures of the russian academy of sciences (IHT) would implement the "Pore" space-based experiment

The objective of this space-based experiment is to obtain experimental data on heat transfer and on the size of vapor bubbles in the normal state liquid helium which is subjected to boiling on surfaces with different coating geometries at four MG levels. The expected result is a determination of the dependence of the heat transfer coefficient, the critical den-

sity of heat flow, and the average departure size of vapor bubbles on the microacceleration and the geometry of the porous coatings.

G. The central research institute of machine building (CRIMB) would implement the "CryoManifold-1" and "Cryomanifold-2" space-based experiments

These experiments are similar to one another. They differ only by the characteristics of the liquid helium supplied to the experimental cell. The experimental cell is typically a channel which is supplied under excess pressure with liquid helium from the standby cryostat.

The ''Cryomanifold-1'' experiment would employ normal state liquid helium at 4.4 K, whereas superfluid helium at 1.8 K would be used in the ''Cryomanifold-2'' experiment.

The objective of this space-based experiment is to obtain experimental data on heat transfer, the hydraulic resistance, and the flow regimes for single- and two-phase flows of liquid helium at different mass flow rates and under the intrinsic microacceleration onboard the ISS.

The expected result is a determination of the dependence of the heat transfer coefficients, the hydraulic resistances, and the flow regimes for single- and two-phase helium flows on the microacceleration and pressure drop.

4. CONCLUSIONS

The current status of the project is as follows. The onboard cryogenic facility and the experimental cells are in the design stage; the relevant documentation is being jointly developed and coordinated by researchers in Russia and Ukraine; the contributions to be made by both parties are being decided; the implementation of the joint ''Boiling'' plan is being prearranged by both parties; mockup versions of the experimental cells are being investigated; model testing is being performed; and, preliminary ground-based experiments with normal and superfluid LH are being undertaken.

A diverse spectrum of all promising research in low-temperature physics and techniques under MG conditions, which would be provided by the onboard cryogenic facility, is a prerequisite for further elaboration of the concept under discussion.

E-mail: mail@cryocosmos.com

[1] K. V. Rusanov and N. S. Shcherbakova, Fiz. Nizk. Temp. **24**, 140 (1998) [Low Temp. Phys. **24**, 100 (1998)].
[2] S. Bondarenko, K. Rusanov, and N. Shcherbakova, J. Low Temp. Phys. **119**, 203 (2000).
[3] S. I. Bondarenko, Yu. A. Melenevsky, K. V. Rusanov, and N. S. Shcherbakova, Space Science Tech. **6**, 134 (2000).
[4] S. Bondarenko, K. Rusanov, and N. Shcherbakova, in *Proceedings of the 5th Sino-Russian-Ukrainian Symposium on Space Science and Technology*, June 6–9, 2000, Kharbin, People's Republic of China (2000), Vol. 2, p. 594.
[5] V. V. Eremenko, S. I. Bondarenko, E. Ya. Rudavskiy, V. K. Chagovets, Yu. A. Melenevskiy, K. V. Rusanov, and N. S. Shcherbakova, in *Proceedings of the 5th Sino-Russian-Ukrainian Symposium on Space Science and Technology*, June 6–9, 2000, Kharbin, People's Republic of China (2000), Vol. 2, p. 486.
[6] I. M. Dergunov, A. P. Kryukov, and A. A. Gorbunov, J. Low Temp. Phys. **119**, 403 (2000).
[7] S. V. Buskin, V. I. Lukyashenko, V. V. Suvorov, I. Yu. Repin, V. A. Shuvalov, and Yu. E. Levitskiy, Fiz. Nizk. Temp. **29**, 633 (2003) [Low Temp. Phys. **29**, 469 (2003)].
[8] P. V. Korolyov and A. P. Kryukov, Vest. MEI, No. 1, 43 (2002).

This article was published in English in the original Russian journal. Reproduced here with stylistic changes by AIP.

Technical integration of low-temperature research on the Russian segment of the ISS and optimization of the experiment packages

S. V. Buskin, V. I. Lukjashchenko, I. Yu. Repin, V. V. Suvorov,* and V. A. Shuvalov

Central Scientific Research Institute of Mechanical Engineering FGUP, 141090 Korolev, Moscow Region, Russia

Yu. E. Levitskiĭ

Russian Aerospace Agency (Rosaviakosmos), Moscow, Russia
(Submitted December 19, 2002)
Fiz. Nizk. Temp. **29**, 633–636 (June 2003)

The principle of integration of the low-temperature research planned for onboard the Russian segment of the International Space Station (ISS) is discussed in relation to the features of the cryogenic experiment packages, including the object of study and the cryostatic system. Systemic questions concerning the creation of a universal cryogenic laboratory on the orbital station for conducting deep-cooling experiments in the microgravity environment of space are examined. A block diagram of the laboratory is given, a classification of the equipment is presented, and the requirements on the experiment packages are discussed. © *2003 American Institute of Physics.* [DOI: 10.1063/1.1542530]

1. INTRODUCTION

The cryogenic equipment necessary for low-temperature research in outer space is rather costly and cumbersome; in addition to a tank of coolant, the cryogenic system in each particular case may include separators of the liquid and vapor and systems for transferring the coolant and for diagnostics and control, etc. These systems have many elements in common. It is therefore advisable that all of the experiments that require deep cooling be grouped together on the station to create a specialized cryogenic workplace served by a single universal cooling system. The presence of such a universal cryogenic workplace onboard the Russian segment of the International Space Station (RS ISS) makes it possible to conduct a wide class of scientific and engineering studies: research on the physical properties of cryogenic liquids under conditions of microgravity and weightlessness, the development of methods for cryostating large volumes of liquids at liquid-helium temperatures and of methods for delivering the cryogenic liquids onboard and resupplying the onboard station in the environment of space, the testing of helium-level onboard refrigerators, the development of a technology for experimental research using high-power superconducting systems onboard spacecraft, scientific research in various fields of knowledge with the use of high-resolution cryogenic equipment, etc.

The presence of a specialized workplace onboard provides the prerequisites for optimizing the scientific equipment of each experiment with respect to the following indicators: reduction of the mass and scale of the experiment packages that must be delivered, simplification of the prelaunch preparations, and enhancing the operational safety of the onboard equipment.

As compared to having individual low-temperature experiments, the integration of the cryogenic equipment on a single platform provides the following advantages:

— multiple use of the basic equipment installed onboard reduces the freight stream and permits the delivery of exchangeable experiment packages under normal conditions (without the need for pre-cooling and the attendant cryostatic systems);

— the possibility of carrying out several different experiments simultaneously;

— an increase in the duration of the experiments, since the time of an experimental run is not limited by the supply of cryoagents that can be delivered from Earth together with the experiment package;

— standardization of the technology for carrying out low-temperature experiments enhances their safety and makes it possible to arrange for several cooling levels to permit more complete utilization of the coolants.

2. ARRANGEMENT OF THE CRYOGENIC PLATFORM

The first studies of the features of operation of technical devices containing liquid helium in a space environment were carried out back in the 1960s.[1] Progress in space technology has led to a marked increase in the number of low-temperature experiments and in the demands placed on the onboard cryogenic equipment.[2,3]

Analysis shows that the elements can be grouped according to their principle of utilization as follows: cryogenic sensors and thermometers, cooled radiation detectors; cryoelectronics and magnetometry, high-resolution measuring devices; superconducting systems for producing high magnetic fields; autonomous metrological devices (atomic clocks, frequency standards, etc.). These elements are used in various combinations both in fundamental scientific research and in engineering experiments on equipment for use in space, and so their development and refinement in ground-based laboratories and under the conditions of experiments in space are topical problems in the space engineering and technology of today.

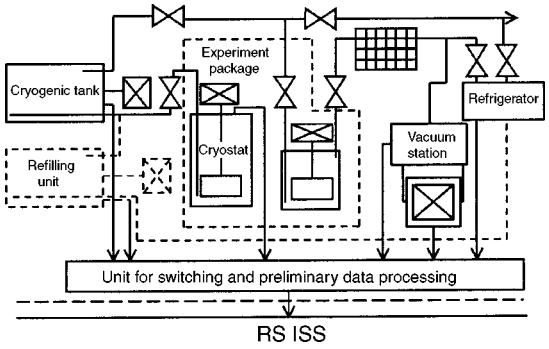

FIG. 1. Block diagram of the cryogenic workplace on the RS ISS.

It is known that any low-temperature experiment (or experiment package) in space consists of two parts: the first is the actual low-temperature object to be studied (receiver, generator, solenoid, SQUID, cryogenic liquid or solid, etc.), and the second is the cryogenic system, which performs service functions in the creation and maintenance of the required conditions. The second can be many times more expensive to make than the first. After completion of the experiment the equipment is usually all brought down from orbit. For this reason it would be advantageous to build a cryogenic platform on the ISS with common cryogenic equipment, monitoring and diagnostic devices, power source, and devices for data acquisition and control (see Fig. 1). The experimental object itself will be delivered to the universal cryogenic workplace (UCWP) of the station and be mounted on a suitable unified platform.

In our proposed project it is assumed that there will be three such workplaces onboard the RS ISS; one for research in the physics of cryogenic liquids and gases, one for studies at high magnetic fields, and one for experiments requiring the use of cryogenic instrumentation. The astrophysical platform, with a small spacecraft which can be incorporated in the infrastructure of the ISS, can be considered separately.

In spite of the diversity of experiments, they have in common the utilization of the same basic equipment onboard the spacecraft, such as the tanks of cryogenic liquids, the systems for transporting the liquid and the cold vapor, refrigerators, the systems for monitoring and controlling the parameter of the cryostats, and the systems for scientific data acquisition and processing. In comparison with the system previously used for conducting cryogenic experiments, the use of the UCWP makes possible the multiple reuse of the basic equipment permanently installed onboard the RS ISS, thus reducing the volume of freight, making it possible to deliver the experiment packages to the station in ''dry'' form (without cryoagents), and extending considerably the duration of the experiments. The standardization of the technology of performing the experiments enhances their safety and makes it possible to organize several cooling levels simultaneously for the purpose of making more complete use of the expended coolant. This makes the RS ISS more competitive in a discussion of the possibilities for conducting scientific and engineering research in space on a commercial basis. In essence, the UCWP will fulfill the role of a permanent cryogenics laboratory intended for the creation of the necessary operating conditions for conducting experiments at low temperatures onboard the RS ISS and also for studying the physical processes in the cryogenic liquids themselves and in their containers.

In accordance with this, all the equipment of the UCWP can be divided into several groups:

1. Permanent service equipment—equipment necessary for conducting all experiments; this includes the cryostatic system, the system for refilling the tank and the transport of cryoagents, the apparatus for monitoring the parameters of the cryoagents and ensuring the safety of the UCWP, the electrical supply units of the equipment supporting the UCWP and the scientific equipment, and units for acquisition, processing, storage, and transmission of the scientific and service data.

2. Replaceable service equipment—equipment that is modified depending on the nature of the research: refrigerators for liquefying the cold vapor, robotic manipulators for mounting, exchanging, and demounting of experiment packages and servicing equipment, the working platforms, supporting framework for mounting the experiment packages, the specific devices for making observations in the course of an experiment, magnetometers, analyzers for determining the composition of the internal atmosphere, electric field sensors, etc.

3. The experiment package, which includes the special equipment designed and delivered by the organizers of an experiment and contains the object of study, special (unavailable in the UCWP) devices for the monitoring and control of the course of the experiment, and special data acquisition systems. This equipment must be compatible with the service systems of the UCWP in all of their parameters and should not duplicate its capabilities. This equipment may be placed inside or outside of the research module (RM) of the RS ISS. The choice of the specifics of the UCWP will depend on the program of low-temperature experiments planned.

The deployment of the UCWP can be divided into several stages.

Stage 1—placing the RM into orbit with the UCWP equipment carried inside a specialized compartment of the RM, checking the equipment to make sure it is working properly; placing experiment packages containing their own cryostats into orbit and mounting them on individual working platforms for performing short-term experiments; starting to create the working platform for a particular version of the UCWP.

Stage 2—finishing the construction of the working platform; completing the systems for replenishing and transport of cryoagents; checking the functioning of the robotic manipulator, checking out the scientific equipment; starting the experiments on the unified platforms with the use of the cryoresources of the UCWP.

Stage 3—executing the program of experiments with the use of the expendable cryoresources of the UCWP; starting to utilize the refrigerators.

Stage 4—full-scale utilization of the UCWP. The schedule for implementation of each stage will depend on the particulars of the construction of the working platform and the freighting capabilities and is determined in the early planning stage.

Requirements on the experiment packages

In the first and part of the second stages of deployment of the UCWP the experiment packages are delivered with their own cryostats and the necessary supply of cryogenic liquid. The experiment package must meet the requirements of operation in outer space. The electrical supply of the experiment package, monitoring of the parameters of the cryogenic liquids, and the data acquisition and processing are handled by the UCWP. The experiment package must admit mounting on the outer surface of the RM and and be pluggable into the cable network of the UCWP by the operator in an EVA. The drainage of the cryoagent should be done through mounted nozzles. In the second (partially) and later stages the experiment package is delivered in a warm, ''dry'' cryostat. This cryostat is mounted on the unified working platform and is connected to the cryogenic system of the UCWP, which provides the required temperature regime for the experiment by its own resources. The experiment package is simultaneously connected to the electrical supply and data acquisition systems. After the circulational cooling system is completed, the experiment packages can be delivered onboard without a cryostat.

Replacement of the experiment packages

In the first and second stages the demounting of an experiment package is done by the operator in an EVA after the experiment is completed (or terminated). If required, a new experiment package is mounted on the same working platform. In the second and later stages the mounting, demounting, and exchange of packages on the unified platforms will be done by a robotic manipulator. The used package will be returned to Earth or utilized in another way.

The existing scientific–engineering and technological resources in the fields of cryogenic technique, applied superconductivity, and cryoelectronics in the Russian Federation are sufficient to implement the UCWP concept on the RS ISS. This would reduce the effort required for Russian and foreign scientists to conduct long-term scientific and applied research.

*E-mail: vadim_suvorov@hotmail.com

[1] A. B. Fradkov and V. F. Troitskiĭ, Tr. Fiz. Inst. Akad. Nauk SSSR (FIAN) **77**, 85 (1974).
[2] C. Jewell, ''Overview of cryogenic develompement in ESA,'' in *Preceedings of the Sixth European Symposium on Space Environmental Control Systems*, Noordwijk, The Netherlands, May 20–22, 1997, p. 447.
[3] B. Collaudin and N. Rando, Cryogenics **40**, 797 (2002).

Translated by Steve Torstveit

Short-range inverse-square law experiment in space

D. M. Strayer*

Jet Propulsion Laboratory, Caltech, 4800 Oak Grove Drive, Pasadena, CA 91109, USA

Ho Jung Paik and M. Vol Moody

Department of Physics, University of Maryland, College Park, MD 20742, USA
(Submitted December 19, 2002)
Fiz. Nizk. Temp. **29**, 637–647 (June 2003)

The objective of ISLES (inverse-square law experiment in space) is to perform a null test of Newton's law on the ISS with a resolution of one part in 10^5 at ranges from 100 μm to 1 mm. ISLES will be sensitive enough to detect axions with the strongest allowed coupling and to test the string-theory prediction with $R \geqslant 5$ μm. To accomplish these goals on the rather noisy International Space Station, the experiment is set up to provide immunity from the vibrations and other common-mode accelerations. The measures to be applied for reducing the effects of disturbances will be described in this presentation. As designed, the experiment will be cooled to less than 2 K in NASA's low temperature facility the LTMPF, allowing superconducting magnetic levitation in microgravity to obtain very soft, low-loss suspension of the test masses. The low-damping magnetic levitation, combined with a low-noise SQUID, leads to extremely low intrinsic noise in the detector. To minimize Newtonian errors, ISLES employs a near-null source of gravity, a circular disk of large diameter-to-thickness ratio. Two test masses, also disk-shaped, are suspended on the two sides of the source mass at a distance of 100 μm to 1 mm. The signal is detected by a supercon-ducting differential accelerometer, making a highly sensitive sensor of the gravity force generated by the source mass. © *2003 American Institute of Physics.* [DOI: 10.1063/1.1542531]

1. OBJECTIVES OF ISLES

The Newtonian inverse-square law ($1/r^2$ law) of gravity is a cornerstone of general relativity (GR). Its validity has been impressively demonstrated by astronomical observations in the solar system, exceeding a level of sensitivity for violations of one part in 10^8 at 10^7-10^9 km. In the wake of interests in searching for a ''fifth force'', the past two decades has seen increased activities on Earth in testing the $1/r^2$ law on the laboratory and geological scales. The experimental limit at ranges of 1 cm^{-10} km now stands at one part in 10^3-10^4. However, due to difficulties associated with designing sensitive short-range experiments, the range below 1 mm has been left largely unexplored.[1]

Figure 1 shows the existing limit for tests of the $1/r^2$ law at ranges below 1 mm and the expected sensitivity of our proposed experiment ISLES for the International Space Station (ISS), plotted as a function of range λ, where the total potential is written as

$$V(r) = -\frac{GM}{r}(1+\alpha e^{-r/\lambda}). \tag{1}$$

Violations predicted by various theories are also indicated. The expected resolution of ISLES on the ISS is $|\alpha| = 1 \times 10^{-5}$ at $\lambda = 100$ μm^{-1} mm and $|\alpha| = 1 \times 10^{-2}$ at $\lambda = 10$ μm. At 100 μm, this represents an improvement over the existing limits[2] by over six orders of magnitude. ISLES reaches four orders of magnitude beyond the level aimed at by Long *et al.*[3] in their ongoing laboratory experiment. The improvement at ranges less than 100 μm is even greater. As indicated on Fig. 1, the ISLES experiment is capable of detecting the axion with highest allowed coupling ($\theta = 3 \times 10^{-10}$) and will test a string theory prediction with $R_2 \geqslant 5$ μm. ISLES is based on the superconducting gravity gradiometer technology fully developed at the University of Maryland.[4]

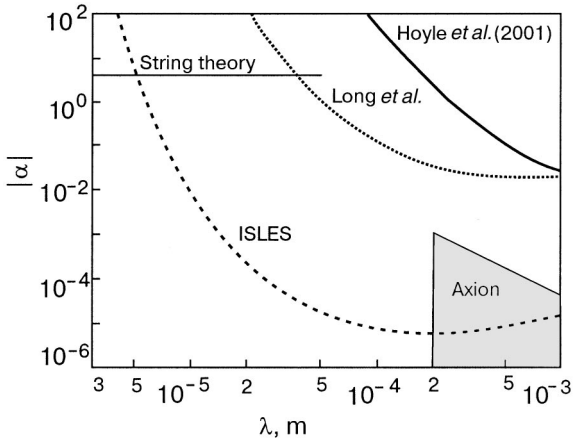

FIG. 1. Sensitivity of ISLES and the existing limits.

However, obtaining the sensitivities displayed in Fig. 1 for ISLES on the ISS is a nontrivial task. The vibration environment observed on the ISS, as seen in the data presently being transmitted down from orbit, is over 100 times worse than that observed in an Earth-bound laboratory. The tech-

niques we intend to apply to reach the sensitivities depicted in Fig. 1 are the main topics of this paper. Again, we shall be describing techniques that have been developed earlier for other experiments at the University of Maryland, techniques that will be adapted to the ISS for ISLES.

2. SCIENTIFIC VALUE OF SHORT-RANGE $1/r^2$ LAW TEST

Test of general relativity

Existence of a short-range mass-mass interaction implies a violation of the $1/r^2$ law, a cornerstone of GR. Such a force may, or may not, have composition dependence. Therefore, the $1/r^2$ law could be violated even when the equivalence principle (EP) holds rigorously. So ISLES will complement STEP (satellite test of the equivalence principle) and other EP experiments that aim at testing the EP to high resolution at ranges near the Earth's radius or longer, $\lambda \geqslant 10^4$ km.

Test of string theories

String theories can be consistently formulated only in nine spatial dimensions. Because the space we observe is three-dimensional, the extra dimensions must be somehow hidden. If there are n compact dimensions with radii R_1, $R_2,\ldots,R_n$, Gauss's law implies that the Planck mass $M_{\rm Pl}$ is related to a fundamental scale M_* by

$$M_{\rm Pl}^2 \approx M_*^{2+n} R_1 R_2 \ldots R_n . \tag{2}$$

In the string theory, as we reduce the distances probed to shorter than one of the radii R_i, a new dimension opens up and changes the r-dependence of the gravitational force law.

One theoretically well-motivated value for M_* is 1 TeV, which solves the gauge hierarchy problem, namely, gravity is so weak compared to the other forces. For two large dimensions of similar size, one obtains $R_1 \approx R_2 \approx 1$ mm.[5] Cosmological and astrophysical constraints give a bound $M_* > 100$ TeV,[6,7] while the most stringent bound, $M_* > 1700$ TeV, comes from the evolution of neutron stars.[8] This most stringent bound corresponds to $R_1 \approx R_2 < 40$ nm. While this range is beyond the reach of ISLES, there are cosmological assumptions going into these bounds, and a null result from ISLES would supply independent confirmation of the model being tested.

Search for the axion

The standard model of particle physics successfully accounts for all existing particle data; however, it has one serious blemish: the strong CP problem. Strong interactions are such that parity (P), time reversal (T), and charge conjugation (C) symmetries are automatically conserved in perturbation theory. However, non-perturbative effects induce violations of P and CP (parameterized by a dimensionless angle θ), but no such violations have been observed in strong interactions. An attractive resolution of this problem is develop in Ref. 9. One ramification of their theory is the existence of a new light-mass boson, the *axion*.[10,11] The axion mediates a short-range mass-mass interaction. The experimental upper bound $\theta \leqslant 3\times 10^{-10}$ corresponds to a violation of the $1/r^2$ law at the level $|\alpha| \approx 10^{-4}$ at $\lambda = 1$ mm, a force strength that is within reach for ISLES as depicted in Fig. 1.

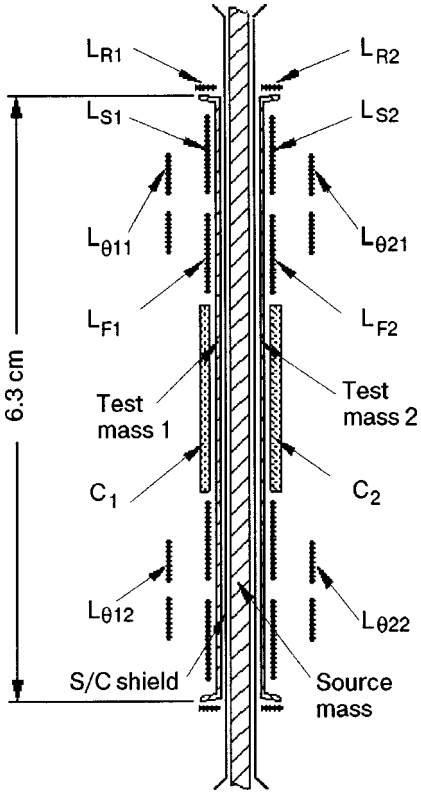

FIG. 2. Configuration of the source and test masses.

The axion could also solve the major open question in astrophysics: the composition of dark matter. Galactic rotation curves and inflation theory require that there should be more mass in the universe than is observed. Although neutrino mass, MACHOs (MAssive Compact Halo Objects), and many hypothetical particles have been offered as explanations, the solution remains elusive. The axion is one of the strongest candidates for the cold dark matter.[12]

3. PRINCIPLE OF THE EXPERIMENT

Newtonian null source

To maximize the masses that can be brought to distances of 100 μm from each other, flat disk geometry is used for both the source and test masses, as is done by Long *et al.*[3] An infinite plane slab is a Newtonian null source in that the gravity force it exerts on a nearby mass does not depend on the distance between the mass and the slab. We approximate such a null source by using a circular disk of sufficiently large diameter. Figure 2 shows the configuration of the source and test masses with associated coils and capacitor plates.

Levitated test masses

Two disk-shaped superconducting test masses are suspended on the two sides of the source mass using magnetic forces and are coupled magnetically to form a differential accelerometer. The motions induced in the test masses are detected by sensing coils (L_{S1} and L_{S2} in Fig. 2).

On Earth it is difficult to suspend two flat disks on opposite sides of the source mass at such proximity without significantly modifying the geometry and stiffening the dif-

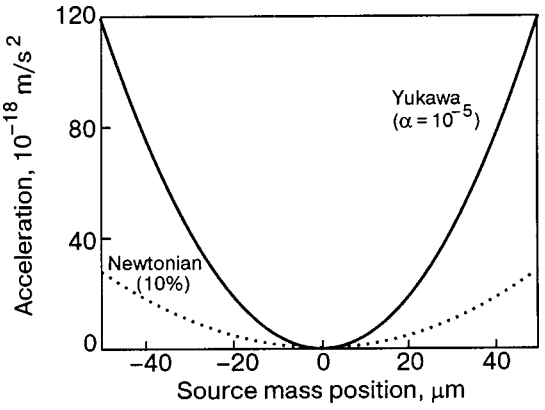

FIG. 3. Newtonian and Yukawa signals versus source position.

ferential mode, thus degrading the resolution of the experiment. In microgravity on the ISS, each test mass can be suspended by applying only minute forces from a pancake coil (L_{S1} or L_{S2}) and from a small ring coil (L_{R1} or L_{R2}) coupled to a narrow slanted rim of the test mass.

Second harmonic detection

As the source mass is driven at frequency f_S along the symmetry axis, the first-order Newtonian fields arising from the finite diameter of the source mass are canceled upon differential measurement, leaving only a second-order error at $2f_S$. By symmetry, the Yukawa signal also appears at $2f_S$. The second harmonic detection, combined with the common-mode rejection ratio (CMRR) of the detector, reduces source-detector vibration coupling by over 300 dB.

Expected signal

The design allows a source displacement of ± 50 μm. The differential acceleration signals expected from the Newtonian force (with correction to 10%) and the Yukawa force with $|\alpha| = 10^{-5}$ and $\lambda = 100$ μm are plotted in Fig. 3 as a function of the source mass position. The rms amplitude of the Yukawa signal corresponding to a ± 50-μm displacement is 1.2×10^{-11} m/s^2. The rms amplitude of the Newtonian error term arising from the finite diameter of the source mass is 1.0×10^{-16} m/s^2 before compensation. While these force amplitudes at $2f_S$ are similar, the Newtonian error will be computed and removed to less than 10% as depicted in Fig. 3, which is straightforward.

Need for low gravity

Sensitive experiments searching for weak forces invariably require soft suspension for the measurement degree of freedom, for which superconducting magnetic levitation offers great promise. Levitation in Earth's gravity, on the other hand, requires a large magnetic field that tends to couple to the measurement axis through metrology errors, and thus stiffens the mode. The large value of magnetic field also makes the suspension more dissipative. Fields close to the critical field H_c of the superconductor must be used to levitate the masses on Earth. Surface impurities will reduce H_c locally. The magnetic field will also be stronger near sharp edges. These effects cause the magnetic fields to be trapped, contributing to damping of the motions through flux creep.

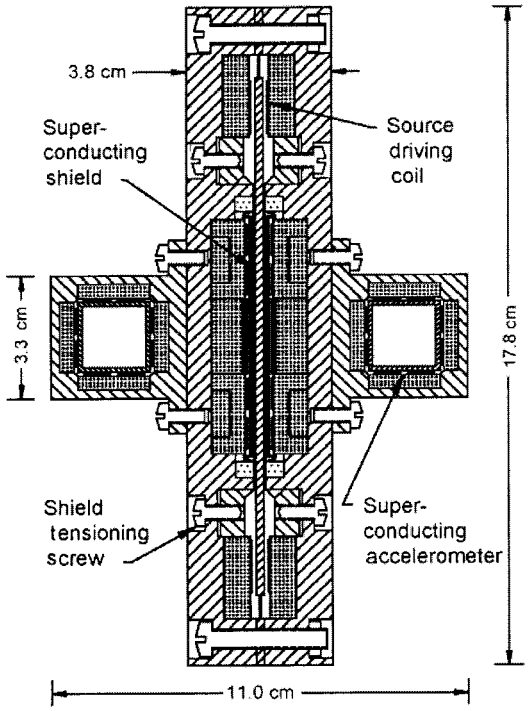

FIG. 4. Cross-section of the ISLES apparatus.

The situation improves dramatically in orbit. The gravity level is reduced by five to six orders of magnitude, so the test masses can be supported with weaker magnetic springs, permitting the realization of both the lowest resonance frequency and lowest dissipation. Our calculations show that, even on such a relatively noisy platform as the ISS, the space experiment will have at least 100 times better resolution over the ground experiment.

4. EXPERIMENTAL HARDWARE

Overview of the apparatus

Figure 4 shows a cross-sectional view of the apparatus. The entire housing is fabricated from niobium. The source mass is made out of tantalum, which closely matches Nb in thermal contraction. This source disk is suspended by cantilever springs at the edge and driven magnetically. A thin Nb shield provides electrostatic and magnetic shielding between the source and each test mass. The test masses are suspended and aligned by magnetic fields from various coils. Two auxiliary three-axis superconducting accelerometers are mounted on opposite sides of the housing to provide linear and angular acceleration signals.

The entire assembly weighs 6.0 kg and fits within the 20-cm diameter envelope of the LTMPF instrument well (see Fig. 5). The masses need not be caged during launch and ISS maneuvers since their sway space will be limited to ± 50 μm by mechanical stops.

The ISLES cryogenic and electrical requirements will be met with the standard LTMPF provision with minor modifications. The entire apparatus is fastened to the second-stage thermal platform of the cryo-insert of LTMPF (Fig. 5). That platform and the instrument will be temperature stabilized to

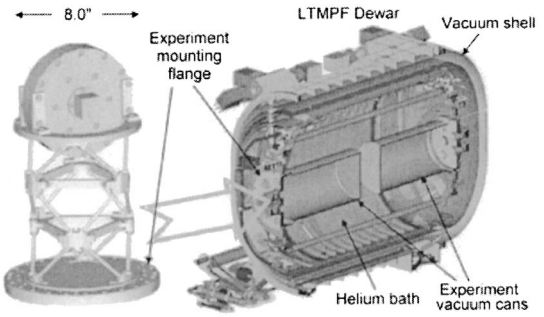

FIG. 5. The ISP mounted on the cryo-insert.

5 μK. The orientation of the detector is chosen so that its sensitive axis is aligned with the pitch (y) axis of the ISS when LTMPF is mounted on JEM-EF. This orientation reduces the centrifugal acceleration noise almost a hundredfold.

Source and test masses

The source mass is a disk 2.0 mm thick by 140 mm in diameter, with mass $M=510$ g. The source mass, cantilever springs, and rim are machined out of a single plate of Ta. Ta is chosen for its high density (16.6 g/cm^3), which increases the signal, and its relatively high H_c. Each test mass is a Nb disk 0.25 mm thick by 63 mm in diameter, with a rim 0.25 mm thick by 2.0 mm wide, which has 5° slant from the axis. The mass of each test mass is $m=7.5$ g. For the 100-μm gap, the test masses are separated by a baseline $\ell=2.45$ mm. The position of each test mass is measured by a capacitor plate located near its center (see Fig. 2) The equilibrium spacing between the source and each test mass is 100 μm. They are shielded from each other by means of a 12.5-μm thick Nb shield, located at 25 μm from the surface of the test mass. The source mass is driven magnetically by coupling a small ac current to a superconducting circuit carrying a large persistent current.

Superconducting circuitry and setup procedure

Schematics of the superconducting circuits for the detector are shown in Fig. 6. These circuits are similar to the standard differencing circuit used in the SGG.[4] The test masses are suspended radially by storing persistent currents I_{R1} and I_{R2} in ring coils L_{R1} and L_{R2} and the pancake coils, as shown in Fig. 6a. Due to the slanted rim of the test masses, currents I_{R1} and I_{R2} will exert an axially outward force on the test masses. This force is balanced by the axially inward forces provided by the currents in the sensing, alignment, and feedback circuits, shown in Figs. 6b–d. The suspension is stable for all degrees of freedom, except for roll about the sensitive axes.

The scale factors of the component accelerometers are matched by adjusting currents I_{S1} and I_{S2} in pancake coils I_{S1} and I_{S2}, as shown in Fig. 6b. The SQUID measures the differential acceleration a_D, or gravity gradient, along the y axis. To align an individual test mass parallel to its shield and

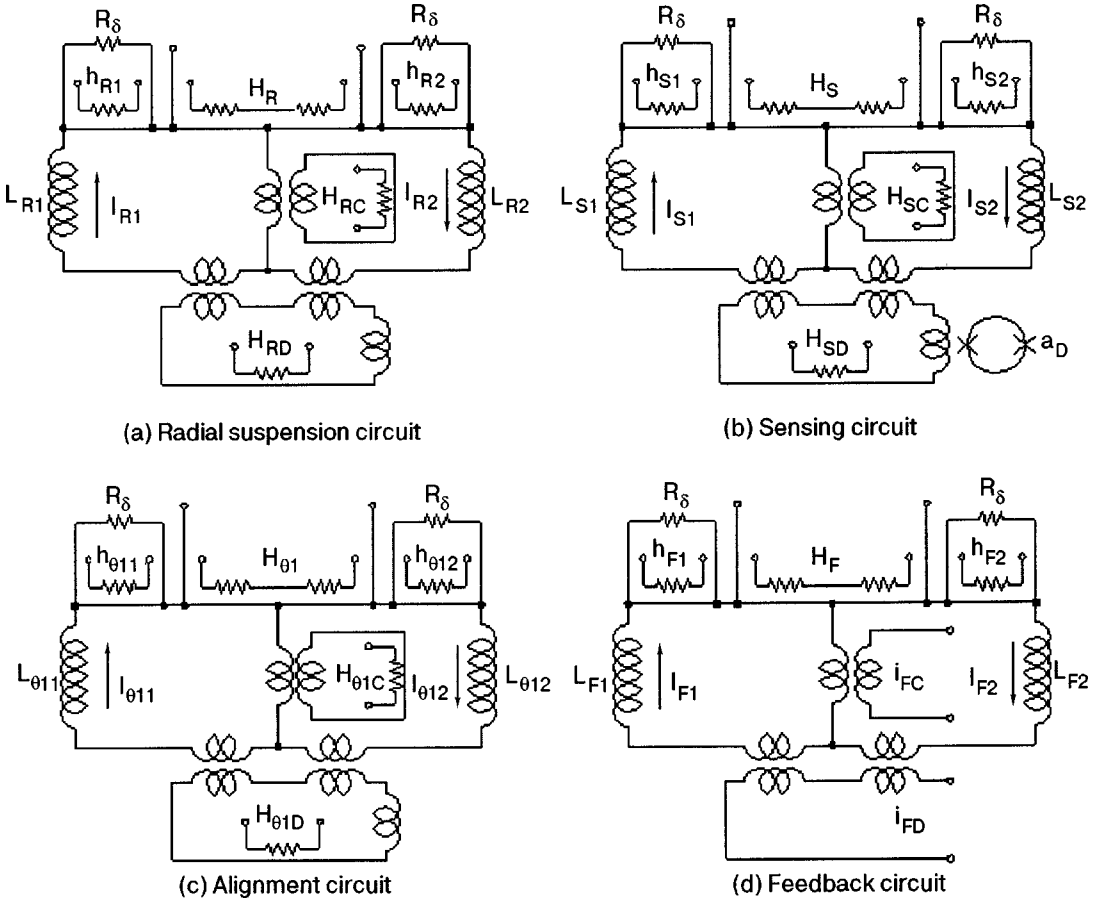

FIG. 6. Superconducting circuits for the detector.

to also align its axis parallel to the axis of the other mass, two alignment circuits are provided for each test mass, one per degree of freedom. Figure 6c shows the alignment circuit of test mass 1 about the x axis. This alignment is accomplished by tuning currents $I_{\theta 11}$ and $I_{\theta 12}$ in remotely coupled pancake coils $L_{\theta 11}$ and $L_{\theta 12}$ (see also Fig. 2). Note that the unique property of long-term stability of persistent currents in superconductors preserves the CMRR tuning over long periods.

The balance procedure matches the linear components of the scale factors but does not completely match the nonlinearity. This mismatched nonlinearity is troublesome since it down-converts the wide-band acceleration noise to the signal frequency. A standard approach to suppressing the nonlinearity is applying a negative feedback to the test masses, which *actively* stiffens the mode. The feedback circuit is given in Fig. 6d. The common-mode (CM) and differential-mode (DM) outputs i_{FC} and i_{FD} are fed back to the test masses. The CM output is derived from the auxiliary accelerometers. Currents I_{F1} and I_{F2} are adjusted to null the effect of the CM feedback on the DM output.

Coarse and fine heat-switches

Due to the high vibration levels of the ISS ($>10^{-6}\,\mathrm{m/(s^2\cdot Hz^{1/2})}$), a special provision must be made to be able to control the magnetic fluxes trapped in various superconducting loops with adequate precision. Coarse heat-switches, denoted by H_{ij}'s, warm up a short length of the Nb wire to a resistance $R\approx 1\,\mathrm{m\Omega}$, resulting in an L/R time of about 10 ms. These coarse switches are used to store currents initially to obtain, for example, the desired spring constants for the suspended masses. Fine heat-switches, denoted by h_{ij}'s, couple a low-resistance path with $R_\delta \approx 0.1\,\mu\Omega$ to the circuit, resulting in a time constant of about 100 s. With 1-ms time resolution of the heat-switch, fluxes can then be adjusted to one part in 10^5. This added precision of the trapped currents gives the ability to match the scale factors to 10^{-5} and to align the sensitive axes to 10^{-5} radian, resulting in an initial CMRR of 10^5 in all three linear degrees of freedom.

Heat-switch H_{SD} in Fig. 6b is turned on to protect the SQUID from a current surge whenever a current is adjusted in the sensing circuit. The output heat-switches H_{iC}'s and H_{iD}'s are turned on to passively damp the corresponding modes in the event large motions of the test masses are excited. While we expect this tuning to maintain its high degree of noise rejection throughout the 5-month period of the experiment on ISS, we use the vibrationally noisy periods of Shuttle dockings and orbit reboosts, when gravity data are unusable or degraded, to test the CMRR and to readjust current values, as found necessary.

Auxiliary superconducting accelerometers

Figure 4 shows two three-axis auxiliary superconducting accelerometers mounted symmetrically on the two sides of the housing. Each test mass is a hollow 20-gram Nb cube, suspended and sensed by Nb pancake coils adjacent to its six faces. The suspension of the cube is stable in all degrees of freedom. The accelerometers are coupled to SQUIDs, two

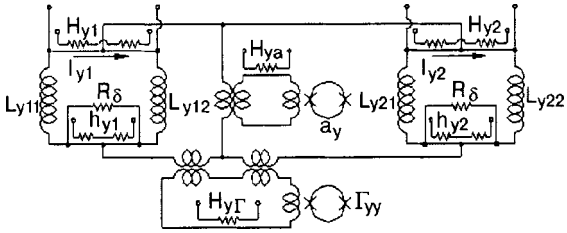

FIG. 7. Superconducting circuit for the y axis of the coupled three-axis auxiliary accelerometers.

SQUIDs per degree of freedom, to measure three linear (a_i) and two angular (α_i) acceleration components, as well as a gravity gradient component (Γ_{ij}).

Figure 7 shows the superconducting circuit for the y axis of the auxiliary accelerometers. The four pancake coils separated along the y axis are combined to sum and difference the signals. The CM and DM signals correspond to a_y and Γ_{yy}, respectively. The gravity gradient signal is used to monitor and remove gravitational disturbances from the detector. The pancake coils separated along the x and z axes are combined in similar circuits to measure a_x and α_z, and a_z and α_x, respectively. The only component that is not measured is α_y, which is not needed for error compensation.

The intrinsic noise of the accelerometers at $f=0.02$ Hz, assuming the noise spectrum of commercial Quantum Design SQUIDs, are $S_a^{1/2}(f)\approx 1\times 10^{-11}\,\mathrm{m/(s^2\,Hz^{1/2})}$, $S_\alpha^{1/2}(f)\approx 3\times 10^{-11}\,\mathrm{rad/(s^2\,Hz^{1/2})}$, and $S_\Gamma^{1/2}(f)\approx 3\times 10^{-11}\,\mathrm{s^{-2}\,Hz^{-1/2}}$).

5. DYNAMIC NOISE REJECTION

Error compensation

Linear and angular accelerations are rejected to 10^{-5} and to 10^{-4} m, respectively, by adjusting persistent currents in the sensing and alignment circuits as described above. To improve the acceleration rejection further, we apply an error compensation technique that has been demonstrated with the SGG.[4] The linear and angular accelerations of the platform, measured by the auxiliary accelerometers, are multiplied by the predetermined error coefficients and subtracted from the detector output to achieve a further reduction of noise by the factor 10^3. By applying the compensation factor 10^3 demonstrated in the laboratory, we should be able to achieve a net CMRR of 10^8 for linear acceleration and a net error coefficient of 10^{-7} m for angular acceleration.

To determine the dynamic error coefficients, accelerations in all degrees of freedom must be provided. If active vibration isolation is implemented as described in the next section, a six-axis shaker will be built into the isolation system that can also be used to apply a sinusoidal acceleration signal in each degree of freedom. If we opt not to employ the vibration isolation system, we will use the ISS vibration noise itself to shake the detector. The accelerations will be random and cross-correlated between degrees of freedom. However, we can apply a well-established procedure in electrical engineering for determining the transfer functions for a multiple-input system using noise alone.[13]

Due to the short but finite baseline ($\ell=2.45$ mm), the $1/r^2$ law detector is a gravity gradiometer that is sensitive to

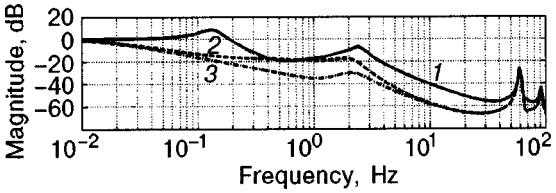

FIG. 8. Frequency response of the vibration isolation system for the *y* axis: (*1*) Passive isolation; (*2*) Active w/translation loop closing; (*3*) Active w/6 DOF loop closing.

attitude modulation of Earth's gravity gradient, gravity noise from ISS, and centrifugal accelerations. Fortunately, the auxiliary gradiometer measures exactly the same gradient noise, except for gravity disturbances from nearby objects (<1 m). This gravity gradient noise can thus be removed from the detector output by applying the above correlation method.

Vibration isolation (option)

With the residual acceleration errors compensated, the most important dynamic error source is the nonlinearity of the scale factors. Vibration isolation of the detector is an alternative way of suppressing the nonlinearity noise.

An active vibration isolation system, combined with a single-stage passive isolation, was studied for LTMPF by Ball Aerospace & Technologies Corp. As LTMPF is designed presently, the sway space is limited to ± 3 mm. This sway amplitude limit constrains our ability to extend the isolation to below 0.1 Hz. Eight D-strut isolators were used to attach the facility frame to the payload interface unit. These isolators provide a 40-dB/decade attenuation from 1 to 200 Hz. Each isolator is also equipped with a voice-coil actuator to provide active isolation. The outputs of the superconducting accelerometers are fed back to these actuators.

The result is shown in Fig. 8. The first curve is the passive isolation provided by the eight D-strut isolators. The first active system (curve *2*) employs only control over the translation degrees of freedom. The second active system (curve *3*) employs closed-loop control over all six degrees of freedom. The isolation system provides only a 10-dB isolation at 0.05 Hz. Its main advantage comes from the reduction of high-frequency acceleration noise, reducing the nonlinearity noise.

6. ERROR BUDGET

Metrology errors

Table I lists the metrology errors estimated using a numerical model. The effects from the finite diameter of the source and the dynamic mass of the suspension springs are corrected to 10 and 20%, respectively. Linear taper and linear density variation of the source produce second-order errors, which become negligible.

The test masses tend to rotate slowly about the sensitive axis, further averaging out the asymmetry about the axis. Hence only the radial taper and the radial density variation are important. Due to the null nature of the source, test mass metrology is not important, except for the extended rim. The rim dimension is corrected to 2.5 μm. The requirements on radial positioning of the test masses are greatly relaxed by the cylindrical symmetry. The total metrology error is $1.5 \times 10^{-17}\,\mathrm{m/s^2}$.

TABLE I. Metrology errors.

Source	Allowance	Error, 10^{-18} m/s^2
Baseline	25 μm	1.0
Source mass		
Finite diameter	10%	12
Suspension spring	20%	2.4
Radial taper	2.5 μm	7.8
Radial density variation	10^{-4}	0.2
Test masses		
Rim dimension	2.5 μm	1.7
Total error		15

The dimensional tolerances are achievable using hand lapping of the parts. Fabrication of the test masses with a slanted rim will require a special procedure. One possibility is machining the entire structure in a single piece by combining regular machining with electric discharge machining. Another possibility is machining the disk and the rim as separate pieces and then diffusion-bonding them in a vacuum oven.

Intrinsic instrument noise

The intrinsic power spectral density of a superconducting differential accelerometer can be written[4,14] as

$$S_a(f) = \frac{8}{m}\left[\frac{k_B T \omega_D}{Q_D} + \frac{\omega_D^2}{2\eta\beta} E_A(f)\right], \tag{3}$$

where m is the mass of each test mass, $\omega_D = 2\pi f_D$ and Q_D are the differential mode resonance frequency and quality factor, β is the electromechanical energy coupling coefficient, η is the electrical energy coupling coefficient of the SQUID, and $E_A(f)$ is the input energy resolution of the SQUID.

Equation (3) shows that the differential-mode frequency f_D is a critical parameter for the intrinsic noise. The microgravity environment on ISS, in principle, allows a suspension 10^6 times softer than on the ground, which corresponds to $f_D < 0.01$ Hz. On the other hand, the differential accelerometer's response to platform vibrations must be minimized to reduce errors caused by electric charge on the test mass, by patch-effect fields, by self-gravity of the ISS, and most importantly by the nonlinearity of the scale factors. Ideally, one would like to increase the common-mode frequency f_C as much as possible, while keeping f_D low. Unfortunately, the nonlinearity of the coils couples a fraction of the CM stiffness to DM, providing a practical limit: $f_C/f_D \leqslant 4$. This limitation forces us to make a compromise. The test masses must remain free before a feedback loop is closed either to the test masses or to the isolator, since otherwise there will be no signal to feed back. Moreover, we need to keep the test mass excursion to $\leqslant 10$ μm. These considerations require

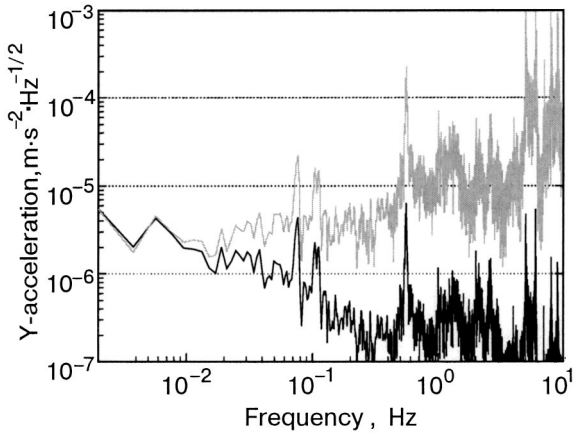

FIG. 9. Linear acceleration along *y* axis: actual (upper) and with active isolation (lower).

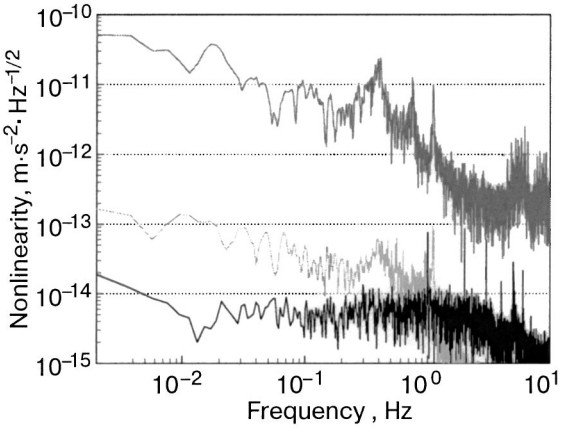

FIG. 10. Nonlinearity error for *y* axis: actual (upper), with active isolation (middle), and with feedback (lower).

$f_C \geqslant 0.2$ Hz and $f_D \geqslant 0.05$ Hz. The result represents a stiffness reduction by 10^4 from the ground experiment.

Analysis of ISLES circuits for the masses chosen shows that $I_{11}=I_{21}\approx 4.7$ mA and $I_{13}=I_{23}\approx 47$ mA gives $f_D=0.05$ Hz and $f_C=0.2$ Hz. For feedback operation of the detector, this choice of mode frequencies, with signal frequency $f=0.02$ Hz, minimizes the total dynamic noise. The radial translational mode frequency is found to be ~ 0.06 Hz. The test masses are free to roll about their axes. Rolling will tend to average out azimuthal asymmetries of the source and the test masses. If active vibration isolation is provided, the optimum frequencies shift slightly to $f=0.05$ Hz, $f_D=0.1$ Hz and $f_C=0.4$ Hz. We compute the intrinsic noise for these two sets of frequencies.

The design values for the other parameters of Eq. (3) are: $T=2$ K, $m=7.5$ g, $Q_D=10^6$, $\beta=\eta=0.5$, and $E_A(f)=10^{-30}(1+0.1\,\text{Hz}/f)$ J/Hz. The SQUID energy resolution corresponds to the flux noise, $5\,\mu\Phi_0\,\text{Hz}^{-1/2}$, originally specified in LTMPF science requirement document, and coincides with the performance typically obtained from commercially available dc SQUIDs. We assume that this SQUID noise level can be achieved for ISLES. With the above parameter values, we find $S_a^{1/2}(f)=7.0\times 10^{-14}\,\text{m}/(\text{s}^2\cdot\text{Hz}^{1/2})$ for $f=0.02$ Hz and $f_D=0.05$ Hz (for feedback), and $S_a^{1/2}(f)=10.8\times 10^{-14}\,\text{m}/(\text{s}^2\cdot\text{Hz}^{1/2})$ for $f=0.05$ Hz and $f_D=0.1$ Hz (for vibration isolation).

Acceleration noise

The upper curve of Fig. 9 shows the *y*-axis linear acceleration spectrum measured by a SAMS II accelerometer in the US Lab of ISS on a typical day. The lower curve is the acceleration spectrum with active isolation, the curve being generated by filtering the acceleration spectrum with the response function given in Fig. 8. The noise is quietest at ~ 0.01 Hz, with a value of $3\times 10^{-6}\,\text{m}/(\text{s}^2\cdot\text{Hz}^{1/2})$. This noise will be reduced to $3\times 10^{-14}\,\text{m}/(\text{s}^2\cdot\text{Hz}^{1/2})$ by the net CMRR of 10^8. The angular acceleration noise is reduced to $2\times 10^{-14}\,\text{m}/(\text{s}^2\cdot\text{Hz}^{1/2})$ by the error coefficient of 10^{-7} m. The centrifugal acceleration noise is negligible.

Using the nonlinearity coefficient measured in the SGG (Ref. 4), we estimate the nonlinearity-induced noise as plotted in Fig. 10. The upper curve is the noise without active isolation or feedback, which is 10^3 times higher than the intrinsic noise of the instrument at 0.01 Hz. The middle curve shows the result of applying the active isolation. At 0.01 Hz, the nonlinearity noise is at $1\times 10^{-13}\,\text{m}/(\text{s}^2\cdot\text{Hz}^{1/2})$. The lower curve shows the nonlinearity noise expected in the detector under a feedback control that stiffens the common mode frequency to 10 Hz.

Assuming that the above acceleration noise represents the actual noise that will be experienced by the ISLES detector, we find a total acceleration noise to be $6.3\times 10^{-14}\,\text{m}/(\text{s}^2\cdot\text{Hz}^{1/2})$ at $f=0.02$ Hz for the feedback option, and $5.9\times 10^{-14}\,\text{m}/(\text{s}^2\cdot\text{Hz}^{1/2})$ at $f=0.05$ Hz for the vibration isolation option.

Gravity noise

Helium tide is absent due to the Earth-fixed orientation of the ISS. Helium sloshing is of minor concern since it is expected to occur at a sufficiently low frequency, ~ 2.5 mHz. The gravity gradiometer along the *x* axis will be used to monitor gravitational disturbances of the experiment. The gravity noise from modulation of the Earth's gravity gradient and ISS self-gravity, including the activities of astronauts, will be taken out, along with the centrifugal acceleration, by the error measurement and compensation scheme.

Magnetic crosstalk

Trapped flux is not of concern if the flux is strongly pinned. Cooling and performing the experiment in a low magnetic field will minimize flux creep. For this purpose, LTMPF is equipped with a cryoperm shield. Material processing and the insertion of flux dams can reduce flux motion that might be induced by the incidence of charged particles in orbit.

With the high magnetic field required to drive the source mass, magnetic crosstalk between the source and the detector is a very important potential source of error. To solve this problem, the entire housing is machined out of Nb and a Nb shield is provided between the source and each test mass. High-purity Nb will be used. The Nb will be heat-treated to bring the material very close to a type-I superconductor, thus minimizing flux penetration. The superconducting shield is expected to provide over 200 dB isolation.[15] This isolation,

combined with 60 dB rejection expected from the second harmonic detection, should provide the required isolation between the source drive signal and the test masses in excess of 260 dB.

Electric charge effects

Levitated test masses in orbit will accumulate electric charge from cosmic rays and from high-energy protons, as the spacecraft traverses through the South Atlantic Anomaly. Scaling from the charge computed for STEP test masses,[16] we find that the total charge accumulated in each ISLES test mass over the entire duration of the experiment will be $Q \approx 1.5\times10^{-13}$ C. In deriving this number, we used a charge trapping efficiency 10% that of STEP to account for the difference in shape, the ISLES test masses are extremely thin (250 μm) and do not trap charge as efficiently as the much thicker STEP test masses.

The charge trapped in the test mass will induce image charges on the neighboring coils and superconducting ground planes. Most of the trapped charge will appear on the surfaces of the test masses facing the shields since the gap is smallest there ($\sim$20 μm). This will generate a differential force $Q^2/\varepsilon_0 A$, where ε_0 is the permittivity of vacuum and A is the area of the test mass. The force results in the maximum differential displacement at the end of the mission:

$$x_{D,\max}=\frac{Q^2}{\varepsilon_0 A}\frac{1}{m\omega_D^2}\approx 7\times10^{-9}\ \text{m}. \tag{4}$$

A differential displacement affects the CMRR through mismatches in the coil areas, gaps and currents. With the initial coil gap of 10^{-4} m and a mismatch of 10%, we find that the CMRR is affected by 7 ppm at most. This should allow the passive CMRR to remain at the required level of 10^5 throughout the mission. So ISLES does not require a discharging system. To make sure that the trapped charge remains below the threshold, the charge will be measured after each 30-days data run and the test masses will be discharged, if necessary, by simply pushing them against the shields. This may necessitate a recalibration of the detector.

Energetic charged particles will also impart momentum and cause heating of the test masses. These effects were found to be less important than the electrostatic force for STEP. In addition, patch-effect potential will be modulated as charge builds up in the test masses, causing a time-varying acceleration. These ac disturbances occur mostly outside the signal band and therefore are averaged out. The Casimir force is not of concern for the present experiment where the gap between the masses is much more 1 μm.[17]

Temperature noise

The modulation of the penetration depth of a superconductor with temperature and residual thermal expansion coefficients for different materials give rise to temperature sensitivity in a superconducting accelerometer. These occur through temperature gradients as well as mismatches in the accelerometers.[14] From our experience with the SGG, however, this noise is expected to be negligible with the platform temperature stabilized to 5 μK.

TABLE II. Error budget.

Error source	Error, 10^{-18} m/s^2	
	w/feedback	w/isolation
Metrology	15	15
Random	(90 days)	(90 days)
Intrinsic	25	39
ISS vibration	23	21
Gravity noise	<1	<1
Vibration coupling	<1	<1
Magnetic coupling	<10	<10
Electric charge	<10	<10
Other (30% margin)	33	41
Total	52	64

Total errors

Table II combines all the errors for the two scenarios: one with feedback and the other with vibration isolation. To reduce the random noise to the levels listed, a 90-days integration was assumed. The vibration isolation approach does not reduce the total noise, but is worth considering because it greatly simplifies the detector design and operation. It allows the use of a slightly stiffer suspension, which will reduce the disturbances from the trapped charge. Therefore, we plan to have a trade study at the beginning of the flight definition phase, comparing the risks and benefits, and the costs of implementing these approaches.

7. EXPECTED RESOLUTION

By equating the noise with the expected Yukawa signal, we compute the minimum detectable $|\alpha|$. Figure 1 shows the $1-\sigma$ error plotted as a function of λ for the feedback approach. The case with active isolation is very similar. The best resolution of ISLES is $|\alpha|=1\times10^{-5}$ at $\lambda=100$ μm^{-1} mm. ISLES will test the $1/r^2$ law with a resolution of 10^{-2} at $\lambda=10$ μm. Figure 1 shows that the string theory predicted violation with $R_2\geqslant 5$ μm will be detected and axions with strength 10–100 times below the maximum will be detected.

ISLES will use the SGG technology fully developed at the University of Maryland. The SGG has been used to perform a null test of Newton's law at a sensitivity ten times beyond that of the other methods at 1-meter distance.[18] The instrument proposed for ISLES is very similar to the existing SGG and will apply noise-compensating techniques already demonstrated on the SGG. The experimental procedure and error analysis are also similar to those in the meter-scale $1/r^2$ law test, also previously carried out with the SGG.

For the modest cost of the ISS experiment, the scientific gain from ISLES is tremendous. ISLES constitutes a new test of general relativity in the hitherto largely untested range

and will perform the first ever test of a prediction of string theory. The experiment will push the frontiers of searching for new weak forces by several orders of magnitude, with a potential to discover new particles.

It should be noted that the instrument will launch while completely inactive, with no currents stored and no electronics turned on. Once on orbit, the SQUIDs and the temperature control circuits will be activated, and the ''levitation'' currents will be set. Then the tuning of the CMRR will proceed, and the error coefficients will be measured. With these data stored, the data for testing the $1/r^2$ law can be gathered. This passive launch implies that no exchange gas need be placed in the vacuum space during launch, so the lowest possible residual gas levels will be obtained in the space around the instrument. Thus, high Q-values can be expected for the test mass motions. Also, being able to adjust all experimental parameters while the instrument is on orbit means that the experimenter is able to monitor and correct any error-inducing disturbances that might occur during the experiment's tenure.

*E-mail: dons@squid.jpl.nasa.gov

[1] E. G. Adelberger *et al.*, Annu. Rev. Nucl. Part. Sci. **41**, 269 (1991).
[2] C. D. Hoyle *et al.*, Phys. Rev. Lett. **86**, 1418 (2001).
[3] J. C. Long *et al.*, Nucl. Phys. B **539**, 23 (1999).
[4] M. V. Moody, E. R. Canavan, and H. J. Paik, (submitted to Rev. Sci. Instrum.).
[5] N. Arkani-Hamed, S. Dimopoulos, and G. Dvali, Phys. Rev. D **59**, 086004 (1999).
[6] S. Cullen and M. Perelstein, preprint hep-ph/9903422 (1999).
[7] L. J. Hall and D. Smith, Phys. Rev. D **60**, 085008 (1999).
[8] S. Hannestad and G. G. Raffelt, Phys. Rev. Lett. **88**, 071301 (2002).
[9] R. D. Peccei and H. Quinn, Phys. Rev. Lett. **38**, 1440 (1977).
[10] S. Weinberg, Phys. Rev. Lett. **40**, 223 (1978).
[11] F. Wilczek, Phys. Rev. Lett. **40**, 279 (1978).
[12] M. S. Turner, Phys. Rep. **197**, 67 (1990).
[13] J. S. Bendat and A. G. Piersol, *Random Data: Analysis and Measurement Procedures*, Wiley, New York (1971), Chapter 5.
[14] H. A. Chan and H. J. Paik, Phys. Rev. D **35**, 3551 (1987).
[15] K. W. Rigby, D. Marek, and T. C. P. Chui, Rev. Sci. Instrum. **2**, 834 (1990).
[16] J.-P. Blaser *et al.*, *STEP (Satellite Test of the Equivalence Principle)*, Report on the Phase A Study, SCI(96)5 (1996).
[17] S. K. Lamoreaux, Phys. Rev. Lett. **78**, 5 (1997).
[18] M. V. Moody and H. J. Paik, Phys. Rev. Lett. **70**, 1195 (1993).

This article was published in English in the original Russian journal. Reproduced here with stylistic changes by AIP.

Thermal gravity-driven convection of near-critical helium in enclosures

V. I. Polezhaev and E. B. Soboleva*

Institute for Problems of Mechanics RAS, pr. Vernadskogo, 101, b. 1, Moscow, 119526, Russia
(Submitted December 19, 2002)
Fiz. Nizk. Temp. **29**, 648–652 (2003)

The results of a numerical simulation of Rayleigh–Bènard convection in ^{3}He near the thermodynamic critical point are presented. The mathematical model includes the full Navier–Stokes equations with two-scale splitting of the pressure and the van der Waals equation of state. The existing experimental data on ^{3}He are used in the simulation. The ''real'' Rayleigh and Prandtl numbers are estimated on the basis of the scaling laws. It is shown that to simulate the experiments more closely these ''real'' similarity criteria must concur for the physical media and the model. The Rayleigh number characterizing convection onset is determined from the calculations. This number is shown to be in good agreement with the existing experimental and theoretical values. © *2003 American Institute of Physics.*
[DOI: 10.1063/1.1542532]

1. INTRODUCTION

Near a thermodynamic critical point media known as near-critical fluids display distinctive thermodynamic and kinetic properties.[1,2] There is an asymptotic discrepancy in the specific heat at constant pressure, the isothermal compressibility, and the thermal expansion coefficient. On the other hand the heat diffusion coefficient tends to zero. These abnormal properties cause distinctive heat transfer and interesting hydrodynamic effects as compared with a perfect gas.

We shall perform a numerical simulation of gravity-driven thermal convection on the basis of a hydrodynamic model using the van der Waals equation of state. The classical problem of steady-state Rayleigh–Bènard convection (with heating from below), well-known for a perfect gas,[3] will be solved for a near-critical fluid and the results will be compared with experimental data. The parameters used in the numerical simulation will be estimated on the basis of the physical properties of helium, and in the limit the model fluid will tend toward a real fluid. Rayleigh–Bènard convection has been simulated in intense near-critical flows.[4] We shall investigate the onset of convection.

2. MATHEMATICAL MODEL OF AN IMPERFECT GAS

The full Navier–Stokes equations and the energy equation for an imperfect gas with the van der Waals equation of state are used. Two-scale splitting of the pressure into volume-average and dynamic parts is used.[5] Integral mass balance is used to close the equations. The governing equations in dimensionless form are:[6]

$$\frac{\partial \rho}{\partial t}+\nabla(\rho \mathbf{U})=0, \tag{1}$$

$$\rho\frac{\partial U}{\partial t}+\rho(\mathbf{U}\nabla)\mathbf{U}=-\nabla p+\frac{1}{\mathrm{Re}}\left(2\nabla(\eta\dot{D})-\nabla\left(\frac{2}{3}\eta-\zeta\right)\nabla\mathbf{U}\right)+\frac{\mathrm{Ra}}{\mathrm{Pr}\Theta\,\mathrm{Re}^2}\rho\mathbf{g}, \tag{2}$$

$$\rho\frac{\partial T}{\partial t}+\rho(\mathbf{U}\nabla)T=-(\gamma_0-1)T\left(\frac{\partial P}{\partial T}\right)_\rho\nabla\mathbf{U}+\frac{\gamma_0}{\mathrm{Re}\,\mathrm{Pr}}\nabla(\lambda\nabla T)+\frac{\gamma_0(\gamma_0-1)M^2}{\mathrm{Re}}\times\left(2\eta\dot{D}^2-\nabla\left(\frac{2}{3}\eta-\zeta\right)(\nabla\mathbf{U})^2\right), \tag{3}$$

$$P=\rho T/(1-b\rho)-a\rho^2,\quad a=9/8,\quad b=1/3, \tag{4}$$

$$P=\langle P\rangle+\gamma_0M^2p, \tag{5}$$

$$\int_V p\,dv=0. \tag{6}$$

Here ρ, $\mathbf{U}$, $\dot{D}$, and T are the density, the velocity, the strain rate tensor, and the pressure, respectively; P, $\langle P\rangle$, and p are the total pressure, the volume-averaged pressure, and the dynamic pressure, respectively; $\mathbf{g}$ is the mass force acceleration; η, ζ, and λ are the coefficients of dynamic and bulk viscosity and the thermal conductivity, respectively; and, dv is an element of volume and V is the total volume. Dimensionless values are marked with primes. The characteristic scales are: length l', velocity U', time l'/U', strain rate U'/l', the acceleration of Earth's gravity g', the critical values ρ_c' and T_c', and λ_0', η_0', and c_{v0}' for a perfect gas; $B'=R'/\mu_g'$, R' is the gas constant for a perfect gas, and μ_g' is the molar mass. Primes denote dimensional values; the subscript c denotes critical values and the subscript 0 denotes values for a perfect gas.

The dimensionless parameters (the ratio of specific heats, the characteristic temperature difference, and the Reynolds, Mach, Prandtl, and Rayleigh numbers for a perfect gas) are

$$\gamma_0=1+\frac{B'}{c_{v0}'},\quad \Theta=\frac{\Theta'}{T_c'},\quad \mathrm{Re}=\frac{\rho_c'U'l'}{\eta_0'},\quad M=\frac{U'}{\sqrt{\gamma_0B'T_c'}},$$

$$\mathrm{Ra}=\frac{\Theta' g' l'^3 \rho_c'^2 (c_{v0}'+B')}{T_c' \lambda_0' \eta_0'}, \quad \mathrm{Pr}=\frac{(c_{v0}'+B')\eta_0'}{\lambda_0'}. \tag{7}$$

The total pressure P is decomposed into two parts (a volume-averaged component $\langle P\rangle$ and a dynamic component p), and the parts are normalized using different scales ($B'\rho_c'T_c'$ for $\langle P\rangle$ and $\rho_c'U'^2$ for p). Splitting and two-scale representations of the pressure and a large time step are used to simulate acoustic and low-speed flows.

For conditions close to a critical isochore the near-critical features are associated with the temperature distance from the critical point (or the reduced temperature) $\varepsilon=(T'-T_c')T_c'$. The coefficient λ increases as $\varepsilon\to 0$ and is given by the relation[1]

$$\lambda=1+\Lambda\varepsilon^{-\psi}, \tag{8}$$

the coefficient η is assumed to be constant, and $\zeta=0$.

The Rayleigh and Prandtl numbers characterize convection motion. As the critical point is approached, these similarity criteria tend to infinity, while the values of Ra and Pr in the governing equations based on the perfect-gas parameters remain unchanged. To describe near-critical convection completely we shall consider the "real" Rayleigh number Ra_r and the "real" Prandtl number Pr_r, which take account of the real physical properties near the critical point. They are denoted by the subscript r and expressed by the scaling laws (near-critical isochore)[7]

$$\mathrm{Ra}_r=\frac{2}{3}\varepsilon^{-1}\left(\frac{1}{\gamma_0}+\frac{\gamma_0-1}{\gamma_0}\,\frac{1+\varepsilon}{\varepsilon}\right)\frac{1}{\lambda}\mathrm{Ra},$$

$$\mathrm{Pr}_r=\left(\frac{1}{\gamma_0}+\frac{\gamma_0-1}{\gamma_0}\,\frac{1+\varepsilon}{\varepsilon}\right)\frac{1}{\lambda}\mathrm{Pr}. \tag{9}$$

The numbers Ra_r and Pr_r diverge asymptotically as the critical point is approached:

$$\mathrm{Ra}_r/\mathrm{Ra}\sim\varepsilon^{\psi-2}\to\infty, \quad \mathrm{Pr}_r/\mathrm{Pr}\sim\varepsilon^{\psi-1}\to\infty\ (\psi<1),$$

$$\text{as}\quad \varepsilon\to 0.$$

3. THE PHYSICAL PROPERTIES OF HELIUM AND THE RAYLEIGH–BÈNARD CONVECTION PARAMETERS NEAR THE CRITICAL POINT

The critical point in ^{3}He is characterized by the parameters[8,9] $T_c'=3.3189$ K, $\rho_c'=0.0414$ g/cm^3, and $P_c'=0.117$ MPa. We shall consider Rayleigh–Bènard convection in ^{3}He, which has been studied experimentally in Refs. 8 and 9. We use the physical properties of ^{3}He at reduced temperatures $5\times10^{-4}\leqslant\varepsilon\leqslant 0.2$.[10] We take the model parameters from the available data.

We fit the relation (8) to the data on the thermal conductivity λ', using the dimensionless quantity $\lambda=\lambda'/\lambda_0'$, where λ_0' is a scale value. The constants Λ, ψ, and λ_0' characterize the best fit

$$\lambda=1+0.0149\varepsilon^{-0.645} \tag{10}$$

normalized by the scale $\lambda_0'=1.73\times10^{-4}$ W/(cm·K). The curve (10) is plotted in Fig. 1 in comparison with the experimental points from Ref 10. The agreement is good.

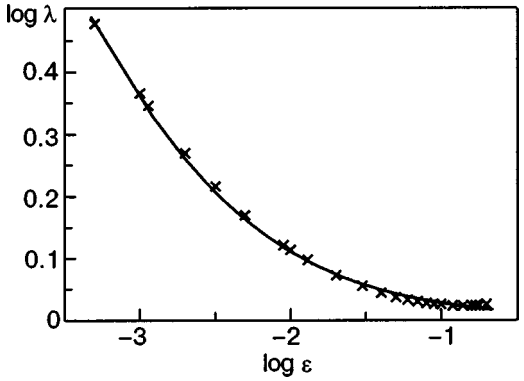

FIG. 1. Computed fit of the thermal conductivity λ (10) (solid line) and the experimental values (marks)[10] as functions of the reduced temperature ε in logarithmic coordinates.

The experimental data of Ref. 10 permit finding the specific heat c_p at constant pressure and the thermal expansion coefficient β according to the relations (in dimensionless form)

$$c_p=c_v\gamma, \quad \beta=c_v(\gamma-1)/[(1+\varepsilon)(\partial P/\partial T)_\rho]. \tag{11}$$

Then the experimental Rayleigh number, which takes account of the real physical properties, is

$$\mathrm{Ra}_r=\mathrm{Ra}\beta c_p Z/(\lambda\gamma_0). \tag{12}$$

Here $Z=P_c'/(B'\rho_c'T_c')$ is the compressibility factor. The classical specific-heat ratio for a perfect gas $\gamma_0=1.67$ is used. The value of Ra is estimated on the basis of the experiments performed in Refs. 8 and 9 and the properties of helium far from the critical point. We shall take the typical temperature difference Θ' from the experimental range and for definiteness we shall use the value 10 μK. We have $l'=0.1$ cm, $g_0'=9.8\times10^2$ cm/s^2, $\Theta'=10^{-5}$ K, $\eta_0'=16.7\times10^{-6}$ g/(cm·s), $\lambda_0'=1.73\times10^{-4}$ W/(cm·K), $c_{v0}'=3.12\times10^7$ erg/(K·g). The experimental values of the Prandtl number Pr_r are taken from Ref. 10 and then Pr can be obtained from Eq. (9). Consequently, the values which take account of the physical properties are $\mathrm{Ra}=9\times10$ and $\mathrm{Pr}=0.501$.

The results reveal discrepancies, which increase as ε decreases, between the experimental and model similarity criteria. These discrepancies are probably due to the equation of state. The van der Waals and other analytic equations of this type, for example, the Redlich–Kwong equation used in Ref. 11, give fixed critical exponents which are different from the experimental values. The scaled equations of state supported by the renormalization-group theory[12,13] give the best agreement between the theoretical and experimental exponents, but they are applicable only asymptotically when $\varepsilon\ll 1$. We cannot employ any scaled equation in our work because ε varies over a wide range.

We shall use the van der Waals equation of state, setting the simulation parameters for different ε so that locally the experimental and "real" model similarity criteria are equal to one another. For example, for $\varepsilon=0.03$ the experimental values are $\mathrm{Ra}_r=1.27\times10^4$ and $\mathrm{Pr}_r=12.4$. As follows from Eq. (9) these values correspond to $\mathrm{Ra}=45.4$ and $\mathrm{Pr}=0.986$, which should be used in the governing equations. As shown in Fig. 2, the experimental and model similarity criteria are equal to one another locally at $\varepsilon=0.03$. To investigate near-critical convection near other temperature distances from the

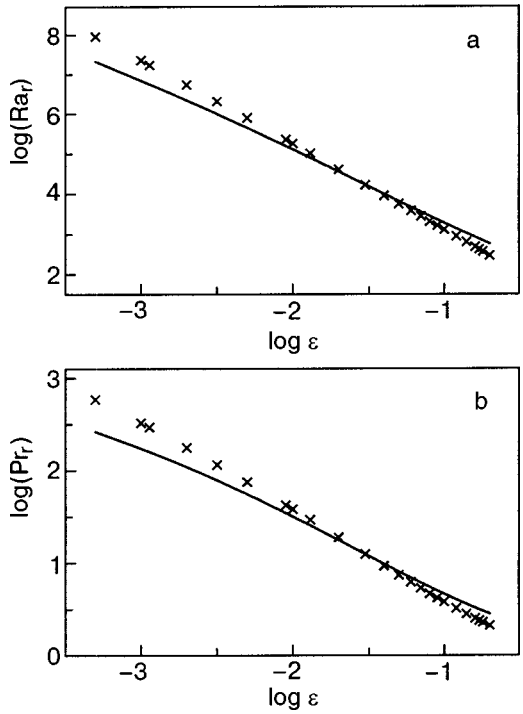

FIG. 2. The ''real'' Rayleigh number Ra_r (a) and Prandtl number Pr_r (b) in the model fluid with local similarity to ^{3}He (solid lines) and in ^{3}He (marks) versus ε.

critical point the parameters Ra and Pr must be reevaluated and the results used in the governing equations. Though the numbers Ra and Pr do not take account of the physical properties of helium far from the critical point, they do ensure that convection processes in the physical and near-critical model fluids correspond to one another near a certain temperature.

4. SIMULATION OF NEAR-CRITICAL RAYLEIGH–BÈNARD CONVECTION

We used the mathematical model described above to perform a 2D simulation of steady-state Rayleigh–Bènard convection in helium along the critical isochore close to experiments in a flat Rayleigh–Bènard cell (height—1 mm, diamter—57 mm).[8,9] The temperature of the top plate was kept fixed; the bottom plate was heated very slowly so as to have a quasisteady state at every moment in time.

We simulated a part of the whole cell (a square with 1 mm edges) containing only a single roll. The conditions were assumed to be nonviscous and adiabatic at the vertical boundaries and viscous and isothermal at the horizontal boundaries. The temperature of the top surface was 0.33 K above the critical value and the temperature of the bottom surface was higher by some amount Θ'. The parameters $\varepsilon = 0.1$, $\mathrm{Re} = 8.33 \times 10^3$, $\mathrm{Pr} = 0.814$, $\gamma_0 = 1.67$, and $\mathrm{M} = 10^{-3}$ were used. The temperature difference Θ and, consequently, the Rayleigh number Ra vary. We used $\Theta = (5.79 - 6.11) \times 10^{-6}$ (corresponding to the dimensional values $\Theta' = 19.2 - 20.7\ \mu\mathrm{K}$) and $\mathrm{Ra} = 45.0 - 47.6$, respectively. The values of Ra and Pr give ''real'' similarity criteria Ra_r and Pr_r which are the same as the experimental values.

The integration of the governing equations is started at the smallest value of Θ and continued until a steady-state is reached. Then the bottom surface is slowly heated to the next value of Θ and integration is continued up to another steady-state regime. This process gives a set of stationary solutions for different values of Θ. These solutions give the Rayleigh number $Ra_{r\text{-onset}}$ characterizing convection onset. We extrapolated the Nusselt number Nu to $\mathrm{Nu} = 1$ for which convection is absent. The Ra_r dependence of Nu should be linear when convection starts. The extrapolation gives the threshold value $Ra_{r\text{-onset}} = 1804$. The relation between Nu and Ra_r is shown in Fig. 3.

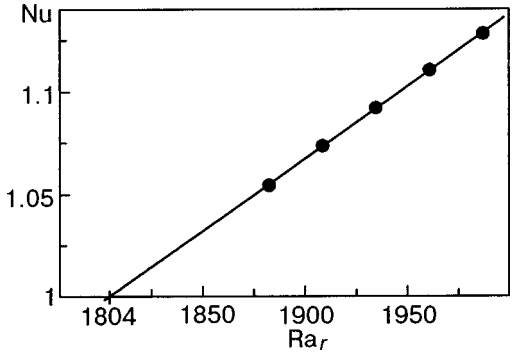

FIG. 3. The Nusselt number Nu versus the ''real'' Rayleigh number Ra_r (marks) and a linear fit (solid line) near convection onset.

The results obtained here are in good agreement with the experimental data[8,9] and calculations[14] for stability problems in compressible media. As predicted, the value obtained for $Ra_{r\text{-onset}}$ is slightly larger than the classical value for incompressible fluids (1708) because the adiabatic temperature gradient is different from zero. These results show that the general approach developed above for simulating near-critical dynamics gives excellent agreement between heat transfer in the model and real fluids under the experimental conditions.

5. DISCUSSION AND CONCLUSIONS

The mathematical model for simulating near-critical dynamics and fitting existing experimental data for helium, the results of a simulation of gravity-driven convection, and an approach for realizing the results obtained were presented. Numerical simulation was performed using a new 2D numerical computer code based on the full Navier–Stokes equations with two-scale splitting of the pressure and the van der Waals equation of state. The scaling laws were used to estimate the ''real'' similarity criteria based on the physical properties of near-critical fluids. It was shown that to simulate the experimental conditions more closely the ''real'' Rayleigh and Prandtl numbers for the physical media and the model must concur.

Steady-state Rayleigh–Bènard convection of helium near the critical isochore, which has been investigated experimentally, was simulated. The Rayleigh number characterizing convection onset was determined from numerical data. This number is shown to be in good agreement with existing experimental and theoretical values.

However, the ''real'' Rayleigh and Prandtl numbers describe the dynamics and heat transfer completely only for an incompressible fluid (in the Oberbeck–Boussinesque model). The analysis of simulated near-critical convection in the general case requires further elaboration taking account of the

compressibility of the medium. In Ref. 14 it was shown that in a near-critical fluid the effect of compressibility and an adiabatic temperature gradient in Rayleigh–Bènard convection increases as the critical point is approached, and as a result the Schwarzchild criterion plays a dominant role. An expression for the adiabatic temperature gradient for a van der Waals gas is given in Ref. 15. Here we have determined convection onset only for a single, quite large value of the reduced temperature $\varepsilon = 0.1$. The experiments of Ref. 9 have shown that the Schwarzchild criterion plays no role at this distance from the critical point. This is why no compressibility parameter is present in the scaling laws and the Schwarzchild number is ignored. But close to the near-critical region the Schwarzchild number must be taken into account.

Nonetheless the mathematical model used, the efficient computer code, and the approach developed for realizing the results obtained can be used to simulate and analyze complex dynamical problems for near-critical fluids close to the experimental conditions. This makes it possible to investigate numerically certain characteristics of the near-critical dynamics which present difficulties in experiments. For example, the ''piston effect'' observed in enclosures with a heat source[16] is known to be very important in unsteady near-critical heat transfer. This effect can alter the thermal and dynamical pictures, but its effect is not always controllable experimentally. This problem can be solved numerically, leading to well-studied and controlled experimental conditions and understandable results. All points discussed above will be elaborated elsewhere.

We gratefully acknowledge Professor H. Meyer for providing to us the experimental data on the physical properties of ^{3}He and for careful correspondence. We also thank Dr. A. Lednev for fruitful discussions. This work was funded by the Russian Foundation for Basic Research (Grant 03-01-00682).

*E-mail: soboleva@ipmnet.ru

[1] H. E. Stanley, *Introduction to Phase Transitions and Critical Phenomena*, Oxford Science Publications, New York (1987).
[2] M. A. Anisimov, *Critical Phenomena in Liquids and Liquid Crystals*, Gordon and Breach, Philadelphia, PA (1991).
[3] V. I. Polezhaev and M. P. Vlasuk, Reports of the Russian Academy of Sciences: Hydrodynamics **195**, 1058 (1970).
[4] S. Amiroudine, P. Bontoux, P. Laroude, B. Gilly, and B. Zappoli, J. Fluid Mech. **442**, 119 (2001).
[5] A. G. Churbanov, A. N. Pavlov, A. V. Voronkov, and A. A. Ionkin, in *Proceedings of the 10th International Conference on Numerical Methods in Laminar and Turbulent Flows, Swansea, 1997*, Pineridge Press, Swansea (1997), p. 1099.
[6] V. I. Polezhaev and E. B. Soboleva, Izv. Akad. Nauk, Mekh. Zhid. i Gaza **1**, 81 (2002) [Fluid Dyn. **37**(1), 72 (2002)].
[7] V. I. Polezhaev and E. B. Soboleva, Izv. Akad. Nauk, Mekh. Zhid. i Gaza **3**, 143 (2001) [Fluid Dyn. **36**(3), 467 (2001)] [*sic*].
[8] A. B. Kogan, D. Murphys, and H. Meyer, Phys. Rev. Lett. **82**, 4635 (1999).
[9] A. B. Kogan and H. Meyer, Phys. Rev. E **63**, 056310 (2001).
[10] H. Meyer, private communication.
[11] E. B. Soboleva, Teplofiz. Vys. Temp. **38**, 928 (2000) [High Temp. **38**, 893 (2000)].
[12] P. Schofield, Phys. Rev. Lett. **22**, 606 (1969).
[13] A. Z. Patashinskii and V. L. Pokrovskii, *Fluctuation Theory of Phase Transitions*, Pergamon Press, New York (1979).
[14] M. Gitterman and V. A. Steinberg, Teplofiz. Vys. Temp. **10**, 565 (1972) [High Temp. **10**, 501 (1972)].
[15] V. I. Polezhaev, A. A. Gorbunov, and E. B. Soboleva, in *Proceedings of the 2nd Pan-Pacific Basin Workshop on Microgravity Sciences, Pasadena, 2001* [Adv. Space Res. **29,** 581 (2002)].
[16] A. Onuki, H. Hao, and R. A. Ferrell, Phys. Rev. A **41**, 2256 (1990).

This article was published in English in the original Russian journal. Reproduced here with stylistic changes by AIP.

Boiling of He II in a porous structure in microgravity: a model representation

I. M. Dergunov, P. V. Korolev, A. P. Kryukov,* and Yu. Yu. Selyaninova

Department of Low Temperatures, Moscow Power Engineering Institute, ul. Krasnokazarmennaya 14, 111250 Moscow, Russia

(Submitted December 19, 2002)
Fiz. Nizk. Temp. **29**, 653–658 (June 2003)

The results of a modeling of the boiling of superfluid helium in a microgravity environment are presented. The evolution of the vapor film on the surface of a cylindrical heater placed inside a thick-walled cylinder with porous walls is analyzed. The methods of molecular kinetic theory are used to describe the heat and mass transfer on the interphase surface. The equation of motion of the vapor–liquid interphase surface is solved. The influence of the parameters of the experiment on the characteristics of the vapor film is studied. The results of the calculation for microgravity and terrestrial environments are compared. © *2003 American Institute of Physics.* [DOI: 10.1063/1.1542533]

1. INTRODUCTION

The formation and growth of vapor bubbles on the surface of a heater immersed in a liquid upon boiling has been studied for a long while. Several models have been proposed for describing these processes. However, these models have been developed mainly for the situation in which heat is transferred to the liquid–vapor interphase surface from the liquid side. At high heat flux densities the opposite situation can be realized: the heater is surrounded by a vapor layer, and the heat is transferred to the surrounding liquid through the vapor–liquid interphase boundary. It is well known that the boiling of He II is accompanied by the formation of a vapor film around the heater, i.e., it takes place only in the form of film boiling. Thus heat is transferred to the He II through the vapor–liquid interphase surface. The heat and mass transfer at this surface are interrelated processes. The heat transfer efficiency in superfluid helium is very high, and because of this the heat transfer from the heater to the boundary of the superfluid helium at high heat fluxes should be limited by phenomena occurring at the vapor–He II interphase surface, unlike the case of ordinary liquids. The temperature of the heater surface can be considerably higher than the temperature of the vapor–He II interphase surface, leading to a nonequilibrium situation at the surface of a heater immersed in superfluid helium. Under these conditions the use of the methods of continuum mechanics is not always justified, whereas an approach based on molecular kinetic theory permits a correct analysis of processes occurring at any degree of disequilibrium.

We have previously analyzed the evolution of the vapor–He II interphase surface under terrestrial conditions. On Earth the pressure difference in the liquid depends on the acceleration of gravity. Accordingly, both the peak and the recovery heat fluxes are determined by the hydrostatic head.[1] At a shallow immersion depth of the heater in He II the thickness of the vapor film increases rapidly with increasing heat flux, leading to a shape instability. In order to study vapor films of large thickness at different heat fluxes, it is necessary to do the study in a microgravity environment. Such an environment can be realized in experiments on the International Space Station (ISS), for example. For simplicity we shall analyze the heat and mass transfer processes in the one-dimensional approximation.

2. STATEMENT OF THE PROBLEM

In a microgravity environment it is necessary to have a system for producing a pressure difference analogous to the hydrostatic difference under terrestrial conditions. For modeling the boiling processes of superfluid helium in microgravity, we use a capillary–porous medium (Fig. 1). A cylindrical heater of radius R_w is placed inside a coaxial thick-walled cylindrical tube (envelope) of radius R_0 and thickness L. Channels of radius R_k are made through the wall of this envelope. The number of channels is determined by the porosity μ, i.e., the ratio of the transverse cross section of all the capillaries to the inner surface area of the envelope. The interior space and the capillaries of the porous medium are entirely filled with superfluid helium. The cell is in theoretical weightlessness. Because of the good wetting, the outer surface of the porous tube is also coated by a film of superfluid liquid.

At a heat flux density q_w above a certain critical value a vapor film of radius R_1 will be formed on the surface of the heater. The vapor pressure in the outer volume of the experimental cell is maintained at a constant level P_b. In the cal-

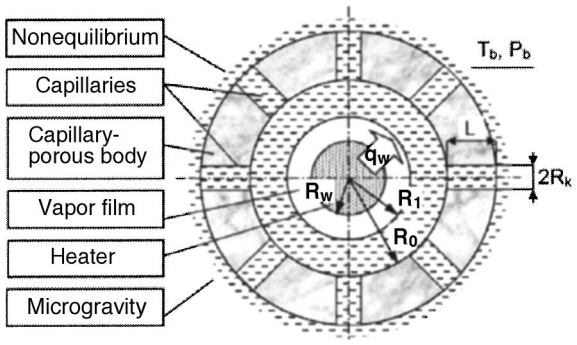

FIG. 1. Model of the experimental cell.

culation we analyze the evolution of the vapor film upon changes in the flux density and pressure and in the geometric dimensions of the cell. It is assumed that the other thermophysical and hydrodynamic parameters needed in the calculation are known or to be specified.

3. DESCRIPTION OF THE MODEL

A complete mathematical description of the proposed model of the experimental cell consists of three parts. The first part, the description of the vapor film, includes the conservation equations for this medium in cylindrical coordinates and also the equation of state. This part of the calculation can be done using the Boltzmann kinetic equation. The second part is the description of the behavior of the liquid in the inner cavity. For this, a system of conservation equations for an incompressible liquid is written in cylindrical coordinates with allowance for the peculiarities of the hydrodynamics and heat transfer in superfluid helium. Finally, the third part of the calculations, which yields the parameters of the system in the capillaries of the porous body, includes the conservation equations for an incompressible liquid flowing in channels of circular cross section, with the specifics of the heat transfer and hydrodynamics in He II taken into account. This system of equations is closed by universal and special conditions of compatibility at the interphase surfaces in the cavity and on the outer surface of the capillary–porous body. The heat flux at the surface of the heater and the vapor pressure in the outer region are treated as boundary conditions of the problem. In the numerical calculations these quantities are assumed given.

Thus the proposed mathematical description consists of a rather large number of partial differential equations. It looks extremely difficult to obtain an analytical solution of this system, and the numerical solution of the complete system of equations entails the accumulation of computational errors. Moreover, the algorithmization of the solution of the system of partial differential equations is a rather laborious process. Therefore, to simplify the system of equations we make some assumptions: a) we consider the one-dimensional problem in a cylindrical coordinate system; b) we assume that the external heat transfer and heat loss are negligible; c) the thermophysical properties of the liquid are independent of temperature; d) all of the energy released by the heater is expended on the evaporation of He II on the outer surface of the capillary–porous cylinder.

The motion of the vapor–liquid boundary is described by an ordinary differential equation:[2]

$$(\ddot{R}_1 R_1 + \dot{R}_1^2)\ln\left(\frac{R_0}{R_1}\right) + \frac{(\dot{R}_1 R_1)^2}{2}\left(\frac{1}{R_0^2} - \frac{1}{R_1^2}\right) = \frac{P_1' - P_0}{\rho'}. \tag{1}$$

Here R_1 [m] is the radius of the vapor film, $\ddot{R} = d^2R/d\tau^2$ [m/s^2] and $\dot{R} = dR/d\tau = V_1$ [m/s] are the acceleration and velocity of the interphase surface, respectively, R_0 [m] is the inner radius of the capillary–porous tube, P_1' [Pa] is the pressure of the liquid near the interphase surface, P_0 [Pa] is the pressure on the inner surface of the capillary–porous body, and ρ' [kg/m^3] is the density of the liquid. The initial conditions at $\tau = 0$ are $R_1 = R_w$ and $\dot{R} = 0$, where R_w is the radius of the heater.

Nonequilibrium effects at the interphase boundary are described by a formula obtained on the basis of the Boltzmann kinetic equation:[3]

$$P_1'' = 0.5 P_{S1}\left(1 + \sqrt{1 + \frac{\sqrt{\pi} q_1}{P_{S1}\sqrt{2RT_1'}}}\right), \tag{2}$$

where P_1'' [Pa] is the pressure in the vapor film, $P_{S1} = P_S(T_1')$ [Pa] is the saturation pressure at the corresponding temperature, q_1 [W/m^2] is the heat flux from the heater to the interphase surface, R is the gas constant for helium [J/(kg·K)], and T_1' [K] is the temperature of the liquid near the interphase surface.

The heat and mass transfer and the hydrodynamics are described by special equations for superfluid helium. The relation for the energy flux in He II without allowance for dissipative processes gives a relation between the heat flux and the velocity of the liquid in the capillaries:[4]

$$q_0 = \rho' S(V_n - V)T, \tag{3}$$

where q_0 [W/m^2] is the heat flux in the capillaries, S [J/(kg·K)] is the entropy of the liquid, V_n [m/s] is the velocity of the normal component of He II in the capillaries, T_b [K] is the temperature of the liquid at the outer surface of the porous body, and T_0 [K] is the temperature of the liquid at the inner surface of the porous tube. Thus $V_n - V$ is the relative velocity of the liquid in the capillaries, and $T = \sqrt{T_0 T_b}$ [K] is the mean temperature of the liquid in the capillary.

The velocity of the liquid and the pressure difference in the channel are interrelated. The acceleration of the liquid is insignificant. The flow of the normal component is assumed to be steady. It is also assumed that a laminar flow regime is realized. The motion of the normal component is described by the Hagen–Poiseuille equation:[5]

$$P_0 - P_b = \frac{32\eta L V_n}{(2R_k)^2}, \tag{4}$$

where $L = R_b - R_0$ [m] is the length of the capillary (R_b is the outer radius of the porous tube), η [Pa·s] is the viscosity of the normal motion of the He II, and R_k [m] is the radius of the capillary.

The difference of the pressures in the capillaries is related to the temperature difference by[5]

$$P_b - P_0 = \rho' S(T_b - T_0). \tag{5}$$

Equations (3)–(5) show that the heat transfer is related to the dynamical processes in the capillaries.

The heat transfer in the cavity of a porous tube filled with superfluid helium is described by the Gorter–Mellink equation:[6]

$$q_1^3 = \frac{2}{R_1 \tilde{f}(T)}(T_1' - T_0)\left(1 - \left(\frac{R_1}{R_0}\right)^2\right)^{-1}, \tag{6}$$

where $\tilde{f}(T)$ is the Gorter–Mellink integral mutual friction function. The stability of equations (1)–(6) is closed by the conservation relations:

$$q_1 = q_w \frac{R_w}{R_1}, \quad q_0 = q_w \frac{R_w}{\mu R_0}, \quad V_1 = V \frac{\mu R_0}{R_1}. \tag{7}$$

The universal condition of compatibility for the momentum flux at the interphase surface has the form

$$P_1' + \frac{\sigma}{R_1} = P_1'' - 2\eta \frac{\dot{R}_1}{R_1}. \tag{8}$$

The system of equations (1)–(8) describes the transfer processes in the experimental cell: a) heat transfer in the vapor film, in the cavity surrounded by the cylindrical envelope, and in the liquid-filled capillaries; b) dynamical effects due to the flow of liquid and surface tension; c) kinetic effects on the interphase surface.

As the above system of equations is difficult to solve analytically, we have used numerical methods to solve this problem.

4. RESULTS AND DISCUSSION

The problem of film boiling of superfluid helium in a porous structure model in microgravity is solved here first. Among the peculiarities of this problem is the fact that the pressure difference in the liquid depends not only on the geometric parameters of the cell but also on the heat flux and the external conditions. The temperature of the liquid depends on the external pressure. The pressure difference in the liquid is due to kinetic effects at the interphase surface (2). Importantly, the main influence on the evolution of the vapor film is the heat flux.

The results of an analysis of the behavior of the transient characteristics of the process are presented below. The main dynamical processes occur at the initial time. When a heat flux greater than a certain critical value is turned on (in this analysis it is assumed *a priori* that the surface of the heater is surrounded by a vapor film) the vapor film grows, the vapor pressure increases, and the liquid is accelerated. As the thickness of the film increases, the heat flux arriving at the interphase surface and the force of surface tension decrease.

Such characteristics of the evolution of a vapor film as the velocity of the interphase surface, the pressure in the film, and the steady-state radius of the film depend on the parameters of the cell. As an example, one of these dependences is shown in Fig. 2. These results were obtained for the following initial data: $q_w = 1000$ W/m^2, $R_w = 0.001$ m, $R_0 = 0.01$ m, $\mu = 0.5$, $L = 0.01$ m, $P_b = 3169$ Pa, and $T_b = 2$ K.

The hydraulic resistance of the channels depends on the diameter (4). A steady state of the film is established for certain values of the radius of the capillaries ($R_k = 5\ \mu$m, ..., $R_k = 10\ \mu$m). The difference of the pressures in the capillaries corresponds to the velocity of the normal component determined by the heat flux. This is seen from Eqs. (3)–(5). The pressure difference of the liquid in the cavity of the capillary–porous tube becomes equal to zero in the steady-state stage. The normal component in the capillaries moves counter to the superfluid component, which has no viscosity. This counterflow ensures the stationarity of the liquid as a whole.

If the radius of the capillaries is small enough ($R_k < 5\ \mu$m), the vapor film cannot grow. The hydraulic resistance and surface tension become greater than the pressure difference between the vapor spaces. In this case the superfluid liquid is overheated, undergoes a transition to the He I state, and then evaporates. If the radius of the capillaries is large enough ($R_k = 15\ \mu$m), the thickness of the vapor film increases rapidly. In this case the stationarity condition is not attained, and the liquid flows out of the inner cavity.

Analogous data were obtained for the other geometric parameters. It follows from these calculations that the value of the steady-state radius of the film increases with increasing inner radius of the sheath, radius of the heater, and porosity and with decreasing length of the capillaries. The choice of the dimensions of the heater also depends on the volume of the inner cavity. The evolution of a vapor film is governed by the heat flux and the pressure in the cryostat. These quantities can be changed during the experiment.

The influence of the heat flux density on the evolution of the vapor film is shown in Fig. 3. The initial data were taken the same as for the calculations presented in Fig. 2 for $R_k = 10\ \mu$m. The steady-state radius of the film and the rate of growth of the vapor film increase with increasing heat flux, while the time of the transient stage decreases. The kinetic

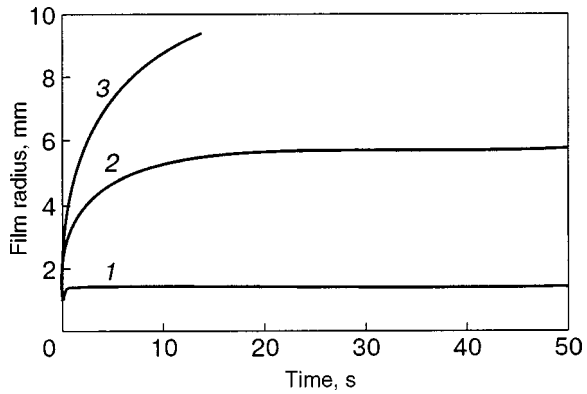

FIG. 2. Influence of the capillary radius on the evolution of the vapor film: $R_k = 5$ (*1*), 10 (*2*), and 15 μm (*3*).

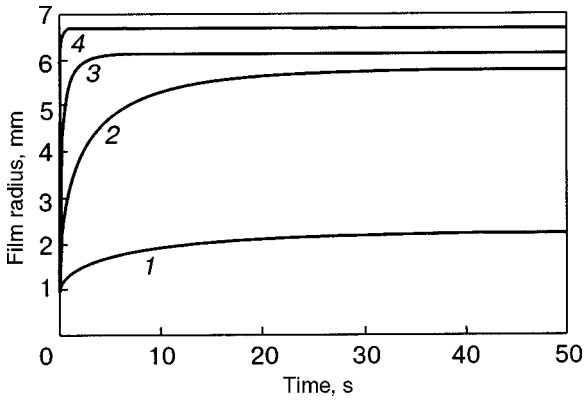

FIG. 3. Influence of the heat flux on the evolution of the vapor film: $q_w = 10^2$ (*1*), 10^3 (*2*), 10^4 (*3*), 10^5 W/m^2 (*4*).

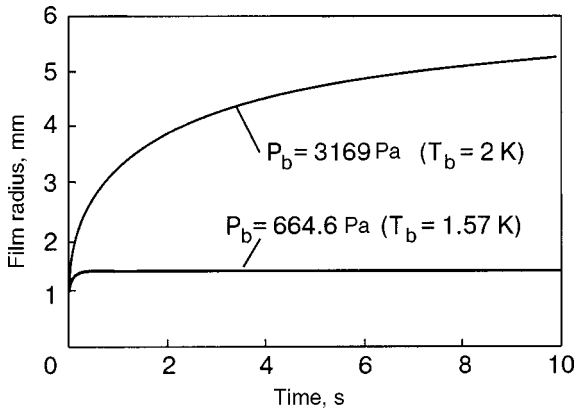

FIG. 4. Influence of the vapor pressure on the evolution of the vapor film.

effects at the interphase surface are governed by the heat flux (2). Here the pressure difference in the capillaries depends on the heat flux and film radius. For a relatively small heat flux ($q_w < 77$ W/m^2) the hydraulic resistance and surface tension prevent the growth of the vapor film.

The influence of the vapor pressure in the cryostat on the evolution of the vapor film is shown in Fig. 4. The initial data are the same as before, but the heat flux density $q_w = 1000$ W/m^2. The calculations show that the steady-state radius increases with increasing vapor pressure. The time of the transient stage also increases. This tendency can be attributed to the following causes. The temperature of the liquid depends on the vapor pressure. At the outer surface the superfluid liquid is maintained close to a state of saturation. The properties of the superfluid helium, viz., the density, viscosity, surface tension, and entropy, are temperature dependent. The saturated vapor pressure is strongly temperature dependent. Therefore, if the vapor pressure decreases by a factor of 4.7, for example, as in Fig. 4, the entropy of the liquid becomes lower by a factor of 4.1. At a constant value of the heat flux the pressure difference increases in accordance with relations (3) and (4). Ultimately, the additional pressure, which is analogous to the hydrostatic head under terrestrial conditions, increases as well. Consequently, the steady-state radius of the vapor film should be smaller for $P_b = 664.6$ Pa than for $P_b = 3169$ Pa.

These results show that the radius of the vapor film is very sensitive to variations of the heat flux q_w and to the vapor pressure in the cryostat, P_b. Thus in an experimental study the values of these quantities must be strictly controlled.

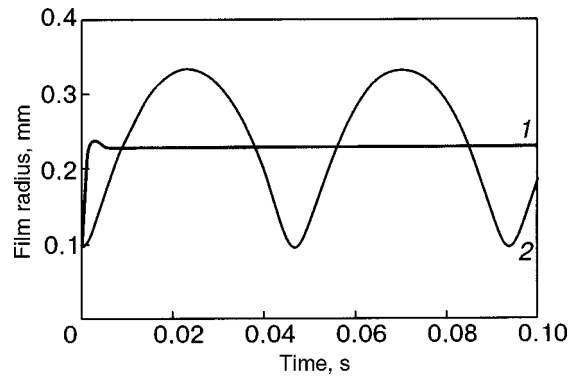

FIG. 5. Comparison of the dynamics of the vapor film in the microgravity (*1*) and terrestrial (*2*) environments.

A comparison of the results of a calculation of the evolution of the vapor film in the microgravity and terrestrial environments is shown in Fig. 5. The radius of the heater, the heat flux, and the temperature of the liquid were taken the same in both calculations ($q_w = 18100$ W/cm^2, $P_b = 664.6$ Pa, $R_w = 95.5$ μm). The other parameters were chosen such that the values of the steady-state radii of these films were equal ($R_0 = 0.02$ m, $\mu = 0.5$, $L = 0.1092$ m, $R_k = 10$ μm; depth of immersion under terrestrial conditions $h = 0.028$ m).

In a microgravity environment the steady state is rapidly attained. The pressure difference in the liquid depends on the heat flux, on the velocity of the liquid, and the present position of the interphase surface. In contrast to terrestrial conditions, the behavior of the system in microgravity is determined mainly by the heat flux. Under terrestrial conditions the pressure difference in the liquid is a function of the immersion depth of the heater and is independent of the heat flux. It should be noted that on Earth the steady state is reached after the oscillations are depressed out by the forces of viscous friction. This depression occurs over a significantly longer time scale than that shown in Fig. 5.

5. CONCLUSION

Calculations have shown that the vapor film can evolve according to three scenarios:

1) the radius of the vapor film does not increase, on account of the hydraulic resistance of the capillaries and the effect of surface tension;

2) the vapor film grows rather rapidly, causing the liquid to be expelled from the capillaries onto the outer surface of the surrounding envelope;

3) a steady state of the film is established.

The pressure difference in the liquid is due to kinetic effects at the interphase surfaces. This pressure difference depends on the heat flux.

The foregoing calculations in the framework of the proposed model of the experimental cell, which is intended for research in a microgravity environment, show that oscillations of the vapor film do not arise when the heater is turned on.

This study was supported by the Russian Foundation for Basic Research, Project No. 02-02-16311.

*E-mail: apk@mcsa.ac.ru

[1] A. P. Kryukov and S. W. Van Sciver, Cryogenics **21**, 525 (1981).
[2] I. M. Dergunov, A. P. Kryukov, and A. A. Gorbunov, J. Low Temp. Phys. **119**, 403 (2000).
[3] P. V. Khurtin and A. P. Kryukov, J. Low Temp. Phys. **119**, 413 (2000).
[4] P. V. Korolev and A. P. Kryukov, Vestn. Mosk. Énerg. Inst., No. 1, 43 (2002).
[5] L. D. Landau and E. M. Lifshitz, *Fluid Mechanics*, 2nd ed., Pergamon Press, Oxford (1987), Nauka, Moscow (1986).
[6] C. J. Gorter and J. H. Mellink, Physica (Amsterdam) **15**, 285 (1949).

Translated by Steve Torstveit

Quantum computing with bits made of electrons on a helium surface

A. J. Dahm*

Department of Physics, Case Western Reserve University, Cleveland, OH 44106-7079, USA
(Submitted December 19, 2002)
Fiz. Nizk. Temp. **29**, 659–662 (June 2003)

We describe a quantum computer based on electrons supported by a helium film and localized laterally by small electrodes. Each quantum bit (qubit) is made of combinations of the ground and first excited state of an electron trapped in the image potential well at the surface. Mechanisms for preparing the initial state of the qubit, operations with the qubits, and a proposed readout are described. This system is, in principle, capable of 10^5 operations in a decoherence time. © *2003 American Institute of Physics.* [DOI: 10.1063/1.1542534]

1. INTRODUCTION

In a quantum computer two stationary states of a quantum system are identified with classical bits 0 and 1. Each quantum bit (qubit) is made up of a superposition of these two quantum states. The state of the *n*th qubit

$$\psi = a|0\rangle + b|1\rangle; \quad |a|^2 + |b|^2 = 1. \tag{1}$$

In the majority of operations $a_n = 0$, 1 or $2^{-1/2}$.

A quantum computer is a superposition of all qubit states. A simple superposition is a product of individual qubit states. The general state of a quantum computer is an entangled state, a state that cannot be made of a product of individual qubits. An example is the state

$$2^{-1/2}(|01\rangle + |10\rangle). \tag{2}$$

One method of producing an entangled state is by using a controlled NOT (CNOT) gate. This gate consists of a control bit and a target bit. If a control bit is $|0\rangle$ the target bit is unchanged, while if the control bit is $|1\rangle$ the components of the target bit $|0\rangle$ and $|1\rangle$ change to $|1\rangle$ and $|0\rangle$, respectively. A CNOT gate is described below. An example of an entangling operation is with the first bit as the control bit

$$2^{-1/2}(|0\rangle + |1\rangle)|1\rangle = 2^{-1/2}(|01\rangle + |10\rangle). \tag{3}$$

The general state is written as

$$\Psi = \sum_j \alpha_j |x_j\rangle, \quad \sum_j |\alpha_j|^2 = 1, \tag{4}$$

where each basis vector $|x_j\rangle$ is one of the 2^n permutations of the zeros and ones representing separate qubits. In the final state one of these basis vectors is the answer to the calculation. The entangled state collapses when one of the qubits is read. For the most general algorithms all qubits must be read out simultaneously.

We describe here a proposed quantum computer that uses laterally confined electrons on the surface of a liquid helium film as qubits and describe operations with these qubits including a simultaneous readout. A full description of quantum computing is beyond the scope of this paper.[1] This concept was first introduced by Platzman and Dykman.[2]

2. ELECTRONS ON HELIUM

Electrons are bound to the surface of liquid helium by the dielectric image potential. A repulsive Pauli potential that can be represented to a good approximation as $V = \infty$ for $z < 0$ prevents them from penetrating into liquid helium. The hydrogenic-like potential for $z > 0$ is

$$V = -\Lambda e^2/4\pi\varepsilon_0 z; \quad \Lambda = (\kappa - 1)/4(\kappa + 1), \tag{5}$$

where z is the coordinate normal to the surface, and κ is the dielectric constant of helium. The energy levels form a Rydberg spectrum, $E_n = -R/n^2$. The parameters for liquid ^{3}He are $\Lambda_3 = 0.00521$, $R_3 = 0.37$ meV, and the effective Bohr radius is $a_B = 10.2$ nm. The average separations of the electron from the surface are $\langle z \rangle = 15.3$ and 61 nm for the ground and first excited state, respectively. The transition frequency between the ground and first excited state is 70 GHz. These transitions can be shifted with a Stark field applied normal to the surface. The potentials are shown in Fig. 1 for applied electric fields $F > 0$, $F = 0$ and $F < 0$.

3. DESIGN OF THE COMPUTER

We identify the ground and first excited states of these electrons with the states $|0\rangle$ and $|1\rangle$, respectively. In order to address and control the qubits each electron must be localized laterally. This will be accomplished by locating elec-

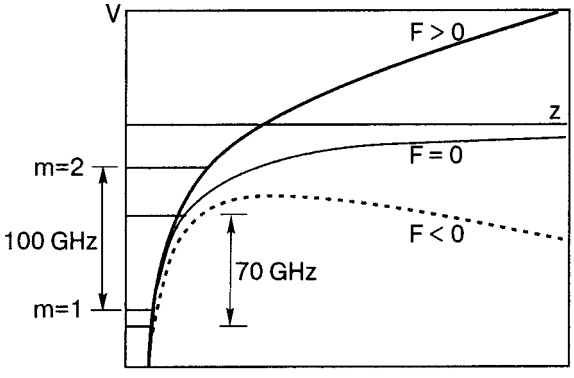

FIG. 1. The potentials and energy levels with and without an electric field F applied normal to the surface. The ground ($m = 1$) and excited ($m = 2$) energy levels are indicated schematically for each potential. The potential for an extracting field $F < 0$ is also shown as a dashed line.

trons above microelectrodes (posts) that are separated by about 1 μm. The electrons will be separated from the posts by an ≈ 1 μm thick helium film. Lateral confinement results from the image potentials of the posts and the potential applied on the posts. The electron will be in the ground state for lateral motion.

A schematic of posts and electrons for a four-qubit system is shown in Fig. 2. A voltage applied to a given post controls the Stark field for the corresponding electron. An array of posts with leads has been fabricated.

A schematic of our cell is shown in Fig. 3. The plates form the top and bottom of an enlarged waveguide that transmits sub-mm radiation to the electrons. Superconducting micro-bolometers will be located at the top of the guide to detect electrons that are allowed to escape from the posts. A tunnel-diode electron-emission source will be located above the electron detectors. Electrons will be loaded onto the film through a hole in the detector chip, and one electron will be trapped over each post by image and applied potentials. The helium film thickness will be measured with a capacitor made of metal strips deposited on the ground plane. The system will be operated at 10 mK to increase coherence times of the qubit states.

4. OPERATIONS

Data input: The operation would normally begin with all qubits in the ground state. Then initial data will be input by preparing each qubit in some admixture of states $|0\rangle$ and $|1\rangle$ by Stark shifting individual qubits into resonance with microwave radiation for a predetermined time. The state of the qubit n will be

$$\Psi_n = \cos(\theta_n/2)|0\rangle - i\sin(\theta_n/2)|1\rangle, \tag{6}$$

where $\theta_n = \Omega\tau_n$, $\Omega = eE_{\rm rf}\langle 1|z|2\rangle/\hbar$ is the Rabi frequency, $E_{\rm rf}$ is the strength of the rf field, and τ_n is the time the nth qubit is in resonance with the microwave field.

Quantum gates: In general, computations will be implemented by applying pulses of radiation to interacting qubits. We illustrate a potential operating mode of the system by describing two qubits operated as a SWAP gate. The interaction is the Coulomb interaction between neighboring electrons. The dipolar component of the direct interaction potential between qubits i and j is

$$V(z_i, z_j) \sim (e^2/8\pi\varepsilon_0 d^3)(z_i - z_j)^2, \tag{7}$$

where d is the electron separation, and z_i is the separation of the ith electron from the helium surface. Start with one qubit in the state $|0\rangle$ and the other in the state $|1\rangle$. Next apply the same Stark fields to both qubits so that the states $|01\rangle$ and $|10\rangle$ would be degenerate. In this condition the system will oscillate between the two states at a frequency given by the interaction energy, which in first order is given by $e^2 a_B^2/4\pi\varepsilon_0 d^3$. This frequency is $\sim 10^8$ Hz for a separation of 1 μm. By leaving the electric fields in this condition for one half cycle of this oscillation, the two qubits will swap states. It will be difficult to tune neighboring qubits to precisely identical Stark shifts, and in practice we may sweep the Stark shift of one qubit through resonance with a neighboring qubit. In this case, the final state of the qubit will depend on the rate at which the electric field is swept through the resonance condition.

A two-qubit CNOT gate can be operated as follows. The energy for the target bit to make a transition depends whether the separation of the electrons is increased or decreased in the transition. The transition frequency is

$$\Delta\nu = \Delta\nu_0 \pm (e^2/8\pi\varepsilon_0 d^3 h)(z_2 - z_1)^2, \tag{8}$$

respectively, when the control bit is in the $|1\rangle$ or $|0\rangle$ state. Here $\Delta\nu_0$ is the frequency in the absence of interactions, h is Planck's constant, and subscripts refer to the ground and excited states. By applying radiation at one of the frequencies, a transition will or will not occur depending on the state of the control bit. The control bit is Stark shifted out of resonance.

Readout. For the general case the states of all qubits must be read within the time scale set by the plasma frequency $\sim$100 GHz. We describe here our initial proposal for a destructive readout pending research into other schemes. We will apply a short, $\sim$1 ns, ramp of an extracting electric field to all qubits. The potential for a fixed value of extracting field is shown in Fig. 1. The tunneling probability is exponential in the time-dependent barrier height and width. All electrons in the upper $|1\rangle$ state will tunnel through the barrier within a short period of time when this probability becomes sufficiently large. For this extracting field the tunneling probability will be negligibly small for electrons in the ground $|0\rangle$ state. After the ramp is removed the remaining

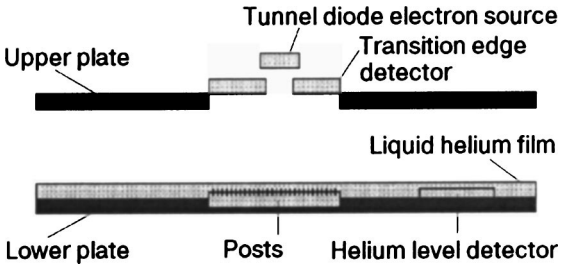

FIG. 3. Schematic of the cell. The upper plate includes detectors used in the readout. The lower plate includes the posts and is covered with the helium film. The electrons float over the posts about 10 nm above the surface of the helium film.

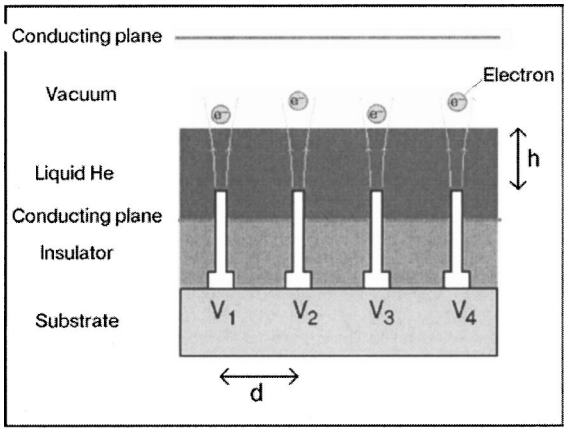

FIG. 2. The geometry of a four-qubit system with electrons above the microstructure and the helium film. The drawing is not to scale. Optimal dimensions are $d \approx h \approx 1$ μm. Control potentials V_n are applied on the microelectrodes.

electrons will be in the ground state. Subsequently, an extracting field sufficiently large so that electrons in the ground state will tunnel from the surface[3] will be applied sequentially to each post. A $|0\rangle$ will be registered for each electron detected by the transition-edge bolometer and a $|1\rangle$ for those states that are empty.

5. DECOHERENCE

T_1: Logic operations must be accomplished in less time than it takes for the interactions of the qubit with the environment to destroy the phase coherence of the state functions. For electrons on ^{4}He the lifetime of the excited state $|1\rangle$ is limited by interactions with ripplons and coupling to phonons in the bulk liquid. These processes are discussed in detail by Dykman *et al.*[4] The electron-ripplon coupling Hamiltonian is

$$\mathcal{H}_{\rm er} = eE_{\perp}\delta, \tag{9}$$

where $E_{\perp}$ is the normal component of the electric field that includes both the applied field and variations in the helium dielectric image field due to surface distortions, and δ is the amplitude of the surface height variation. The average rms thermal fluctuation of the surface is

$$\delta_T = (k_B T/\sigma)^{1/2} \cong 2\times 10^{-9} \ \text{cm}. \tag{10}$$

The transition from the excited to ground state requires a ripplon with a wave vector $\cong a_B^{-1}$. For a single electron on bulk helium a radiationless transition occurs with the energy absorbed by electron plane-wave states for motion parallel to the surface and momentum absorbed by ripplons. For this case a calculation of T_1 yields

$$T_1^{-1} \cong \Delta\nu(\delta_T/a_B)^2, \tag{11}$$

where $\Delta\nu$ is the transition frequency. At $T=10$ mK, $\delta_T/a_B \cong 10^{-3}$, and $T_1 \cong 10\,\mu$s.

For electrons confined by posts, the lateral states are harmonic oscillator states of the image potential well of the posts. These are separated in energy by $\hbar\omega_1 \approx \hbar(eE_{\perp}/4\pi\varepsilon_0 mh)^{1/2} \sim 1$ K for $E_{\perp}=500$ V/cm. For interacting electrons there is a band of plasma oscillations associated with each harmonic oscillator level, which for a crystal array with a separation of 1 μm has a bandwidth that is 300 mK. The frequency ω_1 can be tuned so the transition $|1\rangle \rightarrow |0\rangle$ is incommensurate in energy with the excitation to the plasmon band of any harmonic level and suppresses this channel for decay. This is illustrated in Fig. 4. The separation of energy levels for lateral motion can also be accomplished with the application of a magnetic field.

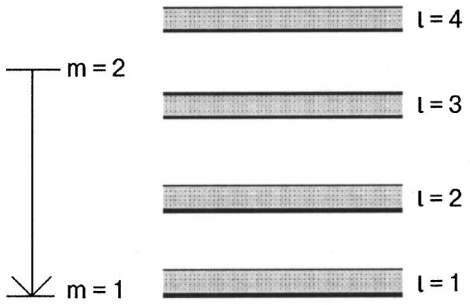

FIG. 4. Energy level schematic. The integer m labels the hydrogenic-like states, and the integer l labels lateral states, which represent harmonic oscillator states or Landau levels in a magnetic field. The hatched region indicates the band of plasma oscillations associated with each level.

Decay can occur with the emission of two ripplons with opposite wavevectors and the excitation of a harmonic level nearest in energy to the $|1\rangle$ state plus plasmons. This yields $T_1 \sim 1$ msec.

The dominant T_1 decay mechanism is the emission of a phonon into the bulk liquid with the excitation of harmonic energy levels. The coupling is through phonon-induced modulation of the image potential of an electron and leads to a decay time ~ 30 μsec.

T_2: The phase of the wave-function varies a $[U(t) + e\phi(t)]t/\hbar$, where U and ϕ are the energy of a state and the electrostatic potential, respectively. Dephasing occurs due to a decay of the phase difference between the two qubit states $|1\rangle$ and $|0\rangle$. The dominant dephasing mechanism is estimated to be Johnson noise in the micro-electrodes. For a 25 Ω resistor at $T=1$ K attached to the posts, the dephasing time is estimated to be $T_2 \sim 100\,\mu$sec. A two-ripplon scattering process modulates the energy of the states and leads to $T_2 \sim 10$ msec.

The author wishes to acknowledge Mark Dykman and John Goodkind for helpful conversations. This work was supported in part by NSF Grant EIS-0085922.

*E-mail: ajd3@cwru.edu

[1] A review of concepts for quantum computers is given in Fortschr. Phys. **48**, 9–11 (2000).
[2] P. M. Platzman and M. I. Dykman, Science **284**, 1967 (1999).
[3] G. F. Saville and J. M. Goodkind, Phys. Rev. A **50**, 2059 (1994).
[4] M. I. Dykman, P. M. Platzman, and P. Seddighrad (to be published).

This article was published in English in the original Russian journal. Reproduced here with stylistic changes by AIP.

Manipulation of a ^{4}He solid–liquid interface by acoustic radiation pressure

R. Nomura,* Y. Suzuki, S. Kimura, Y. Okuda, and S. Burmistov**

Department of Condensed Matter Physics, Tokyo Institute of Technology, 2-12-1, O-okayama, Meguro-ku, Tokyo 152-8551, Japan

(Submitted December 19, 2002)
Fiz. Nizk. Temp. **29**, 663–666 (June 2003)

Acoustic radiation pressure is thought to be very useful for solid ^{4}He experiments under microgravity. We observed the manipulation of a ^{4}He solid–liquid interface by an acoustic wave. We applied a sound pulse in a direction perpendicular to the flat interface between two transducers. At low temperatures the interface moved in the sound direction. We also checked how the interface moved when sound was applied parallel to the interface. The interface dynamics during and after the sound pulse were recorded with a high speed CCD camera. © *2003 American Institute of Physics.* [DOI: 10.1063/1.1542535]

1. INTRODUCTION

In a microgravity environment it is very important to control an object without making direct contact with it. Acoustic radiation pressure is a useful tool for this purpose. It has been used to investigate the dynamics of liquid drops[1,2] and for passive stabilization of liquid capillary bridges[3] under low-gravity conditions.

For crystal growth under microgravity it is difficult to hold and control a crystal in the proper position. Once a crystal detaches from the wall and starts to move freely it is very difficult to stop the crystal, especially in a superfluid with no viscosity. It would be very helpful to be able to control the motion of a ^{4}He crystal easily. This technique will also be used to study new types of dynamics, such as the shape evolution of a rotating quantum crystal under microgravity, collision or friction beween two quantum crystals, and so on. Acoustic radiation pressure is thought to be a good way to manipulate a crystal.

We have found that a sound wave can be used to manipulate a ^{4}He solid–liquid interface, which is known to have ultrahigh mobility.[4,5] When a sound pulse was applied from the liquid side to a flat interface the solid melted at all temperatures below 1.2 K. But when the sound pulse was applied from the solid side the solid melted above 750 mK and grew below this temperature.[6,7] These interface motions were driven by acoustic radiation pressure. In quantum mechanical representations radiation pressure is interpreted as momentum transfer from phonons to the interface.[8] We used a high-speed CCD camera to record the interface dynamics during and after a sound pulse.

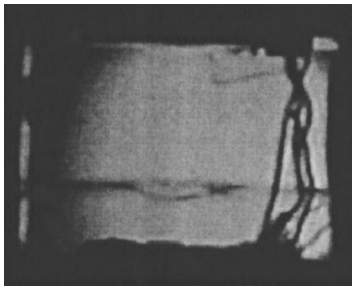

FIG. 1. Melting of a ^{4}He crystal induced by a sound wave from the liquid side.

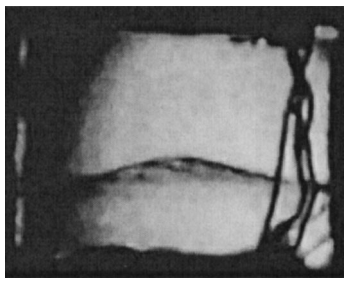

FIG. 2. ^{4}He crystallization induced by a sound wave from the solid side.

2. EXPERIMENTAL RESULTS AND DISCUSSION

The experiments were performed in a cell cooled with a dilution refrigerator. The cell had optical access from room temperature and we could observe the ^{4}He crystal down to 50 mK. Two longitudinal transducers facing one another were prepared in a cell. Their resonance frequency was about

FIG. 3. Melting of a ^{4}He crystal induced by a sound wave left to right.

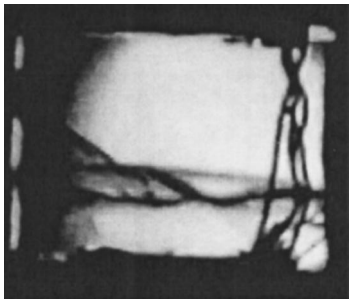

FIG. 4. ^{4}He crystallization induced by a sound wave from left to right.

10 MHz and the separation distance was 10 mm. The sound directions were vertical. A large ^{4}He crystal was grown in the cell and occupied the lower half-space. The solid–liquid interface was adjusted to be midway between the two transducers. Because of gravity it was horizontally flat when no sound was present. A sound pulse was applied to the interface from the liquid side or downward by the upper transducer and from the solid side or upward by the lower transducer. In addition we set up two other transducers. Their sound direction was horizontal or parallel to the interface. One was for longitudinal sound and the other for transverse sound.

Figure 1 shows the shape of a solid–liquid interface when a sound wave was applied from the liquid side. Melting was induced near the center of the cell, where the sound wave was actually applied. The temperature was about 150 mK and the typical sound power density was about 200 W/m^2. When sound was applied from the solid side at the same temperature, the crystal grew as shown in Fig. 2. Therefore at these low temperatures the interface was pushed in the direction of the sound. We could easily induce crystallization and melting by changing the direction of the acoustic wave.

We also applied sound horizontally and checked the response of the interface. The sound direction was parallel to the interface in this case. Longitudinal sound was applied from left to right near 150 mK and it stochastically induced melting (Fig. 3) or crystallization (Fig. 4) near the transducer. These observations support the idea that acoustic radiation pressure caused the interface motion. The interface motion was driven not because the solid or liquid was thermodynamically favored but because the interface felt the force directly exerted by the sound wave. The initial tiny slope of the interface probably determined whether crystallization or melting was induced. When transverse sound was applied from right to left it always induced crystallization (Fig. 5) because it can propagate only through the solid.

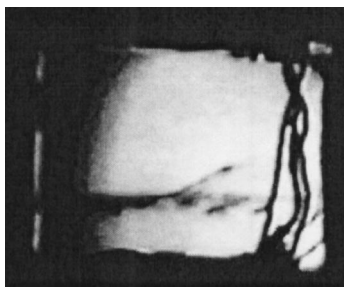

FIG. 5. ^{4}He crystallization induced by a transverse sound wave from right to left.

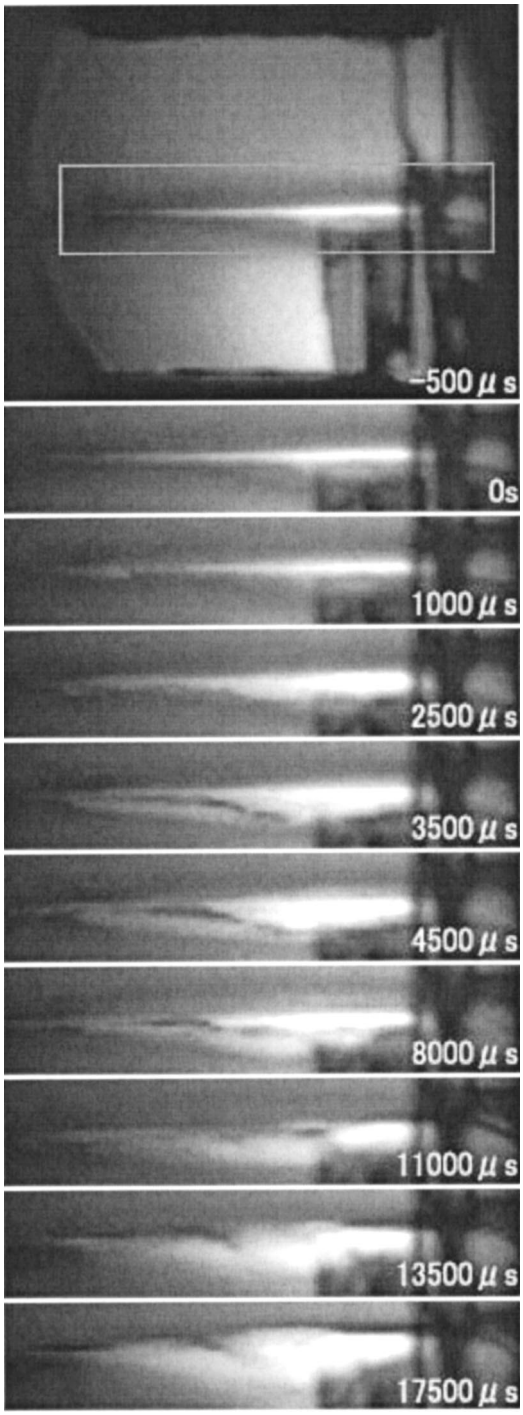

FIG. 6. High-speed solid–liquid interface dynamics triggered by a sound pulse from the liquid side. The white rectangle in the first panel is the region shown in the subsequent panels. The numbers indicate the time in μs elapsed after the sound pulse.

Using a high-speed CCD camera, the interface dynamics was recorded during and after a sound pulse. A 1 msec sound pulse was applied at $t=0$ from the liquid side. First it induced downward motion of the interface. Then the interface oscillated around the equilibrium position as shown in Fig. 6. The white rectangle in the first panel is the region shown in

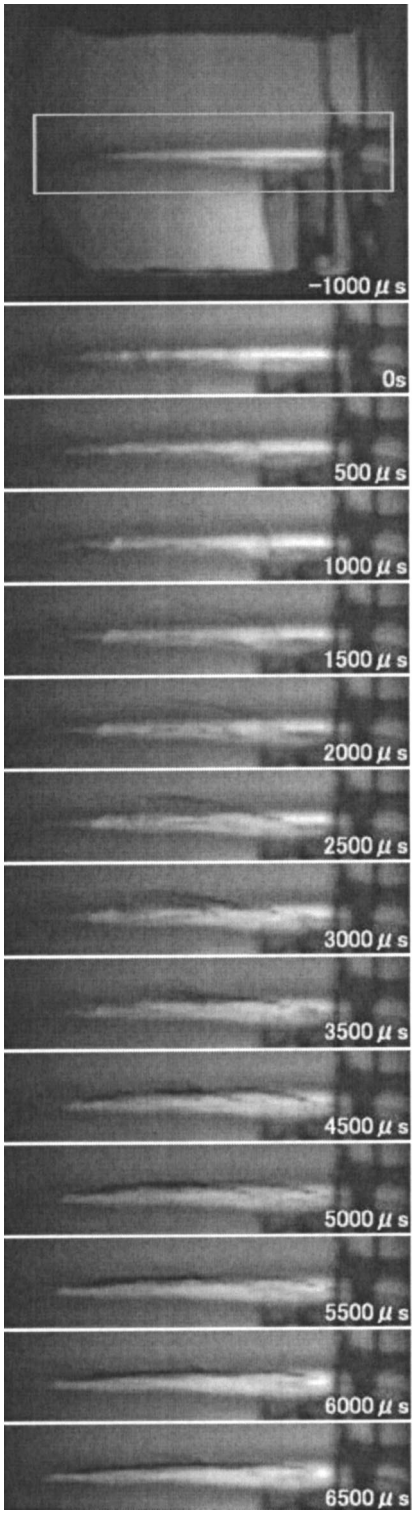

FIG. 7. High-speed solid–liquid interface dynamics triggered by a sound pulse from the solid side. The white rectangle in the first panel is the region shown in the subsequent panels. The numbers indicate the time in μs elapsed after the sound pulse.

the subsequent panels. The temperature was 380 mK in this case. When the sound pulse was applied from the solid side it induced upward motion of the interface first, as shown in Fig. 7. These observations demonstrated that an acoustic wave can excite interface oscillation or crystallization.

What will happen when we make a small ^{4}He crystal and apply a sound wave to it? Will the crystal melt or move in the sound direction? It will be very interesting to see if we can move not only the solid–liquid interface but also the crystal itself. If this is possible, radiation pressue can be used to manipulate ^{4}He crystals in a microgravity environment.

3. SUMMARY

We have demonstrated that a sound wave can be used to manipulate a ^{4}He solid–liquid interface. The interface motion triggered by acoustic radiation pressure was recorded with a high-speed CCD camera. In the future we shall check whether we can manipulate not only the interface but also the crystal itself by means of acoustic pressure.

This work is partly funded by the ''Ground-Based Research Announcement for Space Utilization'' promoted by the Japan Space Forum.

*E-mail: nomura@ap.titech.ac.jp
**Permanent address: Department of Superconductivity and Solid State Physics, Kurchatov Institute, Moscow 123182, Russia

T. G. Wang, E. h. Trinh, A. P. Croonquist, and D. D. Elleman, Phys. Rev. Lett. **56**, 452 (1986).
[2] R. E. Apfel *et al.*, Phys. Rev. Lett. **78**, 1912 (1997).
[3] M. J. Marr-Lyon, D. B. Thiessen, and P. L. Marston, Phys. Rev. Lett. **86**, 2293 (2001).
[4] A. F. Andreev and A. Y. Parshin, Zh. Éksp. Teor. Fiz. **75**, 1511 (1978) [Sov. Phys. JETP **48**, 763 (1978)].
[5] S. Balibar and P. Nozières, Solid State Commun. **92**, 19 (1994).
[6] R. Nomura, M. Maekawa, Y. Suzuki, Y. Okumura, and Y. Okuda, J. Low Temp. Phys. **126**, 39 (2002).
[7] R. Nomura, Y. Suzuki, S. Kimura, and Y. Okuda, Phys. Rev. Lett. **90**, 075301 (2003).
[8] M. Sato and T. Fujii, Phys. Rev. E **64**, 026311 (2001).

This article was published in English in the original Russian journal. Reproduced here with stylistic changes by AIP.

Nonlinear second-sound waves in ^{4}He–^{3}He superfluid mixtures

G. V. Kolmakov*

Institute of Solid State Physics of the Russian Academy of Sciences, 142432 Chernogolovka, Moscow Region, Russia

(Submitted December 19, 2002)
Fiz. Nizk. Temp. **29**, 667–671 (June 2003)

The Hamiltonian formalism in two-fluid hydrodynamics is generalized to the case of ^{4}He–^{3}He superfluid mixtures. The resulting formalism is used to calculate the amplitude of the three-wave interaction for second sound and the nonlinearity coefficient of second sound in He II with a ^{3}He impurity. It is shown that the temperature at which the nonlinearity coefficient of the second sound changes sign from negative to positive is lowered from 1.88 to 1.7 K when a 10% ^{3}He impurity is added to the superfluid ^{4}He. Thus for weak ^{4}He–^{3}He solutions there exists a rather wide interval of temperatures below the superfluid transition temperature T_λ in which the nonlinearity coefficient of the second sound is negative, and the shock front is formed at the trailing edge of the nonlinear second-sound heating wave. © *2003 American Institute of Physics.*
[DOI: 10.1063/1.1542536]

1. INTRODUCTION

We investigate the nonlinear properties of second-sound waves in superfluid ^{4}He containing ^{3}He impurities. It is known[1] that second sound in He II is characterized by considerably stronger nonlinear properties than ordinary (first) sound. For example, a traveling pulse of rotonic second sound of duration $\tau\sim 10$ μs and amplitude $\delta T\sim 10^{-2}$ K is transformed into a shock wave over a distance of the order of 1 cm from the source.[2]

In pure He II the nonlinearity coefficient α, which determines the dependence of the second-sound velocity on the wave amplitude δT, $u_2=u_{20}(1+\alpha\delta T)$ (where u_{20} is the second-sound velocity in the case of small amplitude), is given by the expression[1]

$$\alpha=\frac{\partial}{\partial T}\ln\left(u_{20}^3\frac{\partial\sigma}{\partial T}\right), \tag{1}$$

where σ is the entropy of a unit mass of liquid. The coefficient α appears in the Burgers equation describing the evolution of a weakly nonlinear one-dimensional traveling wave.[3]

The nonlinearity coefficient of rotonic second sound is strongly temperature dependent. In pure He II at the saturated vapor pressure the coefficient α is negative for $1.88\ \text{K}<T<T_\lambda$ and positive for $T<1.88$ K. The coefficient α changes sign at $T=T_\alpha=1.88$ K. Because of this, at temperatures above T_α a shock front (temperature discontinuity) can form on the trailing edge of the second-sound heating wave; this is a property specific to second sound.[1]

In this paper we study the influence of ^{3}He impurities on the nonlinear properties of second sound in superfluid He II. Research on nonlinear second-sound waves in superfluid mixtures is of independent interest and is also important in connection with the study of the interaction between first- and second-sound waves,[4–6] the properties of acoustic turbulence in superfluid helium,[7–9] and also studies of the nonlinear phenomena in superfluid mixtures near the tricritical point.[10]

Expression (1) for the nonlinearity coefficient α of second sound in pure He II does not apply in the case of superfluid mixtures, since the hydrodynamic equations themselves have a different form for them.[1] To calculate the nonlinearity coefficient of second sound in a mixture it is convenient to write the hydrodynamic equations in Hamiltonian variables. In this paper the Hamiltonian formalism set forth for pure He II in Refs. 5 and 11 is generalized to the case of superfluid mixtures. The Hamiltonian approach is convenient for investigating the properties of nonlinear waves because it allows one to calculate in a unified manner not only the nonlinearity coefficients of first and second sound but also their interconversion coefficients. In addition, all of these quantities can be calculated directly in the form in which they appear in the wave kinetic equations used in the study of acoustic turbulence.[7]

The nonlinear hydrodynamic equations of superfluid mixtures were analyzed previously in Ref. 12 without the use of the canonical formalism.

2. HAMILTONIAN FORMALISM IN THE HYDRODYNAMICHS OF SUPERFLUID MIXTURES

It is known[11] that the equations of two-fluid hydrodynamics of pure He II admit formulation in the language of canonical variables. In such a description the role of the Hamiltonian is played by the total energy of the liquid in a stationary reference frame, and the pairs of mutually conjugate canonical variables are (φ,ρ), (β,S), and (γ,f). Here ρ is the density of the liquid, S is the entropy of a unit volume of liquid, φ is the superfluid velocity potential, β is the phase variable conjugate to the entropy S, and γ and f are the Clebsch variables[13] describing the vortical motion of the normal component. The change to normal coordinates—the amplitudes of the traveling waves of first and second sound—is described by the corresponding canonical transformations. The amplitude of the nonlinear interaction of the second-sound waves, which is proportional to the nonlinearity coef-

ficient α, is calculated as a coefficient in the expansion of the Hamiltonian in powers of the normal coordinates.

An "expanded" formalism suitable for describing the hydrodynamics of superfluid mixtures includes additional variables: the impurity concentration ε and the phase variable λ conjugate to it. As compared to the conventional formulation,[11] this description has the feature that the presence of an impurity (and, hence, the appearance of an additional pair of variables in the hydrodynamic equations) does not give rise to a new acoustic mode, since the impurity atoms take part in only the normal motion of the liquid.[1] Consequently, the potential λ should be defined so that the velocity of the impurities coincides with the velocity $\mathbf{v}_n$ of the normal component. This condition gives an additional constraint on the hydrodynamic equations formulated in canonical variables. Thus λ is not an independent variable and, in principle, can be eliminated from the final equations of motion. However, in our calculations it will be more convenient to use the expanded set of variables including the potential λ in explicit form. An analogous situation arises, for example, when the nonisentropic motion of a normal fluid is described in the language of canonical variables.[11] We note that the Hamiltonian formalism for superfluid mixtures can be obtained by starting from the Lagrangian formulation of the hydrodynamic equations of mixtures, in analogy to how this is done in Refs. 11 and 14 for the two-fluid hydrodynamics of pure He II.

Let us turn to the formulation of a canonical formalism in the hydrodynamics of mixtures. The Hamiltonian can be chosen in the form the total energy of the liquid expressed in terms of canonical variables:

$$H=\int d^3\mathbf{r}\left(\frac{1}{2}\rho\mathbf{v}_s^2+\mathbf{p}\cdot\mathbf{v}_s+E_0(\rho,S,\varepsilon,\mathbf{p})\right). \tag{2}$$

Here $E_0(\rho,w,\varepsilon,\mathbf{p})$ is the energy per unit volume of liquid in the reference frame moving at the velocity $\mathbf{v}_s$ of the superfluid component, $\varepsilon=\rho c$ is the impurity density, and c is the concentration of the impurity by mass. We retain the usual definition of the superfluid velocity:

$$\mathbf{v}_s=\nabla\varphi \tag{3}$$

and the momentum of the relative motion is expressed in terms of the canonical variables as

$$\mathbf{p}=S\nabla\beta+f\nabla\gamma+\varepsilon\nabla\lambda. \tag{4}$$

The energy E_0 obeys the familiar thermodynamic relation

$$dE_0=TdS+\mu d\rho+Zdc+(\mathbf{v}_n-\mathbf{v}_s)d\mathbf{p},$$

where μ is the chemical potential of the mixture, and Z is the thermodynamic variable conjugate to the impurity concentration. The momentum of a unit mass of liquid in the stationary reference frame is

$$\mathbf{j}=\rho\nabla\varphi+\mathbf{p}.$$

The canonical equations for the pairs of mutually conjugate variables have the standard form (a dot denotes a time derivative)

$$\dot\rho=\frac{\delta H}{\delta\varphi},\quad \varphi=-\frac{\delta H}{\delta\rho};\quad \dot S=\frac{\delta H}{\delta\beta},\quad \dot\beta=-\frac{\delta H}{\delta S};$$

$$\dot f=\frac{\delta H}{\delta\gamma},\quad \dot\gamma=-\frac{\delta H}{\delta f};\quad \dot\varepsilon=\frac{\delta H}{\delta\lambda},\quad \lambda=-\frac{\delta H}{\delta\varepsilon}. \tag{5}$$

Equations (5) with the Hamiltonian (2) give the equations of motion of the liquid in terms of the canonical variables:

$$\dot\rho=-\operatorname{div}\mathbf{j}, \tag{6}$$

$$\dot\varphi=-\mu-\frac{1}{2}\mathbf{v}_s^2+\frac{Z}{\rho}c, \tag{7}$$

$$\dot S=-\operatorname{div}(S\mathbf{v}_n), \tag{8}$$

$$\dot\beta=-T-\mathbf{v}_n\nabla\beta, \tag{9}$$

$$\dot f=-\operatorname{div}(f\mathbf{v}_n), \tag{10}$$

$$\dot\gamma=-\mathbf{v}_n\nabla\gamma, \tag{11}$$

$$\dot\varepsilon=-\operatorname{div}(\varepsilon\mathbf{v}_n), \tag{12}$$

$$\dot\lambda=-\mathbf{v}_n\nabla\lambda-\frac{Z}{\rho}. \tag{13}$$

Equations (6), (8), and (12) are the continuity equations for the density of the liquid, the entropy, and the impurity concentration. When definition (3) is taken into account, Eq. (7) is the same as the equation of superfluid motion for mixtures from Ref. 1. The well-known equations of the normal component follow from definition (4) and Eqs. (7)–(13).

Thus the system of canonical equations (5) with the Hamiltonian (2) is equivalent to the complete system of hydrodynamic equations for a superfluid mixture.

3. NORMAL COORDINATES

For describing the evolution of the shape of a wave it is convenient to change to new variables: the normal coordinates of the linearized system of equations (6)–(13), i.e., variables in terms of which the traveling waves do not interact in the linear approximation.[5,15] In the problem under consideration the role of the normal coordinates is played by the wave amplitudes of the first and second sound.

Below we shall have need of the explicit form of the transformations to the new coordinates. As the exact expression for the transformation is extremely awkward, we shall write out an approximation to it neglecting terms of order u_2^2/u_1^2 (where u_1 is the first-sound velocity) and also quantities proportional to the coefficient of thermal expansion $\kappa=\rho^{-1}(\partial\rho/\partial T)$, which are assumed small. Furthermore, in this paper we restrict the calculation to the nonlinearity coefficient of second sound. We therefore neglect terms containing a factor of the wave amplitude of the first sound.

Thus the expressions given below for the transformation to the normal coordinates are correct at temperatures not too close to the superfluid transition temperature T_λ. Near T_λ the coefficient of thermal expansion κ of the liquid increases (in absolute value) without bound, so that the approximate formula (14) becomes inapplicable. In calculating the nonlinearity coefficient α of the second sound near T_λ one should make the change to normal coordinates using formulas in which the coefficient κ is taken into account exactly.

We also assume that the waves are propagating in a nonmoving liquid. Then the Clebsch variables f and γ can be set equal to zero.

For the Fourier components of the deviations of the canonical variables from the equilibrium values in the approximation adopted, the transformation under discussion has the following form:

$$\delta\rho_{\mathbf{k}}=c\left(\frac{\partial\rho}{\partial c}\right)B(\omega)(b_{\mathbf{k}}+b^*_{-\mathbf{k}}),$$

$$\delta S_{\mathbf{k}}=S\left(1+\frac{c}{\rho}\frac{\partial\rho}{\partial c}\right)B(\omega)(b_{\mathbf{k}}+b^*_{-\mathbf{k}}),$$

$$\delta\varepsilon_{\mathbf{k}}=\varepsilon\left(1+\frac{c}{\rho}\frac{\partial\rho}{\partial c}\right)B(\omega)(b_{\mathbf{k}}+b^*_{-\mathbf{k}}),$$

$$ik\varphi_{\mathbf{k}}=u_{20}\left(-\frac{\rho_n}{\rho_s}+\frac{c}{\rho}\frac{\partial\rho}{\partial c}\right)B(\omega)(b_{\mathbf{k}}-b^*_{-\mathbf{k}}),$$

$$ik\beta_{\mathbf{k}}=\frac{\overline{\sigma}}{u_{20}(\partial\sigma/\partial T)}B(\omega)(b_{\mathbf{k}}-b^*_{-\mathbf{k}}),$$

$$ik\lambda_{\mathbf{k}}=\frac{1}{u_{20}c}\left[-u_{20}^2\left(\frac{c}{\rho}\frac{\partial\rho}{\partial c}\right)^2-\overline{\sigma}c\frac{(\partial\sigma/\partial c)}{(\partial\sigma/\partial T)}+c^2\frac{\partial}{\partial c}\frac{Z}{\rho}\right]\times B(\omega)(b_{\mathbf{k}}-b^*_{-\mathbf{k}}). \tag{14}$$

Here $\overline{\sigma}=\sigma-c(\partial\sigma/\partial c)$, $b_{\mathbf{k}}$ is the normalized amplitude of a second-sound wave with wave vector $\mathbf{k}$, and $\omega=u_{20}k$ is the frequency of the second-sound wave. The velocity of second sound in the mixture is given by the well-known relation[1]

$$u_{20}^2=\frac{\left(\frac{\overline{\sigma}^2}{\partial\sigma/\partial T}+c^2\frac{\partial}{\partial c}\frac{Z}{\rho}\right)}{\left(\frac{\rho_n}{\rho_s}+\left(\frac{c}{\rho}\frac{\partial\rho}{\partial c}\right)^2\right)}.$$

The normalizing factor

$$B(\omega)=\left(\frac{2\rho u_{20}^2}{\omega}\left[\frac{\rho_n}{\rho_s}+\left(\frac{c}{\rho}\frac{\partial\rho}{\partial c}\right)^2\right]\right)^{-1/2} \tag{15}$$

was chosen such that the canonical equations written in the normal coordinates $b_{\mathbf{k}}$ take the form

$$\dot{b}_{\mathbf{k}}=-i\frac{\partial H}{\partial b^*_{\mathbf{k}}}. \tag{16}$$

The normalizing volume is chosen equal to unity. The Hamiltonian written in the approximation quadratic in the amplitudes $b_{\mathbf{k}}$ takes the standard diagonal form

$$H^{(2)}=\sum_{\mathbf{k}}\omega_{\mathbf{k}}|b_{\mathbf{k}}|^2. \tag{17}$$

4. INTERACTION OF SECOND-SOUND WAVES

In calculating the nonlinear interaction coefficient of second-sound waves we shall follow the general method of canonical variables.[5,15] The Hamiltonian (2) is expanded in a power series in the normal coordinates $b_{\mathbf{k}}$, i.e., $H=H^{(2)}+H^{(3)}+\ldots$. The zeroth- and first-order terms can be eliminated. The quadratic part $H^{(2)}$ is given by Eq. (17) and corresponds to the propagation of linear second-sound waves in the bulk of the liquid. The term proportional to the third power of the amplitudes $b_{\mathbf{k}}$ describes the nonlinear interaction of second-sound waves—the decay of a wave with wave vector $\mathbf{k}$ into two waves with wave vectors $\mathbf{k}_1$ and $\mathbf{k}_2$, and the inverse process of confluence of two waves into one:

$$H^{(3)}=\sum_{\mathbf{k},\mathbf{k}_1,\mathbf{k}_2}V_{\mathbf{k},\mathbf{k}_1,\mathbf{k}_2}b^*_{\mathbf{k}}b_{\mathbf{k}_1}b_{\mathbf{k}_2}\delta_{\mathbf{k}-\mathbf{k}_1-\mathbf{k}_2}+\text{c.c.}, \tag{18}$$

where c.c. stands for the complex conjugate of the first term on the right-hand side of the equation.

An invariant quantity in the theory is the three-wave interaction amplitude $V_{\mathbf{k},\mathbf{k}_1,\mathbf{k}_2}$ taken on the resonance surface

$$\mathbf{k}-\mathbf{k}_1-\mathbf{k}_2=0,\quad \omega-\omega_1-\omega_2=0. \tag{19}$$

This is what is calculated below.

According to Eq. (18), the interaction amplitude of the second-sound waves, $V_{\mathbf{k},\mathbf{k}_1,\mathbf{k}_2}$, multiplies a product of three normal coordinates $b_{\mathbf{k}}$ in the cubic part $H^{(3)}$ of the Hamiltonian. In the general case of arbitrary impurity concentration the calculation leads to an extremely awkward expression for the interaction amplitude. For a weak solution ($c\ll 1$) the expression accurate to quantities of first order in the impurity concentration c is

$$V_{\mathbf{k},\mathbf{k}_1,\mathbf{k}_2}=\left\{-\frac{\sigma^3}{2}\frac{(\partial^2\sigma/\partial T^2)}{(\partial\sigma/\partial T)^3}-\frac{3\sigma^2c}{2(\partial\sigma/\partial T)}\times\left(\frac{1}{\rho}\frac{\partial\rho}{\partial c}+\frac{\partial}{\partial T}\left(\frac{\partial\sigma/\partial c}{\partial\sigma/\partial T}\right)\right)+\frac{c^3}{2}\frac{\partial^2}{\partial c^2}\frac{Z}{\rho}+\frac{\rho_n}{\rho_s}\times\left(\frac{\overline{\sigma}^2}{\partial\sigma/\partial T}+c^2\frac{\partial}{\partial c}\frac{Z}{\rho}\right)\left[\frac{\rho_s}{\rho_n}+\left(1+\frac{\rho}{\rho_n}\right)\frac{c}{\rho}\frac{\partial\rho}{\partial c}+\frac{\rho\overline{\sigma}}{2(\partial\sigma/\partial T)}\frac{\partial}{\partial T}\left(\frac{1}{\rho_n}\right)+\frac{\rho u_{20}^2c}{2}\left(\frac{\partial\rho}{\partial c}\right)\frac{\partial}{\partial\rho}\left(\frac{1}{\rho_n}\right)+\frac{\rho c}{2}\frac{\partial}{\partial c}\left(\frac{1}{\rho_n}\right)\right]\right\}\frac{(kk_1k_2)^{1/2}}{(2u_{20})^{3/2}\rho^{1/2}}. \tag{20}$$

In expression (20) we have changed to new independent thermodynamic variables: the pressure p, temperature T, and mass concentration c.

The desired nonlinearity coefficient α for second sound is proportional to the three-wave interaction amplitude $V_{\mathbf{k},\mathbf{k}_1,\mathbf{k}_2}$. It can be shown that these two quantities are connected by the relation

$$V_{\mathbf{k},\mathbf{k}_1,\mathbf{k}_2}=\frac{\alpha}{3\sqrt{2}}\frac{\overline{\sigma}u_{20}^{1/2}(k,k_1,k_2)^{1/2}}{(\partial\sigma/\partial T)\sqrt{\rho[\rho_n/\rho_s+(\partial\ln\rho/\partial\ln c)^2]}}. \tag{21}$$

A calculation of the temperature dependence of the coefficient α according to formulas (20) and (21) for a solution with a molar concentration of ^{3}He of $x=10\%$ at the saturated vapor pressure shows that the temperature T_α at which the nonlinearity coefficient changes sign from negative to positive is lowered to 1.7 K. Thus an admixture of 10% ^{3}He in He II is analogous, from the standpoint of altering the nonlinear properties of second sound, to increasing the pressure in the liquid to $P\sim 10$ atm.[16] The data of Ref. 17 were used in the calculations. For concentrated solutions additional

study is needed to determine the dependence of the nonlinearity coefficient for second sound on the temperature, concentration, and pressure in the liquid.

This approach allows one to calculate not only the nonlinearity coefficients of the first and second sound but also the interaction coefficients of waves of first and second sound in mixtures, this interaction corresponding to the decay of a wave of first sound into two waves of second sound and the Čerenkov radiation of second sound by the wave of first sound. These quantities are proportional to the coefficients multiplying the cross products of the canonical amplitudes of the first and second sound in the Hamiltonian $H^{(3)}$.

5. CONCLUSION

The hydrodynamic equations of ^{4}He–^{3}He superfluid mixtures admit a Hamiltonian formulation that represents a generalization of the known canonical formalism[11] for pure He II. The use of a Hamiltonian approach for analysis of the nonlinear properties of second sound in superfluid ^{4}He with a ^{3}He impurity has made it possible to calculate the interaction amplitude of second-sound waves, which is proportional to the nonlinearity coefficient of the second sound. For weak solutions there is a rather wide temperature interval below T_λ in which the nonlinearity coefficient of the second sound in a superfluid mixture is negative, and the temperature discontinuity is formed at the trailing edge of the shock wave of second-sound heating.

The author is grateful to L. P. Mezhov-Deglin, V. B. Efimov, and A. A. Levchenko for many helpful discussions and to S. K. Nemirovskiĭ and V. L. Pokrovskii for the interest they have shown in this work. This study was supported by the Ministry of Industry and Science of the Russian Federation as part of the program ''Research on the propagation of nonlinear waves of second sound in superfluid ^{4}He–^{3}He mixtures,'' Government contract No. 40.012.1.1.11.64, and by the Science Support Foundation (Russia).

*E-mail: german@issp.ac.ru

[1] I. M. Khalatnikov, *Theory of Superconductivity* [in Russian], Nauka, Moscow (1971).
[2] V. B. Efimov, G. V. Kolmakov, A. S. Kuliev, and L. P. Mezhov-Deglin, Fiz. Nizk. Temp. **24**, 116 (1998) [Low Temp. Phys. **24**, 81 (1998)].
[3] L. D. Landau and E. M. Lifshitz, *Fluid Mechanics*, 2nd ed., Pergamon Press, Oxford (1987), Nauka, Moscow (1986).
[4] N. I. Pushkina and R. V. Khokhlov, JETP Lett. **19**, 348 (1974).
[5] V. L. Pokrovskiĭ and I. M. Khalatnikov, Zh. Éksp. Teor. Fiz. **71**, 1974 (1976) [Sov. Phys. JETP **44**, 1036 (1976)].
[6] D. Rinberg and V. Steinberg, Phys. Rev. B **64**, 054506 (2001).
[7] S. K. Nemirovskiĭ, Usp. Fiz. Nauk **160**, 51 (1990) [Sov. Phys. Usp. **33**, 429 (1990)].
[8] V. L. Pokrovskiĭ, JETP Lett. **53**, 599 (1991).
[9] G. V. Kolmakov, Physica D **86**, 470 (1995).
[10] V. Dotsenko, A. Tiwari, M. Mohazzab, N. Mulders, A. Nash, M. Larson, and B. Vollmayr-Lee, in *Book of Abstracts, XXIII International Conference on Low Temperature Physics LT-23*, Japan (2002), Report 21AP35.
[11] V. L. Pokrovskiĭ and I. M. Khalatnikov, JETP Lett. **23**, 653 (1976).
[12] M. Mohazzab and N. Muldels, Phys. Rev. B **61**, 609 (2000).
[13] H. Lamb, *Hydrodynamics*, 6th ed., Cambridge University Press, Cambridge (1932), ONTI, Kharkov (1947).
[14] I. M., Khalatnikov, Zh. Éksp. Teor. Fiz. **23**, 169 (1952).
[15] V. E. Zakharov, Izv. Vyssh. Uchebn. Zaved. Radiofiz. XVII, 432 (1974).
[16] V. B. Efimov, G. V. Kolmakov, E. V. Lebedeva, L. P. Mezhov-Deglin, and A. B. Trusov, J. Low Temp. Phys. **119**, 309 (2000).
[17] B. N. Esel'son V. N. Grigor'ev, V. G. Ivantsov, É. Ya. Rudavskiĭ, D. G. Sanikidze, and I. A. Serbin, *Mixtures of Quantum Liquids* ^{3}He–^{4}He [in Russian], Nauka, Moscow (1973).

Translated by Steve Torstveit

Proximity effect at a He II–He I interface under microgravity

L. Kiknadze and Yu. Mamaladze*

E. A. Andronikashvili Institute of Physics of the Georgian Academy of Sciences, 6, Tamarashvili Str., Tbilisi, 380077, Georgia

(Submitted December 19, 2002)
Fiz. Nizk. Temp. **29**, 672–673 (June 2003)

The proximity effect is responsible for the existence of a transition region with graded variation of the superfluid component density instead of a sharp boundary at the level where the hydrostatic pressure induces a He II–He I phase transition. Under microgravity the characteristic length of this effect increases and the conditions become more conducive for performing measurements in the transition region. The problem of expanding the thermodynamic potential in a power series near a He II–He I interface is considered. The critical size of the superfluid region is determined. © *2003 American Institute of Physics.* [DOI: 10.1063/1.1542537]

1. INTRODUCTION

According to the phase diagram of ^{4}He hydrostatic pressure is responsible for the phase transition He II→He I. But because of the proximity effect a transition zone, where the density of the superfluid component varies gradually, instead of a sharp boundary is formed between the superfluid and normal liquids at the level where the λ pressure is reached. The superfluidity penetrates into the normal region.[1–3] The characteristic length of this effect is $\xi_g = 6.5\times 10^{-3}$ cm.[1]

2. MICROGRAVITY

The width of the transition zone (its height) is estimated to be severalfold greater than ξ_g, i.e. it is of the order of 10^{-2} cm. This value is quite macroscopic but nevertheless so small that nobody has been able to study this region experimentally. The sole attempt made thus far[4] was unsuccessful.

More conducive conditions for measurements in the transition region at a He II–He I boundary can be achieved in a microgravity environment, since $\xi_g = \xi_0^{3/5}\alpha^{-2/5}$, where $\xi_0 = 2.73\times 10^{-8}$ cm·K$^{2/3}$ and $\alpha = \rho g/|dP_\lambda/dT|$. That is, to decrease g by a factor of 10^5 the width of the transition region must be increased to centimeters and to decrease g by a factor of 3×10^7 the height must be of the order of 10 cm.

3. THE WAVE-FUNCTION UNITS AND THE "$\Psi = 0$ PROBLEM"

The Ginzburg–Pitaevskii (GP) equation for ^{4}He under hydrostatic pressure can be written in the form (neglecting flow and assuming Ψ to be a positive function)

$$\frac{\hbar^2}{2m}\frac{d^2\Psi}{dz^2} + A\Psi - B\Psi^3 - C\Psi^5 = 0, \tag{1}$$

where A and B are dependent on the distance z from the boundary ($z>0$ is the superfluid region, $z<0$ is the normal region, $A = \pm A_0(\alpha|z|)^{4/3}$ (the minus sign is for the normal region) and $B = B_0(\alpha|z|)^{2/3}$. The asymptotic solution deep in the superfluid region ($z \gg \xi_g$) is

$$\Psi_a = (\alpha z)^{1/3}\Psi_0, \quad \Psi_0^2 = -\frac{B_0}{2C} + \sqrt{\left(\frac{B_0}{2C}\right)^2 + \frac{A_0}{C}}. \tag{2}$$

It is convenient to introduce the parameter $M = C\Psi_0^4/A_0 = 1 - B_0\Psi_0^2/A_0$ and to express the coefficients A_0 and B_0 as

$$A_0 = \frac{1.11\times 10^{-16}}{1+M/3}\,\text{erg}\cdot\text{K}^{-4/3},$$

$$B_0 = 3.52\times 10^{-39}\frac{1-M}{1+M/3}\,\text{erg}\cdot\text{cm}\cdot\text{K}^{-2/3}.$$

Then Eq. (1) can be put into the dimensionless form

$$\frac{d^2\Psi}{d\zeta^2} \pm |\zeta|^{4/3}\Psi - (1-M)|\zeta|^{2/3}\Psi^3 - M\Psi^5 = 0, \tag{3}$$

where $\zeta = z/\xi_{gM}$ and $\psi = \Psi/\Psi_{gM}$,

$$\xi_{gM} = \xi_g(1+M/3)^{3/10},$$

$$\Psi_{gM} = \sqrt{\xi_0/\xi_g}(1+M/3)^{1/10}\Psi_0 \text{ (Ref. 3)}.$$

The GP equation is based on a power-series expansion of the thermodynamic potential. If this expansion is constructed with respect to the ratio of the wave function to its equilibrium value, then the expansion becomes invalid at the He II–He I boundary where this ratio becomes infinite.[3] This problem does not occur for Eq. (3) and for the corresponding power-series expansion with respect to Ψ/Ψ_{gM} because Ψ_{gM} is temperature- and coordinate-independent (if we compare Ψ_{gM} with Ψ_a, the quantity αz in Eq. (2) is replaced by $(\xi_0/\xi_g)^{3/2}(1+M/3)^{3/10}$). These quantities have the dimension of temperature, but the latter is temperature- and coordinate-independent.

In these units the asymptotic solution [Eq. (2)] has the form $\psi_a = \zeta^{1/3}$.

4. CRITICAL SIZES OF THE SUPERFLUID REGION

The superfluid region must contain enough of the superfluid component for superfluid to be present in the normal

region. That is why the size H_s (the height) of the superfluid region has a critical value such that if $H_s<H_{sc}$, then the density of the superfluid component is zero in the entire vessel (more accurately for the case $M>1$, see below). It is determined by the equation

$$J_{0.3}\left(\frac{3}{5}h_{sc}^{5/3}\right)I_{-0.3}\left(\frac{3}{5}h_n^{5/3}\right)+J_{-0.3}\left(\frac{3}{5}h_{sc}^{5/3}\right)I_{0.3}\left(\frac{3}{5}h_n^{5/3}\right)=0, \tag{4}$$

the first variant of which was obtained in Ref. 1; $h_{sc}=2.29$ when $h_n=\infty$ (Refs. 2 and 5) and $h_{sc}=2.55$ when $h_n=0$ (Ref. 5) ($-H_n<z<H_s$, H_n is the size of the normal region, $h=H/\xi_{gM}$). Let us consider the case $h_s-h_{sc}\ll h_{sc}$ and $h_n=0$. Employing the method suggested in Ref. 6 we obtain an approximate solution of Eq. (3) in the form $\psi=c\sqrt{\zeta}J_{0.3}(\zeta^{5/3}j/h_s^{5/3})$, where $j=2.8541$. Analysis of the coefficient c shows that for $M>1$ the size h_{sc} is not critical and that two other critical sizes exist: $h_{\min}$, above which superfluidity becomes possible, and $h_{\rm tr}$, above which superfluidity becomes stable, $h_{\rm tr}>h_{\min}$:

$$h_{\min}=h_{sc}\left[1+\frac{(M-1)^2}{4M}\frac{I_2^2}{I_1I_3}\right]^{-3/10},$$

$$h_{\rm tr}=h_{sc}\left[1+\frac{3}{16}\frac{(M-1)^2}{M}\frac{I_2^2}{I_1I_3}\right]^{-3/10}, \tag{5}$$

where

$$I_1=\int_0^j xJ_{0.3}^2(x)dx=0.91627,$$

$$I_2=\int_0^j x^{6/5}J_{0.3}^4(x)dx=0.37001,$$

$$I_3=\int_0^j x^{7/5}J_{0.3}^3(x)dx=0.16790.$$

We thank the CWS 2002 Organizing Committee for the invitation, which stimulated this work, to attend the workshop and for funding the attendance of one of us (Yu.M.) and G. Kharadze and S. Tsakadze for their interest and attention. The work is partly funded by Grant 2.17.02 from the Georgian Academy of Sciences.

*E-mail: yum@iph.hepi.edu.ge; yum270629@yahoo.com

[1] L. V. Kiknadze, Yu. G. Mamaladze, and O. D. Cheishvili, JETP Lett. **3**, 197 (1966); in *Proceedings of the 10th International Conference on Low Temperature Physics (1966), VINITI*, Moscow (1967), p. 491; L. V. Kiknadze and Yu. G. Mamaladze, Fiz. Nizk. Temp. **17**, 300 (1991) [Sov. J. Low Temp. Phys. **17**, 156 (1991)].
[2] V. A Slusarev and M. A. Strzhemechny, Zh. Éksp. Teor. Fiz. **58**, 1757 (1970) [JETP **31**, 941 (1970)].
[3] A. A. Sobianin, Zh. Éksp. Teor. Fiz. **63**, 1780 (1972) [Sov. Phys. JETP **36**, 941 (1973)]; V. L. Ginzburg and A. A. Sobianin, Usp. Fiz. Nauk **120**, 153 (1976) [Sov. Phys. Usp. **19**, 773 (1976)].
[4] G. Ahlers, Phys. Rev. **171**, 275 (1968).
[5] L. V. Kiknadze, Thesis, Tbilisi State University (1970).
[6] Yu. G. Mamaladze, Bull. Acad. Sci. (Georgia) **109**, 45 (1983).

This article was published in English in the original Russian journal. Reproduced here with stylistic changes by AIP.

Phonons and rotons of trapped atoms in a gravitational field

D. B. Baranov and V. S. Yarunin*

Bogoliubov Laboratory of Theoretical Physics, Joint Institute for Nuclear Research, Dubna 141980, Russia
(Submitted December 19, 2002)
Fiz. Nizk. Temp. **29**, 674–677 (June 2003)

The excitations of trapped atoms with a Bose–Einstein condensate in a trap are determined by the conservation of the total numbers of phonons and rotons of the atomic motion, and these properties depend on the presence of a gravitational field. © *2003 American Institute of Physics.* [DOI: 10.1063/1.1542538]

1. INTRODUCTION

Phonon-like excitations of atoms in traps are observed experimentally. If a trap is put into rotation, a new form of the atomic motion (rotons) can be expected to appear. In ^{4}He the same maxon–roton excitations are followed by vortices. They are defined as singular points of a velocity field $\nabla \times V(r)=0$, connected with the condition that the amplitude ψ vanishes: $\psi(r)=0$.[1,2] In the present paper we shall study the properties of an atomic Bose–Einstein condensate (BEC) in a trap in the rotational (potential) stage of nonsingular excitations. We shall show that the roton properties of a gas in a trap follow from the conservation of the total number of photons and rotons in our model. The additional potential energy of the trapped atoms is due to atoms entering from the outside of the BEC via the increasing phonon and roton energies due to the gravitational field; these contributions are estimated below.

2. PHONONS AND ROTONS

The translational energy $\mathcal{H}_{\rm ph}$ and the orbital rotational energy $\mathcal{H}_{\rm rot}$ of the atoms can be separated if the origin of coordinates is taken as the point of ''equilibrium,'' such as the center of a circle (2D) or a sphere (3D). Each of the N atoms in a trap contributes to the phonon motion, due to the interaction between them, and to rotations. Therefore we shall represent the Hamiltonian of N atoms as the sum of the translational energy $\mathcal{H}_{\rm ph}$, the rotational energy $\mathcal{H}_{\rm rot}$, and the rotation–translation interaction energy $\mathcal{H}_{\text{ph-rot}}$

$$\mathcal{H}_{\rm ph}=\sum_k^{k_{\max}} \omega(k)\psi_k^+\psi_k,$$

$$\mathcal{H}_{\rm rot}=\sum_{i=1}^{N}\left(\frac{\Delta_i}{2m}+\Omega L_z^i\right)+U(r),$$

$$\mathcal{H}_{\rm ph-rot}=\frac{1}{\sqrt{N}}\sum_k^{k_{\max}}\Gamma_k\sum_i^N (L_+^i\psi_k+\psi_k^+L_-^i), \tag{1}$$

$$[\psi_k,\psi_{k'}^+]=\delta_{kk'},[L_+^i,L_-^j]=2L_z\delta_{ij},[L_-^i,L_z^j]=L_-^i\delta_{ij},$$

$$[L_+^i,L_z^j]=-L_+^i\delta_{ij}.$$

Here Ω is the rotational energy; $k_{\max}$ is the upper level of a trap with a potential U; L are orbital angular momentum operators; Γ_k is the phonon–roton interaction; $\omega(k)$ is the energy of a phonon with the momentum k of an atom in a rectangular trap, expressed by the well-known equation[3]

$$ka=\pi n-2\arcsin\frac{\hbar k}{\sqrt{2mU_0}},$$

where U_0 is the trap potential and a is the trap width. In reality, phonons and rotons transform into one another and the relation between them is given by the integral of motion M

$$[\mathcal{H},M]=0,\quad M=\sum_k^{k_{\max}}\psi_k^+\psi_k+\sum_{i=1}^N L_z^i,$$

$$[\mathcal{H},K]=0,\quad K=\sum_{i=1}^N L_i^2, \tag{2}$$

$$\mathcal{H}=\mathcal{H}_{\rm rot}+\mathcal{H}_{\rm ph}+\mathcal{H}_{\text{ph-rot}}$$

of the system (1) represented by the Hamiltonian $\mathcal{H}$. The rotational variables can be mapped onto a couple of Fermi operators for each $i=1,2,\ldots,N$ orbital angular momentum operators by means of the mapping

$$2L_z=a^+a-b^+b,\ L_+=a^+b,\ L_-=b^+a,$$

$$\{a,a\}=\{a,b\}=\{b,b\}=0,$$

$$\{a^+,a\}=\{b^+,b\}=1,\{a,b^+\}=0$$

(we drop the i superscripts and show only a very simple one-particle version $\mathcal{H}\to h$ of the model in the next few formulas). The latter definitions lead to the relations

$$[a^+a+b^+b,\ a^+a-b^+b]=0,\quad [a^+a+b^+b,\ a^+b]=0,$$

so that the initial h can be written in boson–fermion variables with $L^2\to a^+a+b^+b$ for each atom in our mapping

$$h=\omega\gamma^+\psi+\frac{\Omega_a}{2}a^+a-\frac{\omega_b}{2}b^+b+\Gamma(a^+b\psi+\psi^+b^+a),$$

$$\left[h,\psi^+\psi+\frac{1}{2}(a^+a-b^+b)\right]=[h,a^+a+b^+b]=0,$$

where the fermion energies $\Omega_{a,b}$ contain the fermion kinetic energies. These relations hold for large $k_{\max}$, so that the number m_0 of trapped levels satisfies the inequality $m_0\gg 1$,

just as in experiments. Returning to the total Hamiltonian $\mathcal{H}$, the thermodynamic parameters μ and ν now correspond to the integrals of motion K and M

$$\mathcal{H}-\mu K-\nu M=\mathcal{H}_{\text{ph-rot}}+\sum_{k}^{k_{\max}}\psi_k^+\psi_k[\omega(k)-\nu]+\sum_{i=1}^{N}[\Omega_+^a a_i^+ a_i+\Omega_-^b b_i^+ b_i],$$

$$\Omega_{\pm}^{a,b}=\Omega_{a,b}-\mu_{\pm},\quad \mu_{\pm}=\mu\pm\nu/2,$$

$$\{a_i,a_j^+\}=\{b_i^+,\,b_j\}=\delta_{ij}$$

for the partition functions of a system. The latter may be represented as a path integral for the grand Gibbs distribution

$$Q=\operatorname{Tr}\exp[-\beta(\mathcal{H}-\mu K-\nu M)]=\int\prod_k D\psi_k^* D\psi_k\prod_{i=1}^{N}Da_i^* Da_i Db_i^* Db_i\exp S,$$

$$S=\int_0^\beta L\,dt$$

over all the boson ψ,ψ^* (and fermion a,a^*, b,b^*) trajectories, satsifying periodic (and antiperiodic) boundary conditions on $[0,\beta]$ for each k (and i). The Lagrangian L respresents all the degrees of freedom of the system (1) in the usual way. The integral over all fermion (a,b) fields in Q may be calculated exactly as $\operatorname{Det}(\delta^2 S)$.[4,5] Therefore we obtain a path integral over the variables ψ_k and ψ_k^* with the effective action S_{ef} for every k

$$Q=\int\prod_k D\psi_k^* D\psi_k\exp S_{\text{ef}}(0,\beta),$$

$$S_{\text{ef}}(0,\beta)=S_{\text{ph}}+N\ln\operatorname{Det}R_k,$$

$$S_{\text{ph}}=\int_0^\beta\psi_k^*\left(-\frac{d}{dt}-\omega_k+\nu\right)\psi_k dt,$$

$$R_k=\begin{pmatrix}L_+ & \Gamma_k\psi_k/\sqrt{N}\\ \Gamma_k\psi_k^*/\sqrt{N} & L_-\end{pmatrix},$$

$$L_+=-d/dt-\Omega_+^a,\quad L_-=-d/dt-\Omega_-^b.$$

The semiclassical equations of motion

$$\frac{\delta S_{\text{ef}}}{\delta\psi_k}=\frac{\delta S_{\text{ef}}}{\delta\psi_k^*}=0 \tag{3}$$

are used for the extremal trajectories $(\psi_k^0)^*$ and ψ_k^0 that describe the effective translational modes in the roton field. In the $N\gg 1$ limit the transformation $\psi_k\to\sqrt{N}\psi_k$ and $\psi_k^*\to\sqrt{N}\psi_k^*$ leads to the renormalized action S_{eff}

$$S_{\text{ef}}\to S_{\text{eff}}=N(S_{\text{ph}}+\ln\operatorname{Det}R_k|_{|\psi|\to|\sqrt{N}|\psi|}),$$

so that the equation of motion (3) in a new scale of boson trajectories is

$$\frac{\delta S_{\text{eff}}}{\delta\psi_k^*}=\frac{\delta}{\delta\psi_k^*}(S_t+\operatorname{Tr}\ln R_k)=\left(\frac{d}{dt}+\omega_k-\nu\right)\psi_k(t)-\operatorname{Tr}\left(R_k^{-1}\frac{\delta R_k}{\delta\psi_k^*(t)}\right)=0, \tag{4}$$

where the formula $\ln\operatorname{Det}R_k=\operatorname{Tr}\ln R_k$ was used. Since K is an integral of motion for (1), the first relations for the thermodynamic parameters are

$$\frac{1}{\beta}\frac{\partial S_{\text{eff}}}{\partial\mu}=K=\frac{1}{\beta}\sum_k\operatorname{Tr}\left(R_k^{-1}\frac{\partial R_k}{\partial\mu}\right). \tag{5}$$

Similarly, the second relation is

$$\frac{1}{\beta}\frac{\partial S_{\text{eff}}}{\partial\nu}=M=\frac{1}{2\beta}\left[\sum_k\operatorname{Tr}\left(R_k^{-1}\frac{\partial R_k}{\partial\nu}\right)+\int_0^\beta|\psi_k|^2 dt\right]. \tag{6}$$

The calculation of the trace Tr in Eqs. (4)–(6) is performed as done in[4,5] both in the matrix and path integral sense

$$\operatorname{Sp}\ln R_k=\operatorname{Tr}\ln\left\{\begin{pmatrix}L_+ & 0\\ 0 & L_-\end{pmatrix}\left[1+\begin{pmatrix}L_+^{-1} & 0\\ 0 & L_-^{-1}\end{pmatrix}\times\begin{pmatrix}0 & \Gamma_k\psi_k\\ \Gamma_k\psi_k^* & 0\end{pmatrix}\right]\right\}=\operatorname{Tr}\left\{\ln\begin{pmatrix}L_+ & 0\\ 0 & L_-\end{pmatrix}-\sum_{m=1}^{\infty}\frac{1}{2m}\left[\begin{pmatrix}L_+^{-1} & 0\\ 0 & L_-^{-1}\end{pmatrix}\times\begin{pmatrix}0 & \Gamma_k\psi_k\\ \Gamma_k\psi_k^* & 0\end{pmatrix}\right]^{2m}\right\}=\frac{1}{2}\operatorname{Tr}\ln T,$$

$$T=(L_+-\Gamma_k^2\psi_k L_-^{-1}\psi_k^*)(L_--\Gamma_k^{2^-}\psi_k^* L_+^{-1}\psi_k).$$

The particular time-independent solution $(\psi_k^0)^*\to\psi_0^*$, $\psi_k^0\to\psi_0$ is similar to the "slow" trajectories in superfluid ^{4}He theory,[1] associated with the Bose–Einstein condensation (BEC) in a quantum liquid. Similarly, the ψ_0^*, ψ_0 trajectories correspond to the BEC of atoms in a trap observed experimentally in the last few years.[6] Using the BEC assumption we obtain

$$T\to T_0=L_+L_--\Gamma_0^2|\psi_0|^2$$

and the variational equation (4) becomes

$$\omega_0=\frac{\Gamma_0^2}{2\Omega_0}\left[\tanh\frac{\beta}{2}\left(\mu_+ +\frac{\Omega_0^+}{2}\right)-\tanh\frac{\beta}{2}\left(\mu_- -\frac{\Omega_0^-}{2}\right)\right],$$

$$\Omega_0^{\pm}=(\Omega_{\pm}^2+4\Gamma_0^2|\psi_0|^2)^{1/2}, \tag{7}$$

while the integrals of motion K and M are now

$$K=\frac{1}{2}\sum_k\left[\tanh\frac{\beta}{2}\left(\mu_+ +\frac{\Omega_k^+}{2}\right)+\tanh\frac{\beta}{2}\left(\mu_- -\frac{\Omega_k^-}{2}\right)\right]+2,$$

$$M=\frac{1}{2}\sum_k\left[\tanh\frac{\beta}{2}\left(\nu+\frac{\Omega_k^+}{2}\right)-\tanh\frac{\beta}{2}\left(\nu+\frac{\Omega_k^-}{2}\right)\right]+2+|\psi_k|^2.$$

These equations determine the BEC ordering in a trap via the trajectories ψ_0^*, ψ_0 and the chemical potentials μ, ν in terms of the energies $\omega(k)$, Ω, and Γ_k.

The right-hand side of Eq. (7) can be represented as

$$\omega_0=\frac{\Gamma_0^2}{2\Omega_0}\frac{\sinh(A_0^+-A_0^-)}{\cosh A_0^+\cosh A_0^-},$$

$$A_0^{\pm}=\frac{\beta}{2}\left(\mu_{\pm}\frac{\Omega_0^{\pm}}{2}\right),\quad \mu_{\pm}=\mu\pm\frac{\nu}{2}$$

and for a weak phonon–roton interaction $\Gamma_0<\Omega$ the approximation

$$\Omega_0^{\pm}\simeq\Omega_{\pm}+\frac{2\Gamma_0^2|\psi_0^2|}{\Omega_{\pm}},\quad \Omega\beta\ll 1$$

holds, so that $\sinh(A_0^+-A_0^-)\ll 1$. Therefore

$$\Gamma_0^2\ll\omega_0\Omega_0,\ \ \Omega_0=\sqrt{\Omega^2+4|\psi_0|^2\Gamma_0^2}. \tag{8}$$

This means that the BEC trajectories exist only if the phonon–roton interaction is weak. It is noteworthy that for an interaction Γ between polar atoms in ferroelectric media, represented by the same model as (1), the inequality[4]

$$\Gamma^2\gg\omega\Omega,$$

where ω and Ω are the radiation and two-level system frequencies, respectively, is the dipole cooperation condition. In the opposite case the inequality (8) follows from the previous formulas as the condition for Eqs. (4)–(6) to have a BEC solution, and the condition of a high BEC density $\omega_0|\psi_0|\gg\Gamma_0$ is also satisfied. The complete relations between the parameters of the theory are

$$\frac{\Gamma_0}{|\psi_0|}<\frac{\Omega}{|\psi_0^2|}<\omega_0,\ \Omega\beta\ll 1, \tag{9}$$

where the BEC condition (8) and the square-root decay are taken into account. The left-hand side of Eq. (9) leads to the formula (8).

3. TRAPPED ATOMS IN A GRAVITATIONAL FIELD

Now we are going to seek the properties of trapped atoms (BEC) in a gravitational field. Let us consider a pure phonon Hamiltonian $\mathcal{H}_{\rm ph}^{p}$ (no gravitational field) for a finite trap potential. In this case the ordinary commutation relations for the phonon operators does not hold and can be written in the form

$$[\Psi_k,\Psi_k^+]=f(\Psi_k,\Psi_k^+), \tag{10}$$

where $f(\Psi_k,\Psi_k^+)$ is a polynomial function of the operators Ψ_k and Ψ_k^+. Now the Hamiltonian $\mathcal{H}_g=mgz$ of the gravitational field in coordinate space can be written in terms of double-quantized operators b_k, b_k^+ as

$$\mathcal{H}_g=cb_k^+b_k,$$

where c is a constant. After diagonalization $\mathcal{H}_g$ can be represented in terms of the phonon operators Ψ_k, Ψ_k^+

$$\begin{cases} b_k=\alpha_k\Psi_k+\beta_k\Psi_k^+,\\ b_k^+=\alpha_k\Psi_k^++\beta_k\Psi_k,\end{cases}$$

$$\mathcal{H}_g=c_1+c_2\Psi_k^+\Psi_k+c_3(\Psi_k^+\Psi_k^++\Psi_k\Psi_k).$$

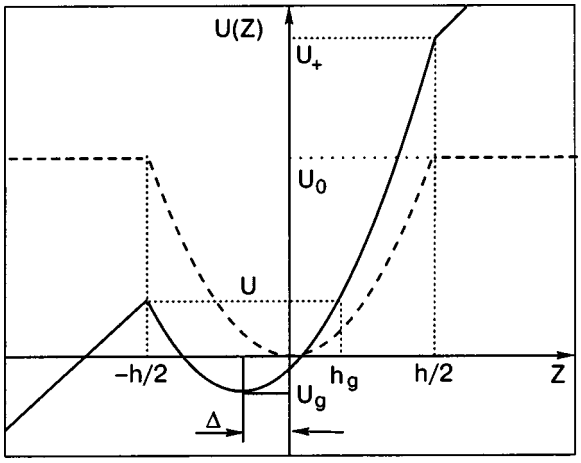

FIG. 1. The deformation of the trap potential. The dashed and solid lines are for a parabolic trap potential in free space (U_0) and in a gravitational field (U_-, U_+).

For a finite trap (10) the commutator of the total Hamiltonian $\mathcal{H}=\mathcal{H}_{\rm ph}^{p}+\mathcal{H}_{\rm rot}+\mathcal{H}_{\rm ph-rot}$ with the Hamiltonian of the gravitational field $\mathcal{H}_g$ is different from zero:

$$[\mathcal{H}_{\rm ph}^{p}+\mathcal{H}_{\rm rot}+\mathcal{H}_{\rm ph-rot},\mathcal{H}_g]\neq 0.$$

The deformation of the trap potential is shown in Fig. 1. Following Ref. 7 we conclude that the gravitational field is manifested as a decrease of the upper level $k_{\max}$ and a shift of the energy levels in the trap. In particular, the critical temperature and the number of condensate particles were compared for an ideal bose gas in a trap[7] for a gravitational field and for a microgravity environment. It was shown that the gravitational field decreases the condensate fraction and increases the critical temperature if the total number of particles in the trap is constant.

4. CONCLUSIONS

A dilute gas of interacting bosons in a magnetic trap under rotation was considered as a system with Hamiltonian $\mathcal{H}$ (1), (2) consisting of three terms: a phonon Hamiltonian $\mathcal{H}_{\rm ph}$, a Hamiltonian for the roton excitations $\mathcal{H}_{\rm rot}$, and a Hamiltonian for the phonon–roton interaction $\mathcal{H}_{\rm ph-rot}$. The partition function of the system was written as a path integral over boson and fermion trajectories with integrals of motion (2). Integrating over fermions gave the semiclassical equations of motion for the boson trajectory in the ground state and their integrals of motion. The conclusions following from Eqs. (4)–(9) are:

a) for given Γ_0 the inequality (8) can be satisfied for large $|\psi_0|$, so that rotons decrease the BEC density;

b) the fewer BEC bosons $|\psi_0^2|$, the larger the rotational angular momentum of an atom in a given trap will be.

These conclusions agree with Popov's result[1] that the zero points of a boson trajectory $\psi=0$ are the starting points for vortices in superfluid ^{4}He. As for the influence of gravity, we note that c) a gravitational field decreases the BEC density in the trap.

*E-mail: yarunin@thsun1.jinr.ru

[1] V. N. Popov, *Functional Integrals and Collective Excitations*, Cambridge University Press (1987).
[2] H. Karatsuji, Phys. Rev. Lett. **68**, 1746 (1992).
[3] L. D. Landau and E. M. Lifshitz, *Quantum Mechanics*, Nauka, Moscow (1985).
[4] V. B. Kiryanov and V. S. Yarunin, Teor. Math. Phys. **43**, 91 (1980).
[5] V. N. Popov and V. S Yarunin, *Collective Effects in Quantum Statistics of Radiation and Matter*, Kluwer Publishers (1988).
[6] F. Dalfovo, S. Giorgini, L. P Pitaevsky, and S. Stringari, Rev. Mod. Phys. **71**, 463 (1999).
[7] D. Baranov and V. Yarunin, JETP Lett. **71**, 266 (2000).

This article was published in English in the original Russian journal. Reproduced here with stylistic changes by AIP.

ESR investigation of hydrogen and deuterium atoms in impurity-helium solids

S. I. Kiselev, V. V. Khmelenko, E. P. Bernard,* and D. M. Lee

Laboratory of Atomic and Solid State Physics Cornell University, Ithaca, NY 14853-2501, USA
(Submitted December 19, 2002)
Fiz. Nizk. Temp. **29**, 678–683 (June 2003)

Impurity-helium solids (Im–He solids) are porous solids created by injecting a beam of mixed helium and impurity gases into superfluid ^{4}He. In this work we use electron spin resonance (ESR) techniques to investigate Im–He solids containing atoms and molecules of hydrogen and/or deuterium. We have performed studies of low temperature ($T \sim 1.35$ K) tunnelling chemical reactions in which deuterium atoms replace the hydrogen atoms bound in H_2 or HD molecules to produce large (up to 7.5×10^{17} cm^{-3}) and relatively stable concentrations of free hydrogen atoms. The time dependence of H and D atom concentrations has been investigated for Im–He samples with different initial ratios of hydrogen and deuterium ranging from 1:20 to 1:1. The satellite ESR lines associated with the dipolar coupling of electron spins of H and D atoms to the nuclear moments of the hydrogen nuclei found in neighboring molecules have been observed in Im–He solids. The forbidden hyperfine transition of atomic hydrogen involving the mutual spin flips of electrons and protons has also been observed.
 [DOI: 10.1063/1.1542539]

1. INTRODUCTION

Investigations of hydrogen and deuterium atoms, stabilized in solid matrices at low temperatures, have attracted the attention of scientists for many years. Possible quantum effects associated with these systems are of special interest. Quantum behavior is expected when the thermal de Broglie wavelength of the atoms becomes comparable with their interparticle spacing. For the case of H atoms in the gas phase, this condition is satisfied for a concentration of 2.6×10^{18} cm^{-3} at a temperature of 30 mK.[1] For the case of a solid phase, the temperature for the onset of any quantum effect may be lower because of the possibility of a larger effective mass. It is always desirable for investigations of quantum behavior to generate the highest possible concentrations of H or D atoms in solid matrixes. Unfortunately, from the earliest investigations of H atoms in solid H_2, it became clear that some tunnelling processes and molecular recombination could lead to a decrease in the concentration of stabilized H atoms.[2] The detailed investigations of the processes of quantum diffusion and tunnelling reactions of H atoms in solid H_2 at $T=1.35-4.2$ K were performed by Ivliev *et al.*[3] and later by Miyazaki *et al.*[4–6] They established that the decay of H atoms could take place in solid H_2 by tunnelling migration, in which H atoms tunnel through a chain of H_2 molecules according to the reaction

$$H+H_2\rightarrow H_2+H, \tag{1}$$

thereby travelling through the solid H_2 to recombine with another H atom. The reaction rate constant k_1, for reaction (1) was found to be $k_1=18\,\mathrm{cm}^3\cdot\mathrm{mol}^{-1}\cdot\mathrm{s}^{-1}$ at $T=4.2$ K.[4] This value remains the same even when the temperature is lowered to 1.9 K, confirming that tunnelling reactions are involved. The behavior of D atoms in solid D_2 is different. The rate constant for the reaction

$$D+D_2\rightarrow D_2+D \tag{2}$$

is four orders of magnitude lower; $k_2=1.8\times10^{-3}\,\mathrm{cm}^3\cdot\mathrm{mol}^{-1}\cdot\mathrm{s}^{-1}$ (Ref. 7) leading to a much lower recombination rate. Therefore it is possible to create a larger concentration of D atoms in solid D_2 as compared with concentrations of H atoms in solid H_2.[7–9] The exchange tunnelling reactions

$$D+H_2\rightarrow HD+H \tag{3}$$

$$D+HD\rightarrow D_2+H \tag{4}$$

lead to the possibility of creating high concentrations of H atoms in solid mixtures of H_2 and D_2 at low temperatures.[8,10,11] When an H atom is surrounded by shell of D_2 molecules, it becomes very stable because it can neither migrate through the solid D_2 nor react further with D_2 by the reaction

$$H+D_2\rightarrow HD+D \tag{5}$$

at low temperatures, since it is an endothermic reaction. Gordon *et al.*[8,12] suggested that high concentrations of H atoms could be stabilized at low temperatures by means of reactions (3) and (4). In their approach, a gas mixture of hydrogen, deuterium and helium gas was transported through a radio frequency discharge onto the surface of superfluid He contained in a small beaker, at a temperature 1.5 K. The jet of impurity and helium gases penetrates the surface of the superfluid He, and then forms a snow-like solid which settles to the bottom of the collection beaker. This solid became known as an Im–He solid.[13,14] In the case of heavy impurities, Im–He solids are built from a loosely connected aggregation of nanoclusters of impurities each surrounded by one or two layers of solid helium. These aggregates form extremely porous solids into which liquid helium easily and completely penetrates. This system, having the high thermal conductance and the high thermal capacitance of superfluid helium, allows preparation and storage of very high concentrations of stabilized atoms. To this date the structures of Im–He solids for light impurities such as hydrogen and deu-

terium atoms and molecules are not fully determined. Our preliminary x-ray investigations of D_2–He samples showed the presence of nanoclusters of D_2 in these solids.[15] Therefore it is reasonable to assume that the structure of Im–He solids formed from light impurities is similar to that of Im–He solids formed from heavy impurities (Ne, N_2, Kr).[16,17] In this work we have studied impurity–helium solids formed by light impurities, namely hydrogen and deuterium atoms and molecules. The method of electron spin resonance (ESR) was used for detailed studies of H and D atoms stabilized in Im–He solids. We have performed studies of the exchange tunnelling chemical reactions (3) and (4) to produce large (up to $7.5\times10^{17}\,\mathrm{cm}^{-3}$) and relatively stable concentrations of H atoms. The kinetics of these reactions have been investigated for Im–He samples formed by introducing gas mixtures with different initial ratios of H_2 to D_2, ranging from 1:20 to 1:1, into He II. We determined the exact positions of the H and D lines by using precise measurements of the magnetic field. Satellite ESR lines associated with the dipolar coupling of the electron spins of H and D atoms to the nuclear moments of hydrogen nuclei in neighboring molecules have been observed. This observation allows us to determine the distances between stabilized H or D atoms and neighboring HD or H_2 molecules in Im–He solids.[18] From the analysis of line widths and the saturation behavior of H and D signals, we estimate the spin-spin relaxation time T_2 and the spin-lattice relaxation time T_1 of H and D atoms in Im–He solids.

2. EXPERIMENTAL METHOD

The experiments were performed in a Janis cryostat with a variable temperature insert (VTI). The lower part of the cryostat was installed between the pole pieces of a Varian electromagnet for these ESR investigations. The home-made insert for the creation and investigation of Im–He solids with stabilized atoms shown in Fig. 1 was placed into the VTI. The details of the experimental procedure were described in our previous work.[17,19] For sample preparation, a gas mixture of H_2, D_2, and He was transported from a room temperature gas handling system to the cryogenic region. To provide H and D atoms, high power radio frequency was applied to the electrodes around the quartz capillary carrying the mixed gases. The jet ($dN/dt\sim5\times10^{19}\,\mathrm{s}^{-1}$) of impurity atoms and molecules as well as helium gas emerged from a small (0.75 mm) orifice and then penetrated the surface of superfluid helium in the collection beaker. The temperature during sample preparation was 1.5 K. The liquid helium level in the beaker was maintained by a fountain pump connected to the main helium bath of the VTI. At the top of the beaker was a funnel that caught the sample as it emerged from the quartz capillary. A set of teflon blades was employed to scrape the sample from the funnel while the beaker was rotated so that the sample could fall to the bottom of the cylindrical part of the beaker. During a period of 10 minutes an impurity–helium solid sample with volume 0.35 cm^3 was formed in the beaker. Following this process, the beaker with the sample was lowered into the ESR cavity, which was situated near the bottom of the VTI in the homogeneous field region of the electromagnet. We used a cylindrical cavity operating in a TE_{011} mode. A ruby crystal was attached to the bottom of the

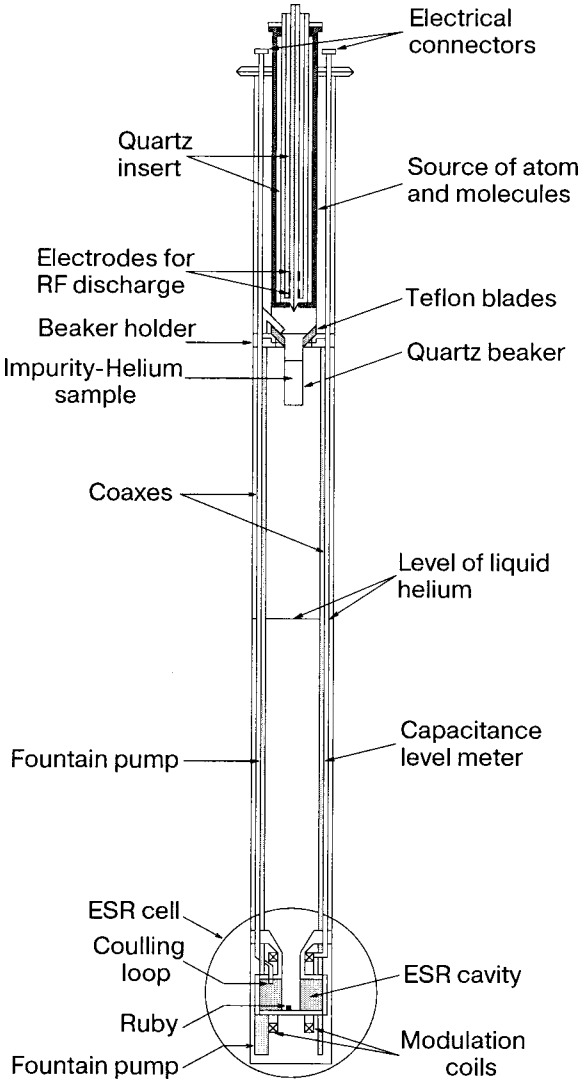

FIG. 1. Low temperature insert for Im–He sample preparation and ESR investigations. The quartz beaker is lowered into the ESR 9.12 GHz TE_{011} resonant cavity for measurements after sample preparation.

cavity. The ruby was used as a secondary standard for the calibration of the measurements of the number of stabilized H and D atoms in Im–He solids. The calibration of the absolute value of number of atoms was made by using a DPPH sample with a known number (2.4×10^{17}) of spins with measurements being carried out at $T=1.35$ K. Special measurements were made to determine the dependence of the signal of the small calibration sample of DPPH on the position along the axis of the cavity. This dependence is consistent with the calculated distribution of the microwave magnetic field in the cavity. ESR signals were measured using a CW reflection homodyne spectrometer ($f_r=9.12$ GHz, $f_{\mathrm{mod}}=100$ kHz). All measurements have been done for Im–He samples at temperatures of 1.35 K and 1.8 K. A calibrated Ge thermometer was used for temperature measurements. Continuously pumping the VTI while supplying liquid helium from the main bath allows us to conduct long term investigations of the Im–He samples. In this paper we present reaction kinetics studies of H and D atoms which continued for ~8 hours at $T=1.35$ K.

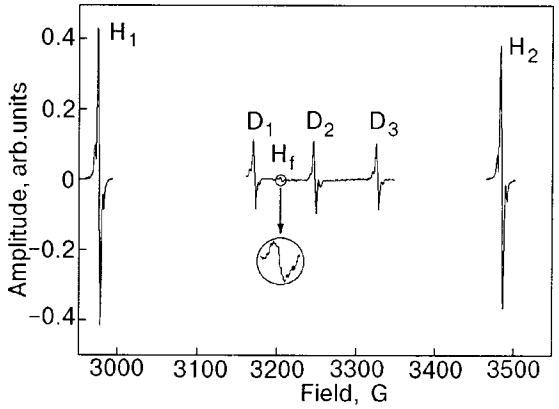

FIG. 2. ESR spectra of H and D atoms for an Im–He solid prepared from the gaseous mixture H_2:D_2:He=1:4:100. Spectra observed at $T=1.8$ K, 182 min after sample collection. The width of each of the main hydrogen and deuterium lines is 3 G. Seven fold magnification of the forbidden line is shown in the inset.

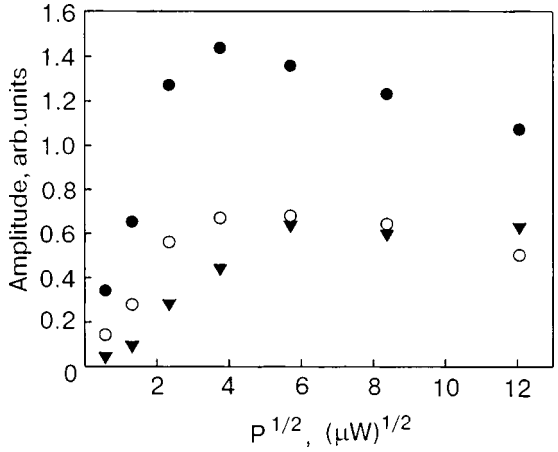

FIG. 3. Microwave power saturation behavior for different ESR lines of H and D atoms in Im–He solid at $T=1.35$ K (see Fig. 2): H_1 (●), D_1 (○), H_f (▼). Im–He solid was formed by initial gas mixture H_2:D_2:He=1:4:100.

3. RESULTS

Figure 2 shows the ESR derivative spectra of H and D atoms in Im–He solids prepared from an initial gas mixture in the ratio of H_2:D_2:He=1:4:100. The positions of observed lines are shown in Table I.

The allowed H and D lines are each accompanied by two satellite lines. The intensity of the small forbidden hydrogen line H_f is about 200 times smaller than that of the allowed hydrogen lines. Figure 3 shows the microwave power saturation behavior of H and D atoms in Im–He solids. Unlike the behavior of H atoms produced by radiolysis in solid H_2,[11] H atoms in Im–He solids saturate at a larger microwave power ~16 μW. ESR signals were normally measured at a microwave power ~5 μW, significantly below the saturation limit.

The spin-spin relaxation time T_2 is calculated from the line-width below saturation by means of the expression[20]

$$T_2=\frac{2}{3^{1/2}\gamma\Delta H_{pp}}, \tag{6}$$

where γ is the gyromagnetic ratio, and ΔH_{pp} is the line width obtained from the peak to peak separation for the derivative of the ESR signal. The line width of ESR lines for H and D atoms was found to be 3 G (see Fig. 2), leading to a value of $T_2=2.2\times10^{-8}$ s for H and D atoms in our Im–He solids. The observed line width is far larger than the inhomogeneous broadening expected from our magnet (~0.1 G). We used a saturation method for determination of the spin-lattice relaxation time T_1 for H and D atoms in Im–He solids. For estimating T_1, we determined the dependence of the signal amplitude on the square root of microwave power as plotted in Fig. 3 for hydrogen and deuterium atoms. Values of T_1 were determined by means of an expression for the maximum values of the peak amplitude of the derivative signal[20]

$$T_1=\frac{1.98\times10^{-7}\Delta H_{pp}}{gH_1^2}, \tag{7}$$

where g is the spectroscopic splitting factor. For H and D atoms $g\simeq2$. We performed calculations of the microwave magnetic field according to the equation[20]

$$H_1^2=2\times10^{-3}PQ\eta\frac{V_c}{V_s}, \tag{8}$$

where P is the microwave power; Q is the quality factor; η is the filling factor; V_c is the cavity volume, and V_s is the sample volume. When we substitute the geometric parameters for our cavity, expression (8) becomes $H_1^2=8P$. From the plot in Fig. 3 we obtained the value of the power $P_{\max}=16\,\mu$W for which the amplitude of the derivative of the ESR signal of the H atoms has a maximum value. From the expression (7) we then find a value of $T_1=(2.3\pm0.5)\times10^{-3}$ s for H atoms in Im–He solids. For D atoms ($P_{\max}=25\,\mu$W, see also Fig. 3) we find a value $T_1=(1.5\pm0.5)\times10^{-3}$ s. The relatively small values of T_1 for D and H atoms in Im–He solids show that the atoms are stabilized in solid clusters of mixtures HD and D_2 molecules, rather than being isolated in liquid and solid helium. In latter case, the T_1 values should be much larger.[21]

We also investigated the evolution of Im–He solids containing H and D atoms as well as H_2, HD, and D_2 molecules in an attempt to maximize the H atom concentration. The investigations were performed for a variety of initial gas mixtures of H_2, D_2, and He. The initial H_2:D_2 ratio was varied from 1:20 to 1:1. The ratio of the concentration of the impurity gases to the He gas in the mixtures was always

TABLE I. Observed positions of ESR lines for H and D atoms in Im–He solids at $T=1.8$ K and a frequency 9.12 GHz.

Line	Transition (F, m_F)	Field, G
H_1	(1,1) ↔ (0,0)	2976.3
H_2	(1,0) ↔ (1,−1)	3484.7
H_f	(1,0) ↔ (0,0)	3205.7
D_1	(3/2,3/2) ↔ (1/2,1/2)	3171.7
D_2	(3/2,1/2) ↔ (1/2,−1/2)	3247.4
D_3	(3/2,−1/2) ↔ (3/2,−3/2)	3326.9

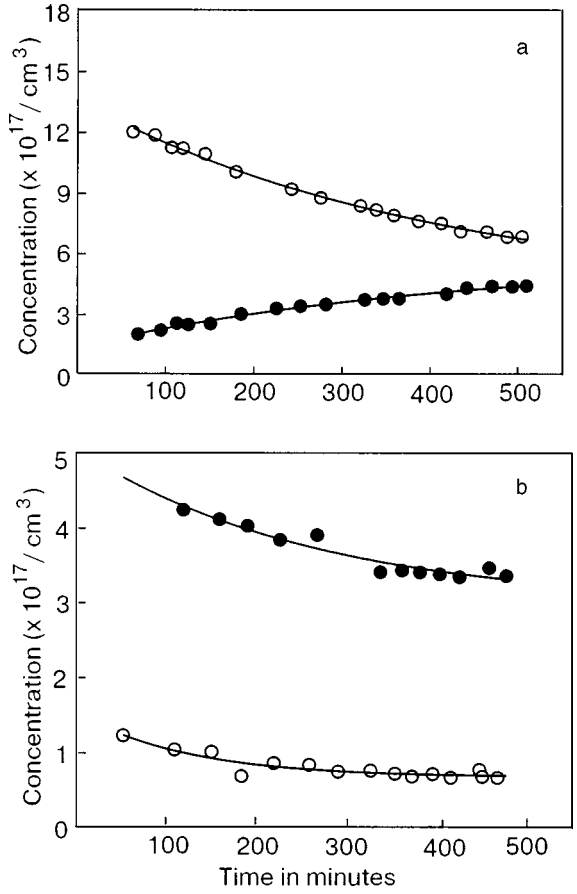

FIG. 4. Time dependence of the concentration of H atoms (●) and D atoms (○) in Im–He solids at temperature $T=1.35$ K prepared from different initial mixtures: $H_2:D_2:He=1:20:420$ (a); $H_2:D_2:He=1:2:60$ (b).

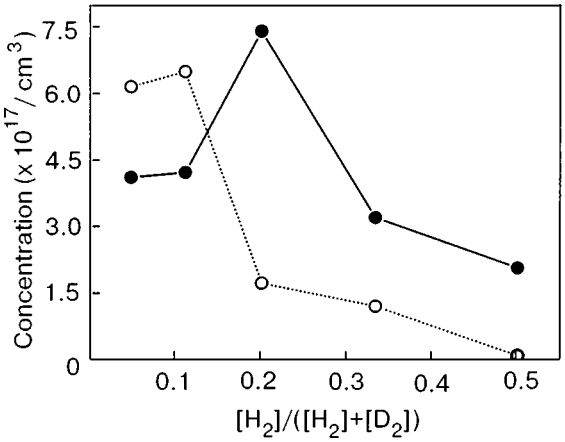

FIG. 5. The dependence of the average concentrations of H atoms (●) and D atoms (○) in Im–He solids on the fraction of hydrogen gas in the make up gas mixture, $[H_2]/([H_2]+[D_2])$. For each point the concentrations were determined after a waiting period of 500 minutes following sample collection.

equal to 1:20. The yields of H and D atoms leaving the radio frequency discharge were proportional to the concentrations of H_2 and D_2 in the initial gas mixture.[12] Figure 4 shows the time evolution of the H and D concentrations in Im–He solids formed by two different initial mixtures. Immediately after preparation of all the Im–He samples, a large enhancement of the concentration of H atoms relative to D atoms was observed compared with the ratio of H_2 to D_2 in the initial gas mixture. This fact indicates that at the earliest stages of sample preparation at $T=1.5$ K, a fast exchange tunnelling reaction leads to a large reduction in the number of D atoms and a corresponding increase in the number of H atoms. According to the calculation by Takayanagi *et al.*[22] the rate constant for reaction (3) is found to be $5.4\times10^{-2}\,\mathrm{cm^3\cdot mol^{-1}\cdot s^{-1}}$, so that the enhancements of the H atom concentrations are attributed to this reaction with a time constant on the order of a few minutes for our samples. Later on, a steady increase of the ratio H:D takes place over a period of hours, during the storage of our Im–He sample at $T=1.35$ K. The kinetics of the changing concentrations of H and D atoms for the sample prepared from the initial gas mixture $H_2:D_2:He=1:20:420$ is similar to that observed by Lukashevich *et al.*[10] and Miyazaki *et al.*[11] for atoms trapped in solid H_2-D_2 mixtures. The concentration of H atoms grows, but the concentration of D atoms is decaying, just as in our Im–He studies. At this stage we believe that the behavior of atoms in our solid is governed by reaction (4) with rate constant $1.9\times10^{-3}\,\mathrm{cm^3\cdot mol^{-1}\cdot s^{-1}}$ (Ref. 22) which further reduces the number of D atoms and increases the number of H atoms. Figure 4a shows that the increase in the number of H atoms is smaller than the decrease in the number of D atoms. This observation could be explained by recombination of H atoms. In this process, the hydrogen atoms migrate through the solid via reaction (1) or the reaction

$$H+HD\rightarrow HD+H. \tag{9}$$

A succession of these reactions allows the transport of H atoms to neighboring positions in the Im–He solid where they recombine to form H_2 or HD molecules via the reactions:

$$H+D\rightarrow HD \tag{10}$$

$$H+H\rightarrow H_2. \tag{11}$$

This mechanism is supported by the results of investigations of Im–He samples prepared from the gas mixture $H_2:D_2:He=1:2:60$ (see Fig. 4b). In this sample the concentration of H_2 and HD molecules is about one order of magnitude larger compared with the former sample, so therefore reactions (1) and (9) should accelerate the recombination processes (10) and (11). It can be seen that the decay of D atoms is more rapid and the H atom population also decays steadily, throughout the experiment. The exchange tunnelling reactions can be used to produce very large concentrations of atomic hydrogen in our samples. As discussed earlier, these large concentrations could allow us to enter the regime where the thermal de Broglie wave-length becomes comparable to the spacing between H atoms, provided that the temperature is low enough. In our experiments we have investigated samples obtained from a variety of initial gas mixtures to determine the one which yields the highest hydrogen atom concentration. The experimental plots shown in Fig. 5 correspond to the H and D atom average concentrations after a storage time ~500 minutes following initial sample preparation. For the optimal gas mixture $H_2:D_2:He=1:4:100$, the largest H atom concentration $(7.5\pm3.0)\times10^{17}\,\mathrm{cm^{-3}}$ was obtained. We are planning investigations with even longer stor-

age times of this optimal sample to obtain the largest possible concentration of H atoms due to exchange tunnelling reactions.

4. CONCLUSION

The observation of satellite lines and the relatively short longitudinal relaxation times T_1 for H and D atoms in impurity-helium solids show that the H and D atoms are stabilized in clusters of solid mixtures of H_2, D_2, and HD. We did not observe any signatures of single atoms perfectly isolated by helium. Observation of these isolated atoms requires the application of much lower microwave power levels to avoid saturation. Our spectrometer was not capable of providing such low powers.

The time dependence of the populations of H and D atoms in the Im–He solids at $T=1.35\,\mathrm{K}$ proves the occurrence of the exchange tunnelling reaction $D+HD\rightarrow H+D_2$. The exchange tunnelling reactions are capable of producing very high concentrations of hydrogen atoms. Our estimations from ESR line intensity measurements indicate that the largest concentration we have obtained is $(7.5\pm3.0)\times10^{17}\,\mathrm{cm}^{-3}$. For this concentration the onset of quantum overlap phenomena may be found at $T\sim13\,\mathrm{mK}$ which can be reached by means of a dilution refrigerator.

The authors are grateful to NASA for supporting this research via grant NAG 8-1445. We also thank P. Borbat, G. Codner, H. Padamsee, V. Shemelin, and R. Silsbee for extremely useful conversations and help with the experiments.

*E-mail: epb22@cornell.edu

[1] T. J. Greytak and D. Kleppner, *Spin Polarized Hydrogen, New Trends in Atomic Physics*, in *Les Houches Summer School*—session XXXVIII (1982), G. Grinberg and R. Stone (Eds.), Elsevier Science Publisher, B.V. (1984), p. 1127.
[2] A. M. Bass and H. P. Broida, *Formation and Trapping of Free Radicals*, Academic Press, New York (1960).
[3] A. V. Ivliev, A. Ya. Katunin, I. I. Lukashevich *et al.*, JETP Lett. **36**, 472 (1982).
[4] T. Miyazaki, N. Iwata, K.-P. Lee, and K. Fueki, J. Phys. Chem. **93**, 3352 (1989).
[5] T. Kumada, S. Mori, T. Nagasaka, J. Kumagai, and T. Miyazaki, J. Low Temp. Phys. **122**, 265 (2001).
[6] T. Kumada, M. Sakakibara, T. Nagasaka, H. Fukuta, J. Kumagi, and T. Miyazaki, J. Chem. Phys. **116**, 1109 (2002).
[7] K. L. Lee, T. Miyazaki, K. Fueki, and K. Gotoh, J. Phys. Chem. **91**, 180 (1987).
[8] E. B. Gordon, A. A. Pelmenev, O. F. Pugachev, and V. V. Khmelenko, JETP Lett. **37**, 282 (1983).
[9] A. S. Iskovskih, A. Ya. Katunin, I. I. Lukashevich, V. V. Sklyarevskii, V. V. Suraev, V. V. Filippov, N. I. Filippov, and V. A. Shevtsov, Zh. Éksp. Teor. Fiz. **91**, 1832 (1986) [Sov. Phys. JETP **64**, 1085 (1986)].
[10] A. V. Ivliev, A. S. Iskovskih, A. Ya. Katunin, I. I. Lukashevich, V. V. Sklyarevskii, V. V. Suraev, V. V. Filippov, N. I. Filippov, and V. A. Shevtsov, JETP Lett. **38**, 379 (1983).
[11] H. Tsuruta, T. Miyazaki, K. Fueki, and N. Azuma, J. Phys. Chem. **87**, 5422 (1983).
[12] E. B. Gordon, A. A. Pelmenev, O. F. Pugachev, and V. V. Khmelenko, Fiz. Nizk. Temp. **11**, 563 (1985) [Sov. J. Low Temp. Phys. **11**, 307 (1985)].
[13] E. B. Gordon, V. V. Khmelenko, A. A. Pelmenev, E. A. Popov, and O. F. Pugachev, Chem. Phys. Lett. **155**, 301 (1989).
[14] E. B. Gordon, V. V. Khmelenko, A. A. Pelmenev, E. A. Popov, O. F. Pugachev, and A. F. Shestakov, Chem. Phys. **170**, 411 (1993).
[15] S. I. Kiselev, V. V. Khmelenko, D. M. Lee, V. Kiryukhin, R. E. Boltnev, E. B. Gordon, and B. Keimer, J. Low Temp. Phys. **126**, 235 (2002).
[16] V. Kiryukhin, B. Keimer, R. E. Boltnev, V. V. Khmelenko, and E. B. Gordon, Phys. Rev. Lett. **79**, 1774 (1997).
[17] S. I. Kiselev, V. V. Khmelenko, D. M. Lee, V. Kiryukhin, R. E. Boltnev, E. B. Gordon, and B. Keimer, Phys. Rev. B **65**, 024517 (2002).
[18] S. I. Kiselev, V. V. Khmelenko, and D. M. Lee, Phys. Rev. Lett. **89**, 175301 (2002).
[19] S. I. Kiselev, V. V. Khmelenko, D. M. Lee, and C. Y. Lee, J. Low Temp. Phys. **128**, 37 (2002).
[20] C. P. Poole, *Electron Spin Resonance. A Comprehensive Treatise on Experimental Techniques*, Interscience Publishers, John Wiley and Sons, New York, London, Sydney (1967).
[21] M. Arndt, S. I. Kanorsky, A. Weis, and T. W. Hansch, Phys. Rev. Lett. **78**, 1359 (1995).
[22] T. Takayanagi, K. Nakamura, and S. Sato, J. Phys. Chem. **90**, 1641 (1989).

This article was published in English in the original Russian journal. Reproduced here with stylistic changes by AIP.

ESR investigation of hydrogen and deuterium atoms in impurity-helium solids

S. I. Kiselev, V. V. Khmelenko, E. P. Bernard,* and D. M. Lee

Laboratory of Atomic and Solid State Physics Cornell University, Ithaca, NY 14853-2501, USA
(Submitted December 19, 2002)
Fiz. Nizk. Temp. **29**, 678–683 (June 2003)

Impurity-helium solids (Im–He solids) are porous solids created by injecting a beam of mixed helium and impurity gases into superfluid ^{4}He. In this work we use electron spin resonance (ESR) techniques to investigate Im–He solids containing atoms and molecules of hydrogen and/or deuterium. We have performed studies of low temperature ($T \sim 1.35$ K) tunnelling chemical reactions in which deuterium atoms replace the hydrogen atoms bound in H_2 or HD molecules to produce large (up to 7.5×10^{17} cm^{-3}) and relatively stable concentrations of free hydrogen atoms. The time dependence of H and D atom concentrations has been investigated for Im–He samples with different initial ratios of hydrogen and deuterium ranging from 1:20 to 1:1. The satellite ESR lines associated with the dipolar coupling of electron spins of H and D atoms to the nuclear moments of the hydrogen nuclei found in neighboring molecules have been observed in Im–He solids. The forbidden hyperfine transition of atomic hydrogen involving the mutual spin flips of electrons and protons has also been observed.
 [DOI: 10.1063/1.1542539]

1. INTRODUCTION

Investigations of hydrogen and deuterium atoms, stabilized in solid matrices at low temperatures, have attracted the attention of scientists for many years. Possible quantum effects associated with these systems are of special interest. Quantum behavior is expected when the thermal de Broglie wavelength of the atoms becomes comparable with their interparticle spacing. For the case of H atoms in the gas phase, this condition is satisfied for a concentration of 2.6×10^{18} cm^{-3} at a temperature of 30 mK.[1] For the case of a solid phase, the temperature for the onset of any quantum effect may be lower because of the possibility of a larger effective mass. It is always desirable for investigations of quantum behavior to generate the highest possible concentrations of H or D atoms in solid matrixes. Unfortunately, from the earliest investigations of H atoms in solid H_2, it became clear that some tunnelling processes and molecular recombination could lead to a decrease in the concentration of stabilized H atoms.[2] The detailed investigations of the processes of quantum diffusion and tunnelling reactions of H atoms in solid H_2 at $T=1.35-4.2$ K were performed by Ivliev *et al.*[3] and later by Miyazaki *et al.*[4–6] They established that the decay of H atoms could take place in solid H_2 by tunnelling migration, in which H atoms tunnel through a chain of H_2 molecules according to the reaction

$$H+H_2\rightarrow H_2+H, \tag{1}$$

thereby travelling through the solid H_2 to recombine with another H atom. The reaction rate constant k_1, for reaction (1) was found to be $k_1=18\,\mathrm{cm}^3\cdot\mathrm{mol}^{-1}\cdot\mathrm{s}^{-1}$ at $T=4.2$ K.[4] This value remains the same even when the temperature is lowered to 1.9 K, confirming that tunnelling reactions are involved. The behavior of D atoms in solid D_2 is different. The rate constant for the reaction

$$D+D_2\rightarrow D_2+D \tag{2}$$

is four orders of magnitude lower; $k_2=1.8\times10^{-3}\,\mathrm{cm}^3\cdot\mathrm{mol}^{-1}\cdot\mathrm{s}^{-1}$ (Ref. 7) leading to a much lower recombination rate. Therefore it is possible to create a larger concentration of D atoms in solid D_2 as compared with concentrations of H atoms in solid H_2.[7–9] The exchange tunnelling reactions

$$D+H_2\rightarrow HD+H \tag{3}$$

$$D+HD\rightarrow D_2+H \tag{4}$$

lead to the possibility of creating high concentrations of H atoms in solid mixtures of H_2 and D_2 at low temperatures.[8,10,11] When an H atom is surrounded by shell of D_2 molecules, it becomes very stable because it can neither migrate through the solid D_2 nor react further with D_2 by the reaction

$$H+D_2\rightarrow HD+D \tag{5}$$

at low temperatures, since it is an endothermic reaction. Gordon *et al.*[8,12] suggested that high concentrations of H atoms could be stabilized at low temperatures by means of reactions (3) and (4). In their approach, a gas mixture of hydrogen, deuterium and helium gas was transported through a radio frequency discharge onto the surface of superfluid He contained in a small beaker, at a temperature 1.5 K. The jet of impurity and helium gases penetrates the surface of the superfluid He, and then forms a snow-like solid which settles to the bottom of the collection beaker. This solid became known as an Im–He solid.[13,14] In the case of heavy impurities, Im–He solids are built from a loosely connected aggregation of nanoclusters of impurities each surrounded by one or two layers of solid helium. These aggregates form extremely porous solids into which liquid helium easily and completely penetrates. This system, having the high thermal conductance and the high thermal capacitance of superfluid helium, allows preparation and storage of very high concentrations of stabilized atoms. To this date the structures of Im–He solids for light impurities such as hydrogen and deu-

terium atoms and molecules are not fully determined. Our preliminary x-ray investigations of D_2–He samples showed the presence of nanoclusters of D_2 in these solids.[15] Therefore it is reasonable to assume that the structure of Im–He solids formed from light impurities is similar to that of Im–He solids formed from heavy impurities (Ne, N_2, Kr).[16,17] In this work we have studied impurity–helium solids formed by light impurities, namely hydrogen and deuterium atoms and molecules. The method of electron spin resonance (ESR) was used for detailed studies of H and D atoms stabilized in Im–He solids. We have performed studies of the exchange tunnelling chemical reactions (3) and (4) to produce large (up to $7.5\times10^{17}\,\mathrm{cm}^{-3}$) and relatively stable concentrations of H atoms. The kinetics of these reactions have been investigated for Im–He samples formed by introducing gas mixtures with different initial ratios of H_2 to D_2, ranging from 1:20 to 1:1, into He II. We determined the exact positions of the H and D lines by using precise measurements of the magnetic field. Satellite ESR lines associated with the dipolar coupling of the electron spins of H and D atoms to the nuclear moments of hydrogen nuclei in neighboring molecules have been observed. This observation allows us to determine the distances between stabilized H or D atoms and neighboring HD or H_2 molecules in Im–He solids.[18] From the analysis of line widths and the saturation behavior of H and D signals, we estimate the spin-spin relaxation time T_2 and the spin-lattice relaxation time T_1 of H and D atoms in Im–He solids.

2. EXPERIMENTAL METHOD

The experiments were performed in a Janis cryostat with a variable temperature insert (VTI). The lower part of the cryostat was installed between the pole pieces of a Varian electromagnet for these ESR investigations. The home-made insert for the creation and investigation of Im–He solids with stabilized atoms shown in Fig. 1 was placed into the VTI. The details of the experimental procedure were described in our previous work.[17,19] For sample preparation, a gas mixture of H_2, D_2, and He was transported from a room temperature gas handling system to the cryogenic region. To provide H and D atoms, high power radio frequency was applied to the electrodes around the quartz capillary carrying the mixed gases. The jet ($dN/dt\sim5\times10^{19}\,\mathrm{s}^{-1}$) of impurity atoms and molecules as well as helium gas emerged from a small (0.75 mm) orifice and then penetrated the surface of superfluid helium in the collection beaker. The temperature during sample preparation was 1.5 K. The liquid helium level in the beaker was maintained by a fountain pump connected to the main helium bath of the VTI. At the top of the beaker was a funnel that caught the sample as it emerged from the quartz capillary. A set of teflon blades was employed to scrape the sample from the funnel while the beaker was rotated so that the sample could fall to the bottom of the cylindrical part of the beaker. During a period of 10 minutes an impurity–helium solid sample with volume 0.35 cm^3 was formed in the beaker. Following this process, the beaker with the sample was lowered into the ESR cavity, which was situated near the bottom of the VTI in the homogeneous field region of the electromagnet. We used a cylindrical cavity operating in a TE_{011} mode. A ruby crystal was attached to the bottom of the

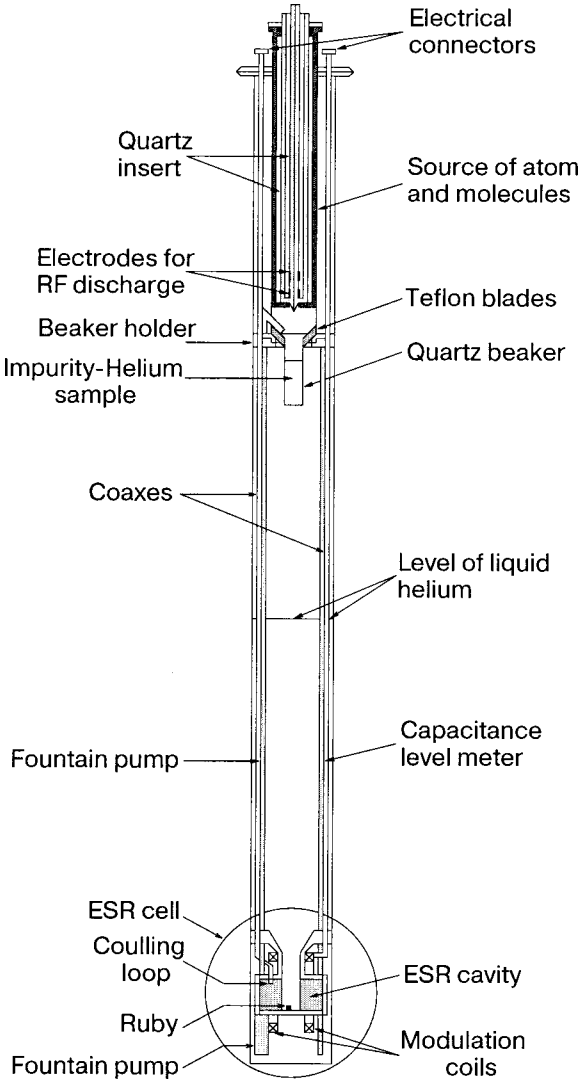

FIG. 1. Low temperature insert for Im–He sample preparation and ESR investigations. The quartz beaker is lowered into the ESR 9.12 GHz TE_{011} resonant cavity for measurements after sample preparation.

cavity. The ruby was used as a secondary standard for the calibration of the measurements of the number of stabilized H and D atoms in Im–He solids. The calibration of the absolute value of number of atoms was made by using a DPPH sample with a known number (2.4×10^{17}) of spins with measurements being carried out at $T=1.35$ K. Special measurements were made to determine the dependence of the signal of the small calibration sample of DPPH on the position along the axis of the cavity. This dependence is consistent with the calculated distribution of the microwave magnetic field in the cavity. ESR signals were measured using a CW reflection homodyne spectrometer ($f_r=9.12$ GHz, $f_{\mathrm{mod}}=100$ kHz). All measurements have been done for Im–He samples at temperatures of 1.35 K and 1.8 K. A calibrated Ge thermometer was used for temperature measurements. Continuously pumping the VTI while supplying liquid helium from the main bath allows us to conduct long term investigations of the Im–He samples. In this paper we present reaction kinetics studies of H and D atoms which continued for ~8 hours at $T=1.35$ K.

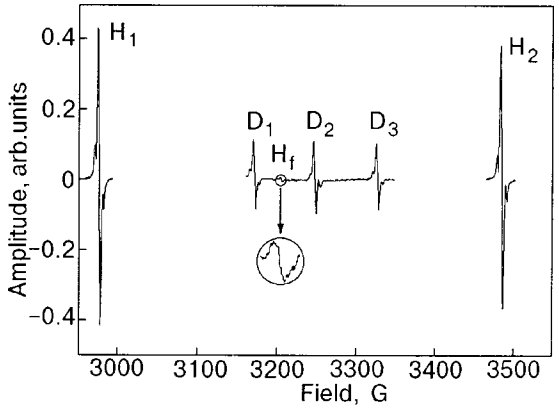

FIG. 2. ESR spectra of H and D atoms for an Im–He solid prepared from the gaseous mixture H_2:D_2:He=1:4:100. Spectra observed at $T=1.8$ K, 182 min after sample collection. The width of each of the main hydrogen and deuterium lines is 3 G. Seven fold magnification of the forbidden line is shown in the inset.

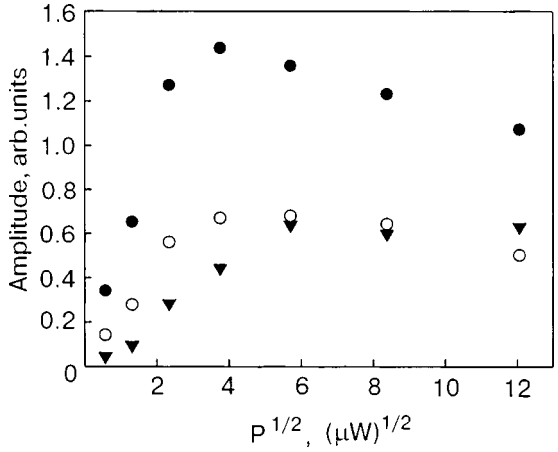

FIG. 3. Microwave power saturation behavior for different ESR lines of H and D atoms in Im–He solid at $T=1.35$ K (see Fig. 2): H_1 (●), D_1 (○), H_f (▼). Im–He solid was formed by initial gas mixture H_2:D_2:He=1:4:100.

3. RESULTS

Figure 2 shows the ESR derivative spectra of H and D atoms in Im–He solids prepared from an initial gas mixture in the ratio of H_2:D_2:He=1:4:100. The positions of observed lines are shown in Table I.

The allowed H and D lines are each accompanied by two satellite lines. The intensity of the small forbidden hydrogen line H_f is about 200 times smaller than that of the allowed hydrogen lines. Figure 3 shows the microwave power saturation behavior of H and D atoms in Im–He solids. Unlike the behavior of H atoms produced by radiolysis in solid H_2,[11] H atoms in Im–He solids saturate at a larger microwave power ~16 μW. ESR signals were normally measured at a microwave power ~5 μW, significantly below the saturation limit.

The spin-spin relaxation time T_2 is calculated from the line-width below saturation by means of the expression[20]

$$T_2=\frac{2}{3^{1/2}\gamma\Delta H_{pp}}, \tag{6}$$

where γ is the gyromagnetic ratio, and ΔH_{pp} is the line width obtained from the peak to peak separation for the derivative of the ESR signal. The line width of ESR lines for H and D atoms was found to be 3 G (see Fig. 2), leading to a value of $T_2=2.2\times10^{-8}$ s for H and D atoms in our Im–He solids. The observed line width is far larger than the inhomogeneous broadening expected from our magnet (~0.1 G). We used a saturation method for determination of the spin-lattice relaxation time T_1 for H and D atoms in Im–He solids. For estimating T_1, we determined the dependence of the signal amplitude on the square root of microwave power as plotted in Fig. 3 for hydrogen and deuterium atoms. Values of T_1 were determined by means of an expression for the maximum values of the peak amplitude of the derivative signal[20]

$$T_1=\frac{1.98\times10^{-7}\Delta H_{pp}}{gH_1^2}, \tag{7}$$

where g is the spectroscopic splitting factor. For H and D atoms $g\simeq2$. We performed calculations of the microwave magnetic field according to the equation[20]

$$H_1^2=2\times10^{-3}PQ\eta\frac{V_c}{V_s}, \tag{8}$$

where P is the microwave power; Q is the quality factor; η is the filling factor; V_c is the cavity volume, and V_s is the sample volume. When we substitute the geometric parameters for our cavity, expression (8) becomes $H_1^2=8P$. From the plot in Fig. 3 we obtained the value of the power $P_{\max}=16\,\mu$W for which the amplitude of the derivative of the ESR signal of the H atoms has a maximum value. From the expression (7) we then find a value of $T_1=(2.3\pm0.5)\times10^{-3}$ s for H atoms in Im–He solids. For D atoms ($P_{\max}=25\,\mu$W, see also Fig. 3) we find a value $T_1=(1.5\pm0.5)\times10^{-3}$ s. The relatively small values of T_1 for D and H atoms in Im–He solids show that the atoms are stabilized in solid clusters of mixtures HD and D_2 molecules, rather than being isolated in liquid and solid helium. In latter case, the T_1 values should be much larger.[21]

We also investigated the evolution of Im–He solids containing H and D atoms as well as H_2, HD, and D_2 molecules in an attempt to maximize the H atom concentration. The investigations were performed for a variety of initial gas mixtures of H_2, D_2, and He. The initial H_2:D_2 ratio was varied from 1:20 to 1:1. The ratio of the concentration of the impurity gases to the He gas in the mixtures was always

TABLE I. Observed positions of ESR lines for H and D atoms in Im–He solids at $T=1.8$ K and a frequency 9.12 GHz.

Line	Transition (F, m_F)	Field, G
H_1	(1,1) ↔ (0,0)	2976.3
H_2	(1,0) ↔ (1,−1)	3484.7
H_f	(1,0) ↔ (0,0)	3205.7
D_1	(3/2,3/2) ↔ (1/2,1/2)	3171.7
D_2	(3/2,1/2) ↔ (1/2,−1/2)	3247.4
D_3	(3/2,−1/2) ↔ (3/2,−3/2)	3326.9

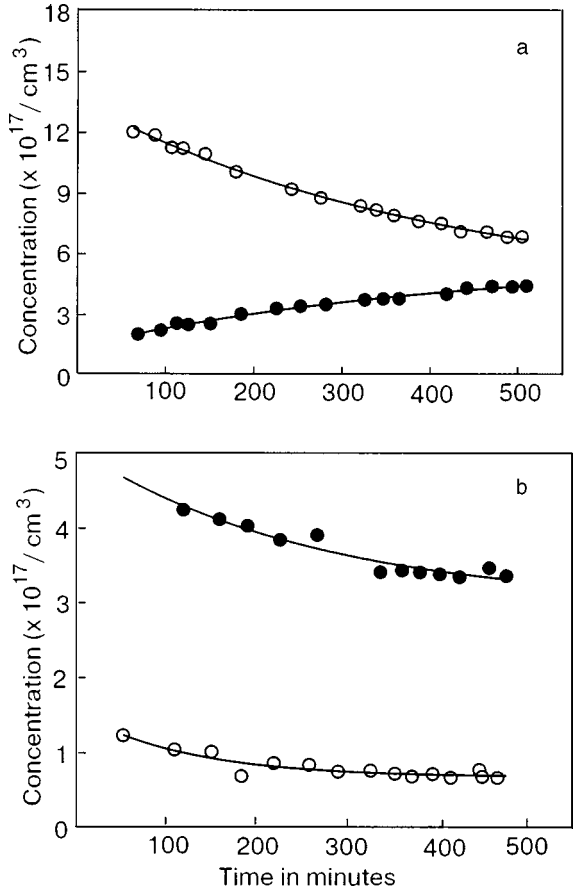

FIG. 4. Time dependence of the concentration of H atoms (●) and D atoms (○) in Im–He solids at temperature $T=1.35$ K prepared from different initial mixtures: $H_2:D_2:He=1:20:420$ (a); $H_2:D_2:He=1:2:60$ (b).

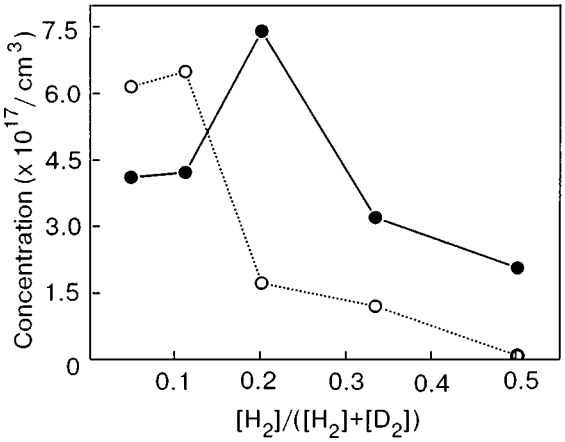

FIG. 5. The dependence of the average concentrations of H atoms (●) and D atoms (○) in Im–He solids on the fraction of hydrogen gas in the make up gas mixture, $[H_2]/([H_2]+[D_2])$. For each point the concentrations were determined after a waiting period of 500 minutes following sample collection.

equal to 1:20. The yields of H and D atoms leaving the radio frequency discharge were proportional to the concentrations of H_2 and D_2 in the initial gas mixture.[12] Figure 4 shows the time evolution of the H and D concentrations in Im–He solids formed by two different initial mixtures. Immediately after preparation of all the Im–He samples, a large enhancement of the concentration of H atoms relative to D atoms was observed compared with the ratio of H_2 to D_2 in the initial gas mixture. This fact indicates that at the earliest stages of sample preparation at $T=1.5$ K, a fast exchange tunnelling reaction leads to a large reduction in the number of D atoms and a corresponding increase in the number of H atoms. According to the calculation by Takayanagi *et al.*[22] the rate constant for reaction (3) is found to be $5.4\times10^{-2}\,\mathrm{cm^3\cdot mol^{-1}\cdot s^{-1}}$, so that the enhancements of the H atom concentrations are attributed to this reaction with a time constant on the order of a few minutes for our samples. Later on, a steady increase of the ratio H:D takes place over a period of hours, during the storage of our Im–He sample at $T=1.35$ K. The kinetics of the changing concentrations of H and D atoms for the sample prepared from the initial gas mixture $H_2:D_2:He=1:20:420$ is similar to that observed by Lukashevich *et al.*[10] and Miyazaki *et al.*[11] for atoms trapped in solid H_2-D_2 mixtures. The concentration of H atoms grows, but the concentration of D atoms is decaying, just as in our Im–He studies. At this stage we believe that the behavior of atoms in our solid is governed by reaction (4) with rate constant $1.9\times10^{-3}\,\mathrm{cm^3\cdot mol^{-1}\cdot s^{-1}}$ (Ref. 22) which further reduces the number of D atoms and increases the number of H atoms. Figure 4a shows that the increase in the number of H atoms is smaller than the decrease in the number of D atoms. This observation could be explained by recombination of H atoms. In this process, the hydrogen atoms migrate through the solid via reaction (1) or the reaction

$$H+HD\rightarrow HD+H. \tag{9}$$

A succession of these reactions allows the transport of H atoms to neighboring positions in the Im–He solid where they recombine to form H_2 or HD molecules via the reactions:

$$H+D\rightarrow HD \tag{10}$$

$$H+H\rightarrow H_2. \tag{11}$$

This mechanism is supported by the results of investigations of Im–He samples prepared from the gas mixture $H_2:D_2:He=1:2:60$ (see Fig. 4b). In this sample the concentration of H_2 and HD molecules is about one order of magnitude larger compared with the former sample, so therefore reactions (1) and (9) should accelerate the recombination processes (10) and (11). It can be seen that the decay of D atoms is more rapid and the H atom population also decays steadily, throughout the experiment. The exchange tunnelling reactions can be used to produce very large concentrations of atomic hydrogen in our samples. As discussed earlier, these large concentrations could allow us to enter the regime where the thermal de Broglie wave-length becomes comparable to the spacing between H atoms, provided that the temperature is low enough. In our experiments we have investigated samples obtained from a variety of initial gas mixtures to determine the one which yields the highest hydrogen atom concentration. The experimental plots shown in Fig. 5 correspond to the H and D atom average concentrations after a storage time ~500 minutes following initial sample preparation. For the optimal gas mixture $H_2:D_2:He=1:4:100$, the largest H atom concentration $(7.5\pm3.0)\times10^{17}\,\mathrm{cm^{-3}}$ was obtained. We are planning investigations with even longer stor-

age times of this optimal sample to obtain the largest possible concentration of H atoms due to exchange tunnelling reactions.

4. CONCLUSION

The observation of satellite lines and the relatively short longitudinal relaxation times T_1 for H and D atoms in impurity-helium solids show that the H and D atoms are stabilized in clusters of solid mixtures of H_2, D_2, and HD. We did not observe any signatures of single atoms perfectly isolated by helium. Observation of these isolated atoms requires the application of much lower microwave power levels to avoid saturation. Our spectrometer was not capable of providing such low powers.

The time dependence of the populations of H and D atoms in the Im–He solids at $T=1.35\,\mathrm{K}$ proves the occurrence of the exchange tunnelling reaction $D+HD\rightarrow H+D_2$. The exchange tunnelling reactions are capable of producing very high concentrations of hydrogen atoms. Our estimations from ESR line intensity measurements indicate that the largest concentration we have obtained is $(7.5\pm3.0)\times10^{17}\,\mathrm{cm}^{-3}$. For this concentration the onset of quantum overlap phenomena may be found at $T\sim13\,\mathrm{mK}$ which can be reached by means of a dilution refrigerator.

The authors are grateful to NASA for supporting this research via grant NAG 8-1445. We also thank P. Borbat, G. Codner, H. Padamsee, V. Shemelin, and R. Silsbee for extremely useful conversations and help with the experiments.

*E-mail: epb22@cornell.edu

[1] T. J. Greytak and D. Kleppner, *Spin Polarized Hydrogen, New Trends in Atomic Physics*, in *Les Houches Summer School*—session XXXVIII (1982), G. Grinberg and R. Stone (Eds.), Elsevier Science Publisher, B.V. (1984), p. 1127.
[2] A. M. Bass and H. P. Broida, *Formation and Trapping of Free Radicals*, Academic Press, New York (1960).
[3] A. V. Ivliev, A. Ya. Katunin, I. I. Lukashevich *et al.*, JETP Lett. **36**, 472 (1982).
[4] T. Miyazaki, N. Iwata, K.-P. Lee, and K. Fueki, J. Phys. Chem. **93**, 3352 (1989).
[5] T. Kumada, S. Mori, T. Nagasaka, J. Kumagai, and T. Miyazaki, J. Low Temp. Phys. **122**, 265 (2001).
[6] T. Kumada, M. Sakakibara, T. Nagasaka, H. Fukuta, J. Kumagi, and T. Miyazaki, J. Chem. Phys. **116**, 1109 (2002).
[7] K. L. Lee, T. Miyazaki, K. Fueki, and K. Gotoh, J. Phys. Chem. **91**, 180 (1987).
[8] E. B. Gordon, A. A. Pelmenev, O. F. Pugachev, and V. V. Khmelenko, JETP Lett. **37**, 282 (1983).
[9] A. S. Iskovskih, A. Ya. Katunin, I. I. Lukashevich, V. V. Sklyarevskii, V. V. Suraev, V. V. Filippov, N. I. Filippov, and V. A. Shevtsov, Zh. Éksp. Teor. Fiz. **91**, 1832 (1986) [Sov. Phys. JETP **64**, 1085 (1986)].
[10] A. V. Ivliev, A. S. Iskovskih, A. Ya. Katunin, I. I. Lukashevich, V. V. Sklyarevskii, V. V. Suraev, V. V. Filippov, N. I. Filippov, and V. A. Shevtsov, JETP Lett. **38**, 379 (1983).
[11] H. Tsuruta, T. Miyazaki, K. Fueki, and N. Azuma, J. Phys. Chem. **87**, 5422 (1983).
[12] E. B. Gordon, A. A. Pelmenev, O. F. Pugachev, and V. V. Khmelenko, Fiz. Nizk. Temp. **11**, 563 (1985) [Sov. J. Low Temp. Phys. **11**, 307 (1985)].
[13] E. B. Gordon, V. V. Khmelenko, A. A. Pelmenev, E. A. Popov, and O. F. Pugachev, Chem. Phys. Lett. **155**, 301 (1989).
[14] E. B. Gordon, V. V. Khmelenko, A. A. Pelmenev, E. A. Popov, O. F. Pugachev, and A. F. Shestakov, Chem. Phys. **170**, 411 (1993).
[15] S. I. Kiselev, V. V. Khmelenko, D. M. Lee, V. Kiryukhin, R. E. Boltnev, E. B. Gordon, and B. Keimer, J. Low Temp. Phys. **126**, 235 (2002).
[16] V. Kiryukhin, B. Keimer, R. E. Boltnev, V. V. Khmelenko, and E. B. Gordon, Phys. Rev. Lett. **79**, 1774 (1997).
[17] S. I. Kiselev, V. V. Khmelenko, D. M. Lee, V. Kiryukhin, R. E. Boltnev, E. B. Gordon, and B. Keimer, Phys. Rev. B **65**, 024517 (2002).
[18] S. I. Kiselev, V. V. Khmelenko, and D. M. Lee, Phys. Rev. Lett. **89**, 175301 (2002).
[19] S. I. Kiselev, V. V. Khmelenko, D. M. Lee, and C. Y. Lee, J. Low Temp. Phys. **128**, 37 (2002).
[20] C. P. Poole, *Electron Spin Resonance. A Comprehensive Treatise on Experimental Techniques*, Interscience Publishers, John Wiley and Sons, New York, London, Sydney (1967).
[21] M. Arndt, S. I. Kanorsky, A. Weis, and T. W. Hansch, Phys. Rev. Lett. **78**, 1359 (1995).
[22] T. Takayanagi, K. Nakamura, and S. Sato, J. Phys. Chem. **90**, 1641 (1989).

This article was published in English in the original Russian journal. Reproduced here with stylistic changes by AIP.

On the formation mechanism of impurity–helium solids: evidence for extensive clustering

E. A. Popov

Department of Chemistry, University of Jyväskylä, P.O Box 35, FIN-40014, Finland and Institute of Energy Problems of Chemical Physics, Russian Academy of Sciences, Chernogolovka, Moscow Region 142432, Russia

J. Eloranta, J. Ahokas, and H. Kunttu*

Department of Chemistry, University of Jyväskylä, P.O. Box 35, FIN-40014, Finland
(Submitted December 19, 2002)
Fiz. Nizk. Temp. **29**, 684–689 (June 2003)

Optical emission studies of a discharged nitrogen–helium gas injected into superfluid helium near 1.5 K are described. Analysis of atomic (α group) and molecular Vegard–Kaplan transitions clearly indicates that the emitting species are embedded inside nitrogen clusters. Cluster formation is most efficient in the crater formed on the liquid surface. Model calculations based on the classical bubble model and density functional theory suggest that under the experimental conditions only clusters consisting of more than 1000 molecules have sufficient kinetic energy for stable cavity formation to occur inside liquid helium. The results obtained suggest that impurity–helium solids formation is a consequence of extensive clustering in the gas jet. © *2003 American Institute of Physics.* [DOI: 10.1063/1.1542540]

1. INTRODUCTION

The experimental approach to stabilizing atoms by injecting an impurity–helium (Im–He) gas jet into superfluid helium (He II) was first developed by Gordon, Mezhov-Deglin, and Pugachev in 1974.[1] The advantages of this approach are due to the efficient precooling of the gas jet prior to its immersion into He II, the high degree of dispersion of the impurity particles, and the efficient heat dissipation by He II. Consequently, stabilization of reactive atoms (N, H, D) with exceedingly high densities has been achieved as indicated by optical emission and electron paramagnetic resonance (EPR) measurements.[2,3] Since its discovery the original approach has undergone rapid advancement and semitransparent gel-like substances with He/Im ratios of 12–60 and thermal stability up to 6–8 K are now routinely grown. Although their interior is filled with liquid He, these macroscopic condensates are historically called impurity–helium solids (IHS).[1–9] An interesting extension to the cited series of investigations is the recent work by Mezhov–Deglin and Kokotin on helium–water condensate.[10]

Studies of the thermal properties of IHS have shown that the presence of ~ 0.5 mole % of an impurity (N_2, Kr) in a condensate completely suppresses the convective flow of the liquid He filling the condensate.[6,9] It was supposed on this basis that IHS consist of a porous network structure and therefore resemble highly porous aerogels filled with liquid He. More recently, a series of structural studies by Lee's group at Cornell University has provided strong support for this hypothesis. Using ultrasound and x-ray diffraction techniques to complement one another it has been shown that Im–He solids are indeed mesoporous with characteristic impurity cluster size close to 6 nm, average impurity density $\sim 10^{20}$ cm^{-3}, and a wide pore-size distribution ranging from 8 to 860 nm.[11–13]

Although the physical characteristics of Im–He solids have been rather extensively studied for years, their formation mechanism and structure are not understood on a molecular scale.

The model suggested by Gordon and Shestakov ascribes the formation of metastable Im–He condensates to an Im–He solid phase (IHSP) consisting of van der Waals impurity–helium clusters Im$(He)_n$ where the particles ''stick together,'' i.e. a bare impurity atom or molecule surrounded by solid layers of He atoms in a superlattice-like arrangement.[4,14] Of course, this is a very hypothetical model, which for example neglects entirely the role of impurity clusters in the formation of these solids.

The objective of the present study is to develop new insights into our understanding of Im–He condensates, among other things, their formation mechanism. Instead of looking at the solids themselves, we shall focus on the processes taking place inside the Im–He gas jet from the discharge zone to its final immersion in He II. The following issues are addressed: (i) the extent of cluster formation in the gas jet, (ii) the interaction of the impurity particles (bare atoms or molecules, small clusters) with a liquid helium surface, and (iii) the factors controlling their probability of penetrating into bulk liquid helium under the experimental conditions. In what follows we shall describe our spectroscopic observations in nitrogen–helium gas jets and present the results of model calculations of the solvation of nitrogen species in He II.

2. EXPERIMENTAL METHODS

Our experimental setup consists of a liquid He bath cryostat fitted with a set of quartz windows (Fig. 1). The inner diameter of the He bath is 120 mm. The bath holds 7 liters of liquid He, which allows operation for more than 12 h. By

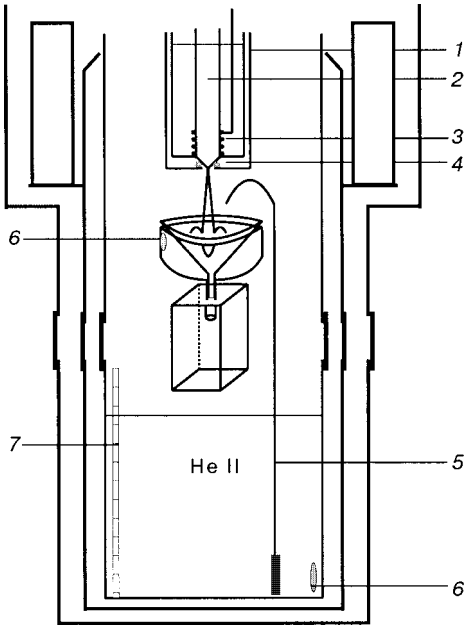

FIG. 1. Experimental setup for injecting Im–He mixtures into superfluid helium: cryogenic discharge source (*1*); quartz tube (*2*); liquid nitrogen cooled induction coil (*3*); nozzle (*4*); fountain pump (*5*); temperature sensor (*6*); He II level gauge (*7*).

pumping the helium reservoir with a one-stage mechanical pump (20 liters/s) the lowest accessible temperature is close to 1.4 K. The He vapor pressure inside the cryostat was measured with an absolute pressure transducer (MKS Instruments, Baratron model 622). The temperature was measured with a silicon diode sensor and Lake Shore 330 temperature controller.

A cryogenic discharge source, an optical cell, and temperature sensors were placed inside the cryostat with insertion in a way that allows for mutually independent operation of the instrumentation. This type of insertion makes it possible to adjust the separation between the discharge tube orifice and the He surface in the sample cell over the range 2–20 cm. An induction coil installed coaxially around the liquid nitrogen cooled quartz discharge tube 2 cm from the nozzle excited an electrodeless discharge. A home-made pulse generator, operating near 40 MHz, was connected to the coil, thereby providing a 10–70 W rf discharge with pulse duration ranging from 1 μs up to continuous operation.

Nitrogen and helium gases with 99.99(9)% nominal purity were premixed in a stainless steel cylinder. A mechanical membrane regulator was used to provide a constant gas flow with accuracy better than 5% for a typical gas flow rate of 5×10^{19} particles/s with pressure drop in the gas cylinder from 5 to 0.2 bars. The optical measurement cell consists of a 40 mm in diameter quartz funnel attached to a standard 10×10 mm quartz optical cuvette. A fountain pump, which supplied superfluid helium from the bottom of the cryostat, maintained the He II level in the sample cell constant.

The experiments were performed by passing a mixture of molecular nitrogen, diluted to 0.3–3% by helium gas, through the discharge zone. The discharged gas escapes through a 0.8 mm in diameter nozzle and flows through dense cold helium gas, forming an intensely glowing jet. The jet strikes the He II surface and produces a visually observable crater. Special attention was devoted to selective collection of emission from three distinct observations zones: the gas jet, the crater, and the bulk He II. For this purpose, in some experiments the quartz funnel was blocked with a black painted Pyrex cover in order to allow light collection solely from the bulk He II.

The collected light was focused onto the entrance slit of a 0.3 m spectrograph (Acton) equipped with 2400, 600, and 600 lines/nm gratings, blazed at 240, 300, and 500 nm, respectively. The spectra were recorded with a thermoelectrically cooled Charge–Coupled–Device (CCD) camera (Princeton Instruments) attached to the spectrograph. Depending on the grating, the spectral bandwidth on the detector was 30, 120, or 120 nm, respectively. A high-grade UV quartz optical fiber bundle was used for more selective light collection from different parts of the jet or bulk He II.

3. EXPERIMENTAL RESULTS

3.1. Characteristics of the jet

After passing throught the rf discharge zone the nitrogen–helium gas mixture undergoes laminar flow in dense cold helium gas (density 3×10^{19} atoms/cm^3, $T=1.7$ K), forming a well-collimated jet (Fig. 2). The peripheral part of the jet is rather cold, but its core is relatively hot and less luminescent. We measured the velocity of the jet at $T=77$ K and cryostat pressure 5 mbar. The measurement was performed by adjusting the discharge to pulse duration

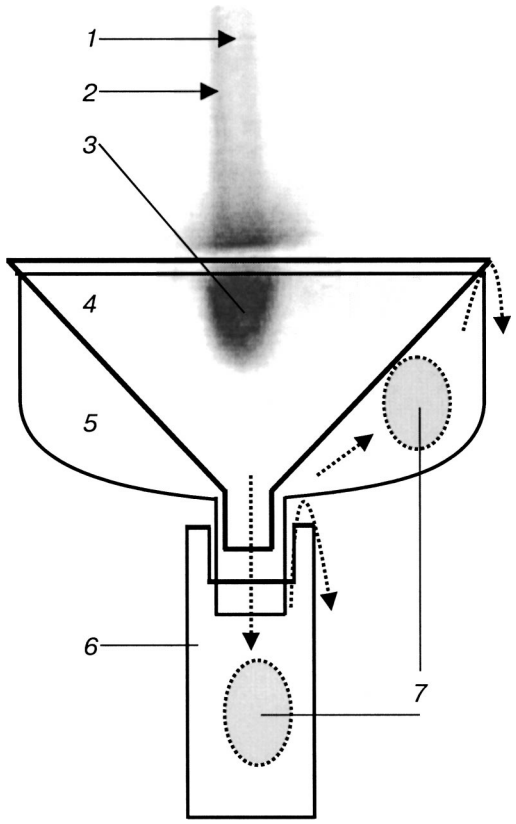

FIG. 2. Photograph of the nitrogen-helium jet penetrating into bulk He II. A schematic view of the optical cell is also shown: the core of the jet (*1*); peripheral part of the jet (*2*); crater (*3*); black painted Pyrex funnel (*4*); quartz funnel (*5*); quartz cuvette (*6*); light collection zones (*7*). The dotted arrows show the circulation of liquid He.

200 μs and pulse repetition rate 500 MHz. Under these conditions the emission was monitored 5 cm from the discharge tube orifice with a photomultiplier tube fitted with a horizontal 1.5 mm slit. The flow velocity was estimated to be $v = 70$ m/s on the basis of the observed phase shift with respect to the pulse train.

When it strikes the He II surface the jet stops and produces a well-defined crater. The crater is the most strongly emitting region due to efficient collisional processes, which in turn promote aggregation of impurities and recombination of nitrogen atoms. The intensity of the emission decreases dramatically in the bulk He II even at distances a few millimeters below the crater. When the distance between the nozzle and the He II surface increased to 10 cm or more we observed a transition from laminar flow (top part) to purely turbulent flow (bottom part), which is visually characterized by a jet bottom that is shaggy.

3.2. Emission spectra

The main monitored emissions were the atomic transition N($^2D-^4S$) (α group, green afterglow) and the Vegard–Kaplan system $A^3\Sigma_u^+ - X^1\Sigma_g^+$ (blue and UV afterglow) of molecular nitrogen. Both transitions are forbidden in the gas phase and thus serve as sensitive probes for various processes related to the formation of impurity clusters and IHS.

A section of the Vegard–Kaplan band of N_2 is presented in Fig. 3. The spectra are almost identical, regardless of the location of the emitter (gas jet, crater, bulk) and are characterized by linewidths ~ 1 nm and a consistent red shift ~ 360 cm^{-1} from the corresponding gas-phase line. As described in the experimental section, special care was taken to eliminate stray light from the other parts of the cryostat. Although the spectroscopy of the IHS falls outside the scope of this paper, the spectrum obtained from explosion of a helium–nitrogen condensate is provided for reference. Apart from the broad and so far unassigned background features, this spectrum clearly resembles the others. These observations strongly suggest that radiative recombination of nitrogen atoms, leading to the Vegard–Kaplan band, occurs in very similar environments in all detection zones.

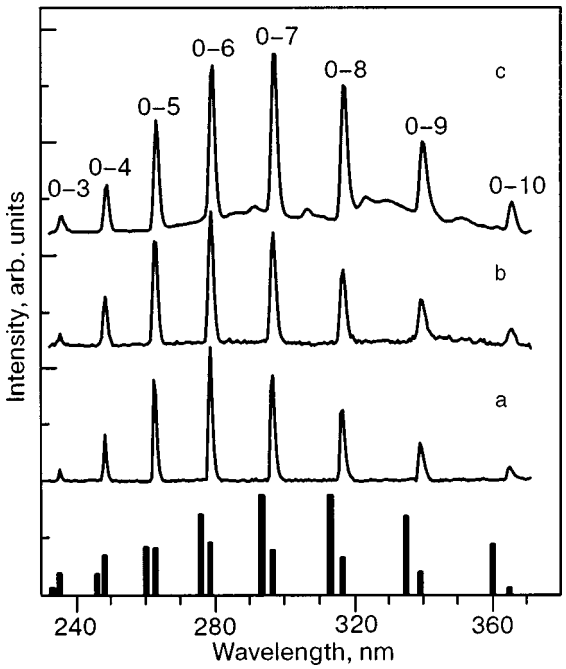

FIG. 3. A section of the Vegard–Kaplan emission band of molecular nitrogen collected from the gas jet (a), bulk He II (b), and upon explosion of the nitrogen–helium solid (c). The numbers refer to the quantum labels ($v'-v''$). The stick spectra show the line positions in the gas phase (black columns[17]) and in the solid nitrogen matrix (gray columns[18]).

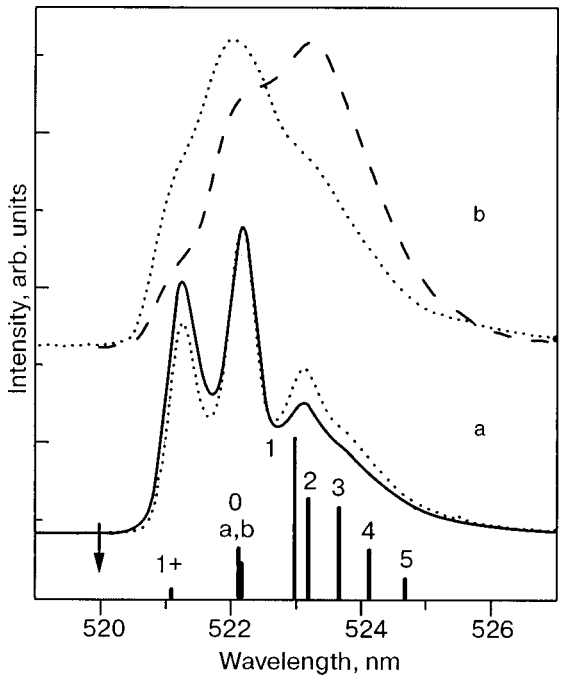

FIG. 4. The effect of the gas mixture on the $^2D-^4S$ emission of atomic hydrogen. N_2/He = 1/400 (solid line), 1/100 (dotted line). A grating with 2400 grooves/mm was used (a). N_2/He = 1/100 (dotted line), 1/30 (dashed line). A grating with 600 grooves/mm was also used (b). The arrow indicates the gas phase position of the transition.[19] The stick spectrum represents observations in a solid nitrogen matrix.[24]

The strongly forbidden green α group emission of atomic nitrogen was detected even in the gas jet far from the liquid helium surface. The α group emission collected near the crater was very intense and the spectrum contained three peaks centered at 521, 522, and 523 nm (see Fig. 4). This observation provides additional support for the idea that instead of monitoring transitions of more or less isolated gas-phase species, the spectra are strongly affected by cluster formation in the gas jet before it enters He II. No significant changes in the α group emission were observed when the signal was collected from bulk He II. Increasing the N_2/He ratio of the gas mixture from 0.3 to 3% shifted the α group emission towards 523 nm in the gas phase. We performed spectroscopic studies on other atomic and molecular transitions such as N($^2P-^2D$), the first positive system ($B^3\Pi - A^3\Sigma$) of N_2, O($^1S-^1D$), the Herzberg I bands ($A-X$) of O_2, and the β, γ, and δ bands of NO. These data, which will be published separately, are consistent with the present observations.

4. DISCUSSION

In the present work we focus our attention on the Vegard–Kaplan (V–K) emission system in the UV range for two main reasons: (i) previous spectroscopic measurements

in IHS were restricted to the visible range[5] and (ii) we expected to observe recombination of atomic nitrogen in bulk He II and in nitrogen–helium solid by monitoring radiative decay of the metastable $A^3\Sigma$ state of the N_2 molecule (triplet exciton in the IHS case). Detecting the V–K emission in the gas phase is a rather challenging task and would require very high-purity gases, especially free of any oxygen-containing impurities. Moreover, the discharge needs to be operated under special conditions.[15,16] Quite surprisingly, we observed rather intense V–K emission from the gas jet even in the presence of oxygen impurities. Equally demonstrative is the observation that the V–K lines are red-shifted with respect to their pure gas-phase counterparts.[17] This would strongly suggest that the emission originates from recombination of atoms embedded in impurity particles. Coletti and Bonnot[18] studied V–K emission in a solid nitrogen matrix. They observed quite intense emission at 20 K with a lifetime of the order of ~ 1 ms. Similarly to our findings in the nitrogen–helium jet, the V–K lines in solid nitrogen are red-shifted from the gas phase by 350 cm^{-1}.

Spin and parity selection rules for electric-dipole transitions strongly forbid the atomic ($^2D_{5/2,\,3/2}-{}^4S_{3/2}$) transitions of nitrogen; observations of these transitions are attributed to electric quadrupole transitions. The $^2D_{5/2}$ and $^2D_{3/2}$ states lie 19224 cm^{-1} and 19233 cm^{-1} (2.38 eV) above the $^4S_{3/2}$ ground state and their computed lifetimes are 44 h and 17 h, respectively.[19] Thus pure atomic emission within the time of flight of the jet should be undetectable under the conditions of the present experiments. Therefore some process taking place in the gas jet is dramatically affecting the transition probability and consequently decreasing the lifetime of the atomic transition. Aggregation of nitrogen molecules around the emitter would obviously be such a process. In fact, unlike in the gas phase the green emission in irradiated solid nitrogen is the most prominent spectral feature.[20] In solid nitrogen this emission consists of eight main lines, the strongest lying at 522 nm (zero-phonon line) and 523–525 nm (phonon-induced wing). Furthermore, the lifetime of $^2D-{}^4S$ emission in solid nitrogen is 40 s.[21] The similarity between our spectra and the spectrum obtained in solid nitrogen is obvious already at the highest dilution, and becomes stronger as the nitrogen content increases (see Fig. 5).

An important factor promoting nucleation and cluster formation in a jet is the jet's ability to switch from laminar to turbulent flow as temperature decreases. Let the jet be an incompressible flow through dense helium gas. The Reynolds number is defined by the straightforward relation $R_e = vD/\nu$. Here v is the velocity of the jet, D is the diameter of the jet (pipe flow), and ν is the kinematic viscosity (the viscosity divided by the density). As the temperature of the nitrogen–helium jet decreases from the initial value $T = 80$ K to $T = 10$ K (the temperature a few mm above the He II surface), the kinematic viscosity of the jet decreases by a factor of 25. In pipe flow characterized by $v = 70$ m/s, $D = 0.005$ m, $\nu(89\text{ K}) = 1.8\times10^{-3}$ m^2/s, and $\nu(10\text{ K}) = 6\times10^{-5}$ m^2/s, the jet should switch from laminar ($R_e = 210$ at $T = 80$ K) to turbulent ($R_e = 5600$ at $T = 10$ K) flow. Indeed, we observed a shaggy jet front near the He II surface. Moreover, the shaggy front was clearly seen even when the distance between the He II surface and the nozzle was more than 10 cm and the jet did not reach the surface. We attribute this observation to the onset of turbulent flow.

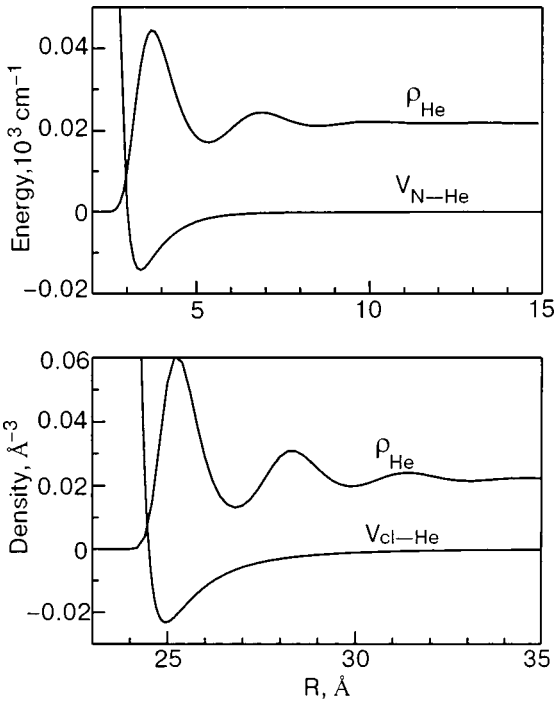

FIG. 5. The density profiles of liquid He near a ground state nitrogen atom (top panel) and a molecular nitrogen cluster with $n = 1000$ (bottom panel) are shown. The corresponding pair potentials are also shown.

Visual observations during preparation of the IHS showed that some small particles penetrate into the bulk He II directly from the jet. However, most of the impurities tend to float on the surface and stick to the walls of the quartz cell, grow on the walls, and finally sink to the bottom. In the following we assume that the penetration of an impurity into liquid He depends on the particle kinetic energy, which in the present case is determined by the velocity of the propagating jet. More precisely, the kinetic energy should exceed the solvation energy of the given species. This energy can be estimated using the classical bubble model:

$$E_b(R_b) = V_{\text{N–He}}(R_b) + 4\pi R_b^2 \gamma, \tag{1}$$

where R_b is the bubble radius and γ is the surface tension ($\gamma_{He} = 3.6\times10^{-4}$ J/m^2). Neglecting all dissipative processes and van der Waals attraction we can obtain a lower bound on the critical velocity required for a species to penetrate into the liquid:

$$v_{cr} > 4R_b(\pi\gamma/m)^{1/2}. \tag{2}$$

To estimate the radius of the cavity produced by a solvated cluster we need to evaluate the interaction potential of a cluster in liquid helium. Here we rely on the approximate N_2–He Lennard–Jones (LJ) potential with $\varepsilon = 18$ cm^{-1} and $R_0 = 3.6$ Å.[22] By assuming a perfect spherical cluster with $N = 1000$, a sharp edge, and $\rho = 1$ g/cm^3 $= 0.0217$ molecules/Å,^{3} we obtain a radius of 22.2 Å. The effective interaction potential can be formulated as

$$V_{\text{eff}}(r) = \int \rho_{N_2}(r') V_{LJ}(|r - r'|) d^3r'. \tag{3}$$

We computed the solvation of impurity N(^2D) and N(^4S) atoms and a $(N_2)_{1000}$ cluster in liquid helium using the density functional theory.[23] Figure 5 shows the results for a bare N atom and a $(N_2)_{1000}$ cluster in a spherical cavity. We can now estimate the critical velocities for a single atom ($R_b = 4$ Å) and a cluster ($R_b = 22.2$ Å). Substituting into Eq. (1) yields $v_N > 400$ m/s and $v_{cl} > 70$ m/s for the atom amd cluster, respectively. We emphasize that we neglected all other dissipative processes, such as ripplon and shock-wave production. Consequently, the real values should be even larger. On the other hand van der Waals binding should slightly favor solvation. Although our theoretical treatment is relatively crude, it clearly shows that under the experimental conditions seeding bare atoms into bulk helium by using a slowly propagating gas jet is not feasible.

5. SUMMARY

We have described optical emission studies on discharged nitrogen–helium gas mixtures under experimental conditions where the IHS are typically prepared. Analysis of the observed atomic (α group) and molecular Vegard–Kaplan transitions clearly indicates that these emissions originate from nitrogen clusters or matrix-like particles instead of isolated atoms or molecules. Cluster formation takes place already in the discharge zone, and it is most efficient at the point where the gas jet strikes the surface of He II and a well-defined crater is formed. The enhancement of emission intensity at the jet bottom is attributed to a change from laminar to turbulent jet flow.

The penetration of chemical species into liquid He II was discussed within the classical bubble model. The computed critical velocity, 400 m/s, needed for solvation of a bare N atom clearly exceeds the measured velocity of the jet, and only clusters consisting of at least 1000 molecules can have sufficient kinetic energy to overcome the barrier for stable cavity formation in bulk He II. From our experimental findings and model calculations we conclude that the formation of impurity clusters, i.e. the building blocks of IHS, occurs via extensive clustering in the jet and, most efficiently, in a crater. Coalescence of these nanosize clusters inside He II then leads to the formation of macroscopic condensates. Finally, the deposition of an impurity–helium jet into liquid helium through its surface could be utilized for efficient production of mass-selected neutral clusters and amorphous materials. Aerogel-like IHS produced from Ne, Ar, Kr, and N_2 impurities are one such example.

We wish to thank David M. Lee and Vladimir Khmelenko for fruitful discussions on impurity helium solids. This work was funded by the Academy of Finland.

*E-mail: Henrik.Kunttu@jyu.fi

[1] B. Gordon, L. P. Mezhov-Deglin, and O. F. Pugachev, JETP Lett. **19**, 63 (1974).
[2] E. B. Gordon, A. A. Pelmenev, O. F. Pugachev, and V. V. Khmelenko, JETP Lett. **37**, 282 (1983).
[3] E. B. Gordon, V. V. Khmelenko, A. A. Pelmenev, E. A. Popov, and O. F. Pugachev, Chem. Phys. Lett. **155**, 301 (1989).
[4] E. B. Gordon, V. V. Khmelenko, A. A. Pelmenev, E. A. Popov, O. F. Pugachev, and A. F. Shestakov, Chem. Phys. **170**, 411 (1993).
[5] R. E. Boltnev, E. B. Gordon, V. V. Khmelenko, I. N. Krushinskaya, M. V. Martynenko, A. A. Pelmenev, E. A. Popov, and A. F. Shestakov, Chem. Phys. **189**, 367 (1994).
[6] M. V. Martynenko, V. N. Novikov, A. A. Pelmenev, E. A. Popov, and E. V. Shilov, Bull. Moscow Univer. **3**, 53 (1996).
[7] R. E. Boltnev, I. N. Krushinskaya, M. V. Martynenko, A. A. Pelmenev, E. A. Popov, and V. V. Khmelenko, Fiz. Nizk. Temp. **23**, 753 (1997) [Low Temp. Phys. **23**, 567 (1997)].
[8] R. E. Boltnev, I. N. Krushinskaya, A. A. Pelmenev, D. Yu. Stolyarov, and V. V. Khmelenko, Chem. Phys. Lett. **305**, 217 (1999).
[9] E. A. Popov, A. A. Pelmenev, and E. B. Gordon, J. Low Temp. Phys. **119**, 367 (2000).
[10] L. P. Mezhov-Deglin and A. M. Kokotin, J. Low Temp. Phys. **119**, 385 (2000).
[11] S. I. Kiselev, V. V. Khmelenko, D. A. Geller, D. M. Lee, and J. R. Beamish, J. Low Temp. Phys. **26**, 874 (2000).
[12] S. I. Kiselev, V. V. Khmelenko, and D. M. Lee, Fiz. Nizk. Temp. **26**, 874 (2000) [Low Temp. Phys. **26**, 641 (2000)].
[13] S. I. Kiselev, V. V. Khmelenko, D. M. Lee, V. Kiryukhin, R. E. Boltnev, and E. B Gordon, Phys. Rev. B **65**, 24517 (2001).
[14] E. B. Gordon and A. F. Shestakov, Fiz. Nizk. Temp. **26**, 5 (2000) [Low Temp. Phys. **26**, (2000)].
[15] R. E. Miller, J. Chem. Phys. **43**, 1695 (1965).
[16] A. M. Provilov, L. G. Smirnova, and A. F. Vilesov, Chem. Phys. Lett. **109**, 343 (1984).
[17] A. Loftus and K. H. Krupenie, J. Phys. Chem. Ref. Data **6**, 113 (1977).
[18] F. Coletti and A. M. Bonnot, Chem. Phys. Lett. **45**, 580 (1977).
[19] B. C. Fawsett, At. Data Nucl. Data Tables **16**, 135 (1975).
[20] A. M. Bass and H. P. Broida, *Formation and Trapping of Free Radicals*, Academic Press, New York (1960).
[21] D. S. Tinti and G. W. Robinson, J. Chem. Phys. **49**, 3229 (1968).
[22] P. Habitz, K. T. Tang, and J. P. Toennies, Chem. Phys. Lett. **85**, 461 (1982).
[23] J. Eloranta, N. Schwentner, and V. A. Apkarian, J. Chem. Phys. **116**, 4039 (2002).
[24] O. Oehler, D. A. Smith, and K. Dressler, J. Chem. Phys. **66**, 2097 (1977).

This article was published in English in the original Russian journal. Reproduced here with stylistic changes by AIP.

On the formation mechanism of impurity–helium solids: evidence for extensive clustering

E. A. Popov

Department of Chemistry, University of Jyväskylä, P.O Box 35, FIN-40014, Finland and Institute of Energy Problems of Chemical Physics, Russian Academy of Sciences, Chernogolovka, Moscow Region 142432, Russia

J. Eloranta, J. Ahokas, and H. Kunttu*

Department of Chemistry, University of Jyväskylä, P.O. Box 35, FIN-40014, Finland
(Submitted December 19, 2002)
Fiz. Nizk. Temp. **29**, 684–689 (June 2003)

Optical emission studies of a discharged nitrogen–helium gas injected into superfluid helium near 1.5 K are described. Analysis of atomic (α group) and molecular Vegard–Kaplan transitions clearly indicates that the emitting species are embedded inside nitrogen clusters. Cluster formation is most efficient in the crater formed on the liquid surface. Model calculations based on the classical bubble model and density functional theory suggest that under the experimental conditions only clusters consisting of more than 1000 molecules have sufficient kinetic energy for stable cavity formation to occur inside liquid helium. The results obtained suggest that impurity–helium solids formation is a consequence of extensive clustering in the gas jet. © *2003 American Institute of Physics.* [DOI: 10.1063/1.1542540]

1. INTRODUCTION

The experimental approach to stabilizing atoms by injecting an impurity–helium (Im–He) gas jet into superfluid helium (He II) was first developed by Gordon, Mezhov-Deglin, and Pugachev in 1974.[1] The advantages of this approach are due to the efficient precooling of the gas jet prior to its immersion into He II, the high degree of dispersion of the impurity particles, and the efficient heat dissipation by He II. Consequently, stabilization of reactive atoms (N, H, D) with exceedingly high densities has been achieved as indicated by optical emission and electron paramagnetic resonance (EPR) measurements.[2,3] Since its discovery the original approach has undergone rapid advancement and semitransparent gel-like substances with He/Im ratios of 12–60 and thermal stability up to 6–8 K are now routinely grown. Although their interior is filled with liquid He, these macroscopic condensates are historically called impurity–helium solids (IHS).[1–9] An interesting extension to the cited series of investigations is the recent work by Mezhov–Deglin and Kokotin on helium–water condensate.[10]

Studies of the thermal properties of IHS have shown that the presence of ~ 0.5 mole % of an impurity (N_2, Kr) in a condensate completely suppresses the convective flow of the liquid He filling the condensate.[6,9] It was supposed on this basis that IHS consist of a porous network structure and therefore resemble highly porous aerogels filled with liquid He. More recently, a series of structural studies by Lee's group at Cornell University has provided strong support for this hypothesis. Using ultrasound and x-ray diffraction techniques to complement one another it has been shown that Im–He solids are indeed mesoporous with characteristic impurity cluster size close to 6 nm, average impurity density $\sim 10^{20}$ cm^{-3}, and a wide pore-size distribution ranging from 8 to 860 nm.[11–13]

Although the physical characteristics of Im–He solids have been rather extensively studied for years, their formation mechanism and structure are not understood on a molecular scale.

The model suggested by Gordon and Shestakov ascribes the formation of metastable Im–He condensates to an Im–He solid phase (IHSP) consisting of van der Waals impurity–helium clusters Im$(He)_n$ where the particles ''stick together,'' i.e. a bare impurity atom or molecule surrounded by solid layers of He atoms in a superlattice-like arrangement.[4,14] Of course, this is a very hypothetical model, which for example neglects entirely the role of impurity clusters in the formation of these solids.

The objective of the present study is to develop new insights into our understanding of Im–He condensates, among other things, their formation mechanism. Instead of looking at the solids themselves, we shall focus on the processes taking place inside the Im–He gas jet from the discharge zone to its final immersion in He II. The following issues are addressed: (i) the extent of cluster formation in the gas jet, (ii) the interaction of the impurity particles (bare atoms or molecules, small clusters) with a liquid helium surface, and (iii) the factors controlling their probability of penetrating into bulk liquid helium under the experimental conditions. In what follows we shall describe our spectroscopic observations in nitrogen–helium gas jets and present the results of model calculations of the solvation of nitrogen species in He II.

2. EXPERIMENTAL METHODS

Our experimental setup consists of a liquid He bath cryostat fitted with a set of quartz windows (Fig. 1). The inner diameter of the He bath is 120 mm. The bath holds 7 liters of liquid He, which allows operation for more than 12 h. By

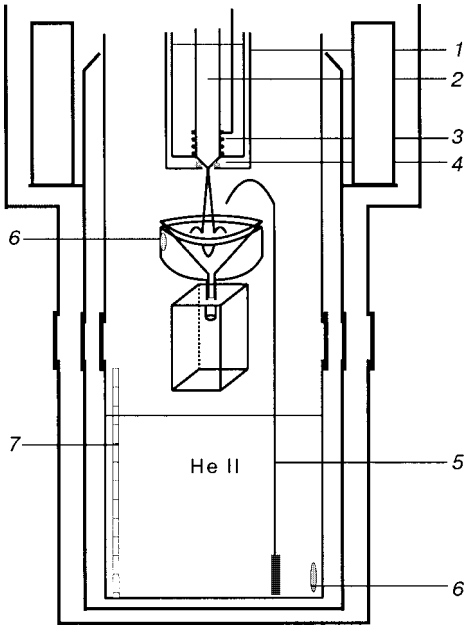

FIG. 1. Experimental setup for injecting Im–He mixtures into superfluid helium: cryogenic discharge source (*1*); quartz tube (*2*); liquid nitrogen cooled induction coil (*3*); nozzle (*4*); fountain pump (*5*); temperature sensor (*6*); He II level gauge (*7*).

pumping the helium reservoir with a one-stage mechanical pump (20 liters/s) the lowest accessible temperature is close to 1.4 K. The He vapor pressure inside the cryostat was measured with an absolute pressure transducer (MKS Instruments, Baratron model 622). The temperature was measured with a silicon diode sensor and Lake Shore 330 temperature controller.

A cryogenic discharge source, an optical cell, and temperature sensors were placed inside the cryostat with insertion in a way that allows for mutually independent operation of the instrumentation. This type of insertion makes it possible to adjust the separation between the discharge tube orifice and the He surface in the sample cell over the range 2–20 cm. An induction coil installed coaxially around the liquid nitrogen cooled quartz discharge tube 2 cm from the nozzle excited an electrodeless discharge. A home-made pulse generator, operating near 40 MHz, was connected to the coil, thereby providing a 10–70 W rf discharge with pulse duration ranging from 1 μs up to continuous operation.

Nitrogen and helium gases with 99.99(9)% nominal purity were premixed in a stainless steel cylinder. A mechanical membrane regulator was used to provide a constant gas flow with accuracy better than 5% for a typical gas flow rate of 5×10^{19} particles/s with pressure drop in the gas cylinder from 5 to 0.2 bars. The optical measurement cell consists of a 40 mm in diameter quartz funnel attached to a standard 10×10 mm quartz optical cuvette. A fountain pump, which supplied superfluid helium from the bottom of the cryostat, maintained the He II level in the sample cell constant.

The experiments were performed by passing a mixture of molecular nitrogen, diluted to 0.3–3% by helium gas, through the discharge zone. The discharged gas escapes through a 0.8 mm in diameter nozzle and flows through dense cold helium gas, forming an intensely glowing jet. The jet strikes the He II surface and produces a visually observable crater. Special attention was devoted to selective collection of emission from three distinct observations zones: the gas jet, the crater, and the bulk He II. For this purpose, in some experiments the quartz funnel was blocked with a black painted Pyrex cover in order to allow light collection solely from the bulk He II.

The collected light was focused onto the entrance slit of a 0.3 m spectrograph (Acton) equipped with 2400, 600, and 600 lines/nm gratings, blazed at 240, 300, and 500 nm, respectively. The spectra were recorded with a thermoelectrically cooled Charge–Coupled–Device (CCD) camera (Princeton Instruments) attached to the spectrograph. Depending on the grating, the spectral bandwidth on the detector was 30, 120, or 120 nm, respectively. A high-grade UV quartz optical fiber bundle was used for more selective light collection from different parts of the jet or bulk He II.

3. EXPERIMENTAL RESULTS

3.1. Characteristics of the jet

After passing throught the rf discharge zone the nitrogen–helium gas mixture undergoes laminar flow in dense cold helium gas (density 3×10^{19} atoms/cm^3, $T=1.7$ K), forming a well-collimated jet (Fig. 2). The peripheral part of the jet is rather cold, but its core is relatively hot and less luminescent. We measured the velocity of the jet at $T=77$ K and cryostat pressure 5 mbar. The measurement was performed by adjusting the discharge to pulse duration

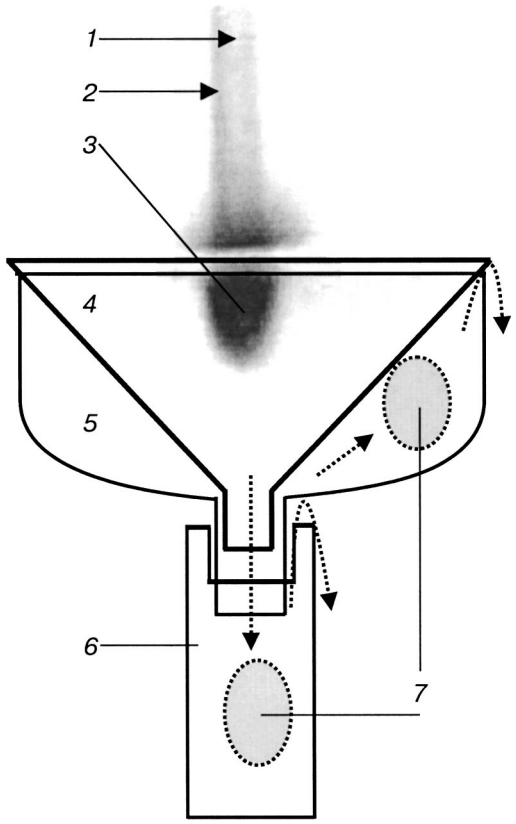

FIG. 2. Photograph of the nitrogen-helium jet penetrating into bulk He II. A schematic view of the optical cell is also shown: the core of the jet (*1*); peripheral part of the jet (*2*); crater (*3*); black painted Pyrex funnel (*4*); quartz funnel (*5*); quartz cuvette (*6*); light collection zones (*7*). The dotted arrows show the circulation of liquid He.

200 μs and pulse repetition rate 500 MHz. Under these conditions the emission was monitored 5 cm from the discharge tube orifice with a photomultiplier tube fitted with a horizontal 1.5 mm slit. The flow velocity was estimated to be $v = 70$ m/s on the basis of the observed phase shift with respect to the pulse train.

When it strikes the He II surface the jet stops and produces a well-defined crater. The crater is the most strongly emitting region due to efficient collisional processes, which in turn promote aggregation of impurities and recombination of nitrogen atoms. The intensity of the emission decreases dramatically in the bulk He II even at distances a few millimeters below the crater. When the distance between the nozzle and the He II surface increased to 10 cm or more we observed a transition from laminar flow (top part) to purely turbulent flow (bottom part), which is visually characterized by a jet bottom that is shaggy.

3.2. Emission spectra

The main monitored emissions were the atomic transition N($^2D-^4S$) (α group, green afterglow) and the Vegard–Kaplan system $A^3\Sigma_u^+ - X^1\Sigma_g^+$ (blue and UV afterglow) of molecular nitrogen. Both transitions are forbidden in the gas phase and thus serve as sensitive probes for various processes related to the formation of impurity clusters and IHS.

A section of the Vegard–Kaplan band of N_2 is presented in Fig. 3. The spectra are almost identical, regardless of the location of the emitter (gas jet, crater, bulk) and are characterized by linewidths ~ 1 nm and a consistent red shift ~ 360 cm^{-1} from the corresponding gas-phase line. As described in the experimental section, special care was taken to eliminate stray light from the other parts of the cryostat. Although the spectroscopy of the IHS falls outside the scope of this paper, the spectrum obtained from explosion of a helium–nitrogen condensate is provided for reference. Apart from the broad and so far unassigned background features, this spectrum clearly resembles the others. These observations strongly suggest that radiative recombination of nitrogen atoms, leading to the Vegard–Kaplan band, occurs in very similar environments in all detection zones.

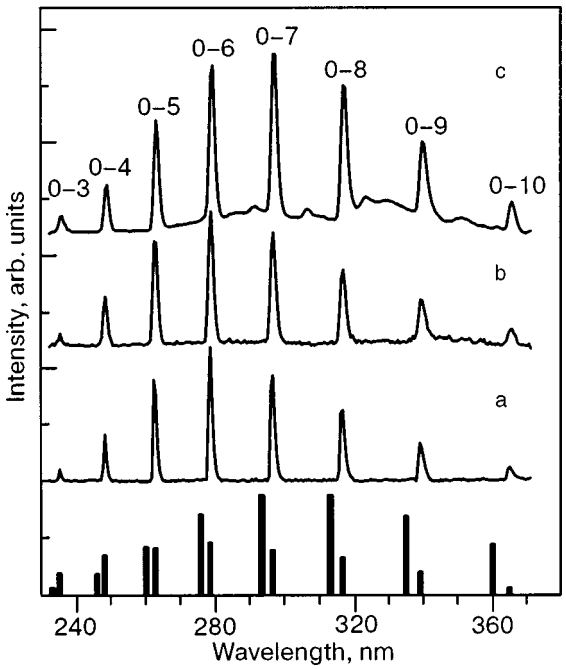

FIG. 3. A section of the Vegard–Kaplan emission band of molecular nitrogen collected from the gas jet (a), bulk He II (b), and upon explosion of the nitrogen–helium solid (c). The numbers refer to the quantum labels ($v'-v''$). The stick spectra show the line positions in the gas phase (black columns[17]) and in the solid nitrogen matrix (gray columns[18]).

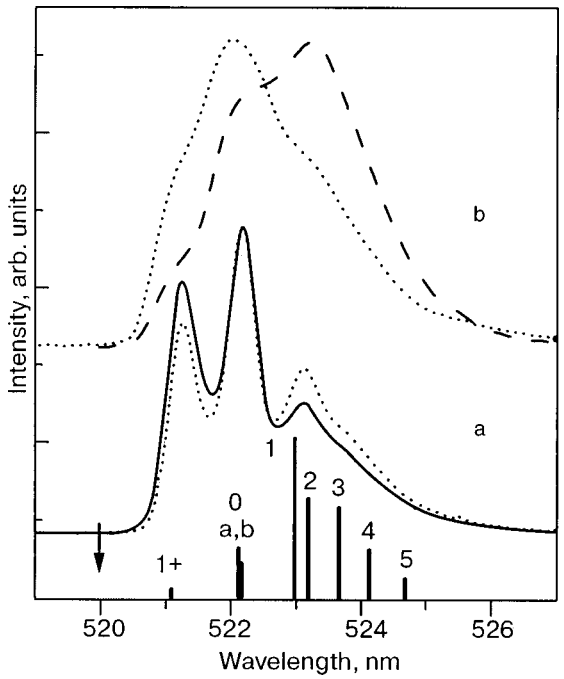

FIG. 4. The effect of the gas mixture on the $^2D-^4S$ emission of atomic hydrogen. N_2/He = 1/400 (solid line), 1/100 (dotted line). A grating with 2400 grooves/mm was used (a). N_2/He = 1/100 (dotted line), 1/30 (dashed line). A grating with 600 grooves/mm was also used (b). The arrow indicates the gas phase position of the transition.[19] The stick spectrum represents observations in a solid nitrogen matrix.[24]

The strongly forbidden green α group emission of atomic nitrogen was detected even in the gas jet far from the liquid helium surface. The α group emission collected near the crater was very intense and the spectrum contained three peaks centered at 521, 522, and 523 nm (see Fig. 4). This observation provides additional support for the idea that instead of monitoring transitions of more or less isolated gas-phase species, the spectra are strongly affected by cluster formation in the gas jet before it enters He II. No significant changes in the α group emission were observed when the signal was collected from bulk He II. Increasing the N_2/He ratio of the gas mixture from 0.3 to 3% shifted the α group emission towards 523 nm in the gas phase. We performed spectroscopic studies on other atomic and molecular transitions such as N($^2P-^2D$), the first positive system ($B^3\Pi - A^3\Sigma$) of N_2, O($^1S-^1D$), the Herzberg I bands ($A-X$) of O_2, and the β, γ, and δ bands of NO. These data, which will be published separately, are consistent with the present observations.

4. DISCUSSION

In the present work we focus our attention on the Vegard–Kaplan (V–K) emission system in the UV range for two main reasons: (i) previous spectroscopic measurements

in IHS were restricted to the visible range[5] and (ii) we expected to observe recombination of atomic nitrogen in bulk He II and in nitrogen–helium solid by monitoring radiative decay of the metastable $A^3\Sigma$ state of the N_2 molecule (triplet exciton in the IHS case). Detecting the V–K emission in the gas phase is a rather challenging task and would require very high-purity gases, especially free of any oxygen-containing impurities. Moreover, the discharge needs to be operated under special conditions.[15,16] Quite surprisingly, we observed rather intense V–K emission from the gas jet even in the presence of oxygen impurities. Equally demonstrative is the observation that the V–K lines are red-shifted with respect to their pure gas-phase counterparts.[17] This would strongly suggest that the emission originates from recombination of atoms embedded in impurity particles. Coletti and Bonnot[18] studied V–K emission in a solid nitrogen matrix. They observed quite intense emission at 20 K with a lifetime of the order of ~ 1 ms. Similarly to our findings in the nitrogen–helium jet, the V–K lines in solid nitrogen are red-shifted from the gas phase by 350 cm^{-1}.

Spin and parity selection rules for electric-dipole transitions strongly forbid the atomic ($^2D_{5/2,\,3/2}-{}^4S_{3/2}$) transitions of nitrogen; observations of these transitions are attributed to electric quadrupole transitions. The $^2D_{5/2}$ and $^2D_{3/2}$ states lie 19224 cm^{-1} and 19233 cm^{-1} (2.38 eV) above the $^4S_{3/2}$ ground state and their computed lifetimes are 44 h and 17 h, respectively.[19] Thus pure atomic emission within the time of flight of the jet should be undetectable under the conditions of the present experiments. Therefore some process taking place in the gas jet is dramatically affecting the transition probability and consequently decreasing the lifetime of the atomic transition. Aggregation of nitrogen molecules around the emitter would obviously be such a process. In fact, unlike in the gas phase the green emission in irradiated solid nitrogen is the most prominent spectral feature.[20] In solid nitrogen this emission consists of eight main lines, the strongest lying at 522 nm (zero-phonon line) and 523–525 nm (phonon-induced wing). Furthermore, the lifetime of $^2D-{}^4S$ emission in solid nitrogen is 40 s.[21] The similarity between our spectra and the spectrum obtained in solid nitrogen is obvious already at the highest dilution, and becomes stronger as the nitrogen content increases (see Fig. 5).

An important factor promoting nucleation and cluster formation in a jet is the jet's ability to switch from laminar to turbulent flow as temperature decreases. Let the jet be an incompressible flow through dense helium gas. The Reynolds number is defined by the straightforward relation $R_e = vD/\nu$. Here v is the velocity of the jet, D is the diameter of the jet (pipe flow), and ν is the kinematic viscosity (the viscosity divided by the density). As the temperature of the nitrogen–helium jet decreases from the initial value $T = 80$ K to $T = 10$ K (the temperature a few mm above the He II surface), the kinematic viscosity of the jet decreases by a factor of 25. In pipe flow characterized by $v = 70$ m/s, $D = 0.005$ m, $\nu(89\text{ K}) = 1.8\times10^{-3}$ m^2/s, and $\nu(10\text{ K}) = 6\times10^{-5}$ m^2/s, the jet should switch from laminar ($R_e = 210$ at $T = 80$ K) to turbulent ($R_e = 5600$ at $T = 10$ K) flow. Indeed, we observed a shaggy jet front near the He II surface. Moreover, the shaggy front was clearly seen even when the distance between the He II surface and the nozzle was more than 10 cm and the jet did not reach the surface. We attribute this observation to the onset of turbulent flow.

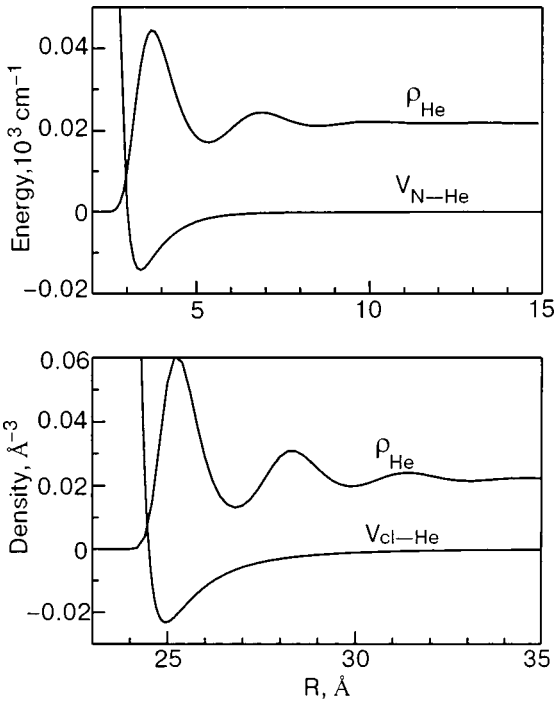

FIG. 5. The density profiles of liquid He near a ground state nitrogen atom (top panel) and a molecular nitrogen cluster with $n = 1000$ (bottom panel) are shown. The corresponding pair potentials are also shown.

Visual observations during preparation of the IHS showed that some small particles penetrate into the bulk He II directly from the jet. However, most of the impurities tend to float on the surface and stick to the walls of the quartz cell, grow on the walls, and finally sink to the bottom. In the following we assume that the penetration of an impurity into liquid He depends on the particle kinetic energy, which in the present case is determined by the velocity of the propagating jet. More precisely, the kinetic energy should exceed the solvation energy of the given species. This energy can be estimated using the classical bubble model:

$$E_b(R_b) = V_{\text{N–He}}(R_b) + 4\pi R_b^2 \gamma, \tag{1}$$

where R_b is the bubble radius and γ is the surface tension ($\gamma_{He} = 3.6\times10^{-4}$ J/m^2). Neglecting all dissipative processes and van der Waals attraction we can obtain a lower bound on the critical velocity required for a species to penetrate into the liquid:

$$v_{cr} > 4R_b(\pi\gamma/m)^{1/2}. \tag{2}$$

To estimate the radius of the cavity produced by a solvated cluster we need to evaluate the interaction potential of a cluster in liquid helium. Here we rely on the approximate N_2–He Lennard–Jones (LJ) potential with $\varepsilon = 18$ cm^{-1} and $R_0 = 3.6$ Å.[22] By assuming a perfect spherical cluster with $N = 1000$, a sharp edge, and $\rho = 1$ g/cm^3 $= 0.0217$ molecules/Å,^{3} we obtain a radius of 22.2 Å. The effective interaction potential can be formulated as

$$V_{\text{eff}}(r) = \int \rho_{N_2}(r') V_{LJ}(|r - r'|) d^3r'. \tag{3}$$

We computed the solvation of impurity N(^2D) and N(^4S) atoms and a $(N_2)_{1000}$ cluster in liquid helium using the density functional theory.[23] Figure 5 shows the results for a bare N atom and a $(N_2)_{1000}$ cluster in a spherical cavity. We can now estimate the critical velocities for a single atom ($R_b = 4$ Å) and a cluster ($R_b = 22.2$ Å). Substituting into Eq. (1) yields $v_N > 400$ m/s and $v_{cl} > 70$ m/s for the atom amd cluster, respectively. We emphasize that we neglected all other dissipative processes, such as ripplon and shock-wave production. Consequently, the real values should be even larger. On the other hand van der Waals binding should slightly favor solvation. Although our theoretical treatment is relatively crude, it clearly shows that under the experimental conditions seeding bare atoms into bulk helium by using a slowly propagating gas jet is not feasible.

5. SUMMARY

We have described optical emission studies on discharged nitrogen–helium gas mixtures under experimental conditions where the IHS are typically prepared. Analysis of the observed atomic (α group) and molecular Vegard–Kaplan transitions clearly indicates that these emissions originate from nitrogen clusters or matrix-like particles instead of isolated atoms or molecules. Cluster formation takes place already in the discharge zone, and it is most efficient at the point where the gas jet strikes the surface of He II and a well-defined crater is formed. The enhancement of emission intensity at the jet bottom is attributed to a change from laminar to turbulent jet flow.

The penetration of chemical species into liquid He II was discussed within the classical bubble model. The computed critical velocity, 400 m/s, needed for solvation of a bare N atom clearly exceeds the measured velocity of the jet, and only clusters consisting of at least 1000 molecules can have sufficient kinetic energy to overcome the barrier for stable cavity formation in bulk He II. From our experimental findings and model calculations we conclude that the formation of impurity clusters, i.e. the building blocks of IHS, occurs via extensive clustering in the jet and, most efficiently, in a crater. Coalescence of these nanosize clusters inside He II then leads to the formation of macroscopic condensates. Finally, the deposition of an impurity–helium jet into liquid helium through its surface could be utilized for efficient production of mass-selected neutral clusters and amorphous materials. Aerogel-like IHS produced from Ne, Ar, Kr, and N_2 impurities are one such example.

We wish to thank David M. Lee and Vladimir Khmelenko for fruitful discussions on impurity helium solids. This work was funded by the Academy of Finland.

*E-mail: Henrik.Kunttu@jyu.fi

[1] B. Gordon, L. P. Mezhov-Deglin, and O. F. Pugachev, JETP Lett. **19**, 63 (1974).
[2] E. B. Gordon, A. A. Pelmenev, O. F. Pugachev, and V. V. Khmelenko, JETP Lett. **37**, 282 (1983).
[3] E. B. Gordon, V. V. Khmelenko, A. A. Pelmenev, E. A. Popov, and O. F. Pugachev, Chem. Phys. Lett. **155**, 301 (1989).
[4] E. B. Gordon, V. V. Khmelenko, A. A. Pelmenev, E. A. Popov, O. F. Pugachev, and A. F. Shestakov, Chem. Phys. **170**, 411 (1993).
[5] R. E. Boltnev, E. B. Gordon, V. V. Khmelenko, I. N. Krushinskaya, M. V. Martynenko, A. A. Pelmenev, E. A. Popov, and A. F. Shestakov, Chem. Phys. **189**, 367 (1994).
[6] M. V. Martynenko, V. N. Novikov, A. A. Pelmenev, E. A. Popov, and E. V. Shilov, Bull. Moscow Univer. **3**, 53 (1996).
[7] R. E. Boltnev, I. N. Krushinskaya, M. V. Martynenko, A. A. Pelmenev, E. A. Popov, and V. V. Khmelenko, Fiz. Nizk. Temp. **23**, 753 (1997) [Low Temp. Phys. **23**, 567 (1997)].
[8] R. E. Boltnev, I. N. Krushinskaya, A. A. Pelmenev, D. Yu. Stolyarov, and V. V. Khmelenko, Chem. Phys. Lett. **305**, 217 (1999).
[9] E. A. Popov, A. A. Pelmenev, and E. B. Gordon, J. Low Temp. Phys. **119**, 367 (2000).
[10] L. P. Mezhov-Deglin and A. M. Kokotin, J. Low Temp. Phys. **119**, 385 (2000).
[11] S. I. Kiselev, V. V. Khmelenko, D. A. Geller, D. M. Lee, and J. R. Beamish, J. Low Temp. Phys. **26**, 874 (2000).
[12] S. I. Kiselev, V. V. Khmelenko, and D. M. Lee, Fiz. Nizk. Temp. **26**, 874 (2000) [Low Temp. Phys. **26**, 641 (2000)].
[13] S. I. Kiselev, V. V. Khmelenko, D. M. Lee, V. Kiryukhin, R. E. Boltnev, and E. B Gordon, Phys. Rev. B **65**, 24517 (2001).
[14] E. B. Gordon and A. F. Shestakov, Fiz. Nizk. Temp. **26**, 5 (2000) [Low Temp. Phys. **26**, (2000)].
[15] R. E. Miller, J. Chem. Phys. **43**, 1695 (1965).
[16] A. M. Provilov, L. G. Smirnova, and A. F. Vilesov, Chem. Phys. Lett. **109**, 343 (1984).
[17] A. Loftus and K. H. Krupenie, J. Phys. Chem. Ref. Data **6**, 113 (1977).
[18] F. Coletti and A. M. Bonnot, Chem. Phys. Lett. **45**, 580 (1977).
[19] B. C. Fawsett, At. Data Nucl. Data Tables **16**, 135 (1975).
[20] A. M. Bass and H. P. Broida, *Formation and Trapping of Free Radicals*, Academic Press, New York (1960).
[21] D. S. Tinti and G. W. Robinson, J. Chem. Phys. **49**, 3229 (1968).
[22] P. Habitz, K. T. Tang, and J. P. Toennies, Chem. Phys. Lett. **85**, 461 (1982).
[23] J. Eloranta, N. Schwentner, and V. A. Apkarian, J. Chem. Phys. **116**, 4039 (2002).
[24] O. Oehler, D. A. Smith, and K. Dressler, J. Chem. Phys. **66**, 2097 (1977).

This article was published in English in the original Russian journal. Reproduced here with stylistic changes by AIP.

Transformation of watergel samples in liquid helium

A. M. Kokotin and L. P. Mezhov-Deglin*

Institute of Solid State Physics of the Russian Academy of Sciences, 142432 Chernogolovka, Moscow Region, Russia
(Submitted November 27, 2002)
Fiz. Nizk. Temp. **29**, 690–694 (June 2003)

It is found that the shape and structure of watergel samples formed in the condensation of gaseous ^{4}He containing a water vapor impurity on the surface of superfluid He II cooled to 1.4 K depend substantially not only on the conditions of admission of the mixture but also on the construction of the experimental cell. The results of observations of the evolution of samples prepared in a wide cell, 29 mm in diameter, at a low rate of admission of the mixture are presented. © *2003 American Institute of Physics.* [DOI: 10.1063/1.1582331]

1. INTRODUCTION

In this report we briefly discuss the results of a study of the properties of samples of an impurity–helium water condensate (watergel) formed in superfluid He II in the condensation of a flow of gaseous ^{4}He containing a water vapor impurity on the surface of a liquid cooled to 1.4 K. The observations were made in two cells of different construction, the second cell having a 4 times greater surface area of the liquid He II on which the gas flow is condensed as compared with the first cell. It is found that increasing the diameter of the working cell leads to a qualitative change in the shape and structure of the samples formed in He II, i.e., the kinetics of the processes governing the formation of the sample of impurity–helium condensate in He II depends substantially on the diameter of the cell and the admission conditions, primarily on the pressure difference ΔP between the inside of the cell and the external Dewar, which determines the velocity of the gas flow.

A comparison of the results of the observations in the different cells indicates that for all the watergel samples studied the existence region of the condensate is limited to helium temperatures, and the decomposition of the sample is accompanied by the formation of a fine-grained powder of ice (apparently amorphous ice) at the bottom of the glass cell and individual grains on the walls. The total volume of the grains formed in the decomposition is approximately two orders of magnitude lower than the volume of the initial condensate, and consequently, the water content in the bulk of the impurity–helium condensate does not exceed 10^{20} molecules/cm^3. The temperature at which the decomposition is observed depends strongly on the pressure and properties of the surrounding medium: in the vapor above the superfluid liquid the samples extracted from the He II begin to decompose on heating above 1.8 K, whereas in the bulk of the liquid they can exist even in the normal fluid He I, and the temperature at which the active decomposition of the water condensate in He I is observed depends strongly on the pressure (we recall that, unlike the case of the superfluid, a temperature gradient of the order of 1 K/cm can exist along a column of normal fluid; this is observed, for example, when the pumping out of the vapor is stopped and warm ^{4}He is admitted to the Dewar from the supply line). At a vapor pressure above the liquid of $P \approx 200$ Torr, the samples begin to decompose at $T \approx 2.5$ K, and when the pressure in the Dewar is increased to 760 Torr the temperature of decomposition increases to 4 K.

As we pointed out in Refs. 1–3, a comparison of the results of our studies with the existing data in the literature (see, e.g., the papers by Khmelenko *et al.*[4] and Popov *et al.*[5] and the literature cited therein) suggests that in a dense vapor above the He II surface the individual H_2O molecules coalesce into clusters with an average diameter of the order of several nanometers, so that the impurity–helium condensate (watergel) formed in the He II consists of nanoclusters of water surrounded by a layer of solid helium (van der Waals complexes), forming the disperse phase of the watergel, while the superfluid He II filling the pores between clusters serves as the dispersion medium.

2. EXPERIMENTAL RESULTS AND DISCUSSION

Samples in the narrow cell

In the first series of experiments[1–3] a cylindrical glass cell with an inner diameter of 9 mm was used for the measurements. It was found that at a low rate of admission of the gaseous mixture ($\Delta P \sim 0.2–0.5$ Torr) a semitransparent condensate cloud formed beneath the surface of the superfluid He II cooled down to 1.4 K. The cloud slowly shifted downward, and in a time of the order of 10 min it was transformed into an immobile iceberg of oval shape, having an average diameter equal to the diameter of the cell and suspended in the volume of the liquid at the walls of the cell.

At a constant temperature the shape of the iceberg remained practically unchanged for several hours. However, when the temperature of the liquid was raised to 1.8 K, the apparent (visual) diameter of the iceberg decreased monotonically by $\sim 10–20\%$, the iceberg slid down the walls of the cell and got hung up on the thermometers mounted in the cell. As the temperature was raised further, the transition of the liquid from He II to He I was not accompanied by noticeable changes of the volume of the samples.

The ''dry'' icebergs extracted from the superfluid liquid

in an atmosphere of gaseous ^{4}He at a pressure close to the saturated vapor pressure above He II decomposed upon heating above 1.8 K. The decomposition was accompanied by the formation of a fine-grained powdered ice on the bottom of the cell and by the release of a rather large amount of gaseous helium. This explains why the icebergs jumped as the liquid level was decreased smoothly: The upper part of the immobile iceberg could protrude 1–2 mm above the He II surface before plunging down and again becoming suspended about 1 cm beneath the surface of the liquid.

By repeating the admission process several times, we could prepare several icebergs lying one on top of another in the bulk of the He II. When the He II level was lowered rapidly, the decomposition of the part of the uppermost iceberg protruding above the surface of the liquid could lead to a jumplike increase in the pressure in the closed cell to $\sim$20 Torr. As a result, the liquid together with the icebergs floating in the cell were forced through a small ($\sim$1 mm) opening in the bottom of the cell into the outer test tube filled with He II. The extrusion of icebergs $\sim$6 mm in diameter through a small opening led to decomposition of the condensate and to the formation of a fine powder that settled on the bottom of the test tube.

As we mentioned in the Introduction, in the bulk of the He I at a vapor pressure above the liquid of $P \approx 200$ Torr the icebergs apparently (visually) decomposed when the temperature of the surrounding liquid was raised to 2.5 K. The ^{4}He saturated vapor pressure at this temperature is around 78 Torr, so that the decomposition of the condensate is not accompanied by the formation of bubbles of gaseous ^{4}He, which can be observed when helium samples decompose in the vapor above He II in a closed cell partially filled with liquid and communicating with the outer test tube through a small opening in the floor of the cell. When the pressure above the He I column in the cell was increased to 760 Torr, the temperature of decomposition of the icebergs increased to 4 K.

The onset of low-frequency thermoacoustic oscillations in the working cell in the region of the transition of the liquid from the superfluid to the normal state was accompanied by oscillations of the He I level in the cell and, hence, by vertical oscillations of the iceberg, which is entrained by the normal liquid. From this we could estimate that the surface of the iceberg was not more than 3% higher than the density of the surround liquid; this number is in agreement with the above estimates of the water content in the impurity–helium condensate in respect to the volumes of the icebergs and the powdered ice formed when they decompose.

Finally, at a high rate of admission of the impurity ($\Delta P \geqslant 1$ Torr) a semitransparent layer of condensate, which is wetted well by the superfluid, began to grow along the He II–vapor interface from the walls of the cell towards the center. If the admission process was continued, then after the formation of a solid layer of condensate on the surface of the liquid the pressure in the cell increased in a jump by more than an order of magnitude, and the entire contents of the cell (the condensate and the He II) were forced out of the volume of the cell into the outer test tube through the opening in the floor of the cell. Then the pressure in the cell fell, the superfluid He II from the test tube again filled the cell, and a layer of powdered ice collected on the bottom of the test tube. In a number of cases we were able to observe individual fragments of unmelted condensate, of the order of 1–2 mm in size, which floated beneath the surface and plunged into the interior of the liquid as the He II level in the test tube was decreased smoothly.

Samples in the wide cell

A discussion of the properties of watergel with V. V. Nesvizhevskii, a specialist in cold neutron physics, led to the idea of trying to use He II-impregnated porous nanocluster systems cooled to a temperature of $\sim$1 mK for the accumulation and storage of cold neutrons.[6] This, of course, requires large samples with a volume of the order of 10^3 cm^3, prepared from substances with practically no neutron absorptivity (heavy water, deuterium, oxygen, etc.).

As a first step toward implementing this idea, we decided to explore the influence of the size of the cell on the properties of water condensate samples. The samples were prepared in a thin-walled glass test tube with an inner diameter of 2.9 cm and a height of 10 cm, with a flat Teflon washer (substrate) 2.8 cm in diameter placed at the bottom of it. Two carbon resistance thermometers were mounted at the center of the washer and at a distance $\sim$1 cm above its surface to permit monitoring of the temperature distribution in the working cell. A flow of gaseous ^{4}He containing a water vapor impurity entered along a glass tube with an inner diameter of 1.9 cm, the lower end of which was placed a distance of 2–4 cm above the surface of the substrate. The scheme used for preparing the mixture remained as before: gaseous helium at room temperature was passed through a layer of water, and then the gas flow containing the water vapor impurity was directed through a coupling sleeve with a cutoff valve and into a glass tube.

Observations showed that the optimal situation for our purposes was one in which the level of superfluid He II in the working cell during the admission of the mixture was $\sim$1 cm above the edge of the admission tube, and the difference of the vapor pressures in the tube and outer Dewar was $\Delta P \sim 0.1$–0.3 Torr. During the preparation of the samples the He II temperature was held constant at 1.4 K to within hundredths of a degree. Changing the admission conditions had a noticeable effect on the shape and structure of the samples that formed. In the majority of cases, as soon as the valve for admission of the mixture was opened, a sample resembling a snow pile or, more precisely, a pillar began to grow on the surface of the Teflon washer under the tube; this sample was made up of materials falling from the end of the tube in the form of flakes of the order of 1 mm in size and vibrating elastic filaments up to 1 cm long. The diameter of the base of the pillar was close to the diameter of the tube, while the height was determined by the admission time (the upper end of the pillar could enter the tube). In addition to the flakes and filaments, we have also observed the formation in a tube of semitransparent ''clouds'' of condensate with a characteristic size close to the diameter of the tube and which formed beneath the surface of the liquid and moved slowly down along the walls of the tube (see frame 1 in Fig. 1; the arrow indicates the He II level). For clarity we specifically chose the rarer case in which an oval cloud is

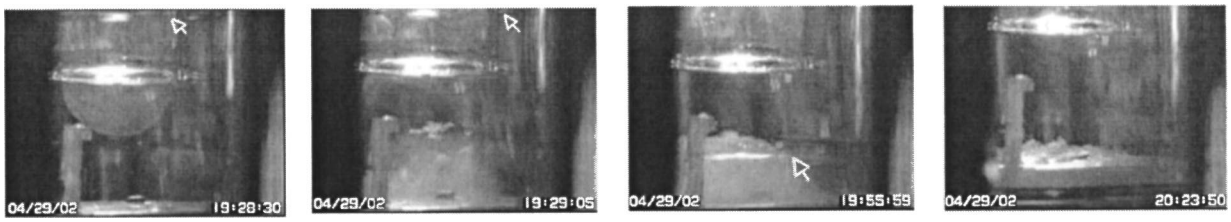

FIG. 1. Formation and evolution of a watergel sample on a Teflon substrate in the wide cell. The arrows in the first three frames indicate the level of superfluid He II in the cell. The temperature of the liquid was maintained at a constant $T \approx 1.40$ K. The frames go from left to right: *1*—cloud of watergel at the exit from the admission tube; *2*—a sample formed when the cloud falls onto the substrate; *3*—evolution of the shape of the sample as the He II level is lowered; *4*—decomposition of the impurity–helium water condensate in helium vapor at a substrate temperature of 2.18 K, a temperature at the level of the upper thermometer of 2.6 K, and a temperature of the He II at the bottom of the working cell of 1.4 K, i.e., the vapor pressure in the cell was $P \approx 2.16$ Torr.

formed in the tube at the start of the admission process and then leaves the tube (frame 1) and slowly sinks to the substrate (frame 2), since in a photograph it would be rather hard to distinguish the oval iceberg from the background of the pile formed by the flakes. The thermometer placed at the center of the substrate and the thermometer mounted on a post above the surface of the Teflon washer are clearly visible in the photographs. The date and the real time of observation are indicated in the left- and right-hand corners, respectively.

If the cloud or, more precisely, oval iceberg at the exit from the tube fell onto the pile of ice flakes, it made a depression in the surface of the pile (as when a dense snowball is dropped on fallen snow), i.e., the mechanical properties and density of the pile and iceberg are noticeably different. Heating the liquid to a temperature $T > 1.8$ K led to partial homogenization of such samples. However, in all cases the diameter of the sample was close to the diameter of the tube, so that we were unable to prepare a sample that uniformly filled the entire surface of the substrate, as we would have liked.

The evolution of the shape of the sample as the He II level was lowered smoothly at a constant temperature $T \approx 1.40$ K is illustrated by frame 3. We see that in the vapor above the liquid the protruding part of the sample gradually decomposed, so that the height of the pillar gradually decreased. It is seen that grains of amorphous ice appeared on the surface and remained even after the complete decomposition of the condensate (frame 4) and the raising of the temperature above 4.2 K. The temperature of the superfluid He II in this experiment was held constant, but on the last frame the liquid level was almost 1 cm below the Teflon washer, so that the temperature registered by the thermometer at the center of the substrate was 2.18 K, while the temperature at the level of the second thermometer was 2.6 K.

At high rates of admission ($\Delta P > 1$ Torr) a plane layer of condensate forms at the He II–vapor interface, growing from the wall towards the center of the tube. As in the narrow cell, the formation of a continuous layer at the phase boundary led to a jumplike growth of the pressure in the tube and to destruction of the condensate layer.

In two trial experiments we replaced the water (a highly polar liquid that tends to form clusters in the saturated vapor even at room temperatures) by ethyl alcohol (a slightly polar liquid that solidifies at the saturated vapor pressure at a considerably lower temperature). As in the experiments with the narrow cell, the transition from water to alcohol did not lead to a qualitative change in the properties of the impurity–helium condensate, i.e., the preparation of a sample with characteristic dimensions of $10 \times 10 \times 10$ cm will require further refinement of the sample preparation scheme. It is possible that in order to obtain samples of the necessary shape, the condensate will have to be pressed into the working cell, as was done in Ref. 4. A series of experiments with deuterium samples in the wide cell is planned for the near future.

CONCLUSION

Research on the properties of impurity–helium condensates, i.e., novel nanocluster systems existing only at low temperatures, has expanded markedly in recent years. Possible uses for these materials in modern science and technology are being explored, e.g., for studying the kinetics of reactions between free radicals at low temperatures, for preparing low-temperature fuel elements containing free radicals on the basis of helium–impurity condensates,[4] for accumulating and storing ultracold neutrons,[6] and for obtaining suspended clouds of ultradisperse metallic powder by the evaporation of a metal suspension in gaseous ^{4}He at helium temperatures (such clouds are used for visualizing the distribution of Abrikosov vortices in superconductors).

Our research experience has shown that the structure and properties of impurity–helium condensate samples depend substantially on the preparation technique and the properties of the surrounding medium. For this reason it would be extremely interesting to conduct experiments on the preparation and properties of such condensates in a microgravity environment, where the structure of levitating and superfluid samples will be determined primarily by the features of the interaction between van der Waals complexes, which form neutral nanoclusters coated with a layer of solidified helium.

These studies were done with the support of the Russian Foundation for Basic Research, the Moscow District Government (Grant 01-02-97037), and the Ministry of Industry and Science of the Russian Federation.

The authors thank their laboratory colleagues G. V. Kolmakov, A. A. Levchenko, V. B. Efimov, A. V. Lokhov, V. N. Khlopinskii, and M. Yu. Brazhnikov for their interest and assistance in this study and V. V. Nesvizhevsky for helpful discussions.

*E-mail: mezhov@issp.ac.ru

[1] L. P. Mezhov-Deglin and A. M. Kokotin, JETP Lett. **70**, 756 (1999).
[2] A. M. Kokotin and L. P. Mezhov-Deglin, Fiz. Nizk. Temp. **28**, 235 (2002) [Low Temp. Phys. **28**, 165 (2002)].
[3] L. P. Mezhov-Deglin and A. M. Kokotin, Prib. Tekh. Éksp., No. 2, 159 (2001).
[4] S. I. Kiselev, V. V. Khmelenko, and D. M. Lee, Fiz. Nizk. Temp. **29**, 678 (2003) [*sic*].
[5] E. A. Popov, J. Floranta, J. Ahokas, and H. Kunttu, Fiz. Nizk. Temp. **29**, 684 (2003) [*sic*].
[6] V. V. Nesvizhevsky and L. P. Mezhov-Deglin, ''Thermalization of neutrons in gels of ultracold particles,'' in *Book of Abstracts, Third Chernogolovka Workshop on Low Temperature Physics in Microgravity Environment CWS-2002, Chernogolovka, Russia (2002)*, p. 40.

Translated by Steve Torstveit

EPR spectra and rotation of CH_3, CH_2D, CHD_2, and CD_3 radicals in solid H_2

Yu. A. Dmitriev* and R. A. Zhitnikov

A. F. Ioffe Physicotechnical Institute, 26 Politekhnicheskaya Str., St. Petersburg 194021, Russia
(Submitted December 19, 2002)
Fiz. Nizk. Temp. **29**, 695–698 (June 2003)

The EPR spectra of CH_3, CH_2D, CHD_2, and CD_3 radicals in a H_2 matrix have been observed in the temperature range 1.6–4.2 K. The radicals were obtained by condensation of two gas flows on a cold substrate: deuterium mixed with 2 mol % methane passed through a discharge and pure hydrogen bypassing the discharge. The CD_3 and CHD_2 spectra were found to be a superposition of two spectra: high- and low-temperature. A transformation of the shape of the CD_3 and CHD_2 spectra with decreasing sample temperature was observed. This was attributed to a change in the populations of the lowest rotational states of the radicals. Compared to the known results for deuterated methyl radicals in Ar, the present observations suggest the existence of a barrier hindering the rotation of radicals in solid H_2. © *2003 American Institute of Physics.*
[DOI: 10.1063/1.1582334]

1. INTRODUCTION

The methyl radical (CH_3) isolated in various matrices has been extensively studied by EPR since the late 1950s.[1–6] At low temperatures near 4.2 K the EPR spectrum of the radical is well-known to consist of four lines with equal intensity 1:1:1:1 instead of with the binomial intensity distribution 1:3:3:1. This effect was first explained by McConnel.[7] The equal intensity of four lines was attributed to the symmetry requirements of the wave functions. According to McConnel and Freed[8] three protons move around a C_3 molecular axis in the matrix in a three-fold potential well with a finite barrier height. The lowest torsional rotational energy level is split into two levels: a lower level with symmtery A and a doubly degenerate upper level with symmetry E. At sufficiently low temperatures only the lowest spin-rotational A state with four symmetric nondegenerate nuclear spin functions is populated. Thus the EPR spectrum is a 1:1:1:1 quartet. The rotation is considered to be a tunneling transition and may occur even at liquid-helium temperatures. In such tunneling rotation not only the A state but also the E nuclear spin states appear when the next higher rotational levels are considered. The EPR transitions corresponding to these states were first observed in Ref. 5 for an isolated methyl radical. In contrast to CH_3 there are only a few studies on deuterated methyl radicals (CD_3, CH_2D, and CHD_2). A spectrum of seven components with a ''nonbinomial'' distribution has been predicted for the CD_3 radical[9] at low enough temperatures. A septet has been observed in a CD_4 matrix[10] at 4.2 K and solid Ar at 13 K.[4] Even though these experimental results are consistent with the above-mentioned theoretical scheme, a different configuration has been observed in Ref. 5 for CD_3 in Ar at 4.2 K showing a strong singlet superimposed on a weak septet. The authors explained their results with a new model based on a free, three-dimensional, quantum rotor with no hindering barrier present. They pointed out that when the Pauli principle is applied the electronic state has to be included in order to obtain the correct overall exchange symmetry for bosons.

The present study is concerned with deuterated methyl radicals in a different matrix in order to clarify whether the effect found in[5] occurs in other matrices and to obtain new experimental results which would be helpful in verifying the free rotation model.[5]

2. RESULTS AND DISCUSSION

The solid samples were obtained by gas condensation on a thin-walled bottom of a quartz finger filled with liquid helium. Located at the center of the microwave cavity in an EPR spectrometer, the bottom is used as a substrate. Both the rf gas discharge (channel A) and the matrix gas flowing through a separate inlet tube to bypass the gas discharge (channel B) can be cooled down to liquid-nitrogen temperature. The products of the gas discharge are fed, without intermediate feed tubes, directly onto the substrate in vacuum to prevent their decomposition on the tube walls. Thus the sample is obtained directly in the cavity of the EPR spectrometer, allowing EPR observation of the sample during condensation and making it possible to study short-lived centers (e.g. free radicals) due to the gas discharge products. The experimental setup has been described in previous papers.[11]

In the present experiments molecular deuterium (D_2) mixed with 2 mol % methane (CH_4) was prepared in a glass vessel and passed through the channel A with the discharge on. Simultaneously, H_2 was fed through the channel B. The latter flow was much larger than the discharge flow, thereby providing an admixture of D_2 as small as about 1:30 in a H_2 matrix. A pulsed discharge was used with an off-duty factor of 10. The substrate temperature during deposition was 4.2 K. Figure 1 shows the EPR spectrum of a sample of solid H_2 with trapped radicals. The experimental spectrum shows seven strong lines due to the CD_3 radical and weak lines due to CH_3, CH_2D, and CHD_2 radicals. High-field lines with a higher gain are superimposed. The outermost peak is a high-field component of the CH_3 spectrum which is composed of four lines of equal intensity and has been studied in a H_2 matrix.[6] Three equally spaced lines are present in the CH_2D

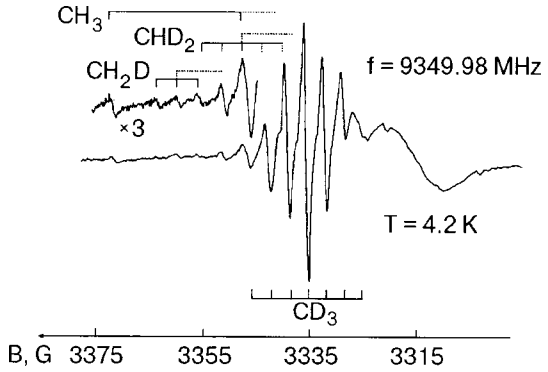

FIG. 1. The EPR spectrum of a solid H_2 sample with trapped methyl radicals. The substrate temperature during depostion was $T_{sub}=4.2$ K.

spectrum. These are a triplet due to the hyperfine (HF) splittings of two hydrogen nuclei, a major triplet, and one minor deuterium triplet. One peak on the left-hand side of the high-gain spectrum is a purely CHD_2 component, while its right-hand neighbor is composed of the outermost left-hand CD_3 component, a CHD_2 line, and a CH_3 transition at $m_F=-1/2$. At high enough temperatures the CHD_2 spectrum is a double quintet. Thus the spectrum in Fig. 2 is a superposition of several spectra.

We have found that the seven CD_3 lines have the same linewidth $\Delta H=0.86(6)$ G with hf splitting $\delta H=3.59$ G. Except for the central line, the relative intensity ratio 1:3:6.5:12:6.5:3:1 is close to the ''binomial'' intensity distribution 1:3:6:7:6:3:1. In Ref. 5 it was observed that at temperatures above 10 K the intensity distribution for CD_3 in Ar is almost ''binomial'' and is due to not only the $J=0$ population but also higher rotational levels. When the temperature was lowered to 4.1 K the central line increased while the other six lines decreased rapidly in intensity. As a result, the intensity of the central peak relative to its neighbor reached 15. It was shown that the spectrum corresponding to the $J=0$ rotational level is a singlet. We can conclude from our study that the spectrum of CD_3 in H_2 at 4.2 K is a superposition of a high-temperature nearly ''binomial'' spectrum and a low-temperature singlet. The above-mentioned CH_3 spectrum with four equal lines corresponds to $J=0$ and is therefore a low-temperature spectrum. Such a difference between the CH_3 and CD_3 spectra is not surprising because the energy gap between the $J=0$ and $J=1$ rotational states for free CH_3 is twice the CD_3 gap. Therefore the $J=1$ state of the CD_3 radical is not populated at low temperatures close to 4 K. We also found that the CHD_2 spectrum is actually a superposition of high- and low-temperature spectra. This will become clear below when we describe temperature effects. We have not been able to draw any conclusions about the CH_2D spectrum appearance because the central CH_2D triplet could not be seen because of the strong CD_3 transitions which are superimposed on it. According to Fig. 1 the amount of CD_3 is well above that of the other radicals. We estimated the yields of the deuterated methyl radicals with respect to the CH_3 yield. These were found to be 35:1 for CD_3, 2:1 for CHD_2, and 1.3:1 for CH_2D. Therefore we conclude that methane in our discharge was almost completely deuterated through the intermediate products CH_2D and CHD_2 to the final product CD_4. The reactions of the

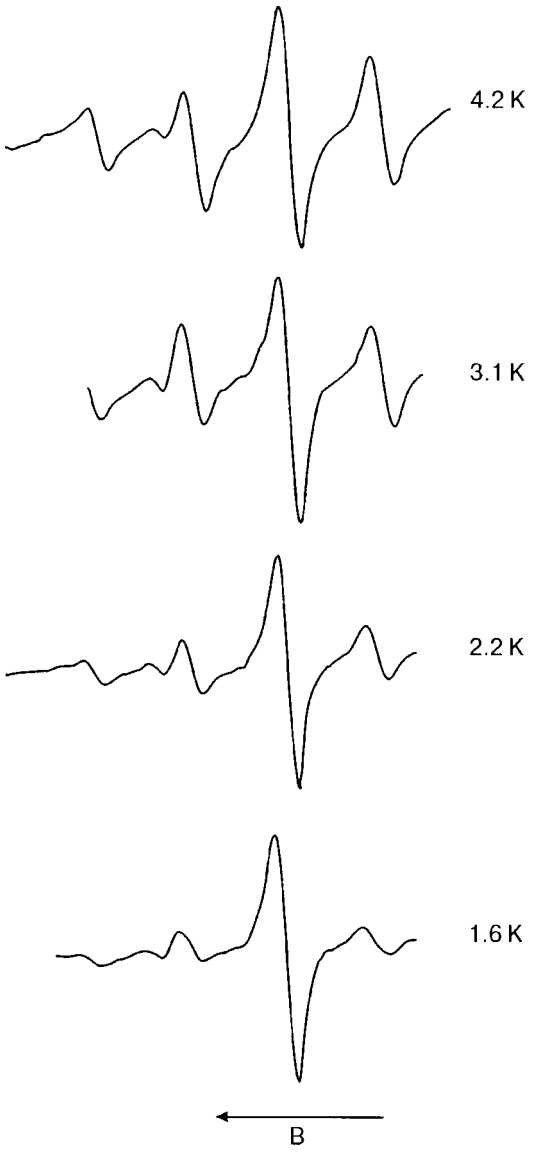

FIG. 2. The central part of the temperature-dependent EPR spectra of a CD_3 radical in a H_2 matrix. The substrate temperature during deposition was $T_{sub}=4.2$ K.

methyl isotopomers (CH_3, CH_2D, and CHD_2) with excess deuterium atoms have been studied previously by discharge flow/mass spectrometry.[12]

Figure 2 shows the central part of the CD_3 spectrum obtained at several temperatures. The central peak with $m_F=0$ clearly increases rapidly with decreasing temperature with respect to the neighboring transitions. We plotted saturation curves, i.e. the intensities of the central and neighboring lines versus the microwave power, and we found that at 4.2 K and 1.6 K the high-temperature spectrum shows no saturation in the experimental power range, whereas the central peak starts to saturate at 4.2 K, reaching prominent saturation at 1.6 K. Such a difference in the saturation behavior between the lines is further evidence that the central peak is actually a superposition of transitions due to different states.

Figure 3 shows the change in the shape of the high-field quintet of the CHD_2 spectrum. The outermost left-hand transition ($m_F(D)=-2$) of CHD_2 is superimposed on the outermost right-hand line of the CH_2D high-field triplet. Here D

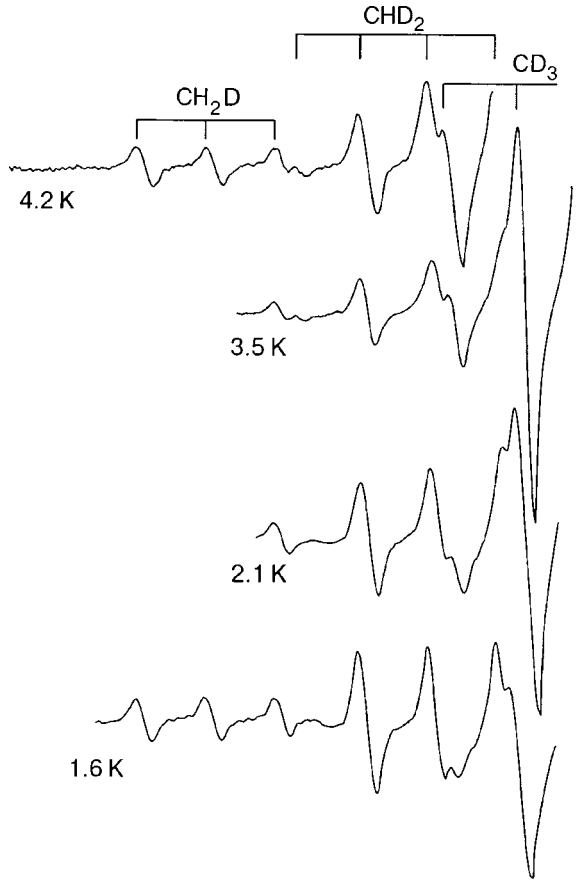

FIG. 3. Temperature-dependent high-field quintet of the spectrum of CHD_2 matrix-isolated in solid H_2. The substrate temperature during deposition was $T_{sub}=4.2$ K.

denotes the splitting due to the deuterium nuclei. The transition of CHD_2 at $m_F(D)=0$ (third from the left) is superimposed on the high-field ($m_F(D)=-3$) CD_3 line. The next two CHD_2 peaks to the right are not seen aganst the strong CD_3 components. In the high-temperature CHD_2 spectrum the quintet components exhibit a ''binomial'' intensity ratio 1:2:3:2:1. It has been found previously[5] that in an argon matrix the quintet transforms into a triplet as the temperature decreases from 10 K to 4.2 K. In our experiments the CHD_2 spectrum in H_2 was still a double quintet at 4.2 K, but the intensity distribution deviated significantly from a binomial distribution. This was evident from the fact that the ratio of the amplitude of the $m_F(D)=-1$ line to that of the outermost $m_F(D)=-2$ line was well above 2. According to Fig. 3 the CHD_2 transition at $m_F(D)=-2$ disappears, while the $m_F(D)=1$ line becomes more pronounced against the decreased high-temperature CD_3 line. Thus the H_2 matrix as well as the CHD_2 quintet changes to a triplet as temperature decreases. This change from a high- to a low-temperature spectrum for CHD_2 corresponds very well to a CD_3 radical in H_2.

3. CONCLUSIONS

The present results not only verify the effect of temperature on the shape of the CD_3 and CHD_2 spectra first observed in Ar.[5] In addition, comparing the temperature ranges for these spectral transformations 10–4.2 K and 4.2–1.6 K in Ar and H_2 yields new information. Since the spectrum changes which we discuss are due mainly to changes in the population of the lowest states $J=0$ and $J=1$ of the trapped radicals, the difference in the range suggests that the energy interval between the above rotational states is larger in Ar than in H_2. In turn, the decrease of this interval for a trapped molecule as compared with a free molecule is due to hindering of the rotation of the molecule in the matrix. Since the CD_3-H_2 interaction energy is lower than that of CD_3-Ar, the rotation of CD_3 in H_2 should be freer, i.e. the effect on the rotation of the radical should be weaker in Ar. Indeed, solid H_2 is well known to have a smaller effect on the parameters of various radicals than many other matrices. However, our result suggests that the phonon–rotation coupling for CHD_2 and CD_3 molecules in H_2 is surprisingly large. This unexpected conclusion requires further theoretical and experimental study.

*E-mail: dmitriev.mares@pop.ioffe.rssi.ru

[1] R. L. Morehouse, J. J. Christiansen, and W. Gordy, J. Chem. Phys. **45**, 1751 (1966).
[2] G. S. Jackel and W. Gordy, Phys. Rev. **176**, 443 (1968).
[3] C. K. Jen, S. N. Foner, E. L. Cochran, and V. A. Bowers, Phys. Rev. **112**, 1169 (1958).
[4] E. Ya. Misochko, V. A. Benderskii, A. U. Goldschleger, A. V. Akimov, A. V. Benderskii, and C. A. Wight, J. Chem. Phys. **106**, 3146 (1997).
[5] T. Yamada, K. Komaguchi, M. Shiotani, N. P. Benetis, and A. R. Sornes, J. Phys. Chemical A **103**, 4823 (1999).
[6] Yu. A. Dmitriev and R. A. Zhitnikov, J. Low Temp. Phys. **122**, 163 (2001).
[7] H. M. McConnel, J. Chem. Phys. **29**, 1422 (1958).
[8] J. H. Freed, J. Chem. Phys. **43**, 1710 (1965).
[9] *Formation and Trapping of Free Radicals*, edited by A. M. Bass and H. P. Broida, Academic Press, New York (1960).
[10] K. Toriyama, M. Iwasaki, and K. Nunome, J. Chem. Phys. **71**, 1698 (1979).
[11] R. A. Zhitnikov and Yu. A. Dmitriev, Astron. Astrophys. **386**, 129 (2002).
[12] P. W. Seakins, S. H. Robertson, M. J. Pilling, D. M. Wardlaw, F. L. Nesbitt, R. P. Thorn, W. A. Payne, and L. J. Stief, J. Phys. Chem. **101**, 9974 (1997).

This article was published in English in the original Russian journal. Reproduced here with stylistic changes by AIP.

Quench deposited $Kr-H_2$ and $Ar-H_2$ mixtures: in quest of impurity–hydrogen gels

M. A. Strzhemechny, N. N. Galtsov,* and A. I. Prokhvatilov

B. Verkin Institute for Low Temperature Physics and Engineering of the National Academy of Sciences of Ukraine, 47 Lenin Ave., Kharkov 61103, Ukraine
(Submitted December 19, 2002)
Fiz. Nizk. Temp. **29**, 699–705 (June 2003)

The structure and morphology of low-temperature quench condensed binary alloys of hydrogen with argon and krypton were studied by powder x-ray diffraction. The nominal hydrogen fraction c in both systems was varied from 0 to 50%; the condensation was performed at 5–6 K; both as-prepared and annealed samples were examined by x-ray diffraction. Few reflections (and often only one) can be unambiguously detected for the as-grown alloy samples. In $Kr-H_2$ condensates with $c<10\%$ the x-ray patterns show fine-grain krypton-rich crystallites with a rather high actual hydrogen content as estimated from Vegard's law. For high nominal hydrogen fractions ($c\geqslant 10\%$) no reflections attributable to the krypton lattice were recorded and the incoherent background showed no characteristic swelling around the position of the (111) reflection from pure Kr; instead, the reflections from a hydrogen-rich hcp phase were distinct. As the temperature was steadily raised the hydrogen reflections disappeared first. Then at a certain temperature the samples underwent an abrupt transformation as a result of which heat was released and larger x-ray detectable textured krypton crystallites were formed. In the as-grown $Ar-H_2$ samples only the (111) reflections from the argon-rich phase were recorded. Warmup led to the same consequences, i.e. hydrogen effusion followed by recrystallization. In both systems the recrystallization onset temperature depends substantially on the nominal hydrogen fraction in the gas. The shift of the lattice parameter in the as-grown argon-based phases suggests strong suppression of the quantum nature of hydrogen in the argon lattice environment. The experimental findings viewed as a whole can be construed as evidence of the fact that quench-condensed hydrogen-containing alloys morphologically resemble helium-impurity solids (gels) whose structure and morphology are currently being studied at Cornell University. [DOI: 10.1063/1.1582335]

1. INTRODUCTION

Binary systems such as mixtures of hydrogen and rare gas (RG) species are interesting for solid state physics because the relative simplicity of the basic interactions involved permits an unambiguous interpretation of the phenomena observed. Because of the large difference in the molecular parameters σ and ε between hydrogen and the heavier rare gas atoms one can hardly expect an appreciable equilibrium low-pressure solubility in the solid of these mixtures at both ends of the fraction range. Only the appplication of a considerable pressure makes some of these mixtures form stoichiometric compounds like $Ar(H_2)_2$ (Ref. 1) or a series of such compounds in hydrogen–methane mixtures.[2] There are other high-pressure hydrogen-based compounds (cf. Schouten's review.[3]) The low mutual miscibility of hydrogen with the heavier rare gas species might be helpful in producing hydrogen-based self-sustained condensed media. This idea with ^{4}He as the binding material was first suggested[4] and subsequently implemented[5] in Chernogolovka, Russia. The preparation technique consists in blowing a jet of the species chosen into superfluid ^{4}He. The pivotal factor is the extremely high thermal conductivity of superfluid helium, which enables rapid dissipation of the energy accompanying the particles in the jet. These helium–impurity solids with different impurities were extensively studied later by Gordon's group (for references see Ref. 6). Subsequently, studies at Cornell[7–9] led to the conclusion that these materials are highly porous amorphous media made up of particles or small clusters surrounded by layers of helium, which could be considered to be solidified because of the external forces due to the impurity–helium interaction. Since hydrogen cannot guarantee heat removal as in superfluid ^{4}He, in order to get a hydrogen–impurity solid it seems worthwhile to try quench condensation of the corresponding mixture at high deposition rates. So, one of our main objectives was to look for possible highly amorphized states in both systems. On the basis of the known mismatch of the molecular parameters between the heavier rare gas atoms and hydrogen we expected to obtain condensates whose properties would resemble those of impurity–helium solids (gels).

Apart from this main objective we wanted to elucidate the structural consequences of admixing heavy RG species to hydrogen and quench condensing the mixture. This is important for several reasons. It was of greatest interest to determine the equilibrium miscibility edge on the RG side, which is important for low-temperature thermodynamic investigations of dilutions of various molecular species in solid hydrogen (cf. the overview by Manzhelii *et al.*[10]).

In the present paper we report the results of powder x-ray studies of the binary systems $Ar-H_2$ and $Kr-H_2$ for concentrations rich in the rare gas elements. Special attention was paid to the structure and phase state of the samples and

the effect of the deposition rate of the gas mixtures. These results are analyzed in the light of possible hydrogen–impurity solids (gels).

2. EXPERIMENTAL

The structural studies were performed with a DRON-3M x-ray diffractometer equipped with a liquid-helium cryostat. FeK_α radiation was used. Diffractometer control and data acquisition and processing were performed from a PC. Samples were produced by condensing gas mixtures with known composition directly in the solid phase onto a flat copper substrate at temperature 5 or 6 K. This procedure allowed us to suppress hydrogen's natural tendency to grow into large single crystals and instead to obtain 0.1 mm thick polycrystal samples with coherent scattering area of the order of $10^{-4}-10^{-5}$ cm in size. The H_2, Ar, and Kr gases used were 99.99% pure. The fraction of normal hydrogen in the Ar–H_2 and Kr–H_2 gas mixtures was varied from 1 to 50%. The relative error in the composition of the binary gas mixtures did not exceed 5% with respect to the amount of hydrogen introduced.

The sample preparation procedures employed in this investigation was based on our experience in working with solid hydrogen[11] and hydrogen doped with neon[12] and some other simple molecules.[13] The condensate was grown in two deposition regimes differing by the amount of material in a single gas deposition burst. In one regime every deposition step resulted in a 3 to 4 torr pressure drop inside the gas mixing chamber; in the other regime the pressure drop was typically twice as large. In order to avoid selective freeze-out of the less volatile rare gas component from the gas mixture flowing from the chamber to the substrate the temperature of the filling duct was maintained at a sufficiently high level close to room temperature. To this end the thin-walled stainless steel filling capillary was connected to the cooling chamber through a teflon capillary.

The samples were examined by x-ray powder diffraction immediately after deposition and then after stepped warmup (every 5 or 10 K) to 50 K. The temperature was stabilized to within ± 0.05 K at every working point. Because the number of recordable reflections was small and individual reflections from different phases overlapped with one another the lattice parameter was determined with an error that was appreciably larger than is typical for x-ray studies of pure cryocrystals, but the error did not exceed $\pm 0.05\%$.

3. RESULTS AND DISCUSSION

One of the main goals of this work was to determine the structural state of as-grown samples and, when possible, to evaluate the limiting solubility of hydrogen in the two rare gas solids under the condensation conditions specified above. The structure of freshly grown samples differed substantially for different nominal hydrogen contents c in the gas mixture.

A. Krypton

In experiments with elevated hydrogen content ($c = 10-40\%$) we obtained patterns with rather unexpected properties. First, not all as-grown samples deposited on a 5 K substrate produced reflections characteristic of a krypton lattice. Second, no smeared maxima (diffuse halo), which are typical of systems with well-formed short-range order, were present in the incoherent background. Third, even though the hydrogen fraction in the mixture was lower, we saw distinct reflections from a crystal phase that could be attributed to a hydrogen crystal, possibly with nonzero krypton content (Fig. 1). The substantial qualitative changes in the diffraction patterns between 4 and 10% allowed us to infer that the samples with 10% and higher nominal hydrogen content have an unusual morphology. To all appearances the krypton-rich phase in those as-grown samples was in an amorphous or/and highly dispersed state, while part of the hydrogen fraction with a relatively low krypton content was crystallized into a fine-grained textured phase, which was recordable by x-rays. The hydrogen-rich phase observed within the range of 10–40% nominal concentrations was nonstrained and structurally perfect; the (002) reflection had a small width of 0.1–0.15°. Variations of the deposition rate did not affect the sample's parameters. By applying the straightforward Vegard law, i.e. using the cube root of the molar volume of pure krypton and hydrogen, we estimated the actual krypton concentration x_{Kr} in hcp H_2 to be around 4%. It should be added here that the angular position of the mixed crystals depends not only on the impurity concentration but also on the stacking-fault density α, which could be quite high, especially in freshly grown samples. It is quite safe to evaluate the impurity concentration using the (002) reflection of a hcp structure, because it is the position of this reflection that is unaffected by stacking faults.[14] The fcc (111) reflection, which we have at our disposal for the Kr-rich phases shifts to higher angles owing to stacking faults.[14] The (111) reflection from pure quench condensed krypton in Fig. 1 is appreciably shifted to larger angles. Attributing this shift to stacking faults we find[14] that α corresponds to on average 11 ± 3 planes beween faults, which is a very high density but fairly consistent with the reflection width and intensity. The strong effect of stacking faults on the position of the (111) reflection makes the estimate of the actual hydrogen concentration uncertain, and it tends to be underestimated because both factors (impurities and faults) shift the (111) line to higher angles.

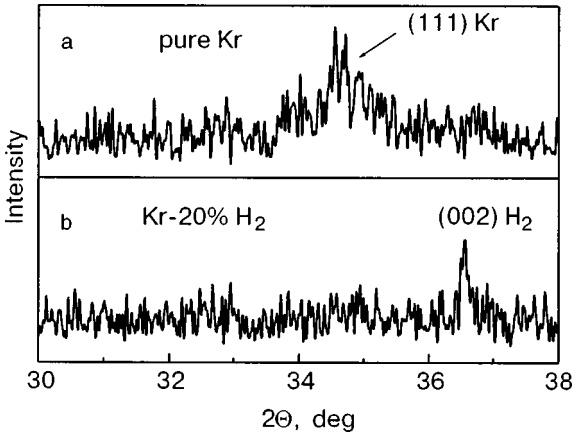

FIG. 1. Fragment of x-ray powder patterns from pure krypton (a) and Kr–20%H_2 (b), both obtained by quench deposition from gas onto a flat copper substrate at $T = 5$ K. The arrows indicate reflections from the respective crystal planes. Note the absence of Kr reflections from the hydrogen-doped as-grown sample.

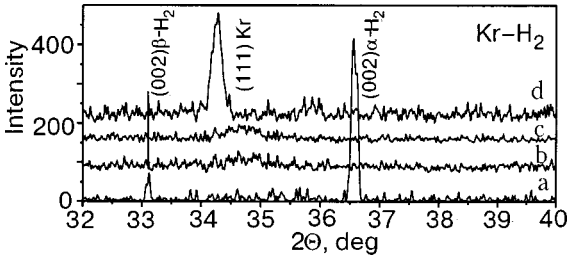

FIG. 2. Effect of warmup on the structural state of a Kr−30%H_2 alloy, quench deposited at $T=5$ K. All patterns were recorded without a filter to see the evolution of the sample more clearly. Pattern (a) is from a sample freshly quench deposited at 5 K; only the (002) reflection from the basal plane of the hexagonal hydrogen-rich lattice can be seen; a K_β reflection from hydrogen is seen at smaller angles. The patterns (b) through (d) correspond to annealing temperatures 35, 43, and 48 K, respectively.

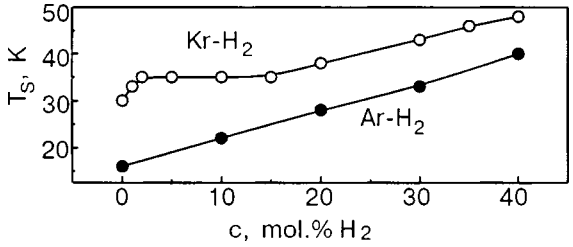

FIG. 3. Annealing onset temperatures of Kr–H_2 (○) and Ar–H_2 (●) alloys as a function of the nominal hydrogen fraction in the source gas mixture.

There is another consideration that should be taken into account when Vegard's law is used to estimate the actual H_2 content in Kr. As will be shown below, when H_2 dissolves in an argon lattice the quantum nature of the hydrogen molecules is strongly suppressed. Although we do not have direct unambiguous evidence for Kr-based mixtures, it seems quite reasonable to assume that this consideration is also applicable for the Kr matrix. If the zero-point motion of the hydrogen molecules is ignored, then the lattice parameter appearing in Vegard's law should be calculated not from the actual molar content of H_2 but rather from the value of σ[3,15] where $\sigma=2.96$ Å is the van der Waals radius of the hydrogen molecule.

When samples with a high nominal hydrogen content were warmed up to 14 K or higher, the reflection from the hydrogen phase disappeared (compare *a* and *b* in Fig. 2). When the temperature was increased to 30 K, a very broad and weak reflection identified as the (111) reflection from the krypton-rich phase appeared (curve *c*). As the temperature was raised still higher, the reflection grew in intensity and became narrower (curve *d*). It can be surmised that hydrogen effusion from krypton started within this temperature range. At a certain temperature T_s abrupt annealing and (re)crystallization occurred, which was manifested as much higher intensities and smaller widths of the reflection.

The traces *b*, *c*, and *d* in Fig. 2 can be used to evaluate the actual concentration x_H in the Kr-rich phase at higher temperatures. Here we must take into account the numerous stacking faults which are inevitably present in the sample. Assuming their density to be the same $\alpha\simeq 1/11$ as that found in the quench condensed sample of Fig. 1, we obtain $x_H=(3.8\pm 0.4)\%$ at 35 K and $(3.5\pm 0.5)\%$ at 43 K. (We made use of the lattice parameters measured for pure Kr at different temperatures by Losee and Simmons.[16]) After the quick recrystallization is completed (trace *d*), the sample should be virtually hydrogen-free. Indeed, to within the total error, the position of the (111) line is identical to the position for pure Kr at the same temperature; this implies that the stacking-fault and impurity concentrations are close to zero.

For lower nominal hydrogen fractions ($c\leqslant 10\%$) we saw only reflections that could be attributed to the (111) line from a krypton-rich cubic lattice with a somewhat smaller lattice parameter than in pure krypton. Within a rather large uncertainty, the respective lattice parameter shifts for $c=1,2$, and 5% may be considered as constant and corresponding to the absolute lattice instability edge. The uncorrected Vegard's law gives an appreciable hydrogen concentration $x(H_2$ in $Kr)=(1.4\pm 0.3)\%$, the presence of hydrogen being manifested in a slight lattice constriction. However, it should be kept in mind that this estimate neglects stacking faults. The reflections observed were all the more intense, the lower the nominal hydrogen fraction. Irrespective of the condensation rate the reflections were broadened, which suggests small grain sizes and a high concentration of lattice defects.

The gas deposition rate was manifested primarily in the variations of the temperature T_s where recrystallization and annealing of amorphous specimens occurred. In general, the crystallization temperature was somewhat higher at higher condensation rates. Thus, for the low-rate condensation regime crystallization of the apparently amorphous Kr−20%H_2 condensate was observed at 35 K. At double the deposition rate crystallization started at around 40 K.

A more pronounced dependence of the crystallization onset temperature for krypton-based mixtures was observed by varying the composition of the source mixtures (Fig. 3). Samples with 10 to 25% H_2 started to recrystallize at 35–40 K. The crystal phase in recrystallized samples was strained and imperfect; this was inferred from the broad and low-intensity reflections. Keeping the samples for 5 h even at the crystallization onset temperature resulted in complete recrystallization, the intensity and width of the Kr reflections approaching the values observed previously for pure krypton. A slight temperature increase considerably quickened the process. Samples with the nominal hydrogen content ranging from 30 to 40% recrystallized at higher temperatures in the range 45–55 K (Fig. 3). The curve for the Kr–H_2 system has a kink at lower *c* values, which might reflect the basic differences in the structure and morphology between samples grown from hydrogen-dilute and hydrogen-concentrated gas mixtures. The distinct shift of the crystallization onset temperature to higher values at higher nominal hydrogen fractions indicates that hydrogen tends to stabilize the unusual amorphous krypton phase in as-grown samples.

The latest results obtained by the Cornell group[9,18] show that morphologically the so-called impurity–helium solids are highly amorphous media where the impurities form a multiply connected network of separate atoms, *n*-mers, chains, nanoparticles, and so on isolated from one another by layers of helium, presumably in the solid state. Basically, the impurity system can be treated as a non-self-sustained gel, which is stabilized at low enough temperatures by the helium spacer layers. As the sample is warmed up, the impurity fraction starts to coalesce and the latent heat causes helium

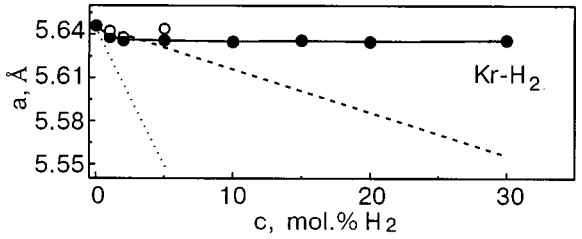

FIG. 4. The cubic lattice parameter of the krypton-rich phases in $Kr–H_2$ mixtures *versus* the nominal hydrogen fraction in the source gas (the open and filled circles are, respectively, for as-grown and completely annealed samples). The long-dash curve shows the uncorrected Vegard law for this sytem. The dotted curve is the corrected Vegard law (for an explanation see the argon subsection in Sec. 3).

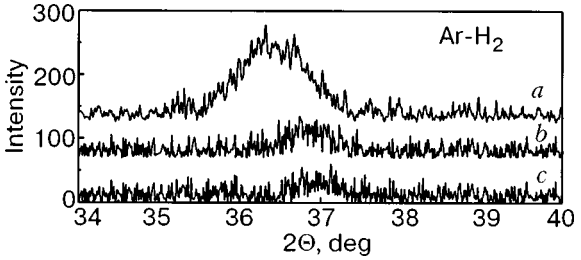

FIG. 5. Effect of hydrogen impurities on the angular postion and intensity of the (111) reflection from quench grown $Ar–H_2$ samples: pure argon (a); condensates with nominal hydrogen fractions of 10% (b) and 30% (c).

atoms to effuse, which in turn causes an abrupt reorganization of the material. In many respects, the hydrogen-containing krypton-based mixtures studied in this work resemble impurity–helium media. There is some evidence confirming this assumption, among other things, the highly amorphous state of the krypton-rich phase: the strong dependence of the crystallization onset temperature T_s on the nominal and, presumably, actual hydrogen concentrations and the very existence of T_s at which a sample undergoes radical and fast reconstruction. What can be said for sure is that hydrogen is a factor that stabilizes those amorphous states.

In Fig. 4 we plot the post-annealing lattice parameter a of the samples as a function of the nominal hydrogen fraction c in the gas mixture. All values of a were determined at 5 K. The ''final'' value of a is virtually independent of c. Assuming no stacking faults and using the corrected Vegard's law (dotted line) we evaluate the actual hydrogen concentration x_H to be close to 1% (the uncorrected Vegard's law yields 4%). This figure is the ultimate estimate of the equilibrium solubility of H_2 in solid crystalline krypton.

B. Argon

The structural characteristics of as-grown $Ar–H_2$ condensates differ considerably from those observed for $Kr–H_2$ condensates. There was an important peculiarity: the brightest reflections–(111) from the Ar cubic phase and (002) from the hexagonal H_2 phase–overlap, which makes it difficult to identify reflections. Other reflections could not be used because, just as in the $Kr–H_2$ system, they were absent, which might be indicative of texture even in very fine-grained samples. Therefore some conclusions for the $Ar–H_2$ system are less reliable than for the $Kr–H_2$ system.

We call attention to the following findings for the $Ar–H_2$ mixtures. First, irrespective of the growth regime, for nominal hydrogen concentrations up to $c=50\%$ mixed samples gave reflections that were broader and weaker than pure solid argon prepared under similar deposition conditions (Fig. 5). Pure argon was easily annealed at a comparatively low temperature around 16 K. The annealing onset temperature increased almost linearly with c but always remained lower than for the $Kr–H_2$ system (Fig. 3). Second, although the assignment of the only recordable reflection was dubious (Gaussian deconvolution always gave only one line), judging from its position and the general behavior as a function of temperature we identified this reflection as the (111) line from the hydrogen-rich fraction. Over the entire nominal H_2 concentration range we did not identify any reflections from the hydrogen-rich phase, either upon condensation or after annealing for 1 h at 10–12 K.

The above findings allow us to conclude the following. Since it is unlikely that hydrogen formed a superfine-grain phase we surmise that H_2 entered completely into the argon lattice as well as the hydrogen–argon gel, whose existence cannot be ruled out. The following facts support this assumption: 1) reflections from as-grown condensates are weaker and wider than those from pure as-grown samples; 2) reflections from the argon-rich phase are substantially shifted to larger angles than for pure argon; 3) a considerable increase of the recrystallization onset temperature with increasing nominal hydrogen fraction was observed. At the same time annealing of the samples resulted not only in higher intensities and smaller widths of the reflections but also a substantial shift to smaller angles, i.e. larger lattice parameters of the argon lattice, closer to the values typical for pure crystalline argon. The effect of annealing on the intensities and line widths of the argon matrix is clearly demonstrated in Fig. 6. Annealing at $T>20$ K resulted in stronger and narrower reflections from the (111) plane of the argon matrix. A shift of this line to smaller angles is clearly seen, which again means an increase in the lattice parameter. Figure 7 shows the effect of hydrogen impurities on the cubic lattice parameter a of the Ar matrix in as-grown and annealed samples. An unusual finding is that a in the as-grown argon-based phase, where a finite hydrogen concentration is expected, is *smaller* than in annealed samples, which are presumably devoid of hydrogen impurities, opposite to what can be expected from a straightforward Vegard line, whose slope (however small) must be positive. This fact suggests the following reasoning. The in-

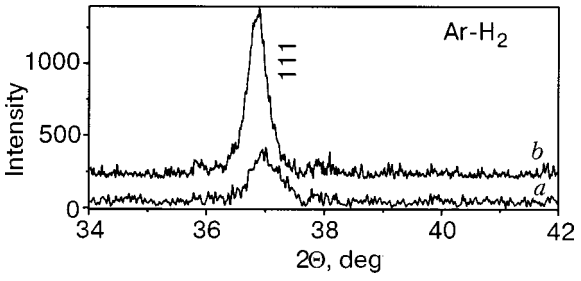

FIG. 6. Effect of annealing on the intensity and half-width of the (111) reflection in the $Ar–H_2$ system. Trace (a) is from an as-grown $Ar–20\%H_2$ condensate; trace (b) is from the same sample upon annealing.

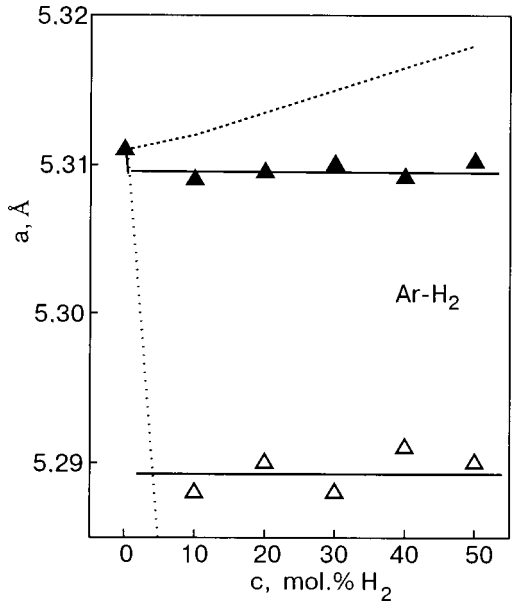

FIG. 7. The cubic lattice parameter of krypton-phases in $Ar–H_2$ mixtures *versus* the nominal hydrogen fraction in the source gas for freshly deposited specimens (△); annealed specimens (▲). The dashed curve shows the uncorrected Vegard law for this system; the dotted curve is the corrected Vegard law (for an explanation see the argon subsection in Sec. 3).

termolecular spacing in pure hydrogen is governed by an effective potential, renormalized considerably to account for large zero-point vibrations. If a hydrogen molecule is placed in an argon lattice, one can expect that because of the much stronger interactions with the argon environment the quantum nature of the H_2 molecule will be substantially suppressed. If this suppression is ultimate, then the intermolecular distance used in Vegard law estimates should be close to the hydrogen van der Waals diameter σ, as is the case for any ''classical'' heavy particle. That is, the effective hydrogen molar volume to be used in Vegard law calculations on the argon side of the (a, x) phase diagram should be σ^3.[15] The Vegard line corrected in this way is shown in Fig. 7 as a (relatively) steep line with a negative slope. Using the corrected Vegard law we estimate the hydrogen concentration in as-grown argon-based phase to be 3.6%. Stacking faults which are inevitably present in as-grown samples should reduce this estimate by at least a factor of 2. The corrected actual hydrogen concentration (1 or 2%) in as-grown samples and the still smaller value in annealed samples (see Fig. 7) compares well with the upper estimate of 0.5 mole % found by Loubeyre *et al.*[1] for the solubility of hydrogen in solid argon.

4. CONCLUSIONS

1. When room-temperature $Kr–H_2$ and $Ar–H_2$ gas mixtures are quench condensed on a substrate at 5 K, the condensates tend to grow as highly amorphized structures. This is particularly true for Kr-based samples with nominal hydrogen fractions above 10%, when as-grown samples did not give any reflections that could be attributed to a krypton-rich phase.

2. When quench condensed samples were warmed up, the recrystallization onset temperature depended appreciably on the nominal hydrogen fraction; this is indicative of certain differences in the morphology and structure of as-grown samples, including the actual hydrogen content in the phases rich in both rare gases. (Re)crystallization occurred rather quickly, releasing an appreciable amount of latent heat.

3. On the basis of the above experimental findings we believe that the states formed in as-grown samples are in many respects analogs of helium–impurity media (gels). These mixtures, which comprise two substances differing strongly with respect to the molecular parameters and are self-sustaining at low temperatures, have a highly amorphous structure and undergo explosive separation at a certain temperature whose value depends on the impurity employed.

4. As-grown $Ar–H_2$ condensates exhibited a weaker tendency to form hydrogen–impurity media than Kr-based samples. This finding can also be an indirect confirmation of the assumption made, since the difference in the $Kr–H_2$ system is larger than in the $Ar–H_2$ system, so that the latter system should be more likely to form the standard substitutional solid mixtures.

This work was funded by the CRDF (Grant UP2-2445-KH-02). We thank V. V. Khmelenko for communicating his results prior to publication and A. A. Solodovnik for valuable discussions.

*E-mail: galtsov@ilt.kharkov.ua

[1] P. Loubeyre, R. LeToullec, and J. P. Pinceaux, Phys. Rev. Lett. **72**, 1360 (1994).
[2] M. S. Somayazhulu, L. W. Finger, R. J. Hemley, and H. K. Mao, Science **71**, 1400 (1996).
[3] J. Schouten, J. Phys.: Condens. Matter **7**, 469 (1995).
[4] E. B. Gordon, L. P. Mezhov-Deglin, and O. F. Pugachev, JETP Lett. **19**, 63 (1974).
[5] E. B. Gordon, V. V. Khmelenko, A. A. Pelmenev, E. A. Popov, and O. F. Pugachev, Chem. Phys. Lett. **155**, 301 (1989).
[6] R. E. Boltnev, E. B. Gordon, I. N. Krushinskaya, M. V. Martynenko, A. A. Pelmenev, E. A. Propov, V. V. Khmelenko, and A. F. Shestakov, Fiz. Nizk. Temp. **23**, 753 (1997) [Low Temp. Phys. **23**, 567 (1997)].
[7] S. I. Kiselev, V. V. Khmelenko, D. M. Lee, V. Kiryukhin, R. E. Boltnev, E. B. Gordon, and B. Keimer, Phys. Rev. B **65**, 024517 (2001).
[8] S. I. Kiselev, V. V. Khmelenko, D. M. Lee, and C. Y. Lee, J. Low Temp. Phys. **128**, 37 (2002).
[9] V. V. Khmelenko, S. I. Kiselev, D. M. Lee, and C. Y. Lee [to be published in Physica Scripta (2003)].
[10] V. G. Manzhelii, A. I. Prokhvatilov, I. Ya. Minchina, and L. D. Yantsevich, *Handbook of Binary Solutions of Cryocrystals*, Begell House, New York (1996).
[11] I. N. Krupskii, A. I. Prokhvatilov, and G. N. Shcherbakov, Fiz. Nizk. Temp. **9**, 83 (1983) [Low Temp. Phys. **9**, 42 (1983)]; Fiz. Nizk. Temp. **9**, 858 (1983) [Low Temp. Phys. **9**, 446 (1983)].
[12] A. S. Barylnik, A. I. Prokhvatilov, M. A. Strzhemechny, and G. N. Shcherbakov, Fiz. Nizk. Temp. **19**, 625 (1993) [Low Temp. Phys. **19**, 447 (1993)].
[13] A. S. Barylnik, A. I. Prokhvatilov, and G. N. Shcherbakov, Fiz. Nizk. Temp. **21**, 787 (1995) [Low Temp. Phys. **21**, 607 (1995)].
[14] Ya. S. Umanski, *X-Ray Diffractometry of Metals*, Metallurgiya, Moscow (1967).
[15] M. A. Strzhemechny, A. I. Prokhvatilov, and L. D. Yantsevich, Physica B **198**, 267 (1994).
[16] D. L. Losee and R. O. Simmons, Phys. Rev. **172**, 944 (1968).
[17] P. Loubeyre, R. Letoullec, and J. P. Pinceaux, Phys. Rev. B **45**, 12844 (1992).
[18] S. I. Kiselev, V. V. Khmelenko, E. P. Bernard, and D. M. Lee, Fiz. Nizk. Temp. **29**, 678 (2003). [Low Temp. Phys. **29**, 505 (2003)].

This article was published in English in the original Russian journal. Reproduced here with stylistic changed by AIP.

Thermal conductivity of solid parahydrogen with methane admixtures

A. I. Krivchikov* and O. A. Korolyuk

B. Verkin Institute for Low Temperature Physics and Engineering of the National Academy of Sciences of Ukraine, 47, Ave. Lenin, Kharkov, 61103, Ukraine

V. V. Sumarokov, J. Mucha, P. Stachowiak, and A. Jeżowski

W. Trzebiatowski Institute for Low Temperature Physics and Structure Research of the Polish Academy of Sciences, P.O. Box 937, 50-950 Wroclaw, Poland

(Submitted December 19, 2002)
Fiz. Nizk. Temp. **29**, 706–709 (June 2003)

The thermal conductivity of a solid parahydrogen crystal with methane admixtures was measured in the temperature range 1.5 to 8 K. Solid samples were grown from the gas mixtures at 13 K. The concentration of CH_4 admixture molecules in the gas varied from 5 to 570 ppm. A very broad thermal conductivity peak with an absolute value of about 110 W/(m·K) was observed at 2.6 K. The data were interpreted using Callaway's model with resonance scattering of phonons by quasilocal vibrations of CH_4 molecules and phonon–grain boundary and phonon–phonon scattering. As grain boundary scattering increases, the broadening of the peak decreases. The analysis shows that a solid mixture of p-H_2 and CH_4 is a heterogeneous solution for CH_4 concentration higher than 0.1 ppm. © *2003 American Institute of Physics.*
[DOI: 10.1063/1.1582336]

Crystalline parahydrogen can be used as an ''inert'' matrix to study the dynamics of matrix-isolated atoms and molecules and their interaction with the crystal environment.[1–5] The thermal conductivity is very sensitive to the dynamic impurity–matrix interaction. At liquid-helium tempertures ($T<\Theta$) the inelastic anharmonic phonon–phonon U processes in p-H_2 freeze out. A considerable fraction of the p-H_2 molecules are in the rotational ground state. As a result, a defect-free pure p-H_2 crystal has a very high thermal conductivity.[6–9] The introduction of even small amounts of molecular or atomic impurity decreases strongly the value and temperature dependence of the thermal conductivity $K(T)$ at temperatures near the phonon peak.[9–11] The main source of phonon scattering is the dynamic disorder produced in the crystal by the sharp mass difference between the substitution impurity and the matrix molecule. Another factor reducing $K(T)$ could be resonance phonon scattering by molecular clusters—orthohydrogen clusters or impurity molecules with rotational degrees of freedom.[12,13]

In the present study $K(T)$ of pure p-H_2 and CH_4-doped p-H_2 was measured to determine how the rotational motion of the CH_4 molecules affects $K(T)$ in p-H_2. A CH_4 molecule in a H_2 matrix can be treated as a heavy point defect $[(m_{CH_4}-m_{H_2}/m_{H_2})=7]$ and as a weakly hindered quantum CH_4 rotor.[1,2] Strong resonance phonon scattering by the rotational CH_4 excitations has been detected previously. It is manifested as a dip in the temperature dependence $K(T)$ for solid krypton with CH_4 impurity.[14]

The experiment was performed using a specially designed liquid-^{4}He cryostat.[15] The samples were prepared and $K(T)$ was measured directly in a glass ampul (6.7 mm in diameter and 67 mm long) in the sample chamber of the cryostat. The samples were grown from p-H_2 gas near 13 K. After controlled cooling down to 4.2 K, $K(T)$ of the sample was measured by the steady-state flow method in the temperature range 1.5–8 K. The samples were prepared using H_2 gas (99.9999 vol.%, Messer Co.) and CH_4 gas (99.5%). The chemical impurities in H_2 were $O_2\leqslant 0.5$ ppm, $N_2\leqslant 0.5$ ppm, $H_2O\leqslant 0.5$ ppm, $HC\leqslant 0.1$ ppm, $CO(CO_2)\leqslant 0.1$ ppm. The CH_4 gas contained 1.76% CH_3D, 0.12% CHD_3, 0.043% N_2, and 0.007% O_2. Parahydrogen containing less than 0.2% orthohydrogen was obtained by conversion of L-H_2 in contact with $Fe(OH)_3$ below 20 K. The gas mixtures were prepared in a stainless steel vessel at room temperature. The error in the estimated CH_4 concentration in the mixture was less than 20%. Optical polarized light observation showed that the solid samples all consisted of several (two or three) parts, which differed with respect to the directions of the **c** axis of their hcp lattice. Unlike pure p-H_2, the p-H_2–CH_4 samples were multicolored and their colors changed with the angle between the light polarization vector and the **c** axis.

$K(T)$ was measured for several pure p-H_2 samples and $(p\text{-}H_2)_{(1-c)}(CH_4)_c$ solutions. The CH_4 concentration (c) in the initial gas mixture varied from 5 to 570 ppm. The experimental temperature dependences $K(T)$ for pure p-H_2 in this work and in the published data[7–9] are shown in Fig. 1. $K(T)$ for pure p-H_2 at temperatures near the phonon peak agrees well with the published data,[7,9] but it is one-tenth the record-high value reported in.[8] The good agreement observed for the thermal conductivity in pure p-H_2 measured in three independent experiments could be due to the close isotopic (natural) compositions of the H_2 gas used in this work. In other words $K(T)$ at its peak was limited by phonon scattering by H_2 isotopes, mainly HD molecules. The isotopic ratio $R=[D]/[H]$ for H_2 with the natural composition is $(1.39-1.56)\cdot 10^{-4}$. Mass-spectrometric analysis of H_2 gas showed that HD molecules were present in the initial gas.

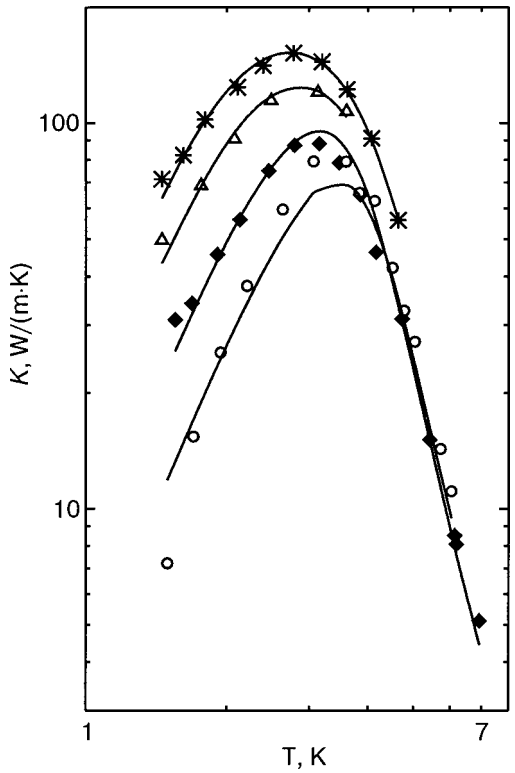

FIG. 1. The temperature dependence of the thermal conductivity of solid parahydrogen. ○ (Ref. 8); ● (Ref. 9); ◇, △ (Ref. 7)—for p-H_2 with 0.2% o-H_2 and p-H_2 with 0.34% o-H_2, respectively; ⋆, *—present data for samples 1 and 2, respectively.

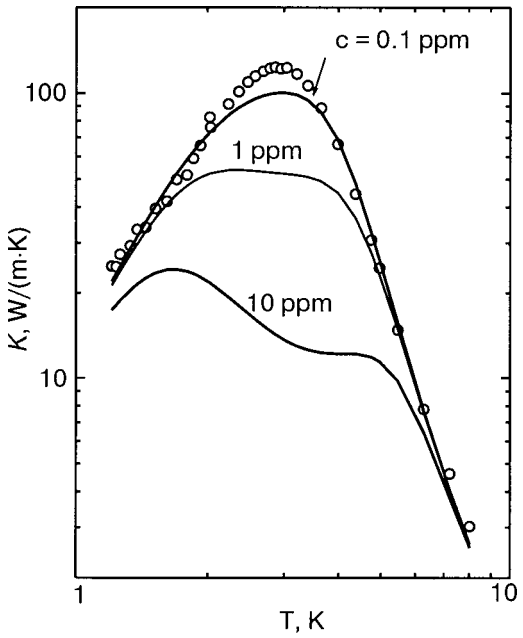

FIG. 2. The temperature dependence of the thermal conductivity of parahydrogen with a CH_4 admixture. The points are our experimental data for pure parahydrogen; the solid lines are the theoretical calculations for $c=0.1$, 1, and 10 ppm CH_4 in p-H_2.

The large difference between the record-high value of $K(T)$ and the results of this study can be interpreted as an isotopic effect in $K(T)$ for p-H_2. The isotopic composition of H_2 was not specified in Ref. 8. However, judging from the value of the $K(T)$ peak the HD content in H_2 is an order of magnitude lower than in gas with the natural isotopic composition. At temperatures below the phonon peak the structural imperfections of the sample affect $K(T)$. Above the peak $K(T)$ is influenced by U processes which are in turn sensitive to the hcp lattice anisotropy of p-H_2.[16] The contribution of the CH_4 impurity to $K(T)$ in solid p-H_2 can be detected only if it exceeds the isotopic effect. Figure 2 shows the calculated $K(T)$ curves for p-H_2 with different CH_4 concentrations (0.1, 1, and 10 ppm) assuming that the CH_4 molecules scatter phonons as heavy point defects.

The experimental curves $K(T)$ for pure p-H_2 and three p-H_2–CH_4 samples are shown in Fig. 3. $K(T)$ for a sample with 500 ppm CH_4 is only slightly lower than for pure p-H_2 and is even higher than for the sample with 28 ppm CH_4. The CH_4 effect on $K(T)$ in p-H_2 is found to be weak. One reason for this could be the very low solubility of CH_4 in solid H_2 (less than 0.1 ppm). The experimental samples were heterogeneous solid solutions. The main factors limiting the thermal conductivity are phonon scattering by grain boundaries, HD impurity, and U processes. We note that the spectroscopy of matrix-isolated molecules in solid H_2 samples with 10 ppm grown at $T\approx 8$ K detected no significant deviation of CH_4 from a random configuration distribution.[1,2]

The experimental results were analyzed using Callaway's theory allowing for the special role of phonon–phonon scattering processes in the thermal conductivity and using the Debye approximation to describe the phonon spectrum. In solid p-H_2 the resistive processes are due to phonon-phonon scattering, U processes ($\tau_U(x,T)$), scattering by the boundaries of crystalline grains and low-angle boundaries

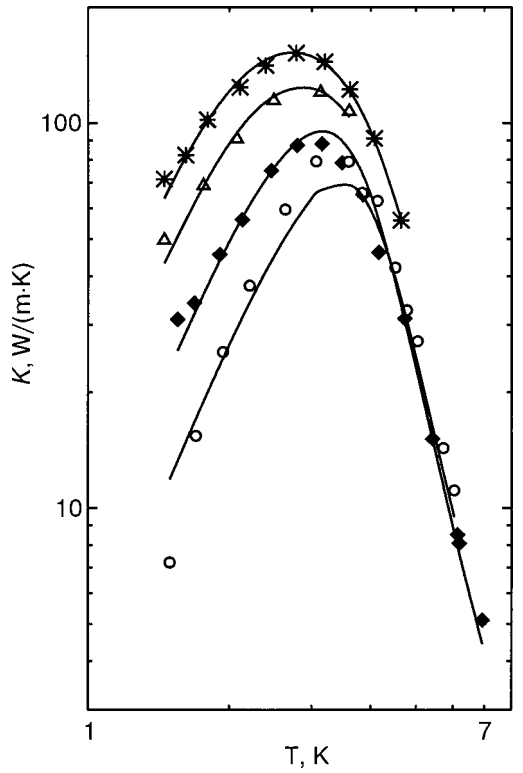

FIG. 3. The temperature dependence of the thermal conductivity of $(p\text{-}H_2)_{(1-c)}(CH_4)_c$. The points are the experimental data: pure hydrogen sample 2 (*); $c=28$ ppm CH_4 (◆); $c=116$ ppm CH_4 (○); $c=500$ ppm CH_4 (△). The solid lines are the best-fit curves.

TABLE I. The best-fit parameters, the phonon mean-free path L (boundary scattering), the HD concentration ξ, and the parameters A_U and E found by analyzing the experimental results for $K(T)$ in different samples of pure p-H_2 and p-H_2–CH_4.

Sample	ξ, ppm	L, mm	A_U, $10^7 K^{-3} s^{-1}$	E, K
p-H_2, sample 1	300±40	0.57±0.05	4.20	36
p-H_2, sample 2	300±40	1.11±0.05	2.11	36
p-H_2+28 ppm CH_4	300±40	0.34±0.05	4.80	36
p-H_2+116 ppm CH_4	300±40	0.17±0.05	4.20	36
p-H_2+500 ppm CH_4	300±40	0.71±0.05	4.20	36

($\tau_B(x,T)$), and scattering due to isotopic disorder (by HD molecules) ($\tau_I(x,T)$):

$$\tau_R^{-1}(x,T)=\tau_U^{-1}(x,T)+\tau_B^{-1}(x,T)+\tau_I^{-1}(x,T).$$

The characteristics of three-phonon U and N processes are determined only by the properties of the hcp lattice of H_2 and are virtually independent of the impurity molecules at low concentrations:

$$\tau_U^{-1}(x,T)=A_U x^2 T^3 e^{(-E/T)}, \quad \tau_N^{-1}(x,T)=A_N x^2 T^5.$$

The parameters A_U and E depend on the heat flow direction with respect to the **c** axis of the hcp lattice of H_2.[16] The boundary scattering is dependent on the mean crystal grain size L: $\tau_B^{-1}(x,T)=s/L$, where s is the sound speed. The intensity of N processes is taken from[17] ($A_N=6.7\times10^5$ $s^{-1}\cdot K^{-5}$).

The scattering due to isotopic disorder is characterized by the Rayleigh relaxation rate

$$\tau_I^{-1}=\xi\left(\frac{\Delta m}{m_{H_2}}\right)^2\frac{\Omega_0}{4\pi s^3}\omega^4,$$

where ξ is the HD concentration, Ω_0 is the volume per atom, and $\Delta m=1$ for HD impurity in H_2. The fit parameters used to match the calculated curves and the experimental results were the HD concentration ξ and the parameters L, A_U, and E (see Table I). It was assumed for p-H_2-CH_4 samples that the parameter L characterizes the structure of defects in the sample.[18] L varied nearly five-fold (see Table I). This variation of L in samples prepared from the gas mixtures p-H_2-CH_4 indicates that the density of low-angle boundaries in the sample increases as a result of stress appearing when the crystal is grown and cooled.

The new measurements for $K(T)$ in pure p-H_2 have been interpreted as a manifestation of the isotopic effect. $K(T)$ in the samples prepared by depositing gas mixtures $(p\text{-}H_2)_{(1-c)}(CH_4)_c$ in the interval $c=5-570$ ppm at temperatures near the triple point of p-H_2 varied only slightly with concentration. Because of the low solubility of CH_4 in p-H_2 we were unable (unlike in the Kr–CH_4 case) to detect resonance phonon scattering by the rotational excitations of the CH_4 molecules (a dip in the temperature dependence of $K(T)$ of solid H_2 with CH_4 impurity). The upper limit of CH_4 solubility in solid p-H_2 was estimated from the thermal conductivity values. It does not exceed 0.1 ppm.

We are grateful to Professor V. G. Manzhelii and Dr. B. Ya. Gorodilov for helpful discussions. The work described in this paper was made possible in part by grant N 2M/78-2000 from the Ukrainian Ministry of Education and Science.

*E-mail: krivchikov@ilt.kharkov.ua

[1] T. Momose, M. Miki, T. Wakabayashi, T. Shida, M.-Ch. Chan, S. S. Lee, and T. Oka, J. Chem. Phys. **107**, 7707 (1997).
[2] M. Miki and T. Momose, Fiz. Nizk. Temp. **26**, 899 (2000) [Low Temp. Phys. **26**, 661 (2000)].
[3] H. Katsuki and T. Momose, Phys. Rev. B **84**, 3286 (2000).
[4] J. Z. Li, M. Suzuki, M. Katsuragawa, and K. Hakuta, J. Chem. Phys. **115**, 930 (2001).
[5] R. J. Hinde, D. T. Anderson, S. Tam, and M. E. Fajardo, Chem. Phys. Lett. **356**, 355 (2002).
[6] R. W. Hill and B. Schneidmesser, Z. Phys. Chem. (Munich) **16**, 257 (1958).
[7] R. G. Bohn and C. F. Mate, Phys. Rev. B **2**, 2121 (1970).
[8] N. N. Zholonko, B. Ya. Gorodilov, and A. I. Krivchikov, JETP Lett. **55**, 167 (1992).
[9] B. Ya. Gorodilov, O. A. Korolyuk, A. I. Krivchikov, and V. G. Manzhelii, J. Low Temp. Phys. **119**, 497 (2000).
[10] V. G. Manzhelii, B. Ya. Gorodilov, and A. I. Krivchikov, Fiz. Nizk. Temp. **22**, 174 (1996) [Low Temp. Phys. **22**, 131 (1996)].
[11] O. A. Korolyuk, B Ya. Gorodilov, A. I. Krivchikov, and V. G. Manzhelii, Fiz. Nizk. Temp. **25**, 944 (1999) [Low Temp. Phys. **25**, 708 (1999)].
[12] B. Ya. Gorodilov and V. B. Kokshenev, J. Low Temp. Phys. **81**, 45 (1990).
[13] T. N. Antsygina, V. A. Slyusarev, and K. A. Chishko, Zh. Eksp. Teor. Fiz. **87**(2), 555 (1998) [JETP **114**, 303 (1998)].
[14] V. V. Dudkin, B. Ya. Gorodilov, A. I. Krivchikov, and V. G. Manzhelii, Fiz. Nizk. Temp. **26**, 1023 (2000) [Low Temp. Phys. **26**, 762 (2000)].
[15] A. Jeżowski and P. Stachowiak, Cryogenics **32**, 601 (1992).
[16] O. A. Korolyuk, B. Ya. Gorodilov, A. I. Krivchikov, A. S. Pirogov, and V. V. Dudkin, J. Low Temp. Phys. **111**, 515 (1998).
[17] T. N. Antsygina, B. Ya. Gorodilov, N. N. Zholonko, A. I. Krivchikov, and V. G. Manzhelii, Fiz. Nizk. Temp. **18**, 417 (1992) [Low Temp. Phys. **18**, 283 (1992)].
[18] O. A. Korolyuk, A. I. Krivchikov, and B. Ya. Gorodilov, J. Low Temp. Phys. **122**, 203 (2001).

This article was published in English in the original Russian journal Reproduced here with stylistic changes by AIP.

Vibrational dynamic and thermodynamic characteristics of metal–hydrogen superlattices

S. B. Feodosyev,* I. A. Gospodarev, V. I. Grishaev, and E. S. Syrkin

B. Verkin Institute for Low Temperature Physics and Engineering of the National Academy of Sciences of Ukraine, 47 Lenin Ave., Kharkov, 61103, Ukraine

(Submitted December 19, 2002)
Fiz. Nizk. Temp. **29**, 710–714 (June 2003)

The phonon spectra and vibrational thermodynamic characteristics of Pd–H superlattices are investigated. Our calculations show that the neutron scattering and calorimetric data are consistent with one another and make it possible to explain for such systems the atomic mean-square amplitudes and the correlations between them. © *2003 American Institute of Physics.*
[DOI: 10.1063/1.1582337]

1. INTRODUCTION

It has been known since the mid-1800s that metals, especially palladium, absorb hydrogen. This knowledge is widely used in applications, among other things, for purifying hydrogen. In the 1970s and then again at the end of the 1980s there was a natural explosion in the study of the physical properties of Pd. As a result many of these properties were investigated very explicitly and in detail (see, for example Ref. 1). However, the crystal-lattice dynamics and the vibrational properties of such systems have not been adequately studied.

Among existing results we mention neutron diffraction investigations of the dispersion law for phonons in the solid solution $PdD_{0.63}$ performed in 1974.[2] On this basis it is possible to judge the interatomic interaction and the vibrational spectrum of hydrogenated palladium. It is known that the contribution of lattice vibrations to the different dynamic and thermodynamic characteristics of Pd–H can be substantial and even determining. Therefore it is important and topical to compare the data obtained in Ref. 2 to the results of different mesurements of these properties.

In a recently published work[3] the temperature dependence of the specific heat of PdH_x was measured for different hydrogen concentrations x. It was found that at $T \gtrsim 10$ K the specific heat increases with x, while the electronic component decreases sharply[1] (the temperature dependence as $T \to 0$ in Ref. 3 at $x = 0.71$ also shows this directly). The sign of the change in the lattice contribution to the specific heat with increasing x is not obvious from.[2] Actually, an increase in the lattice constant by approximately 5% should noticeably weaken the interaction between Pd atoms and reduce the vibrational frequency making the determining contribution to the lattice specific heat. But the appearance of new neighbors (hydrogen atoms) around these atoms closer than other Pd atoms can compensate this bond weakening. Moreover, it is important to determine how such weakening of the interatomic interaction (if it occurs) affects the atomic vibrational amplitudes, i.e. the stability of the crystal lattice.

Microscopic calculations are necessary to answer these questions concerning the vibrational thermodynamic characteristics of crystal structures such as Pd–H. This paper is devoted to such calculations for high and uniformly distributed hydrogen concentrations in palladium.

2. INTERATOMIC INTERACTION AND PHONON SPECIFIC HEAT IN PD–H SOLUTIONS

The palladium crystal lattice is cubic face-centered. The dissolved hydrogen atoms occupy octahedral positions[1] and at high hydrogen concentrations one can talk about superstructural ordering of the solution.

Here we study two kinds of such superstructures: the first corresponds to atoms occupying sites or the centers of the edges of cubes in the Pd lattice, while the centers of the cubes remain empty (R filling); the other corresponds to the case where the centers of cubes also are filled (V filling). R filling corresponds to $PdH_{0.75}$; V filling corresponds to PdH. In V filling two fcc lattices with the same period are immersed in one another with detrusion by $a_0/2$ along the edges of a cube (a_0 is the lattice constant). R filling corresponds to the formation in V filling of a periodic (with period a_0) system of vacancies in the hydrogen sublattice.

In Ref. 4 the force constants of pure Pd were determined from neutron scattering data. The phonon density of states $\nu(\omega)$ so constructed for palladium is essentially identical to that calculated in the approximation of a central interaction between nearest neighbors. It reconfirms that for close-packed crystals the interatomic interaction, as a rule, can be described in this approximation. The interaction potential $\varphi(\mathbf{r}, \mathbf{r}')$ between atoms occupying their equilibrium positions $\mathbf{r}$ and $\mathbf{r}'$ can taken to be a pair interaction and isotropic: $\varphi(\mathbf{r}, \mathbf{r}') = \varphi(\Delta)$, where $\Delta = \mathbf{r} - \mathbf{r}'$.

Then the force-constants matrix $\Phi_{ik}(\mathbf{r}, \mathbf{r}')$ is

$$\Phi_{ik}(\mathbf{r}, \mathbf{r}') = \Phi_{ik}(\Delta) = -\alpha(\Delta)\frac{\Delta_i \Delta_k}{\Delta^2} - \beta(\Delta)\delta_{ik}, \qquad (1)$$

where δ_{ik} is the Kronecker delta function; the parameters α and β characterize, respectively, the central and noncentral interactions between the atoms:

$$\beta(\Delta) = \frac{\varphi'(\Delta)}{\Delta}; \quad \alpha(\Delta) = \varphi''(\Delta) - \beta(\Delta). \qquad (2)$$

Figure 1 shows the force constants α and β together with the Einstein frequency of an fcc crystal with a central nearest-neighbors interaction as functions of the interatomic distance (lattice constant). For definiteness the Lennard–Jones potential is taken for $\varphi(\Delta)$. Since we are interested in the change in the force constants as the lattice swells, for

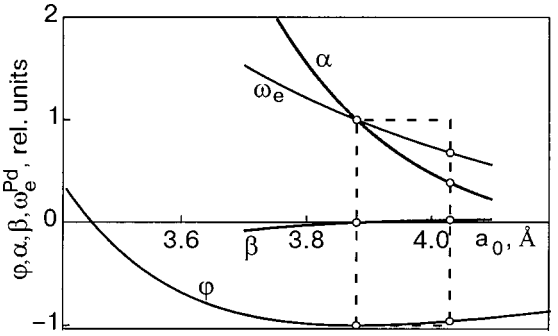

FIG. 1. Relative variation with increasing lattice constant of the interatomic interaction potential φ, the force constants α and β, and the Einstein vibrational frequency ω_e of palladium atoms. All quantities are given in relative units: $\alpha(a_0)=\omega_e(a_0)=-\varphi(a_0)=1$ ($a_0\approx 3.88$ Å is the lattice constant of pure Pd).

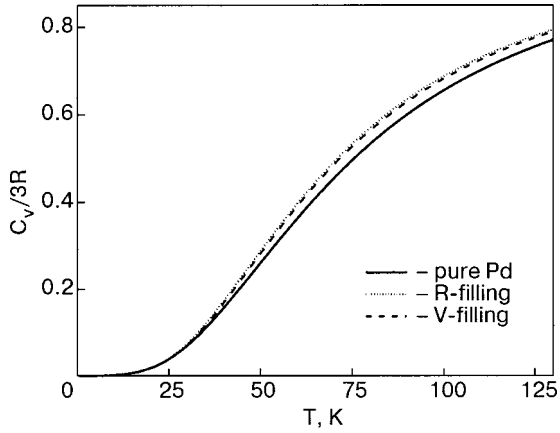

FIG. 2. Temperature dependences of the phonon specific heat of pure Pd (solid line), $PdH_{0.75}$ (the dashed line represents R filling), and PdH (the dot–dash line represents V filling).

$\Delta>\Delta_0$ ($\varphi'(\Delta_0)=0$), the results presented here are applicable in a wider range than for the Lennard–Jones potential because for $\Delta>\Delta_0$ a van der Waals interatomic attraction ($\varphi\sim\Delta^{-6}$) is typical in most crystals. The values of $\alpha(\Delta_0)$ and $\omega_e(\Delta_0)$ are assumed to be 1 unit [$\beta(\Delta_0)$ is given in the units $\alpha_0\equiv\alpha(\Delta_0)$] and $\varphi(\Delta_0)=-1$. It is evident that as the lattice constant increases from $a_0=3.88$ Å (the lattice constant of pure Pd) to $a_0\approx 4.03$ Å (palladium with hydrogen concentration 0.7–1.0; see, e.g., Ref. 1) the central interaction between Pd atoms decreases by more than a factor of 2 in magnitude and the Einstein frequency of the palladium atoms decreases by approximately a factor of 1.5. The neutron scattering data of Ref. 2[1)] can be used to reconstruct the interatomic interaction constants in Pd–H solid solutions. According to these data the maximum frequency of the acoustic band is ≈ 6 THz (the maximum vibrational frequency of the lattice in pure palladium is ≈ 7 THz); the gap width is ≈ 6 THz; and, the maximum frequency of optical vibrations is ≈ 21 THz. Since hydrogen is approximately 106.4 times lighter than palladium, the gap width is quite small, and the dispersion of optical phonons is considerable, it can be assumed that the interaction between palladium and hydrogen atoms is much weaker than the Pd↔Pd interaction. The force constants obtained from the data in Ref. 2[2)] are in good agreement with the above estimates based on the analysis of the interatomic interaction potential. If the force constant describing the central interaction between the nearest neighbors in a pure palladium lattice is taken to be 1, then we obtain for a Pd–H solution

$$\alpha_{\mathrm{Pd}\leftrightarrow\mathrm{Pd}}\sim 0.48;\quad \alpha_{\mathrm{Pd}\rightarrow\mathrm{H}}\approx 0.12;\quad \alpha_{\mathrm{H}\leftrightarrow\mathrm{H}}\approx 0.05;$$

$$\beta_{\mathrm{Pd}\leftrightarrow\mathrm{Pd}}\approx 0.05;\quad \beta_{\mathrm{Pd}\leftrightarrow\mathrm{H}}=\beta_{\mathrm{H}\leftrightarrow\mathrm{H}}=0. \qquad (3)$$

On the basis of these force constants it can be assumed that hydrogenization should increase noticeably the low-temperature phonon specific heat of palladium. In reality, the vibrations of the heavy Pd atoms, whose interaction is two times weaker than in a pure palladium lattice because of lattice ''swelling,'' make the main contribution to this property. The additional interaction between palladium and hydrogen is much weaker than even the attenuated interaction between the metal atoms. The Einstein vibrational frequency of palladium atoms will be higher, because of the Pd↔H interaction, than that shown in Fig. 1 for the lattice constant of hydrogenized palladium but it is noticeably lower than for pure Pd. This should increase the specific heat at low temperatures.

The results of more accurate calculations of the temperature dependence of the phonon specific heat of Pd–H solid solutions are presented in Figs. 2 and 3. The calculations were performed by the Jacobi-matrix method[5–7] using the force constants (3). Figure 2 shows $C_v(T)$ for pure palladium (solid line) and for the solutions PdH_x: the dashed line is for $x=0.75$ (R filling) and the dots are for $x=1.00$ (V filling). Actually, when hydrogen is implanted the phonon specific heat noticeably increases because the lattice constant increases by approximately 5%.

Figure 3 shows the temperature dependences of the difference $\Delta C_v(T)$ of the specific heats of hydrogenized Pd and pure Pd. The top panel shows these functions in a wide temperature range and the bottom panel show these functions at low temperatures.

In both panels the curves *1* and *2* show the values of $\Delta C_v(T)$ for R and V filling, respectively. The fact that the curve *1* lies above the curve *2* is apparent in our model; for the same value of the lattice constant R filling corresponds to a more ''open'' structure. To determine how such a nonmonotonic concentration dependence of the specific heat can actually be observed it is natural to investigate the concentration dependence of the lattice constant in the indicated concentration range. Comparing the curves *1* and *2* with the temperature dependence of the electronic specific heat of pure palladium[1,4] (curve *3*—the dashed line at the bottom of the figure) shows that already at $T\approx 10-12$ K the increase in the phonon part of the specific heat can compensate *any* (down to zero) decrease of the electronic component. This result agrees with,[3] and at any rate qualitatively explains the effect.

3. MEAN-SQUARE AMPLITUDES AND CORRELATION OF ATOMIC VIBRATIONS IN PD–H SOLID SOLUTIONS

The increase in the lattice constant with hydrogen saturation of Pd crystals and the resulting decrease in the force constants of palladium atoms should, at first glance, result in an increase of the vibrational amplitudes of these atoms; this can destabilize the lattice. To study this we calculated the

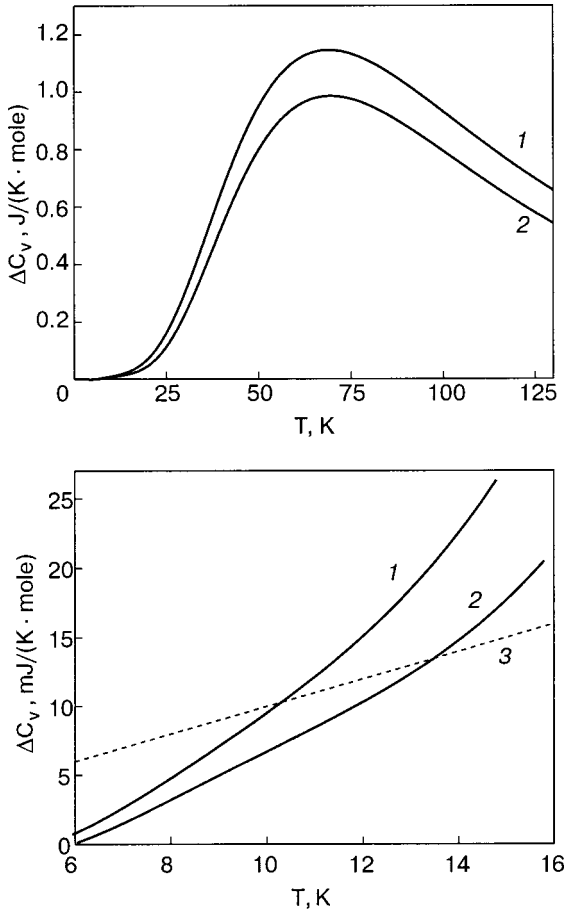

FIG. 3. The difference of the lattice specific heats of hydrogenized Pd and pure Pd: curve *1* is for R filling; curve *2* is for V filling. The dependences $\Delta C_v(T)$ in a wide temperature range are presented at the top. These dependences at low temperatures are presented at the bottom (on an enlarged scale). The dashed curve *3* is the electronic specific heat of pure palladium.[1,4]

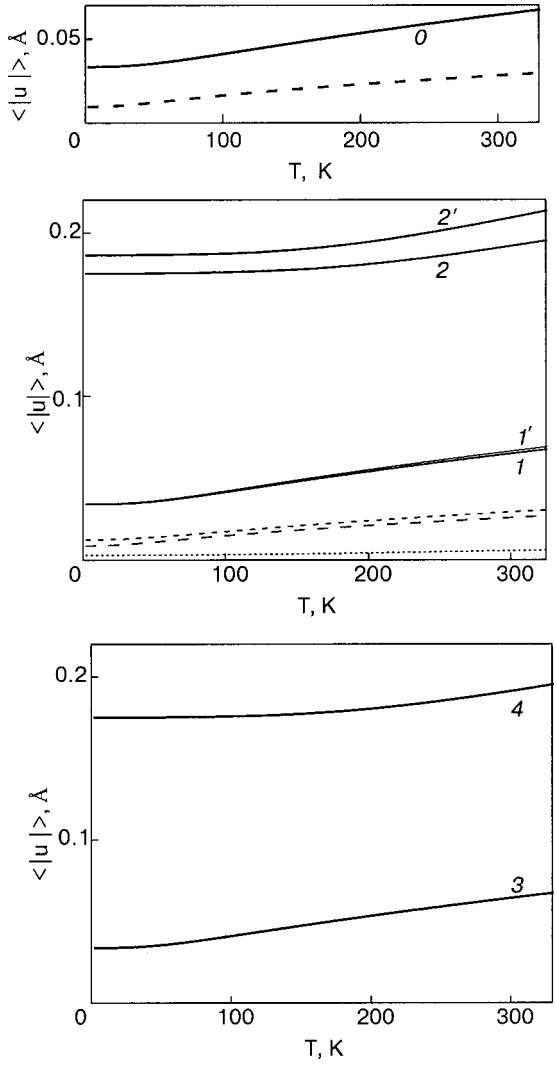

FIG. 4. The temperture dependences of the mean-square amplitudes and correlations of the displacements. The curves *0* correspond to pure Pd; the continuous line is the mean-square amplitude, the dashed line is the correlation of the displacements of the atoms Pd↔Pd. The curves *1* and *1′* correspond to the mean-square amplitudes of the Pd atoms in the solution $PdH_{0.75}$; the curves *2* and *2′* are for hydrogen atoms in the same solution (curves *1′* and *2′* correspond to the displacements toward the center of a cube, which is vacant in this case); the long-dash curves show the correlations of the displacements Pd↔Pd; the short-dash curve is for Pd↔H; and, the dotted curve is for H↔H. The curves *3* and *4* are the mean-square vibrational amplitudes of palladium and hydrogen atoms, respectively, in a PdH solution (V filling).

mean-square atomic vibrational amplitudes for palladium and hydrogen using the same models and the same Jacobi-matrix method.

The mean-square atomic vibrational amlitudes in a crystal lattice are one of the main characteristics of a crystal. In addition, the stability and melting temperature of a crystal can be judged on the basis of their behavior. These values determine the dispersion of sound and electromagnetic waves in a crystal. The mean-square amplitude of an atom with the position vector $\mathbf{r}$ in the crystallographic direction i is determined as the diagonal element (for $i=k$ and $\mathbf{r}=\mathbf{r}'$) $\sqrt{\langle|u_i^2(\mathbf{r})|\rangle_T}$, where $\langle|u_i^2(\mathbf{r})|\rangle_T$ is the mean-square displacement, of the correlation matrix $\langle|u_i(\mathbf{r})u_k(\mathbf{r}')|\rangle_T$ given by

$$\langle|u_i(\mathbf{r})u_k(\mathbf{r}')|\rangle_T=\frac{\hbar}{2\sqrt{m(\mathbf{r})m(\mathbf{r}')}}\int_{\mathcal{D}}\frac{1}{\sqrt{\lambda}}\coth\left(\frac{\hbar\sqrt{\lambda}}{2kT}\right)\times\frac{1}{\pi}\operatorname{Im}\mathcal{G}_{ik}(\lambda,\mathbf{r},\mathbf{r}')d\lambda. \quad (4)$$

Here $m(\mathbf{r})$ is the mass of an atom with the position vector $\mathbf{r}$; λ is the squared eigenfrequency; $\mathcal{G}_{ik}(\lambda,\mathbf{r},\mathbf{r}')$ is the Green's function tensor of the lattice; T is the temperature; and, $\hbar$ and k are Planck's and Boltzmann's constant, respectively.

The results of a calculation of the tempearture dependence of the mean-square amplitude by the Jacobi-matrix method are displayed in Fig. 4 (solid lines). The curves *0* correspond to pure Pd. The curves *1*, *1′*, and *3* show the mean-square amplitudes for Pd in the presence of hydrogen (the curve *3* corresponds to V filling, all other curves correspond to R filling). Curve *1* corresponds to the displacement of a $Pd^{(0)}$ atom (in any direction) and a $Pd^{(1)}$ atom toward the nearest hydrogen atom; the curve *1′* shows the displacements of $Pd^{(1)}$ toward the center of a cube (R filling vacancy). This is why the curve *1′* lies slightly above the curve *1*. The curves *0*, *1′*, and *3* are all essentially identical to one

another. The curves *2* and *2′* show the mean-square vibrational amplitudes of hydrogen atoms in a direction along (curve *2*) and perpendicular (curve 2′) the edge whose center it occupies. The curve *4*, virtually coinciding with curve *2*, corresponds to the mean-square amplitude of a hydrogen atom for V filling. Here we have obtained a result which is unexpected at first glance: the change of the mean-square vibrational amplitudes of palladium atoms in a Pd–H solution, as compared to pure Pd, is very small. Because of the huge mass difference between palladium and hydrogen the mean-square amplitudes of the unit cell in Pd–H solutions and pure palladium are essentially the same. The lattice of such solutions will be essentially just as stable as the lattice of pure palladium.

To understand why a weakening of the interatomic interaction has not led to any noticeable increase of the vibrational amplitudes of palladium we shall consider the correlations of the displacements in our systems. To compare such correlations to the mean-square amplitude of a correlation it is convenient to use $\sqrt{\langle |u_i(\mathbf{r})u_k(\mathbf{r}')| \rangle_T}$, where the radicand is determined by the relation (4). The temperature dependences of such functions for displacements of neighboring atoms along the line connecting them (when the correlation is maximum) are also shown in Fig. 4 (dashed lines): the long dashes correspond to the corerlation of the displacements Pd↔Pd; the short dashes correspond to Pd↔H; and, the dots correspond to H↔H. The data are essentially the same for R and V filling. The diagrams of the displacement correlations are not shown on the V filling fragment.

The large correlation of the displacements Pd↔H shows that considerable vibrational energy is transferred from palladium to hydrogen atoms. The amplitudes of the Pd atoms essentially do not increase as the interatomic interaction decreases during hydrogenization with the palladium atoms ''shaking'' the hydrogen atoms.

4. CONCLUSIONS

Our microscopic calculations of the thermodynamic properties have shown that the neutron scattering[2] and calorimetric[3] data are mutually consistent. In particular we have shown that the weakening of the interatomic interactions by an increase in the lattice constant as a result of hydrogen implantation in palladium noticeably increases the phonon contribution to the low-temperature specific heat. For $T \gtrsim 10-12$ K this phonon contribution to the specific heat compensates the decrease in the specific heat as a result of hydrogenization of palladium.[1,4]

It has been shown that at temperatures up to 400 K the mean-square amplitudes of palladium and hydrogen are negligible compared with the lattice constant (3.88 Å for pure palladium and ≈ 4.03 Å for strongly hydrogenized palladium), showing that this compound has a large margin of stability. Thus the weakening of the interatomic interaction by hydrogenization of the metal does not noticeably increase the amplitude of the eigenoscillations of the metal, and because of the strong correlation between the displacements of the neighboring atoms Pd↔H the palladium atoms ''shake'' the light hydrogen atoms.

*E-mail: feodosiev@ilt.kharkov.ua

1) These data are also given and analyzed in.[1]

2) Since our results are only qualitative we did not consider the accuracy of the calculations of the force constants based on the data in.[2]

[1] *Hydrogen in Metals*, Vols. 1 and 2, edited by G. Alefeld and J. Völkl, Springer-Verlag, New York (1978).
[2] J. M. Rowe, J. J. Rush, H. G. Smith, M. M. Mostoller, and H. E. Flotow, Phys. Rev. Lett. **33**, 1297 (1974).
[3] H. Araki, S. Harada, M. Fukuda, V. Syvokon, and M. Kubota, Physica B **284–288**, 1266 (2000).
[4] A. P. Miller and B. N. Brockhouse, Can. J. Phys. **49**, 704 (1971).
[5] V. I. Peresada, in *Physics of the Condensed State* [in Russian], Kharkov (1968), p. 172.
[6] V. I. Peresada and V. N. Afanas'ev, Zh. Éksp. Teor. Fiz. **58**, 135 (1970) [Sov. Phys. JETP **31**, 78 (1970)].
[7] V. I. Peresada, V. N. Afanas'ev, and V. S. Borovikov, Fiz. Nizk. Temp. **1**, 461 (1975) [Sov. J. Low Temp. Phys. **1**, 227 (1975)].

This article was published in English in the original Russian journal. Reproduced here with stylistic changes by AIP.

Thermal expansion of $Kr-CH_4$ solid solutions at liquid-helium temperatures

A. N. Aleksandrovskii,* V. G. Gavrilko, A. V. Dolbin, V. B. Esel'son, V. G. Manzhelii, and B. G. Udovidchenko

B. Verkin Institute for Low Temperature Physics and Engineering of the National Academy of Sciences of Ukraine, 47 Lenin Ave., Kharkov 61103, Ukraine

(Submitted December 19, 2002)
Fiz. Nizk. Temp. **29**, 715–721 (June 2003)

A negative contribution of the CH_4 impurity to the thermal expansion of a solution was observed in dilatometric studies of the solid solutions $Kr+0.76\%CH_4$, $Kr+5.25\%CH_4$, and $Kr+10.5\%$ CH_4 at 1–23 K. It was shown that the negative contribution is due to changes in the occupancy of the ground state of the A modification of isolated CH_4 molecules. The contributions of the CH_4 impurity singles and clusters to the thermal expansion were estimated assuming them to be independent of one another. The contribution of the singles to the thermal expansion of the solid solution was found to be negative. The energies of the first excited rotational states were determined for singles and two- and three-body clusters of CH_4 molecules. © *2003 American Institute of Physics.* [DOI: 10.1063/1.1582338]

1. INTRODUCTION

This is a study of the thermal expansion of solid Kr solutions containing 0.76, 5.2, and 10.5 mol%CH_4. A CH_4 molecule is a regular tetrahedron formed by hydrogen (protium) atoms with a carbon atom at the center. Since the nuclear spin of carbon ^{12}C is zero and the nuclear spin of the hydrogen atom is $I=1/2$, the rotational levels can have three types of symmetry corresponding to the total nuclear spin of methane. As a result, there are three modifications of the tetrahedral CH_4 molecules (A, T, and E) with total nuclear spin 2, 1, and 0, respectively. For high-lying rotational levels the equilibrium concentrations of these nuclear spin CH_4 modifications are in the ratio 5:9:2. The A modification has the lowest-energy rotational state. This state is five-fold degenerate and characterized by the rotational quantum number $J=0$. The levels with different symmetries relative to the nuclei do not combine much with each other.[1] Nevertheless, in experiments the spin modifications of CH_4 are observed to undergo mutual transformations (conversion). The transformation rate is largely dependent on the conditions experienced by the molecule. The conversion mechanism is not completely understood yet.

According to the theoretical calculations performed by Yamamoto, Kataoka, and Okada,[2,3] in high-symmetry crystal fields a transition of CH_4 molecules into the rotational ground state ($J=0$) is accompanied by a reduction of the multipole part of the molecular interaction and thus leads to an increase in the crystal volume as the temperature decreases (a negative thermal expansion coefficient). We shall call this effect the YKO mechanism. It can readily be explained by recalling that the rotational ground state ($J=0$) of a free CH_4 molecule is characterized by a spherically symmetric probability distribution function, and therefore the CH_4 molecule has a zero octupole moment in this state. In a crystal the CH_4 molecule in this state is closer to being spherical than molecules in other states and hence has a lower effective octupole moment. As temperature decreases, the increasing occupancy of the rotational $J=0$ state can obtain contributions not only from the original A modifications of CH_4 but from the E, $T\rightarrow A$ conversions also. Conversion is a much slower process than thermalization of the rotational spectra of the CH_4 modifications. The thermal expansion of the solution is determined by the competition between two contributions—the phonon contribution responsible for the thermal expansion of the crystal lattice and the contribution of the rotational motion of the molecules. In the fcc case the first contribution is positive and the other is negative (at sufficiently low temperatures). If the characteristic thermalization time is considerably shorter than the characteristic conversion time, the latter can be estimated from the time dependence of the sample length with rapidly varying temperature. Negative thermal expansion induced by the YKO mechanism[2,3] has been observed experimentally only in solid CH_4 at liquid-helium temperatures.[4–6]

The above considerations pertain to disordered sublattices of solid CH_4 and some crystals including CH_4 as an impurity and to solid $Kr-CH_4$ solutions in particular. In the latter case a CH_4 molecule is in the octahedral crystal field produced by spherically symmetric Kr molecules.

If the above reasoning is correct, the CH_4 impurity should make a negative contribution to the thermal expansion coefficient of the solid solution $Kr-CH_4$ at low temperatures. Using the dependence of the rotational energy spectrum of CH_4 on the crystal field in the disordered phase, we can estimate the energy barriers hindering the rotation of CH_4 molecules in solid Kr. In addition, the time dependence of a $Kr-CH_4$ solid sample length as a function of the temperature of the environment around the sample was studied to obtain information on the conversion rate of CH_4 molecules.

2. EXPERIMENT

To answer the questions raised in this study we have performed a dilatometric investigation of the thermal expansion of the solid solutions $Kr+0.76\%$, $Kr+5.25\%$, and $Kr+10.5\%$ CH_4 at 1–23 K. At these temperatures the solubil-

ity of methane in krypton is about 80%.[7] The CH_4 concentration in the solution Kr+0.76% CH_4 is such that the concentration of isolated CH_4 molecules to the thermal expansion of the solid solution predominates. The solutions Kr+0.25% CH_4 and Kr+10.5% CH_4 were intended to study the contributions of clusters of two or three CH_4 molecules to the thermal expansion. The linear thermal expansion coefficient of the solid solutions Kr–CH_4 was measured with a high-sensitivity capacitance dilatometer (2×10^{-9} cm resolution).[8] The krypton used (99.937%) contained the impurities Ar (0.012%), N_2 (0.046%), and O_2 (0.005%). The purity of the gas was checked chromatographically. The methane used to prepare the solid solutions Kr–CH_4 contained N_2 (0.03%) and O_2 (<0.01%). The solution was prepared at room temperature in a special stainless steel measuring vessel. The rated composition of the solution was checked with a gas chromatograph. The solid samples were grown in a glass ampul of the measuring cell of the dilatometer by condensation directly from the solid phase at ~63 K. The growth rate was about 2 mm/h. Growth was checked visually. The samples were transparent and had no visible defects. A sample was then separated by thermal etching from the glass ampul walls to make a polycrystalline cylinder about 22 mm in diameter and 24.6 mm (Kr +0.76% CH_4), 31 mm (Kr+5.25% CH_4), and 24.9 mm (Kr+10.5% CH_4) high. The grain size was about 1 mm. The thermal expansion was measured along the cylinder axis. The dilatometer was also used to measure the thermal expansion of the matrix (solid Kr) grown by the same technique. The thermal expansion of the solutions was studied under isothermal conditions in the range 1–23 K. Temperature was measured with germanium resistance thermometers. A distinctive feature of the experimental technique is that the sample temperature was changed by abruptly increasing the power fed to the heater, after which the power was kept constant. The time to measure the new temperature and the length of the sample varied from 0.5 to 1.5 h. The temperature and length data were recorded every minute, computer-processed in real-time, and displayed as plots and numerical data. The change-over to a new temperature was automatic and occurred after the sample attained a ''stable'' state where its temperature changed by not more than 0.01 K in 10 min. The measurements were performed with increasing and decreasing temperature.

3. RESULTS AND DISCUSSION

The contribution of the CH_4 impurity to the thermal expansion coefficient of the solutions Kr–CH_4 can be estimated if information about the thermal expansion coefficient of the matrix (pure solid Kr) is available. To reduce the influence of experimental systematic errors we performed our own investigation of the thermal expansion coefficient of pure Kr at 1–25 K (this krypton was used in our solid solutions). Our coefficients and the published data[9] vary within 7% over the entire temperature range. The thermal expansion coefficients α_{sol} of the solid solutions Kr+0.76% CH_4, Kr+5.25% CH_4, and Kr+10.5% CH_4 were investigated. The CH_4 impurity decreases the thermal expansion coefficient below that of pure solid Kr. The difference between the thermal expansion coefficients of the solid solutions and the Kr matrix (α_{Kr}) is found as $\Delta\alpha=\alpha_{sol}-\alpha_{Kr}$.

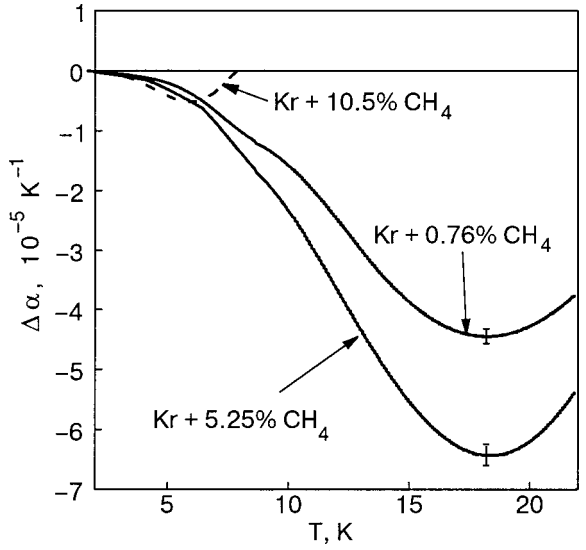

FIG. 1. The contributions of impurity CH_4 to the linear thermal expansion coefficient of the solid solutions Kr–CH_4.

The temperature dependence of $\Delta\alpha$ is shown in Fig. 1. It is interesting that $\Delta\alpha$ is negative for all solutions in the entire temperature range. However, this result is not surprising if we extend the thermal expansion calculations of Refs. 2 and 3 for solid CH_4 to our solutions; this extension is quite valid. According to neutron diffraction data for the solid solutions Kr–CH_4,[10,11] the rotational spectrum of CH_4 in solid Kr is very close to that of orientationally disordered CH_4 molecules in solid CH_4. The dependence of the rotational spectrum of CH_4 molecules in the disordered sublattices of solid methane on the coefficient f_c characterizing the crystal field value is shown in Fig. 2.

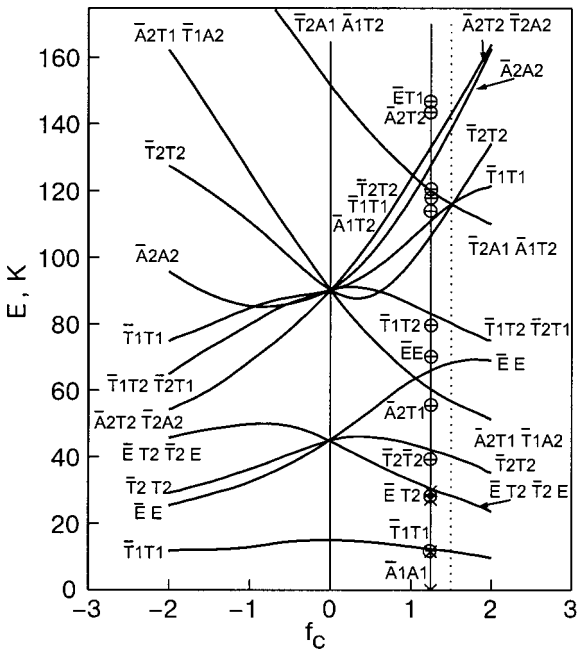

FIG. 2. The rotational spectrum of CH_4 molecules in a solid solution Kr–CH_4 and in pure solid CH_4: Kr–CH_4 (Ref. 13) (⊖); Kr–CH_4 (Ref. 10) (×); O_h is the symmetry of the sublattice of the antiferrorotational phase of solid CH_4 (Ref. 3) (curves).

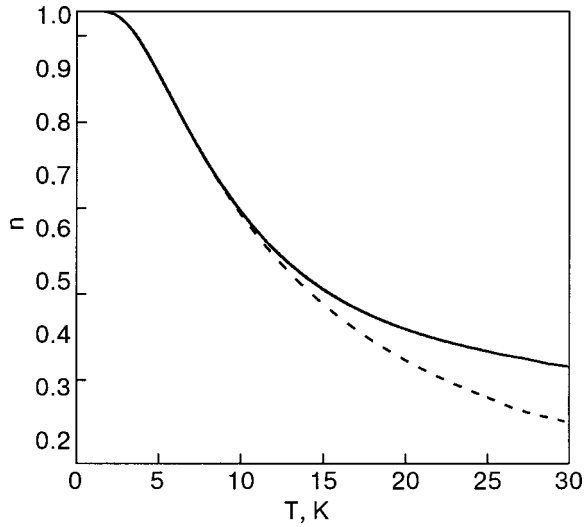

FIG. 3. The equilibrium concentration of the A modification and the occupancy of its ground rotational state. Occupancy of the rotational level $J=0$ (––); equilibirum concentration of the A modification of CH_4 (——).

The authors of Refs 1 and 2 believe that the crystal field value corresponding to the section of the rotation spectrum on the line $f_c=1.25$ (solid line in Fig. 2) matches best the experimental data on the rotational levels of CH_4 in disordered sublattices.

An investigation of inelastic neutron scattering by the solid solution $Kr+0.76\%\ CH_4$ revealed the energy position of the peaks in the rotational transitions of CH_4.[10,11] The rotational energy levels[10] measured from the ground state $J=0$ are shown in Fig. 2 (crosses). Unfortunately, at present there are no published experimental data on the higher-energy part of the rotational spectrum of CH_4 in a $Kr–CH_4$ solution. Since the rotational spectra of CH_4 in the solid solutions $Kr–CH_4$ and in the disordered phase are very close,[2,3] we shall use the spectrum for the disordered phase in our calculations of the CH_4 behavior in $Kr–CH_4$.

The authors of Refs. 2 and 3 mentioned above, are of the opinion that the negative thermal expansion of solid CH_4 is due to a decrease in the noncentral molecular interaction when the molecule passes into the ground state. The process is energetically favorable because the rotational ground state of the A modification has the lowest energy. The excess thermal expansion $\Delta\alpha$ is thus dependent on the concentration of the A modification in the ground state. The temperature dependences of the A modification (solid line) and the equilibrium occupancy of its ground state (broken line) are shown in Fig. 3. The curves were calculated for the equilibrium composition of the spin modifications. The calculation was based on the rotational $Kr–CH_4$ spectrum obtained from experimental inelastic neutron scattering data for the states with $J=1$ and $J=2$. The values for $J=3$ were taken from the rotational spectrum.[2,3] As can be judged from the figure, the contribution of the YKO mechanism should be observed at the temperatures of our experiments as the occupancy of the $J=0$ level appreciably changes at these temperatures. This conclusion agrees with the behavior of the excess thermal expansion coefficient of the solid solutions $Kr+0.76\%\ CH_4$ and $Kr+5.25\%\ CH_4$ (Fig. 1).

Apart from single impurity molecules, real solid solutions always contain clusters of molecules. Assuming the contribution of the impurity singles and clusters to the thermal expansion to be independent of one another and the CH_4 molecules to be randomly distributed in the fcc lattice of the Kr matrix and using the method proposed in Ref. 12, we calculated the number of clusters consisting of one, two, and three impurity molecules in solutions with 0.76, 5.25, and $10.5\%\ CH_4$. Then the concentration of the CH_4 singles is 0.69% in Kr in the solid solution $Kr+0.76\%\ CH_4$, 2.74% in Kr in $Kr+5.25\%\ CH_4$, and 2.77% in Kr in $Kr+10.5\%\ CH_4$. Assuming $\Delta\alpha$ of a solid solution to be the sum of the contributions from single, double, and triple clusters and knowing the content of the clusters in a solution, we can estimate their specific contributions with respect to the concentration n of singles, pairs, and triples, respectively (Fig. 4). The contributions of various clusters to the thermal expansion of each solid solution are shown in Fig. 5 [(a) $Kr+0.76\%\ CH_4$, (b) $Kr+5.25\%\ CH_4$, (c) $Kr+10.5\%\ CH_4$].

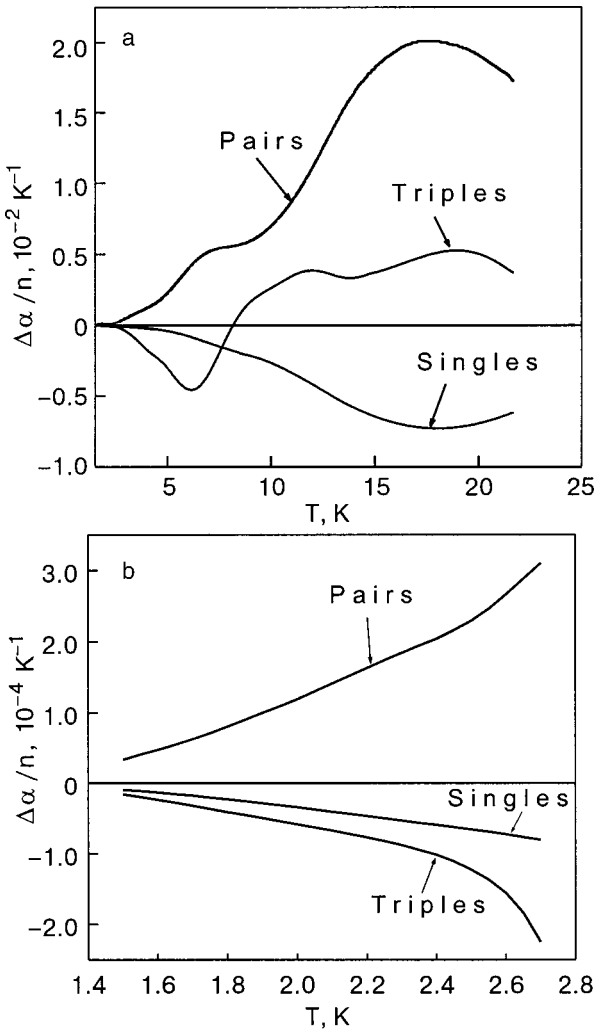

FIG. 4. Specific contributions of various clusters to the thermal expansion of the solid solutions $Kr–CH_4$ (n–concentration of singles, pairs, and triples, respectively) (a). Low temperature fragment of the specific contributions of various clusters to the thermal expansion of the solid solution $Kr–CH_4$ (b).

It should be noted that before starting the calculations we had to construct a correspondence between each value of the temperature and an experimental value of the thermal

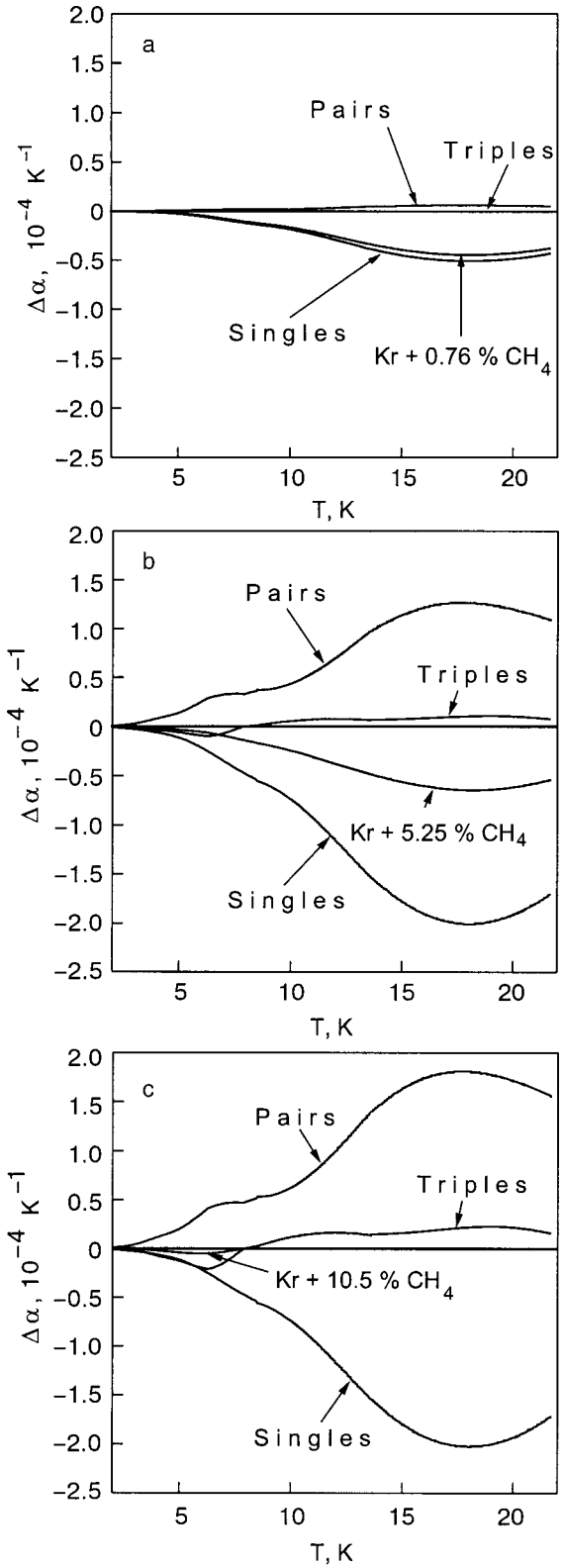

FIG. 5. Contributions of clusters consisting of 1, 2, and 3 impurity methane molecules to the thermal expansion of the solutions Kr+0.76% CH_4 (a); Kr+5.25% CH_4 (b); Kr+10.5% CH_4 (c).

expansion coefficient. For this, polynomial functions were fit to the experimental values of $\alpha(T)$ for all solutions.

According to our calculations the CH_4 singles make the main contribution to the negative thermal expansion of the solutions. Pair clusters make a large positive contribution. Triple clusters have only a slight effect on the thermal expansion of the solid solutions Kr–CH_4.

4. CONTRIBUTION OF MATRIX-ISOLATED CH_4 MOLECULES TO THE THERMAL EXPANSION OF THE SOLID SOLUTIONS KR–CH_4

In this section we shall concentrate on the behavior of the thermal expansion of the solid solutions Kr–CH_4 where the main contribution to the thermal expansion is due to the two lowest rotational levels.

If we extend the YKO mechanism[2,3] explaining the nature of negative thermal expansion of solid CH_4 to the interpetation of the behavior of CH_4 impurity in a solid solution Kr–CH_4 which is not concentrated, the negative contribution of the impurity moelcules to the thermal expansion of the solid solution Kr–CH_4 is no longer surprising. This extension is quite reasonable. According to neutron diffractometry[10,11] data for the solid solutions Kr–CH_4, the rotational spectrum of CH_4 in solid Kr is close to that of orientationally disordered CH_4 molecules in the antiferrorotational phase.[3] This fact is completely consistent with theoretical predictions.[2,13]

The authors of Refs. 2 and 3 believe that the crystal field value corresponding to the rotational spectrum on the section on the line $f_c=1.25$ (the solid line in Fig. 2) correlates best with the experimental rotational levels of CH_4 in the antiferrorotational phase. The energies of the peaks of the rotational transitions in CH_4 were found from inelastic neutron scattering data[10,11] for the solid solution Kr+0.76% CH_4. The rotational level energies of CH_4 measured from the ground state $J=0$[10,11] are shown in Fig. 2 (crosses). We can infer from the figure that the CH_4 rotational spectrum in the antiferrorotational phase and the CH_4 rotational spectrum in the solution Kr–CH_4 are fairly close, but in the solid solution Kr–CH_4 the section on the line $f_c=1.5$ gives better agreement between the calculations and the experimental data (the broken line in Fig. 2). On the basis of the similarity of the rotational spectra of CH_4 in the solid solution Kr–CH_4 and in the antiferrorotational phase,[2,3] we shall use the spectrum in the antiferrorotational phase in our calculations of the behavior of CH_4 in the solid solutions Kr–CH_4. In Ref. 14 a special case is considered, where the free energy of the system can be written as a sum of the free energies of the translational lattice vibrations and the rotational motion of the molecules. In this case the contribution $\Delta\beta$ of the rotational motion of noninteracting CH_4 molecules to the volume thermal expansion coefficient of the solid solutions Kr–CH_4 can be expressed as

$$\Delta\beta=3\Delta\alpha=\frac{c\chi N_A}{VkT^2}\{\langle E^2\Gamma\rangle-\langle E\Gamma\rangle\langle E\rangle\}. \tag{1}$$

Here V is the molar volume, χ is the compressibility of the solution, c is the molar concentration of the CH_4 in the solid solution Kr–CH_4, and N_A is Avogadro's number. Thermodynamic averaging is performed over the CH_4 rotational spectrum,

$$\langle\ldots\rangle=\sum_i (\ldots)g_i e^{-E_i/kT} \Big/ \sum g_i e^{-E_i/kT}, \tag{2}$$

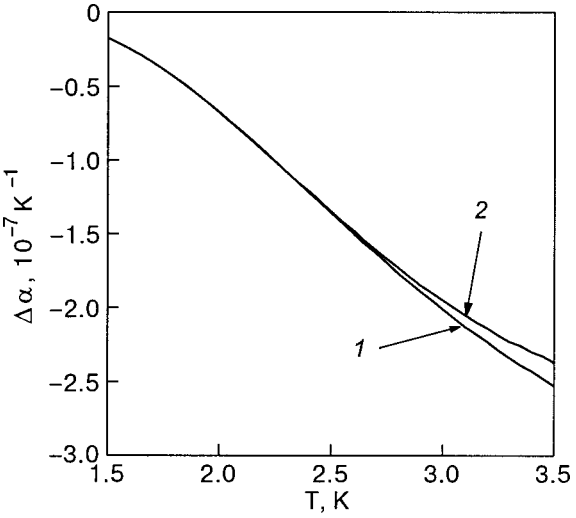

FIG. 6. Low-temperature part of the computed temperature dependence of the excess thermal expansion coefficient of the solution Kr+0.76% CH_4: twelve low-lying rotational levels (*1*), two-level system (*2*).

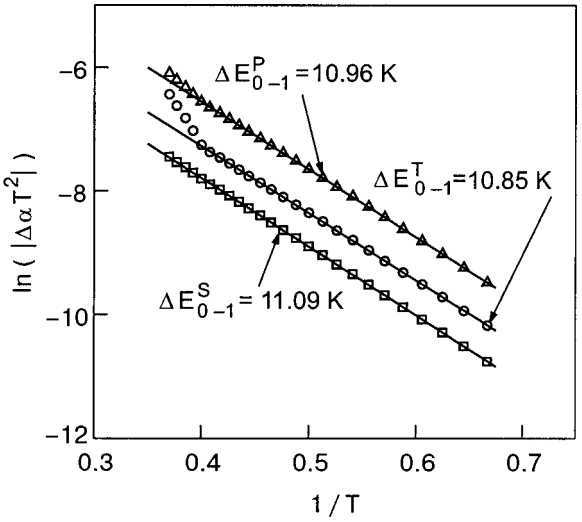

FIG. 7. Computed dependences used to estimate ΔE_{0-1} in the libration spectra of single CH_4 molecules (□), two-body clusters (△), and three-body clusters (○).

where E_i and g_i are, respectively, the energy and the degeneracy of the energy levels of CH_4; $\Gamma_i = -\partial \ln E_i / \partial \ln V$ is the Grüneisen parameter of the ith rotational level of CH_4.

Unfortunately, we cannot use this expression to make a quantitative comparison of the calculations and the experimental data on $\Delta\alpha$, since the calculation involves contradictory values of Γ_i from different published sources (e.g. see Refs. 3 and 15). Therefore we reduced our task and tried to estimate the energy gap between the ground and first excited rotational states of the CH_4 molecules from our experimental results. As the first step we found the temperature below which the contribution of the $J>1$ levels to $\Delta\alpha$ of the solutions Kr+0.76% CH_4 is negligible. For this, we calculated [see Eq. (1)] $\Delta\alpha$ for the case where only the two lowest levels $A1A1$ and $T1T1$ are involved in thermal expansion (Fig. 2). The temperature dependence of $\Delta\alpha$ calculated for an equilibrium distribution of the spin modifications of CH_4 is shown in Fig 6. The Γ_i values can be found from the rotational spectra of the orientationally disordered CH_4 molecules (O_h spatial symmetry) in the antiferrorotational phase of solid methane (Fig. 2).

Curve *1* is $\Delta\alpha(T)$ with twelve low-lying rotational levels (Fig. 6); curve *2* is calculated for a spectrum with only the two lowest levels. It is evident that both thermal expansion coefficients are identical below 2.7 K.

Denoting the energy gap between the ground ($A1A1$) and first excited ($T1T1$) states by ΔE_{0-1} and the Grüneisen coefficient calculated with respect to the ground state by Γ_{0-1}, Eq. (1) can be written as

$$\Delta\alpha = \frac{c\chi N_A}{3VkT^2}\frac{g_1}{g_0}\Gamma_{0-1}\Delta E_{0-1}^2 e^{-\Delta E_{0-1}/T} \times\left(1+\frac{g_1}{g_0}e^{-\Delta E_{0-1}/T}\right)^{-2} \approx \frac{c\chi N_A}{3VkT^2}\frac{g_1}{g_0}\Gamma_{0-1}\Delta E_{0-1}^2 e^{-\Delta E_{0-1}/T}, \quad (3)$$

where g_0 and g_1 are the degeneracies of the ground and first excited states.

The approximate equality sign in Eq. (3) is used because the factor enclosed in brackets is equal to approximately 1. Our estimates show that at 1.5–2.7 K the bracketed factor varies from 1.00078 to 1.024. Since the isothermal compressibility χ and the molar volume V are practically temperature-independent in this interval, in our calculation of ΔE_{0-1} we rewrite Eq. (3) as

$$\ln(|\Delta\alpha|T^2) = B - \Delta E_{0-1}\frac{1}{T}, \quad (4)$$

where B is the temperature-independent part. Equation (4) is a linear dependence on $1/T$ where ΔE_{0-1} is the slope coefficient. Using Eq. (4) we found ΔE_{0-1} for the solid solution Kr+0.76% CH_4, which appears to be 11.23 K. The solution Kr+0.76% CH_4 was chosen because it has the lowest content of two- and three-body clusters. Similarly, using Eq. (4) we found ΔE_{0-1} for the specific contributions of single molecules and two- and three-body clusters to the thermal expansion of our solutions (see Fig. 7).

TABLE I. The values of ΔE_{0-1} obtained for single molecules (ΔE^S_{0-1}), two-body clusters (ΔE^P_{0-1}), and three-body clusters (ΔE^T_{0-1}).

Concentration of CH_4, mol.%	ΔE^S_{0-1}, K	ΔE^P_{0-1}, K	ΔE^T_{0-1}, K
0.3	11.61	–	–
3.2	11.57	11.0*	–
6.5	11.50	10.9*	10.32*
This study	11.09	10.96	10.85

*Data from the diagram in Ref. 11.

The values obtained for ΔE_{0-1} for single molecules (ΔE^S_{0-1}), two-body clusters (ΔE^P_{0-1}), and three-body clusters (ΔE^T_{0-1}) are shown in Table I. For comparison the table also contains the corresponding energies calculated from inelastic neutron scattering data at $T=4$ K.[11]

5. CONCLUSIONS

Our dilatometric studies of the solid solutions Kr–CH_4 show that 0.76%, 5.25%, and 10.55% CH_4 impurities make a negative contribution to the thermal expansion of the solution, the value of the contribution being nonproportionally dependent on the impurity concentration.

Assuming a random distribution of the CH_4 impurity over the fcc lattice of krypton we found the contributions of single molecules and two- and three-body clusters to the thermal expansion of the solutions. We found that single molecules made mainly a negative contribution. As the CH_4 concentration increases, the negative contribution of the single molecules is partially compensated by the positive contribution of two-body clusters. Thus, in low-concentration solid solutions Kr–CH_4 the thermal expansion is determined by the competition between the positive contributions due to the thermal expansion of the matrix lattice and two-body clusters on the one hand and the negative contribution due to single impurity molecules on the other.

Using our experimental data on the thermal expansion of a solid solution with the highest concentration of single impurity molecules (Kr+0.76% CH_4) we estimated the energy gap between the ground and first excited rotational states. Also, ΔE_{0-1} was found for single impurity molecules and two- and three-body clusters. The results were compared with the published data.

*E-mail: aalex@ilt.kharkov.ua

[1] G. Herzberg, *Infrared and Raman Spectra of Polyatomic Molecules*, New York (1945).
[2] T. Yamamoto and Y. Kataoka, Suppl. Prog. Theor. Phys. **46**, 383 (1970).
[3] T. Yamamoto, Y. Kataoka, and K. Okada, J. Chem. Phys. **66**, 2701 (1977).
[4] D. C. Heberlein and E. D. Adams, J. Low Temp. Phys. **3**, 115 (1970).
[5] A. N. Aleksandrovskii, V. I. Kuchnev, V. G. Manzhelii, and A. M. Tolkachev, Phys. Status Solidi B **73**, K111 (1976).
[6] A. N. Aleksandrovskii, V. B. Kokshenev, V. G. manzhelii, and A. M. Tolkachev, Fiz. Nizk. Temp. **4**, 915 (1978) [Low Temp. Phys. **4**, 435 (1978)].
[7] V. G. Manzhelii, A. I. Prokhvatilov, I. Ya. Minchina, and L. D. Yantsevich, *Handbook of Cryocrystals*, Begell House, New York (1996).
[8] A. V. Soldatov, V. I. Kuchnev, A. M. Tolkachev, A. N. Aleksandrovskii, A. Yu. Ivanov, and I. Ya. Minchina, Prib. Tekh. Éksp. **4**, 237 (1990).
[9] C. R. Tilford and C. A. Swenson, Phys. Rev. **5**, 719 (1972).
[10] B. Asmussen, M. Prager, W. Press, H. Blank, and C. J. Carlile, J. Chem. Phys. **97**, 1332 (1992).
[11] B. Asmussen, W. Press, M. Prager, and H. Blank, J. Chem. Phys. **98**, 158 (1993).
[12] R. E. Behringer, J. Chem. Phys. **28**, 537 (1958).
[13] K. Nishiyama and T. Yamamoto, J. Chem. Phys. **58**, 1001 (1973).
[14] A. N. Aleksandrovskii, E. A. Kosobutskaya, V. G. Manzhelii, and Yu. A. Freiman, Fiz. Nizk. Temp. **10**, 1001 (1984) [Low Temp. Phys. **10**, 522 (1984)].
[15] A. Cabana, G. B. Savitsky, and D. F. Hornig, J. Chem. Phys. **39**, 2942 (1963).
[16] I. Ya. Minchina, V. G. Manzhelii, M. I. Bagatskii, O. V. Sklyar, D. A. Mashchenko, and M. A. Pokhodenko, Fiz. Nizk. Temp. **27**, 773 (2001) [Low Temp. Phys. **27**, 568 (2001)].

This article was published in English in the original Russian journal. Reproduced here with stylistic changes by AIP.